

An Automated Setup for Battery Electrolyte Research in Distributed Materials Acceleration Platforms

Monika Vogler

Vollständiger Abdruck der von der TUM School of Natural Sciences der Technischen
Universität München zur Erlangung einer

Doktorin der Naturwissenschaften (Dr. rer. nat.)

genehmigten Dissertation.

Vorsitz: Prof. Dr. Christopher Stein

Prüfende der Dissertation:

1. Prof. Dr.-Ing. Helge Stein
2. Prof. Dr. Dominik Bucher
3. Priv.-Doz. Dr. Benno Meier

Die Dissertation wurde am 05.11.2024 bei der Technischen Universität München eingereicht
und durch die TUM School of Natural Sciences am 22.11.2024 angenommen.

Zusammenfassung

Diese Arbeit beschreibt den automatisierten Versuchsaufbau *Autonomous Synthesis and Analysis of Battery Electrolytes* (ASAB) zur Formulierung und Analyse von flüssigen Batterieelektrolyten mit seinen verschiedenen Betriebsmodi. Trotz der Möglichkeit in vollautomatisierten Materialbeschneunigungsplattformen (engl. *Materials Acceleration Platforms* (MAPs)) betrieben zu werden, ermöglicht der modulare Aufbau des Systems den teilautomatisierten oder konventionellen Betrieb der Einzelkomponenten.

Eine der Komponenten ist ein Tischgerät für die Kernresonanzspektroskopie (engl. *nuclear magnetic resonance spectroscopy* (NMR)), welches in dieser Arbeit als ein Beispiel für den konventionellen Betriebsmodus dient. Seine Anwendung zur Bestimmung von Selbstdiffusionskoeffizienten für Anionen in Elektrolyten, die Lithiumhexafluorophosphat (LiPF_6) oder eines der Hückelsalze Lithium 4,5-dicyano-2-(trifluoromethyl)imidazol (LiTDI), Lithium 4,5-dicyano-2-(pentafluoroethyl)imidazol (LiPDI) oder Lithium 4,5-dicyano-2-(n-heptafluoropropyl)imidazol (LiHDI) als Leitsalz enthalten, wird dargestellt. Diese Daten werden anschließend mit Viskositäts- und Leitfähigkeitsmesswerten sowie weiterer spektroskopischer Analysen, die von Projektpartnern beigetragen wurden, kombiniert, um mögliche Unterschiede zwischen den Elektrolyten zu untersuchen.

Des Weiteren schließt diese Arbeit zwei Demonstrationen des ASAB Versuchsaufbaus ein, in denen dieser durch Integration in verteilte MAPs in seinem autonomen Betriebsmodus arbeitet. Diese verteilten MAPs verbinden Geräte and Computerprogramme verschiedener europäischer Standorte. In diesem Zusammenhang wird gezeigt, dass der ASAB Versuchsaufbau in der Lage ist, experimentell bestimmte Daten für die Dichte, Viskosität und ionische Leitfähigkeit zu den MAPs beizutragen. Neben diesen direkten Beiträgen, erlaubt der ASAB Versuchsaufbau auch eine Einbindung in einen Arbeitsablauf, in welchem er dazu dient, Elektrolyte für die weitere Verwendung in einem anderen Aufbau bereitzustellen. Diese Funktionalität wird in der zweiten dieser Demonstrationen gezeigt.

Insgesamt wird die Betriebsfähigkeit und Vielseitigkeit des ASAB Versuchsaufbaus sowohl in verteilten MAPs sowie in einer konventionellen Studie im Bereich der Batterieforschung dargestellt. Dies deckt verschiedene Konfigurationen des ASAB Versuchsaufbaus ab, welche die angeschlossenen Methoden, den Betriebsmodus, das Ziel der jeweiligen Studie und die Art, wie der Versuchsaufbau zur Studie beiträgt, betreffen. Darüber hinaus wird die hohe Relevanz der Laborautomatisierung aus den vorgestellten Anwendungsfällen deutlich und motiviert weitere Forschung in diesem Bereich.

Abstract

This thesis describes the automated *Autonomous Synthesis and Analysis of Battery Electrolytes* (ASAB) setup for the formulation and analysis of liquid battery electrolytes with its different modes of operation. Despite its capability to operate in fully autonomous *Materials Acceleration Platforms* (MAPs), the modularity of the setup also allows the partially automated or conventional use of its individual components.

One of the connected components is a benchtop *nuclear magnetic resonance spectroscopy* (NMR) instrument, which in this thesis serves as an example for the conventional mode of operation. Its deployment for the determination of self-diffusion coefficients of anions in electrolytes containing *lithium hexafluorophosphate* (LiPF_6) or one of the Hückel-type salts *lithium 4,5-dicyano-2-(trifluoromethyl)imidazolid* (LiTDI), *lithium 4,5-dicyano-2-(pentafluoroethyl)imidazolid* (LiPDI), and *lithium 4,5-dicyano-2-(n-heptafluoropropyl)imidazolid* (LiHDI) as a conducting salt is shown. This data is subsequently combined with values for viscosity, ionic conductivity, and additional spectroscopic analyses contributed by project partners to investigate potential differences between the electrolytes.

Further, this thesis includes two demonstrations of the ASAB setup operating in its autonomous mode through the integration into distributed MAPs that connect hardware and software modules from various locations across Europe. In this context, the capability of the ASAB setup to contribute experimentally determined data for the density, viscosity, and ionic conductivity of electrolytes to the MAPs is shown. Besides these direct contributions, the ASAB setup also allows to be integrated into a workflow, in which it serves to provide electrolytes for further use in a different setup. This functionality is shown as a part of the second of these demonstrations.

Overall, the functionality and versatility of the ASAB setup in distributed MAPs as well as in a conventional study in the field of battery research is depicted. This covers different configurations of the ASAB setup concerning the connected experimental methods, the mode of operation, the aim of the respective study, and the means by which the setup contributes to the study. Furthermore, the high relevance of laboratory automation gets apparent from the demonstrated use cases and motivates further research in this field.

Contents

Acronyms	ix
1 Introduction	1
2 Background and State of the Art	3
2.1 Lithium-ion Batteries	3
2.2 Battery Electrolytes	4
2.3 Materials Acceleration Platforms (MAPs)	7
3 Methods	11
3.1 Nuclear Magnetic Resonance Spectroscopy (NMR)	11
3.2 Electrochemical Impedance Spectroscopy (EIS)	15
3.3 Densimetry	17
3.4 Viscometry	18
3.5 The Walden Plot	20
4 The ASAB Setup	23
4.1 The hardware setup	24
4.1.1 The formulation unit	25
4.1.2 The analysis instrumentation	26
4.2 The software package	27
4.3 A typical experiment	28
4.4 Modes of operation	29
4.5 The connection to FINALES	29
5 Investigation of Hückel-type conducting salts for battery electrolytes	31
6 Geographically distributed autonomous MAPs	71
6.1 Autonomous operation as part of a MAP	71
6.2 Integration into a workflow in parallel to direct contribution to a MAP	92
7 Discussion and Conclusion	141
8 Outlook	147
Bibliography	149
Glossary	161
A Rights and Permissions from publishers	169
A.1 Novel imidazole salts	169
A.2 Brokering between tenants	169
A.3 Autonomous battery optimisation	170
B Additional resources and tools	171

Acronyms

D ₂ O	deuterium oxide
HF	hydrogen fluoride
LiCoO ₂	lithium cobalt oxide
LiFePO ₄	lithium iron phosphate
LiF	lithium fluoride
LiPF ₆	lithium hexafluorophosphate
PF ₅	phosphorus pentafluoride
AI	artificial intelligence
AiiDA	automated interactive infrastructure and database for computational science
API	application programming interface
ASAB	Autonomous Synthesis and Analysis of Battery Electrolytes
AutoBASS	Automatic Battery Assembly System
BattINFO	Battery Interface Ontology
CE	counter electrode
CEI	cathode-electrolyte interphase
CPE	constant phase element
DMC	dimethyl carbonate
DTDPh	benzo[d][1,3,2]dioxathiole 2,2-dioxide
EC	ethylene carbonate
EIS	electrochemical impedance spectroscopy
EMC	ethyl methyl carbonate
EOL	end-of-life
FAIR	findable, accessible, interoperable, reusable
FEC	fluoroethylene carbonate
FEP	fluorinated ethylene propylene
FID	free induction decay
FINALES	Fast Intention-Agnostic Learning Server
GUI	graphical user interface
HELAO	Hierarchical Experimental Laboratory Automation and Orchestration software
IR	infrared spectroscopy

J-PGSE	J-compensated pulsed gradient spin echo
LECA	Liquid Electrolyte Composition Analysis
LiDFTFSI	lithium (difluoromethanesulfonyl)(trifluoromethanesulfonyl)imide
LiHDI	lithium 4,5-dicyano-2-(n-heptafluoropropyl)imidazolid
LiPDI	lithium 4,5-dicyano-2-(pentafluoroethyl)imidazolid
LiTDI	lithium 4,5-dicyano-2-(trifluoromethyl)imidazolid
LNO	LiNiO ₂
MADAP	Modular and Autonomous Data Analysis Platform
MAP	Materials Acceleration Platform
MD	molecular dynamics
ML	machine learning
NMC811	LiNi _{0.8} Mn _{0.1} Co _{0.1} O ₂
NMR	nuclear magnetic resonance spectroscopy
OVERLORT	Overlooking Orchestrating Tenant
PC	propylene carbonate
PGSE	pulsed gradient spin echo
ppm	parts per million
PTFE	polytetrafluoroethylene
RE	reference electrode
SDK	software development kit
SDL	self-driving laboratory
SEI	solid-electrolyte interphase
SQL	Structured Query Language
TMS	tetramethylsilane
UV-VIS	ultraviolet visible spectroscopy
VC	vinylene carbonate
VTD	vibrating tube densimetry
WE	working electrode

1 Introduction

In its report from 2023, the Intergovernmental Panel on Climate Change (IPCC) names the intensified use of renewable energies such as wind or solar energy among the valid measures to counter climate change [1]. These renewable energy sources do, however, not allow for an as easy balancing of fluctuations in the demand and supply of energy as the technologies based on fossil fuels [2]. The necessary management of energy availability, even in times when it cannot be obtained directly from the renewable sources, can be achieved by using energy storage technologies [2]. The IPCC further mentions the electrification in the urban areas as a relevant approach in the mitigation of climate change and states that electric vehicles got more widely used in the time between 2010 and 2019, while the price for lithium-ion batteries was significantly reduced over this period [1]. A shift towards electric vehicles and renewable energies therefore suggests an increased demand for energy storage systems in these sectors.

Batteries as energy storage solutions are advantageous in this context as they do not require specific local conditions like for example a mountain and a storage reservoir as it would be necessary for pumped storage power plants [2]. They are also comparatively compact and low maintenance [2] devices that do not require external fuels to be provided [3]. Furthermore, their ability to directly convert chemical energy to electrical energy renders them efficient means of energy storage [2, 4]. These aspects make batteries ubiquitous energy storage devices in our modern society with new applications being opened up at a high rate on various scales ranging from consumer products like mobile phones and notebooks up to stationary storages and battery electric vehicles. All these applications come with their respective set of requirements for the battery to fulfil [2]. However, materials with high performance over a wide range of parameters are unlikely to be found for example for the electrolyte [5, 6]. In the context of materials selection, the IPCC mentions the environmental impacts and criticality of raw materials and suggests among other strategies to diversify the choice of used materials [1]. The identification of novel cell chemistries is therefore a key task of current battery research. Fast developments in the market, such as the ones recorded between 2010 and 2019 [1], present the research environment with the challenge of keeping up with the pace and provide the novel materials enabling improved cycle life, higher energy density, increased safety or lower cost to name just a few examples.

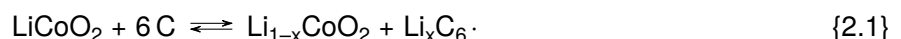
Batteries are at least composed of two electrodes and an electrolyte [3] and each of these materials can be optimised such that the cell meets certain requirements. In the case of an electrolyte that is typically a mixture of a salt, solvents, and additives, this results in numerous parameters to be optimised [7]. Such experimental series are often time-consuming and expensive [8]. At the same time, to obtain precise predictions from *machine learning* (ML) models, large amounts of high-quality data are required [8]. Depending on the kind of data, the generation of experimental datasets of the required size and quality may exceed the capabilities of a single laboratory or researcher due to a lack of equipment, expertise or the availability of personnel. The automation of experimental procedures can narrow this gap since it renders the rate of data generation independent of the working hours of human researchers. Upon coupling of automated setups with ML models, the model can immediately process the available data and suggest the most promising follow-up experiment in a so-called *closed-loop* [8]. Since experiments using this approach can operate without human input, they further decouple the experimental throughput from the availability of human researchers. If such systems are created for the purpose of accelerating the research process itself, they are referred to as *Materials Acceleration Platforms* (MAPs) [9, 10] or *self-driving laboratories* (SDLs) [11]. Recently developed distributed MAPs [12–14] take this approach even further by enabling autonomous workflows including contributors from different locations.

This thesis demonstrates these approaches in the field of liquid battery electrolyte research. A modular automated experimental setup capable of formulating and characterising liquid electrolyte solutions is demonstrated in different modes of operation. First, the conventional use of individual components of the setup exploiting the degree of automation provided by the manufacturer is demonstrated. Subsequently, two configurations of the setup, each comprising a different subset of the available components, are demonstrated using their autonomous mode of operation in the context of fully autonomous and distributed MAPs.

2 Background and State of the Art

2.1 Lithium-ion Batteries

Batteries are a flexible and well established means of storing energy. Their function is based on oxidation and reduction reactions that transform stored chemical energy to electrical energy [3, 4]. The minimal unit capable of fulfilling this function is referred to as a *cell* and batteries can be composed of a single cell or several interconnected cells depending on the requirements [3, 4]. During discharge, the stored chemical energy is transformed into electrical energy in a spontaneous reaction [3]. Batteries that need to be discarded after discharge are named *primary batteries* while those that can be recharged are called *secondary batteries* [3, 15]. Recharging the latter type of batteries requires a potential to be applied that drives the redox processes in reverse direction [3]. Repeated charging and discharging leads to a decrease of the capacity that is the amount of charge that can be stored in the battery [16]. The number of charge-discharge cycles a secondary battery can perform prior to its capacity dropping below a certain threshold is an important characteristic. A battery is typically considered to have reached its *end-of-life* (EOL) once the capacity fell below 80 % of its initial value. [17] For experimentally determining the EOL of batteries, they are cycled applying protocols defining for example the temperature and applied current to obtain the achieved number of cycles before reaching the 80 % threshold. An example of secondary batteries are lithium-ion batteries whose layout is schematically shown in Figure 2.1. A cell of such a battery typically contains a graphitic carbon material as the anode and a transition metal oxide as the cathode [3, 6, 15, 18], which are usually coated onto a copper and an aluminium current collector, respectively [19, 20]. Placed in between the two electrodes, a porous separator establishes a distance blocking the direct exchange of electrons but it allows for the diffusion of ions through its pores [21]. Furthermore, the separator is designed to act as a safety measure by melting at a certain temperature to block also the ions from passing and therefore stopping further energy from being released in the case of overheating of the cell [20, 21]. In currently commercially available lithium-ion batteries, a liquid electrolyte fills the cell and soaks the separator. An electrolyte is generally defined as a material enabling conductivity based on the movement of ions and at the same time showing no or minimal electronic conductivity [22, 23]. In batteries, its key task is to enable ions to move between the electrodes while preventing electrons from crossing [3, 6, 19]. In this way, the electrons are forced to move through the electrical circuit outside the battery to reach the opposite electrode. These electrons provide the necessary power to the connected load. Newly assembled lithium-ion cells are in their discharged state [15]. Upon charging, the lithium cations move *via* the electrolyte to the anode and travel in reverse direction towards the cathode when the cell is being discharged [15]. The total cell reaction of a lithium-ion cell using for example *lithium cobalt oxide* (LiCoO_2) as a cathode material and graphite as the anode can be written as [3, 6]



In this process, the lithium remains in its ionic form and the active materials of the electrodes perform the release or uptake of electrons [3, 6, 19]. In the course of the initial charging of the cell, some of the electrolyte components react at the electrodes and form a *solid-electrolyte interphase* (SEI) [19] at the anode and a *cathode-electrolyte interphase* (CEI) at the cathode. It is crucial for the performance of the cell that the SEI film on the anode is permeable for the cations but also protects the electrode and hinders further consumption of the electrolyte due to the continuation of the film-forming reactions [19, 24, 25].

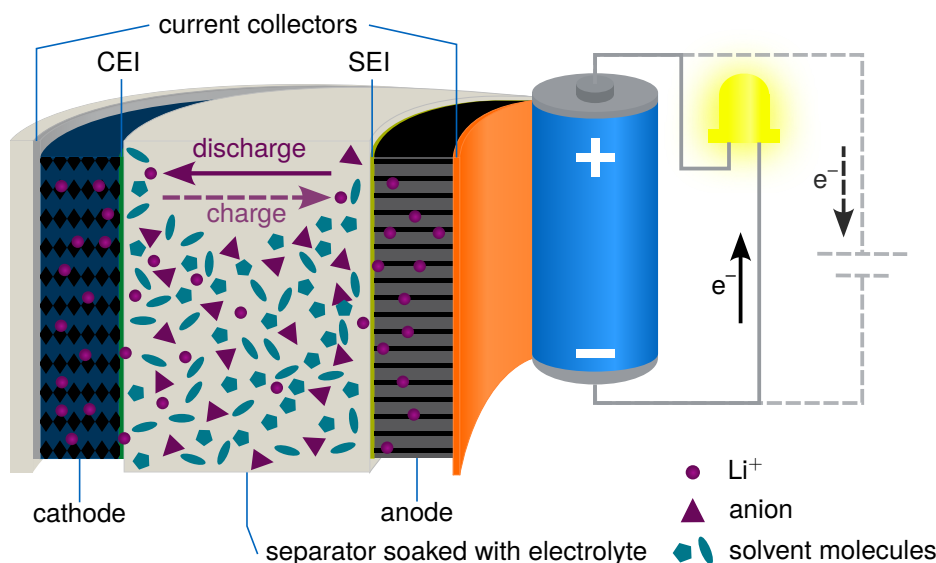


Figure 2.1 A schematic representation of the components and the flow of ions and electrons in a typical state-of-the-art lithium-ion battery. The electrodes are labelled according to their function during discharge. The dashed lines and arrows correspond to the situation during charge. Graphic inspired by [15].

The electrolyte's crucial role in the movement of the ions within the cell and the film formation on the electrodes draws research attention towards the optimisation of existing and the development of new electrolyte systems.

2.2 Battery Electrolytes

Its function in the battery gives rise to a set of requirements for an optimal electrolyte. Most of the electrolytes used in modern lithium-ion batteries are made up from a salt solution containing a lithium salt, a mixture of solvents and often also additives [6, 7, 18, 19, 26–28]. Upon dissolution and dissociation in the solvent, the salt provides mobile ions in the electrolyte. The solvation of these ions is important to obtain high performance electrolytes [7, 18, 19, 28, 29]. Solvents with a high dielectric constant can effectively dissolve the salt, but this property often conflicts with the requirement of low viscosity to enable the necessary high mobility of the ions [19]. Highly mobile ions and high ionic conductivity of the electrolyte are important characteristics for its application in batteries [18, 19, 23, 26, 28, 30, 31]. Electrolytes are typically designed to possess a high ionic conductivity at various temperatures [18, 26]. The mobility of the ions and the viscosity of the solvent are both correlated with the diffusion coefficient D of the ions. The Einstein relation connects the absolute mobility μ with the diffusion coefficient D at a given temperature T using the Boltzmann constant k_B [32]

$$D = \mu k_B T. \quad (2.1)$$

The Stokes-Einstein equation in turn relates the diffusion coefficient D with the viscosity η_{solV} of the solvent and the radius r of the solvated species at temperature T [32–36]:

$$D = \frac{k_B T}{6\pi\eta_{\text{solV}}r}. \quad (2.2)$$

These relations illustrate that the diffusion coefficients of the ionic species and the viscosity of the solvent are relevant indicators for the mobility of the ions in an electrolyte. The viscosity of the electrolytes and their solvents can for example be measured using the rolling ball method explained in chapter 3.4 [37]. The self-diffusion coefficients of various molecules in the electrolytes are experimentally accessible for example by *nuclear magnetic resonance spectroscopy* (NMR) as described in chapter 3.1 [38]. It should

be noted that self-diffusion coefficients determined using NMR techniques do not distinguish between freely moving species and aggregates containing the observed species [7, 39, 40]. This is especially relevant when observing the ionic species in electrolytes since uncharged aggregates or paired ions do not contribute to the ionic conductivity [7, 40]. In liquid electrolytes, the solidification temperature and the boiling point are considered to be further important properties as they determine the temperature range, in which the electrolyte is liquid and can be used [7, 18, 19, 23, 26, 29]. This liquid range is significantly influenced by the temperature range corresponding to the liquid phase of the solvent [19]. Since all these requirements are hardly achieved by a single solvent, electrolytes typically rely on mixtures of several solvents with different properties to achieve the desirable overall performance [19, 28]. While the aforementioned functions of the salt and the solvent are rather clear, the effects of additives can be diverse. They are typically added in small amounts and can for example reduce the flammability or increase the ionic conductivity of the electrolyte. Alongside the salt and the solvent, there are also additives that contribute to the composition of the SEI and CEI formed on the electrodes. [18, 19, 24, 26, 29] Examples of commonly used additives in electrolytes for lithium-ion batteries are *fluoroethylene carbonate* (FEC) and *vinylene carbonate* (VC) [7, 41]. Especially the composition and morphology of the SEI is crucial as it must render the film permeable for the cations but blocking for electrons. The film may further not be dissolved by the electrolyte and needs to maintain the contact to the electrode even upon the volume changes occurring during operation. [19] Apart from the desired initial reactions at the electrode surfaces to form the SEI and CEI layers, typically no further reactions of the electrolyte with any components of the cell are desired [7, 19, 23, 25, 26, 28–31]. Another important aspect in this context is the so-called *electrochemical stability window* of the electrolyte as it defines the voltage range, in which the electrolyte is not involved in oxidation or reduction reactions. The electrochemical stability window therefore limits the potentials at the electrodes that may occur in a cell using the respective electrolyte. [19] In the light of efficient charge transfer, the electrolyte further needs to properly wet the separator and the electrodes [18, 19, 31] to ensure sufficient contact for charge transfer.

On cell level, the effect of the electrolyte on the *energy density* of a cell also needs to be considered [30]. This term can either refer to the amount of energy that can be withdrawn from a battery relative to its volume or it can report the energy relative to the mass of the battery. The latter is preferably referred to as *specific energy*. [4] Although the theoretical energy density is defined by the electrode materials, the energy density achieved in practice is influenced by the amount of electrolyte added to the cell, among other factors [30]. Reducing the amount of electrolyte added to a cell results in a higher energy density due to less added mass [30, 42]. The contribution to the mass of the cell by a certain volume of electrolyte, is determined by its density. Hence, in applications, where the energy density of the battery is of interest, a low density of the electrolyte while maintaining its other performance characteristics is beneficial. Further, the density correlates with the viscosity of liquid electrolytes based on organic solvents [13]. Besides these technical requirements, safety aspects such as toxicity and flammability of the used materials influence the design of electrolyte systems [6, 18, 19, 23–25, 28, 30]. For the successful commercialisation of novel electrolyte solutions, it is further important for the material to be cost-effective [6, 19, 23, 25, 26, 28, 30].

Electrolytes based on organic solvents suffer from their inherent flammability [18, 24, 30]. Hence, research efforts include the optimisation of solvent based electrolytes alongside the investigation of alternative electrolyte systems such as ionic liquids, polymer or solid electrolytes [6, 18, 28]. This work focuses on liquid electrolytes based on organic solvents since they are currently widely used in lithium-ion batteries [6] and also relevant in the research of emerging post-lithium systems [7, 43]. Further, electrolytes of this class show high ionic conductivity and provide good contact with the electrodes. The facile adjustment of their formulation for different choices of electrodes is an additional advantage. [6] Therefore, this type of electrolytes is still a part of active research geared towards improved formulations enabling enhanced performance [5, 18, 24, 26, 44–46].

As mentioned previously, the established liquid electrolyte solutions are composed of a lithium salt dissolved in organic solvents [6, 7, 18, 19, 26, 28]. The solvents are frequently mixtures of a large amount of

one solvent and additions of a co-solvent to maximise the dielectric constant, which is relevant for the dissociation of the salt, while maintaining reasonably low viscosity to reduce hindrance of the ion transport [7, 18, 19, 28]. A commonly used conducting salt is *lithium hexafluorophosphate* (LiPF₆), which is often dissolved in a mixture of linear carbonates with low viscosity like *ethyl methyl carbonate* (EMC) or *dimethyl carbonate* (DMC) with *ethylene carbonate* (EC) as a co-solvent due to its high dielectric constant [6, 7, 18, 19, 29]. This electrolyte system has several drawbacks, which are currently researched to be mitigated or avoided. Among the main disadvantages are the instability of LiPF₆ at elevated temperatures and its reactivity with water and other protic molecules [26, 29, 47, 48]. LiPF₆ forms *phosphorus pentafluoride* (PF₅) and *lithium fluoride* (LiF) in an equilibrium reaction [19, 29, 47–50]



that is intensified at elevated temperatures [19, 29]. The *hydrogen fluoride* (HF) formed upon further reaction of PF₅ in the presence of even traces of water according to the reaction suggested in literature [19, 29, 47–50]



has toxic properties and attacks various materials within the cell [29, 47, 49, 51]. Since the above reactions generate several gaseous products, the pressure inside the cell can be increased to dangerously high values [19].

This situation motivates the investigation of alternative salts such as the *lithium 4,5-dicyano-2-(trifluoromethyl)imidazolidine* (LiTDI), *lithium 4,5-dicyano-2-(pentafluoroethyl)imidazolidine* (LiPDI), and *lithium 4,5-dicyano-2-(n-heptafluoropropyl)imidazolidine* (LiHDI) reported by Niedzicki *et al.* [52, 53] and reviewed by Armand *et al.* [54]. Additionally, the properties of electrolytes containing two salts are explored [6, 18, 26]. For example, Yan *et al.* [55] recently published their findings on improved cycling performance of cells using graphite and *LiNi_{0.8}Mn_{0.1}Co_{0.1}O₂* (NMC811) electrodes upon the addition of *lithium (difluoromethanesulfonyl)(trifluoromethanesulfonyl)imide* (LiDFTFSI) to an electrolyte containing LiPF₆ dissolved in a solvent composed of EC and EMC. They found that the addition of VC to the electrolyte system leads to a more homogeneous CEI and SEI layer in this cell chemistry and further improves the behaviour during cycling. [55] At the same time, the investigation of novel additives is ongoing. In recent research, Wölke *et al.* [44] presented the novel additive *benzo[d][1,3,2]dioxathiole 2,2-dioxide* (DTDPH) and investigated its effects in electrolytes based on LiPF₆ dissolved in EC:EMC (3:7 by weight) as a single additive and in combination with VC. For their experiments, cells with *LiNiO₂* (LNO) as the cathode and graphite as the anode active material were used. They reported enhanced cycle life and accumulated energy upon discharge compared to the reference electrolyte without additives if DTDPH is used as the only additive in the electrolyte. [44] Wölke *et al.* [44] provided analysis indicating that decomposition products of DTDPH lead to a composition of the SEI and CEI that differs from the one formed without the additive. They also mentioned that the combination of DTDPH and VC as additives achieved less favourable results [44]. Broszkiewicz *et al.* [46] investigated the suitability of LiHDI as an additive to improve the properties of the formed SEI. They studied electrolytes containing LiTDI as the salt in a solvent composed of EC and DMC with additives being either VC and FEC or different amounts of LiHDI. Compared to samples containing VC and FEC additives, the samples using LiHDI instead were found to have higher ionic conductivity of the electrolyte and improved capacity retention at 60 °C in coin cells using graphite and *lithium iron phosphate* (LiFePO₄) as electrodes with the LiFePO₄ limiting the capacity. [46] Although these are only a few examples, they illustrate the continuing relevance of research in the field of electrolytes based on organic solvents.

The elucidations in this chapter further illustrate the diversity of electrolyte systems and the requirements they need to fulfil. Besides the bulk properties of the electrolytes, also their behaviour at the numerous interfaces within the battery plays a significant role when designing electrolytes for high performance batteries [30]. A study by Rahmanian *et al.* [5] showed, that there is no globally optimized formulation for an electrolyte composed of LiPF₆, EC, EMC, and *propylene carbonate* (PC) providing high ionic conductivity across various temperatures. The composition of electrolytes is therefore typically tailored for the relevant

parameter range [6, 25], which usually requires a large number of experiments due to the numerous components constituting a battery electrolyte and various parameters influencing its performance [7]. In pursuit of a reduction of experiments required for such studies while deepening the understanding of the investigated processes, automated and computational approaches such as those by Chen *et al.* [27] and Yan *et al.* [45] are increasingly deployed.

2.3 Materials Acceleration Platforms (MAPs)

Automation increasingly dominates various sectors of modern society. Equipment manufacturers progressively offer *application programming interfaces* (APIs) and *software development kits* (SDKs) enabling the users to interact with the devices using a computer [56, 57]. This development allows to incorporate such devices into computer-controlled workflows as was for example demonstrated by Rahmanian *et al.* [58]. Recent efforts in the automation of materials research are focused on MAPs as suggested by Aspuru-Guzik and Persson [9]. According to Tom *et al.* [11], the concept is also referred to as SDLs in recent literature. These platforms combine automated experimental and computational capabilities and complement them with *artificial intelligence* (AI) functionalities to guide the research process with the aim of shortening the time for the development of novel materials [9–11, 59]. Further, a more efficient use of infrastructure and devices is fostered in MAPs by ML-based planning of the experiments [11, 59]. At the same time, the achievable repeatability is improved by the extensive automation of the involved processes [11, 60]. These aspects of automation allow the researchers to leave the technical execution of experiments or computations to the MAP while focusing on generating or intensifying the understanding of the scientific coherences [10, 59]. Although, the majority of data generated in modern laboratories are output in a digital form, they are sometimes still read from screens to be subsequently processed and analysed in partially manual procedures. MAPs that can handle the raw data formats output by the various connected modules, significantly facilitate the data management and in parallel collect further metadata while performing their tasks resulting in a more comprehensive documentation of the procedures [9–11, 58]. Since this metadata is also collected for procedures that do not finish successfully, valuable datapoints can be obtained, which are currently rarely available but valuable for the training of ML models [9, 11, 61, 62]. Overall, the reduced human effort to generate data can provide large, consistently formatted datasets like the ones reported by Rahmanian *et al.* [63] or Nuss *et al.* [64] that can be used for the training of ML or AI models [9, 11]. An overarching goal for MAPs is the implementation of inverse design procedures, where a set of predefined properties is provided and the MAP is charged with the task to find a material showing these properties. The features of MAPs elucidated above enable researchers to deploy methods that would not be available for them in a regular laboratory setting for example due to lack of equipment. This empowers further parts of the research community to get involved in solving current research questions. [9, 10]

For MAPs to effectively improve the research process, they need to fulfil certain design criteria. A key challenge in MAPs is to achieve a high degree of automation and autonomy while at the same time maintaining flexibility and adaptability to varying research tasks [59, 65]. The human efforts and tasks related to configuring and operating a MAP for a study must be minimised, because otherwise the MAP-approach will be less efficient than conventionally performing the relevant procedures. In this context, it is important to also consider manual preparations and subsequent work. [65] The necessary versatility of MAPs is frequently achieved by modular designs, which for example enable the facile addition or removal of modules [9, 58, 59, 65]. Along with the modularity of the system comes the challenge of enabling efficient and robust collaboration and communication between the modules [10, 65]. Therefore, standardised interfaces for the modules and defined structures for communication within a MAP are needed [9–11]. In this context, Tom *et al.* [11] mention orchestrators such as the *Hierarchical Experimental Laboratory Automation and Orchestration software* (HELAO) [58] or ChemOS [66, 67], to name only two of their examples, that approach the topic of coordinating the activities of the instruments connected to a MAP. Additionally, Tom *et al.* [11] note the development of ontologies in the field of MAPs that serve to communicate details

about the performed research. This is enabled by ontologies since they are, according to Clark *et al.* [68], networks of interconnected concepts that enable machines to process the meaning of data. Consistent and standardised data structures are further relevant when reporting the data generated by a MAP to open databases like for example Zenodo [69] or the Materials Cloud Archive [70] as it facilitates the reusability of the data and promotes *findable, accessible, interoperable, reusable* (FAIR) [71] data standards.

Besides the requirements that need to be fulfilled by the individual MAP, changes in the research environment are needed. Due to the inherent multidisciplinary nature of the development and operation of MAPs, tight collaborations within the research community will be crucial to achieve further progress [9, 10]. An even more profound issue is that programming and software development skills are often not included in the curricula of natural scientists or engineers, but are typically needed in the field of MAP development [10, 11, 59]. Ongoing efforts of incorporating these topics in the study plan need to be continued and intensified.

In 2024, Hung *et al.* [72] and Tom *et al.* [11] presented classification systems to rank the automation and autonomy of laboratories. Hung *et al.* [72] suggest six levels of autonomy ranging from 0 to 5 and consciously refrain from separately considering hardware and software automation but suggest to assign the levels in various categories associated with the research process. Tom *et al.* [73] propose to assign levels from 0 to 3 for software and hardware separately and subsequently deduce a level ranging from 0 to 5 for the SDL based on these. Hung *et al.* [72] and Tom *et al.* [11] both note that full automation of the research processes in a laboratory may, however, not be desirable in all use cases for example due to high requirements in versatility or safety concerns in laboratories commonly used by automated setups and human researchers.

By the time this work commenced in 2021, Dave *et al.* [74] had recently published an autonomous study performed with their automated experimentation platform coupled with a Bayesian optimiser that they had developed. Their setup autonomously identified novel electrochemically stable aqueous electrolytes for battery applications by preparing electrolyte formulations from stock solutions and measuring their ionic conductivity alongside further electrochemical measurements and the pH value [74]. This publication inspired the creation of the *Autonomous Synthesis and Analysis of Battery Electrolytes* (ASAB) system presented in this thesis. Earlier work on automated and autonomous research setups includes the *Chemputer* by Steiner *et al.* [75] and the *Artificial Chemist* by Epps *et al.* [76] that can perform flow chemistry experiments. Steiner *et al.* [75] additionally report an abstraction of chemical synthesis processes for improved shareability and reproducibility of the procedures. In 2020, Burger *et al.* [77] reported a setup consisting of a robotic arm on a mobile base that could move in a laboratory and autonomously perform experiments in a very similar manner as a human researcher would do it. Moreover, software packages enabling the orchestration of automated experimental setups were being developed at that time such as HELAO [58] or had already been published like ChemOS [66]. Further software frameworks in the field of computational research focused on data and workflow management such as the *automated interactive infrastructure and database for computational science* (AiiDA) [78] or Globus [79, 80] were available and continuously developed further. The domain ontology *Battery Interface Ontology* (BattINFO) for the electrochemistry community was under development by Clark *et al.* [68, 81]. The above examples are not exhaustive, but they illustrate that this work was started in an environment of vivid development of diverse aspects of automated experimentation and data management. The experimental platforms were mostly constrained to individual laboratories and MAPs at that time rarely included instruments and facilities across different locations or institutions nor was it common to include automated and manual procedures in a single MAP.

In the following years, Dave *et al.* [82] presented another closed-loop autonomous study using a different automated experimentation setup connected to their Bayesian optimiser for the investigation of non-aqueous battery electrolytes for lithium-ion batteries. Around the same time, Krishnamoorthy *et al.* [83] reported an automated high-throughput setup for electrolyte screening that can handle liquid as well as

solid components to prepare electrolyte formulations for subsequent measurement of their ionic conductivity. This setup is capable of generating large datasets like the one used by Flores *et al.* [84] to investigate the influence of salt concentration and temperature on the ionic conductivity of electrolytes and by Rahmanian *et al.* [5] for the optimisation of electrolyte formulations. The latter study demonstrated the *Modular and Autonomous Data Analysis Platform* (MADAP) [85] designed for the automated analysis of electrochemical data that was used with the version of the ASAB setup deployed in chapter 6.2 [14, 86] for the automated analysis of results obtained from *electrochemical impedance spectroscopy* (EIS) measurements. Another application building on the large datasets generated using the setup reported by Krishnamoorthy *et al.* [83] was recently communicated by Yan *et al.* [45], who presented their *Liquid Electrolyte Composition Analysis* (LECA) package capable of creating workflows deploying a variety of existing ML packages to facilitate data analysis and model selection with the aim of generating more insights from the obtained datasets. In parallel to these activities, Zhang *et al.* [41, 60] developed and presented two versions of the *Automatic Battery Assembly System* (AutoBASS) robotic setup to demonstrate the precision and repeatability of robotic coin cell assembly and its application in battery research. These examples for the development in the field of automated and autonomous experimentation show the continued integration of experimental setups with ML functionalities and the further exploitation of the thus achievable repeatability and acceleration. The ASAB setup described in the present thesis resembles the examples of the flow setups presented above but is designed with a strong focus on versatility, modularity and connectivity to MAPs in mind.

In parallel to the developments in the area of experimentation, improvements of orchestrators included for example a new version of ChemOS reported by Sim *et al.* [67] and the publication of HELAO by Rahmanian *et al.* [58], who in this context demonstrated its capability to enable the operation of two devices in a laboratory setting such that their results complement each other in the ML-guided optimisation of a mathematical function used to replace experimental results for the purpose of this demonstration. Expanding the idea of the latter demonstration beyond an individual laboratory, the *Fast Intention-Agnostic Learning Server* (FINALES) framework was designed as a central unit for communication connecting resources at various geographically distributed locations [13, 14]. The initial demonstration of FINALES was published in 2023 [13] and is included in this thesis in chapter 6.1. The result of the continued development of FINALES is shown in chapter 6.2 and was published in 2024 [14] shortly after Strieth-Kalthoff *et al.* [12] communicated their design of a decentralised MAP demonstrated in a study identifying organic molecules suitable for the use in lasers guided by a central AI unit.

3 Methods

3.1 Nuclear Magnetic Resonance Spectroscopy (NMR)

The NMR method is based on the interaction of nuclear spins with an external homogeneous magnetic field overlaid with a second magnetic field. In the experiment, a homogeneous magnetic field \vec{B}_0 is applied across the sample in z -direction. [38] As a consequence of the applied field, the spins in the sample reorient [38, 87]. From quantum mechanics it is known, that the spins orient in a way that makes the z -component of their angular momentum, P_z , a half-integer or integer multiple of the reduced Planck constant, $\hbar = \frac{h}{2\pi}$ [38]. This results in a quantisation of the magnetisation along \vec{B}_0 , μ_z , described by [38]

$$\mu_z = m \cdot \gamma \cdot \hbar \quad (3.1)$$

with the gyromagnetic ratio of the nucleus γ and m being the magnetic quantum number. The quantisation results in several possible orientations of the spin with respect to \vec{B}_0 . [38] The preferred orientation of the spins along \vec{B}_0 gives rise to a net magnetisation of the sample, which in the classical picture is thought of as being precessing around the direction of \vec{B}_0 with the so-called *Larmor frequency* [38, 87]. The Larmor frequency is expressed as [38]

$$\nu_L = \left| \frac{\gamma}{2\pi} \right| \cdot B_0, \quad (3.2)$$

where ν_L and B_0 denote the Larmor frequency and the magnetic flux density, respectively [38]. Since the gyromagnetic ratio is specific for a nucleus, the Larmor frequency is a characteristic measure for a nucleus as long as its environment remains unchanged [87].

NMR experiments exploit transitions between different orientations of spins with respect to \vec{B}_0 , which are associated with different energy levels [38, 87]. The relative occupation of two energy levels in thermal equilibrium at a given absolute temperature T in K is described by the Boltzmann statistics as [38]

$$\frac{n_{high}}{n_{low}} = e^{-\frac{\Delta E}{k_B \cdot T}}. \quad (3.3)$$

In equation 3.3, n_{high} and n_{low} are the number of spins in the higher and lower energetic state, respectively. ΔE represents the energy difference between the states and k_B is the Boltzmann constant. From this it can be seen that the two energy levels are not occupied equally. Since the factor $k_B T$ typically is significantly higher than the energy difference between the states, the occupation of the lower energetic state is marginally higher in the order of *parts per million* (ppm). [38] As a consequence of this difference in occupation, the sum of the μ_z of all nuclei yields a resulting equilibrium magnetisation M_0 along the z -axis, which is oriented parallel to \vec{B}_0 [38, 87]. A state, in which the occupation of both energy levels is equilibrated is called *saturated* and no NMR signal is detected in this case [38]. In modern NMR experiments, radio frequency pulses are used to excite transitions between the energy levels. The absolute value of the frequency ν of a photon able to excite a transition corresponds to the Larmor frequency of the nucleus. [38, 87] Based on equation 3.2, the energy E_{photon} of the photon required to trigger a transition can be expressed as [38, 87]

$$E_{\text{photon}} = h \cdot \nu_L = \hbar \cdot \gamma \cdot B_0, \quad (3.4)$$

where h is the Planck constant. The slightly higher occupation of the lower energy level in equilibrium gives rise to a predominance of absorption transitions, which leads to an NMR signal. From the elucidations

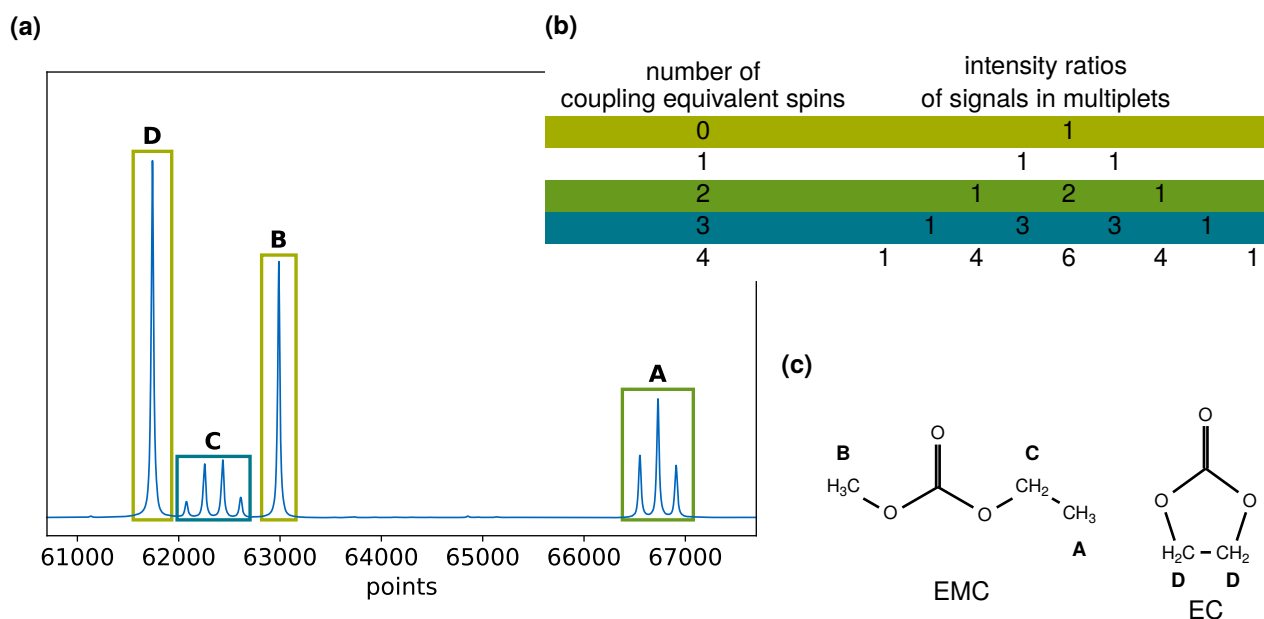


Figure 3.1 (a) The ^1H -NMR spectrum of an electrolyte containing LiPF_6 , EC and EMC. The data is used from [88]. Further analysis of the spectrum can be found in the second row of Table S5 in the Supporting Information shown in chapter 6.2. (b) An excerpt of Pascal's triangle, which is relevant when determining the multiplet structure and the relative intensities of signals for nuclei with spin equal to $\frac{1}{2}$ based on the number of coupling nuclei [38]. The colours relate the multiplets in the spectrum to the applicable row in Pascal's triangle. (c) The molecules giving rise to the NMR signals in this example. The letters in bold assign the signals in the spectrum to the relevant groups in the molecules.

above, the proportionality relation between the difference in the occupation of the energy levels and the NMR signal intensity gets evident. This renders the signal also proportional to the concentration, which determines the number of spins in the measured sample volume. Two specifically important pulses in NMR experiments are the 90° pulse and the 180° pulse, which rotate the net magnetisation by 90° and 180° away from its equilibrium orientation, respectively. [38]

So far, this section described how NMR signals arise for different nuclei. NMR techniques also provide information about the surrounding of the nuclei. Various shielding effects originating, for example from the electronic structure around a nucleus, alter the effective magnetic field acting on the nucleus. This results in different resonance frequencies and consequently in separated NMR signals for differently surrounded nuclei. Additionally, neighbouring nuclei affect the resonance frequency observed in the spectra. [38] The interaction among nuclei, which are close to each other, is called spin-spin coupling, scalar coupling or *J-coupling*. The coupling can be thought of as arising from neighbouring spins influencing the effective field at the position of the observed nucleus. [38, 87] Consequently, the resonance frequency of the observed nucleus as per equation 3.2 is also affected by the state of the surrounding spins. These interactions among the nuclei cause a fine structure in the spectra, meaning that not a single signal is observed, but it splits up into multiplets. The number of signals in a multiplet depends on the number of chemically equivalent nuclei coupling with the observed nucleus. [38] The separation between the signals in a multiplet is designated by the coupling constant J [38, 87]. This quantity is reported in the unit Hz, because of its independence from the magnetic field strength B_0 [38, 87]. The number of signals and the ratio of their intensities within a multiplet can be obtained from Pascal's triangle [38]. Figure 3.1 shows the relation between Pascal's triangle and a ^1H -NMR spectrum of an electrolyte containing LiPF_6 , EC and EMC with a molar ratio of EC:EMC of approximately 1.11. Further details can be found in the second row of Table S5 in the Supporting Information included in chapter 6.2.

The quantity, which is actually measured during the experiment, is the voltage induced in a receiver coil mounted along the y -axis. The voltage in this coil is induced by the transversal component of the macroscopic magnetisation, M_y . [38, 87] It shows a periodic time dependence with a decreasing amplitude due to transverse relaxation [87]. The recorded signal is therefore called a *free induction decay* (FID). The commonly reported spectra in the frequency domain are obtained from the FID by application of a *Fourier transform*. [38, 87] Usually, the reported spectra use the so-called *chemical shift* δ as their x -axis, which is a scale relative to a reference. For organic molecules, mostly *tetramethylsilane* (TMS) is used as a reference. This substance may be added to the sample as an *internal standard* or kept separate as an *external standard* but still measured together with the sample. [38] The dependency of the resonance frequency on the field strength as shown in equation 3.2 necessitates the use of a relative scale, if measurements using various magnetic field strengths B_0 are to be compared [38, 87]. The definition of the chemical shift is [38]

$$\delta = \frac{\nu - \nu_{\text{ref}}}{\nu_{\text{ref}}}. \quad (3.5)$$

It can be seen, that equation 3.5 relates the resonance frequency ν of the observed nucleus in the molecule of interest and the resonance frequency of the same type of nucleus in the reference substance ν_{ref} . Chemical shifts are usually given in ppm with the chemical shift of the reference substance being considered to be 0 ppm. [38, 87]

To record high resolution NMR spectra, the \vec{B}_0 field needs to be very stable and well-defined [89]. The stability of the \vec{B}_0 field is improved by using a lock signal [87, 89], which is monitored by an additional NMR experiment running on a separate channel of the instrument, typically measuring the signal of *deuterium oxide* (D_2O) used as a lock solvent [89]. A feedback loop adjusts the current in a coil such, that the resonance frequency of the lock signal remains unchanged [87]. Just as mentioned before for the reference compound, the lock solvent may be internal or external to the sample [89].

In this thesis, NMR spectra serve to analyse the formulated electrolytes regarding their composition and self-diffusion coefficients. Information about the composition allows inferences about the accuracy of the sample preparation, which is of specific interest in the case of samples prepared in an automated manner. The investigation of the composition relies on the direct proportionality of the integral of NMR signals to the number of nuclei contributing to the signal observed under ideal conditions [89–91]. This relation can be used to determine numerical proportions of molecules by analysing their respective signals [89–91]. After recording a regular FID, the spectrum must be thoroughly phased and baseline corrected to ensure proper integration of the signals. The values of the integrals subsequently need to be normalised by the number of contributing nuclei prior to calculating their ratio. The thus obtained ratio provides information about the relative amount of the respective nuclei present in the sample. [89] The pulse sequence used for recording an FID, which can be used for this analysis, is shown in Figure 3.2.

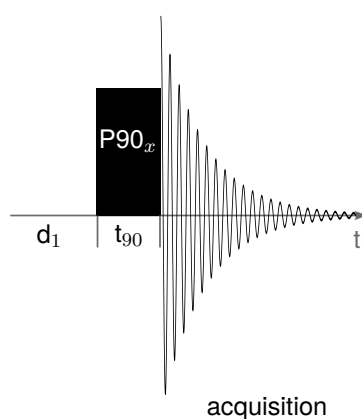


Figure 3.2 The pulse sequence of a regular FID, which can be used to analyse the composition of samples. The durations are not to scale. Based on [89].

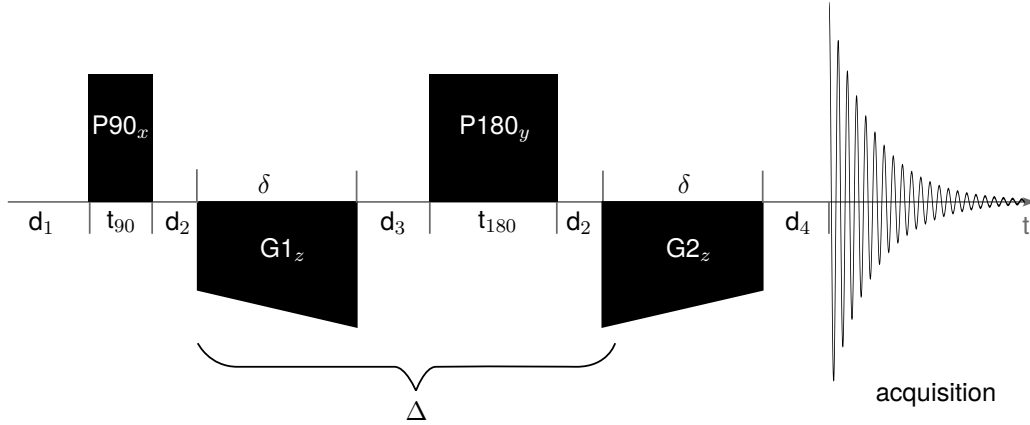


Figure 3.3 The pulse sequence used in a PGSE experiment. The durations are not to scale. Based on [89].

The determination of self-diffusion coefficients in liquid samples is possible with NMR using the *pulsed gradient spin echo* (PGSE) method [89]. The pulse sequence applied during a PGSE experiment is shown in Figure 3.3. After the 90° pulse created a transversal magnetisation, the first gradient pulse $G1$ marks the nuclei according to their position within the gradient field [89]. This is possible due to the dependence of the Larmor frequency on the local magnetic field as can be extracted from equation 3.2 [38]. The additionally applied field of the gradient pulse oriented parallel to \vec{B}_0 with its strength depending linearly on the z -position in the sample volume therefore alters the Larmor frequency depending on the location of the respective spin in the magnetic field [38]. After allowing for diffusion during the time Δ and inversion of the transversal magnetisation by the 180° pulse, the second gradient pulse $G2$ reverts the effect of $G1$ resulting in a coalescence of the transversal magnetisations giving rise to a spin echo measured in the detector coil. However, the coalescence is only complete for those spins, which did not change their z -position during the time period Δ . For spins, which diffused in the z -direction, the echo signal will have a reduced intensity I_G compared to their intensity in the homogeneous field I_0 [38, 89]. The reduction of intensity can be used to determine diffusion coefficients [38]. Self-diffusion coefficients D are obtained from the measured intensities of the signals according to [89, 92]

$$\ln\left(\frac{I_G}{I_0}\right) = -\gamma^2 \cdot \delta^2 \cdot G^2 \cdot \left(\Delta - \frac{\delta}{3}\right) \cdot D. \quad (3.6)$$

In equation 3.6, γ represents the gyromagnetic ratio of the observed nucleus, δ is the duration of the gradient pulses, and G denotes the applied gradient strength [89]. Based on equation 3.6, the self-diffusion coefficient D can be obtained from the slope of $\ln(I_G/I_0)$ versus G^2 [89] or $\ln(I_G/I_0)$ versus $\gamma^2\delta^2G^2(\Delta - (\delta/3))$. To minimise effects of J-coupling between nuclei of the same type on the phase of spectra recorded with the PGSE method, Torres, Zheng and Price [93] developed so-called *J-compensated pulse sequences*. The one they identified as the most effective includes two subsequent PGSE pulse sequences with the time for diffusion being reduced to $\Delta/2$ and the 90° and 180° following shorter after each other. They called this pulse sequence *J-compensated pulsed gradient spin echo* (J-PGSE). [93]

In this work an *Oxford Instruments X-Pulse* (Oxford Instruments plc, United Kingdom) benchtop NMR device is used. The NMR spectra can be recorded in a conventional setup by manually inserting glass tubes into the probe or a flow-through configuration shown in Figure 4.3a can be used, in which a *fluorinated ethylene propylene* (FEP) tube is fed through the bore of the probe. The latter setting allows to automatically supply samples to the NMR and perform measurements using the external D_2O -lock of the used device. In either setting the measurements are to be triggered manually. Due to the partially automated handling of the samples and possible effects on the self-diffusion coefficients, the addition of a reference substance and a deuterated lock solvent were omitted in this work. Instead, the spectra were recorded using either the digital or the external lock provided with the instrument. Due to the lack of a

reference substance, the chemical shift of the signals could not be determined except for values saved in the *MestReNova* [94] (Mestrelab Research S.L., Spain) software. Therefore, the assignment of the signals was done by relying on the structures of the multiplets and the knowledge about the compounds contained in the samples [95].

3.2 Electrochemical Impedance Spectroscopy (EIS)

In the analysis of electrochemical systems like batteries, the *electrochemical impedance spectroscopy* (EIS) enables the investigation of processes taking place at different rates. During an EIS measurement, a periodic input signal of either voltage or current is applied to an electrochemical system in equilibrium and the resulting output current or voltage signal is measured [96, 97]. The frequency of the input signal is varied across several orders of magnitude during a measurement [96, 97] and the input signal may be applied additional to a constant voltage or current, respectively [96]. Typically, measurements at high frequencies are performed first with subsequent measurements using successively lower frequencies [97]. Figure 3.4a shows a schematic representation of an input voltage signal $U(t)$ and an output current signal $I(t)$ for a frequency ω with a phase ϕ between the input and output signal. The measurement principle relies on a linear and causal relation between the input and output signals [96–98]. Since real electrochemical systems typically deviate from linearity for larger perturbations, it is important to choose a low amplitude for the input signal [96, 97]. Since the ratio of signal to noise decreases for lower amplitudes, the amplitude must be chosen such that linearity is maintained while achieving a sufficiently high signal-to-noise ratio [97, 98]. Furthermore, the properties of the system defining the response must be stable over time [96, 97]. If these conditions are met, the output signal is related to the input signal *via* a so-called *transfer function* [96, 98].

As indicated in the name of the method, the *impedance* of the system under study is the central property. It represents the resistance, which the full system opposes to a current, and is a frequency-dependent complex number [96]. It is typically denoted as $Z = Z' + iZ''$. The frequency-dependence of the impedance enables the identification of processes in the investigated system based on their time constants. Since the recorded impedance includes all the contributions present in the system, an equivalent electrical circuit selected to represent the different contributions is fitted to the data. [96] An example of such an equivalent circuit is depicted in Figure 3.4c. It can be composed of passive elements such as resistors, capacitors, and inductors [98]. There is no unique equivalent circuit to represent a dataset, but usually several circuits are able to fit the data [96, 97]. It is therefore crucial to select each component of the equivalent circuit such that it can be related to a physical process in the system under investigation. Overly complex circuits containing elements not related with a plausible process are to be avoided as they may result in a good fit at the expense of scientific interpretability. [96] The values determined for the components included in the equivalent circuit provide information about the processes taking place in the system [96], like e.g. the resistivity and thus also the ionic conductivity of battery electrolytes, which is what this technique is used for in this work.

For the analysis, *Bode plots* [99] and *Nyquist plots* [100] are commonly used to present the data [96]. A Bode plot shows the logarithm of the module of the impedance $\log(|Z|)$ and the negative phase between the input and output signal $-\phi$ as a function of $\log(\nu)$, where ν is the frequency of the applied input signal [96, 98]. This plot provides information about a large range of frequencies while directly relating the $|Z|$ and ϕ to ν [96]. The Nyquist plot presents the negative of the imaginary part $-Z''$ plotted against the real part Z' of the impedance [96]. A schematic of a Nyquist plot for a so-called *Randles circuit* [101] is shown in Figure 3.4b. In this graph, ω represents the angular frequency of the input signal [96]. The resistor R_{ct} and the capacitor C_{dl} connected in parallel in Figure 3.4c cause the Nyquist plot to include a semicircle. The distance between the onset point of the semicircle and the origin of the plot is defined by the resistor R_e . For lower frequencies (i.e. towards the right side of Figure 3.4b), the impedance Z_W shows its effect. The impedance response of this equivalent circuit is typical for electrochemical

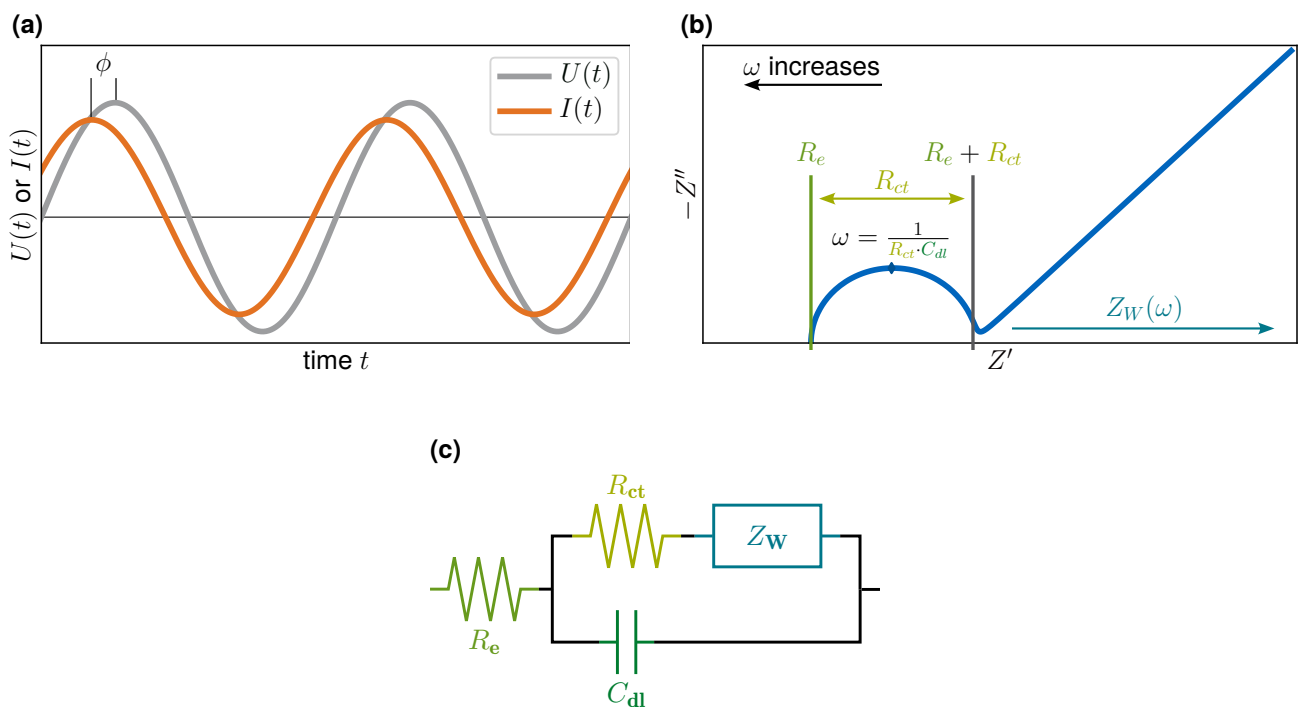


Figure 3.4 (a) A schematic representation of an applied periodic input voltage $U(t)$ and an output current $I(t)$ with a phase shift ϕ . (b) A schematic depiction of a Nyquist plot for an impedance response obtained from a Randles circuit and (c) a representation of a Randles circuit. Schematics based on [96].

systems including an electrochemical reaction [96]. Such systems are therefore frequently represented using this circuit with the resistor R_e representing the electrolyte resistance, the C_{dl} being assigned to the capacitance of the electrical double layer forming at the electrodes, and the additional resistor R_{ct} associated with the resistance of charge transfer between the electrochemically active species and the electrode [96, 98]. Randles [101] used a capacitor combined in series with a resistor to model the chemical reaction. In today's literature, this is replaced by R_{ct} combined with the impedance element Z_W instead with the latter accounting for the resistance due to mass transfer [96, 98]. Pure capacitive behaviour should result in a phase of $\phi = -90^\circ$ between the input and output signal [96]. In situations where this is not the case due to non-idealities in the investigated system, *constant phase elements* (CPEs) are used to model non-ideal capacitors [96]. Since the CPE makes some assumptions about the non-idealities of the system, the interpretation of the obtained results is not straightforward in some systems [98].

The most frequently used experimental setup to perform EIS measurements includes three electrodes, a *working electrode* (WE), a *reference electrode* (RE) and a *counter electrode* (CE). Under potentiostatic control, the potential between the WE and RE is regulated to a constant value using a potentiostat while the current passing through the CE is measured. [96] However, there is also the possibility to use a setup comprising only two electrodes [96–98]. This setup is often deployed for the investigation of battery cells because the use of a reference electrode is impractical for example due to poor accessibility [97]. In such a setup, an auxiliary electrode combines the RE and CE of the three electrode setup [96, 98]. Due to this double role of the auxiliary electrode, the control of the potential of the WE is not as accurate as in the three electrode setup [96]. The impedance measured in a two-electrode setup includes contributions from all the components and interfaces in between the electrodes [98]. Additionally, contributions of the wiring used to connect all the components can influence the measurements in a two electrode setup [96].

As described before, the resistance of the electrolyte R_e is accessible from EIS data. The resistance is related to the conductivity κ via the distance between the electrodes d and their area A according to [98]

$$\kappa = \frac{1}{R_e} \cdot \frac{d}{A}. \quad (3.7)$$

For a specific measuring cell, d and A are fixed and can therefore be summarised in a so-called *cell constant*, which can be determined from calibration with a sample of known conductivity [102]. The equation to determine the ionic conductivity of electrolytes in this work thus reads

$$\kappa = \frac{c_{\text{cell}}}{R_e} \quad (3.8)$$

with the cell constant c_{cell} [95, 102].

EIS was performed in this work using a two electrode setup with two blocking stainless steel electrodes under potentiostatic control. Details about the calibration procedure, the determined cell constant and photos of the used electrochemical cell are given in the Figures SI-5a and SI-5b in section 2.2 of the Supporting information in chapter 6.2. [14]

3.3 Densimetry

The field of densimetry of liquids provides a variety of methods for the measurement of the density of fluids [103]. Among these methods is the *vibrating tube densimetry* (VTD), which is based on the mass dependence of an oscillator's resonance frequency [103–106]. Kratky, Leopold, and Stabinger announced a densimeter device based on the VTD method in 1967 [107] and reported about it in subsequent publications [104–106, 108]. The concept suggested by Kratky, Leopold, and Stabinger is still applied in densimeters used today. Modern vibrating tube densimeters consist of a U-shaped glass tube with the open ends mounted to a heavy component acting as a counter mass minimizing influences from the device during the vibration of the tube [103, 109]. The tube typically has an outer diameter of a few millimetres and a length in the range of centimetres resulting in a small sample volume required for the measurement [109]. The vibration of the tube is created by a *drive element* and the vibration period is recorded by a *pick-up element*, for both of which various operation principles exist [103]. A frequently applied concept uses a set of permanent magnets attached to the tube and an electromagnetic coil to generate the vibration and another set of these components for detecting the vibration and determining the frequency [109]. During the measurement, the vibration frequency generated by the drive element is varied until it matches the resonance frequency of the tube. The tube is typically surrounded by a gas to minimize the friction for the vibrating tube. Further, sensors for temperature and pressure are included in the setup as these parameters are crucial to be stable during the measurement. [103] For precise measurements, variations in temperature should not exceed 0.01 K [103–105], while pressure needs to be controlled with a precision of 0.01 MPa [103]. The duration of the vibration is essential for an accurate determination of the density [103], because a sufficient number of vibration periods needs to be evaluated [103, 109].

The VTD method is based on the dependency of the vibration period in resonance from the density of the sample [103]. The measured quantity is the voltage induced in the pick-up coil [108], from which the period of the vibration under resonance conditions is determined, which in turn acts as an indirect measure of the density [103]. The density of the sample ρ_{sample} can be determined according to [103, 109]

$$\rho_{\text{sample}} = \frac{K}{4\pi^2 V_{\text{tube}}} \cdot \tau^2 - \frac{m_{\text{tube}}}{V_{\text{tube}}}, \quad (3.9)$$

with m_{tube} and V_{tube} representing the mass and the volume of the empty tube, respectively, while K is the spring constant assigned to the tube in the spring-mass-model applied, and τ denoting the period

of the vibration [103]. For an undamped oscillator, the resonance frequency is obtained according to equation 3.10 [103, 108]

$$\omega_{\text{res}} = 2\pi f_{\text{res}} = \sqrt{\frac{K}{m}} \quad (3.10)$$

with ω_{res} being the angular resonance frequency and f_{res} the resonance frequency of the vibrating tube and $m = m_{\text{sample}} + m_{\text{tube}}$ representing the mass of the tube filled with the sample [103, 108]. Since the damping must be counteracted by the excitation of the vibration, the excitation frequency must equal the resonance frequency ω_{res} [103]. Combining equation 3.10 with the relation $\omega_{\text{res}} = \frac{2\pi}{\tau}$ gives [103, 108]

$$\omega_{\text{res}} = \frac{2\pi}{\tau} = \sqrt{\frac{K}{m_{\text{sample}} + m_{\text{tube}}}} \quad (3.11)$$

Using the relation $m_{\text{sample}} = \rho_{\text{sample}} \cdot V_{\text{tube}}$ introduces the density of the sample ρ_{sample} and allows to rearrange equation 3.11 to give equation 3.9 [103].

Extracting a relation between ρ_{sample} and τ , equation 3.9 reduces to [103]

$$\rho_{\text{sample}} = p_1 \cdot \tau^2 - p_2 \quad (3.12)$$

with the parameters p_1 and p_2 [103, 104]. It is important to note, that p_1 and p_2 are functions of temperature and pressure and can be determined from calibration of the system using standards, for which the density at the temperature and pressure of interest is known [103, 109]. The range of densities used for calibration should include the sample density as extrapolations can lead to errors in the measured density due to τ^2 not being perfectly proportional to ρ across large ranges of ρ [103].

Another important aspect when aiming for precise density measurements is the cleanliness of the sample tube since residues affect the resonance frequency resulting in an erroneous determination of the sample's density. In case of residues, which cannot be removed, they must be accounted for by repeated calibration. Further, the formation of gas bubbles within the sample volume must be avoided when filling the measuring cell, because these hinder a reliable determination of the vibration period. [108]

The *DMA 4100* (Anton Paar GmbH, Graz, Austria) densimeter used in this work is based on the working principle described above and applies several advancements regarding the measurement [110, 111] and instrumentation [112, 113]. The calibration of the instrument is performed manually by detaching it from the ASAB system and hence the inert atmosphere of the glovebox. Subsequently, the calibration procedure as suggested by the manufacturer using water as a calibration liquid can be used. After draining the water from the measuring cell and careful drying using the air pump internal to the instrument, the preparations are finished by reconnecting the tubes. In the latest version of the ASAB setup, the draining of samples during the autonomous operation of the instrument is achieved by blowing pressurized nitrogen through the sample tube for a predefined period of time. Since the samples within one study typically contain the same components in varying ratios and the sample volume supplied for the measurements exceeds the minimum amount needed, potentially remaining residues of previous samples are expected to be drained by the subsequent sample or having a negligible effect on the resulting density values. Earlier implementations, such as the one used in the publication included in section 6.1 [13], accomplished the draining of the samples by pumping gas aspirated from the inert atmosphere of the glovebox to the syringe pumps through the sample tube several times. This procedure was only able to drain the sample, but not to dry the measuring cell. Hence, the subsequent sample had to drain the residues and their influence on the density measurement had to be neglected. [13]

3.4 Viscometry

The viscosity is a property of fluids, which describes the capability to accommodate stress during deformation [114]. It can also be thought of as the resistance, which needs to be overcome to make a liquid

flow [115]. Under laminar flow conditions, layers of liquid are thought to move relative to each other with a gradient in velocity [116]. The viscosity can then be understood based on the friction between the layers of liquid [117]. This approach leads to the definition of the *dynamic viscosity* η as the factor of proportionality between the shear stress τ and the shear rate $\dot{\gamma}$ [114, 117]

$$\tau = \eta \cdot \dot{\gamma}. \quad (3.13)$$

Values of the dynamic viscosity are typically reported in units of mPa s [114, 117].

Since a part of the force applied to the liquid is required to move the fluid rather than overcoming the viscosity, the *kinematic viscosity* is defined as [117]

$$\nu = \frac{\eta}{\rho}, \quad (3.14)$$

where ρ is the density of the fluid [117]. The kinematic viscosity is usually reported in units of $\text{mm}^2 \text{s}^{-1}$ [114, 117].

The dynamic and the kinematic viscosity depend on the pressure and the temperature of the fluid. Fluids, for which the viscosity is additionally dependent on the shear rate are called *non-Newtonian fluids*. In contrast, *Newtonian fluids* are characterized by their viscosity being independent of the applied shear rate. [114] The following elucidations consider the laminar flow of Newtonian fluids.

For the measurement of viscosity, various methods are available. The method applied in this work is the rolling ball viscometry, which was first suggested by Flowers [37]. The measuring setup is a variation of the falling ball viscometer [117] after Höppler [118].

In the falling ball viscometer, a ball is falling through a tube filled with the sample fluid [117]. Due to the viscosity of the sample, the ball experiences a drag force, which can be described based on Stokes' law [117, 119]

$$F_d = 6\pi\eta r v \quad (3.15)$$

relating the drag force F_d with the dynamic viscosity η of the sample, the radius of the ball r and the velocity of the ball v [117, 119]. For equation 3.15 to hold and the relation between F_d and v to be considered linear, the movement of the ball needs to be sufficiently slow [118, 119]. Besides the drag force, the buoyant force $F_b = \frac{4}{3}\pi r^3 g \rho$ acts on the ball with density ρ_{ball} , which is accelerated by the gravitational force $F_g = \frac{4}{3}\pi r^3 g \rho_{\text{ball}}$ with g being the gravitational acceleration [117]. If a balance between the accelerating force F_g and the resisting forces F_d and F_b is reached, the ball is not accelerated further and reaches its terminal velocity [117], which can be expressed as [37, 117, 119]

$$v_{\text{terminal}} = \frac{2}{9} \cdot r^2 g \cdot \frac{\rho_{\text{sample}} - \rho_{\text{ball}}}{\eta}. \quad (3.16)$$

For an experimental setup, ρ_{ball} , r , and ρ_{sample} can be determined and even chosen according to the range of viscosities of interest [37, 117]. Hubbard and Brown [120] report a simplified version of equation 3.16 as

$$\eta = k \cdot \frac{\rho_{\text{sample}} - \rho_{\text{ball}}}{v_{\text{terminal}}} \quad (3.17)$$

with k being a parameter specific for the used setup [117, 120]. Due to the temperature dependence of k [120], the temperature must be stable to 0.1 °C during the measurement [114]. The crucial influence of temperature arises due to effects of thermal expansion of the ball and the tube [37, 120, 121], which may affect the ratio of their diameters [120, 121]. Besides the temperature requirement, it is vital, that the ball rolls through the tube in a uniform motion. Therefore, irregularities at the surface of the ball or the tube must be minimised. [37]

In the falling and rolling ball viscometers, the time required by the ball to pass a defined measuring distance in the sample fluid is measured [37, 117, 118]. From this measurement, the evaluation of the viscosity

according to equation 3.17 is possible [37, 117, 120]. In the case of the rolling ball viscometer, the tube filled with the sample is inclined compared to the vertical orientation in the falling ball viscometer [37, 117]. This change in the setup allows a facile adjustment of the accelerating force by selecting the inclination angle of the tube [37]. It further allows for the tube to be inclined back and forth using the backward motion as check or additional measurements [37, 117]. The use of only small sample volumes not exposed to the laboratory environment is an additional advantage of this method [37].

The *Lovis 2000 ME* (Anton Paar GmbH, Graz, Austria) rolling ball microviscometer used in this work operates according to the Höppler method [117]. Note that Höppler's viscometer also includes a tilt of the tube in a steep angle enabling the ball to roll along its inner wall [118]. It is attached to the *DMA 4100* (Anton Paar GmbH, Graz, Austria) densimeter allowing for the direct measurement of the density in only one filling. The measurements reported in the publication in section 6.1 [13] use a gold coated steel ball 1.5 mm in diameter with a density of 7.90 g cm^{-3} rolling through a tube with an inner diameter of 1.59 mm made of borosilicate glass. The instrument is set to automatically choose an appropriate inclination angle for each measurement. Calibrations and adjustments are performed by manually loading pure deionised water into the instrument using a single-use syringe. Electrolyte samples are provided to the instrument using the ASAB setup [13].

3.5 The Walden Plot

In the context of electrolytes, viscosity values combined with data for the ionic conductivity can be used to qualitatively analyse the *ionicity* of the conducting salt in an electrolyte [122]. The ionicity can be quantified as the value obtained when dividing the molar conductivity of an electrolyte solution determined in a measurement by the value obtained from the Nernst-Einstein equation [40, 122, 123]. This interpretation of ionicity assumes the aggregation of ions as the only cause for a reduction in ionic conductivity of the electrolyte [123]. The Nernst-Einstein equation for a salt dissociating into two single-charged ions can be expressed as [32, 40, 122, 123]

$$\Lambda_m = \frac{eF}{k_B T} \cdot (D^+ + D^-) \quad (3.18)$$

with the molar conductivity Λ_m , Faraday constant F , the Boltzmann constant k_B , the elementary charge e , temperature T and the diffusion coefficients of cations, D^+ , and anions D^- , respectively [32, 40, 122, 123]. The Nernst-Einstein equation reported in 3.18 is in this form only valid for single-charged ions. In the case of multivalent ions, the equivalent conductivity (conductivity per mole of charge) is to be used instead of the molar conductivity. [32] The same is valid for the subsequent equations in this chapter.

The relation [124]

$$\Lambda_m^0 \cdot \eta_{\text{solv}} = \text{const.} \quad (3.19)$$

between the limiting molar conductivity Λ_m^0 and the viscosity of the solvent η_{solv} found by Walden in 1906 [124] is usually referred to as the *Walden rule* [28, 125]. When initially deriving this relation, Walden [124] assumed very low concentrations of the salt and variations only in the solvent for a fixed choice of the salt. It is suitable for electrolytes, in which the ions move mostly independent of each other and no distinct interactions with the solvent are present [28].

A variation of the Walden rule, which is referred to as the *fractional Walden rule* relates the molar conductivity Λ_m and the viscosity of the electrolyte η [125–129]:

$$\Lambda_m \eta^\alpha = \text{const.} \quad (3.20)$$

In equation 3.20, α is a parameter ranging between 0 and 1 [125, 127–129]. A value of α close to unity indicates a correlation between the mobility of the ions and the viscosity of the electrolyte [128]. Deviations from the unity slope indicate influences on conductivity additional to the effect of viscosity [130].

Plots of the molar ionic conductivity of the electrolyte *versus* the inverse of the dynamic viscosity, also called the *fluidity* [125] are commonly referred to as *Walden plots* [122, 125]. An example of such a plot can be found in the publication included in chapter 5 [95]. Typically, a 0.01 mol dm⁻³ aqueous KCl solution is used as a reference [122, 131] assuming the salt being fully dissociated and both ions showing the same mobility [125]. Often it is represented by a 45° line within the Walden plot choosing the units of the molar conductivity as S cm² mol⁻¹ and those for the fluidity as P⁻¹ [125]. Although the choice of KCl as a reference was criticised as being arbitrary and unsuitable especially in the context of ionic liquids [123, 132], it is still commonly used. The parameter α in equation 3.20 is the slope of the Walden plot [125, 128]. The non-ideality of the electrolyte can be quantified based on the offset from the ideal KCl line in *y*-direction, ΔW , in the Walden plot [126, 128]. ΔW can be interpreted related to the degree of dissociation of the salt in the electrolyte [125, 128]. The less dissociated the salt is, the further the electrolyte is located from the ideal KCl line [128]. Electrolytes located in the bottom right half of the graph are interpreted as having a lower ionicity meaning that the ions are not moving fully independently of each other [122] and the salt is not fully dissociated or ions are otherwise not available for conductivity [128]. If an electrolyte is located in the top left area of the Walden plot, it is referred to as showing *superionic* [31, 125] or *superconductive* [128] behaviour indicating that mobility is not purely based on the vehicular mechanism describing the joint motion of an ion and its solvation shell [133], but other transport mechanisms are active [31, 128].

A form of the Walden rule can be obtained by combining the Nernst-Einstein equation, given in equation 3.18, with the Stokes-Einstein equation shown in equation 2.2. Both of these equations involve the Einstein relation reported in equation 2.1. [32] Assuming the diffusion coefficient D for a species defined by the Stokes-Einstein equation and the Nernst-Einstein equation to be equal, leads in the case of single-charged ions to the equation [32]

$$\frac{k_B T}{6\pi\eta_{\text{solv}} r} = \frac{k_B T}{N_A e^2} \cdot \Lambda_m. \quad (3.21)$$

For a constant radius of the moving species, this results in the Walden rule (compare equation 3.19). Deviations from the Nernst-Einstein equation occur for example for paired ions or in systems, where the diffusion coefficient of the mobile species and the molar or equivalent conductivity show different behaviour with changes in concentration. [32] Based on the above derivation, it can be understood that these aspects also reason deviations from the ideal behaviour in the Walden plot.

Although, the Walden rule is frequently applied in the field of ionic liquids [122, 125, 126], there are also studies employing it to qualitatively investigate various liquid electrolyte solutions [31, 131, 134–138]. The publication presented in chapter 5 [95] includes a Walden plot analysis of ionic conductivity and viscosity data of electrolyte systems for lithium ion batteries.

4 The ASAB Setup

This section presents the ASAB setup, which was developed in the scope of this work for the automated and autonomous formulation and analysis of liquid battery electrolytes. The setup is not published in a research article on its own, but its latest code is publicly available under the URL <https://github.com/Helge-Stein-Group/ASAB>. Different stages of development and modes of operation of the setup are a significant part of the publications presented in the subsequent chapters. The NMR device included in the setup is used in the publication presented in chapter 5 [95] and used again in chapter 6.2 [14]. Different stages of the setup operating in the autonomous mode enabled the studies presented in the chapters 6.1 [13, 139] and 6.2 [14, 86, 140]. Therefore, the ASAB setup including its associated software is described in the following.

Monika Vogler presented this setup as part of a talk at the *2023 Spring Meeting of the European Materials Research Society* in Strasbourg, France in May 2023 (contributed talk 1317) and at the *11th International Workshop on Combinatorial Materials Science and Technology* in Golden, Colorado, USA in September 2022 (contributed talk #5), and as part of a poster at the *POLiS Annual Conference 2024* in Karlsruhe, Germany in June 2024, and several presentations in the context of the BIG-MAP project.

Contributions to the initial start-up phase of the setup by Lisa Schröder and to the inclusion of an Arduino® board by Bojing Zhang are gratefully acknowledged.

In this work, the hardware setup and software package constituting the *Autonomous Synthesis and Analysis of Battery Electrolytes* (ASAB) setup were developed and demonstrated. It serves to automatically or autonomously formulate liquid electrolytes based on stock solutions, which can subsequently be automatically characterised using various physicochemical and electrochemical methods or provided for the use in other systems like the AutoBASS system [41, 60] for coin cell assembly [13, 14]. The ASAB setup is designed to operate with minimal human intervention. The degree of automation achieved with the setup in the course of this work allows researchers to focus on the design of new studies and the interpretation of results while leaving the experimentation tasks to the device. Upon integration into MAPs, the automated operation of the ASAB setup enables fully autonomous research campaigns as is reported in the publications presented in sections 6.1 [13] and 6.2 [14]. This section provides detailed information about the ASAB hardware and software. A schematic representation of the ASAB setup including the connected analysis hardware, software components and the connection to FINALES is shown in Figure 4.1. Details about the different components and the operation will be provided in the respective subsections. Since several versions of the used software were deployed during the course of this work, only the latest used version of each software is referenced in this chapter.

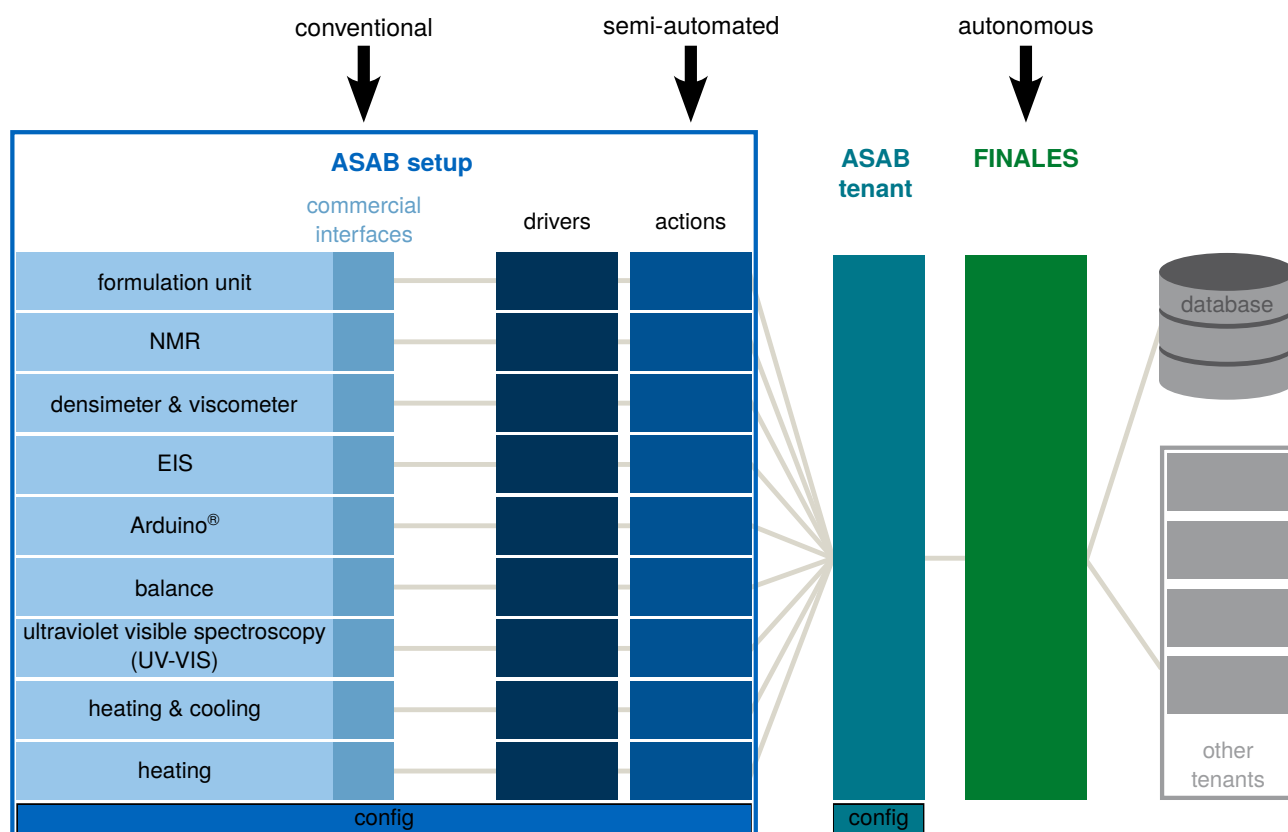


Figure 4.1 A schematic overview of the ASAB setup including the connected modules with their respective commercial interfaces on the left, the driver and action layers of the ASAB software package [140], the ASAB tenant [86] and the respective configuration files labelled as *config*. The graphic also includes the connection to FINALES [14, 141], which connects it to a MAP and provides an additional possibility to interact with the setup. The arrows at the top indicate possible entry points for the interaction with the ASAB setup depending on the mode of operation.

4.1 The hardware setup

The hardware of the ASAB setup comprises a formulation unit, a densimeter and viscometer unit, a bench-top NMR device and a two-electrode electrochemical measuring cell [13, 14]. Additionally, units for heating

and cooling of the electrolyte samples and a module for *ultraviolet visible spectroscopy* (UV-VIS) are attached to the setup but not used in this work. The formulation unit, the electrochemical cell, the balance, the heating and cooling as well as the UV-VIS modules are located within a nitrogen-filled glovebox [13, 14]. The densimeter, viscometer and the NMR instrument are located outside of the glovebox in the air atmosphere and natural humidity of the laboratory and connected to the components inside the glovebox via *polytetrafluoroethylene* (PTFE) tubes.

4.1.1 The formulation unit

The formulation unit shown in Figure 4.2 comprises six syringe pump modules of the type *neMESYS low pressure* and ten *Qmix V* eleven-port rotary valve modules connected to a base module *BASE 600* [13, 14]. Furthermore, a *Qmix Q+* module for heating, a UV-VIS spectrometer module *Qmix λ* and a *Qmix Q-* heating and cooling module are attached to the formulation unit. The latter modules are not actively used in the studies presented in this work. All the aforementioned modules are commercially available from Cetoni GmbH (Korbussen, Germany), which also provides the software *Cetoni Elements* [142], which is used in this work for manual control of the formulation unit. The *CETONI SDK for Python* [57], which is also available from Cetoni GmbH (Korbussen, Germany), is used to interface the formulation unit using the Python programming language. To enable the detection of incomplete filling of the syringes, an *Entris II* balance (Sartorius Lab Instruments GmbH & Co. KG, Göttingen, Germany) is connected to the setup and read via its serial interface. The formulation unit is further equipped with a connection to a pressurised nitrogen line used for draining residues from the tubes and drying relevant parts of the fluid paths. The connection to the nitrogen line is implemented using a solenoid valve *LVM105R-5C2U-1-10-Q* (SMC Corporation, Japan) controlled by an *Arduino® Uno* (Arduino.cc) and an *Arduino® 4 Relays Shield* (Arduino.cc). To respect the pressure limit of the valve, a pressure delimiter of the type *AR20-F01H-1-B* (SMC Corporation, Japan) reduces the gas pressure of the line to a maximum of 2.0 bar.

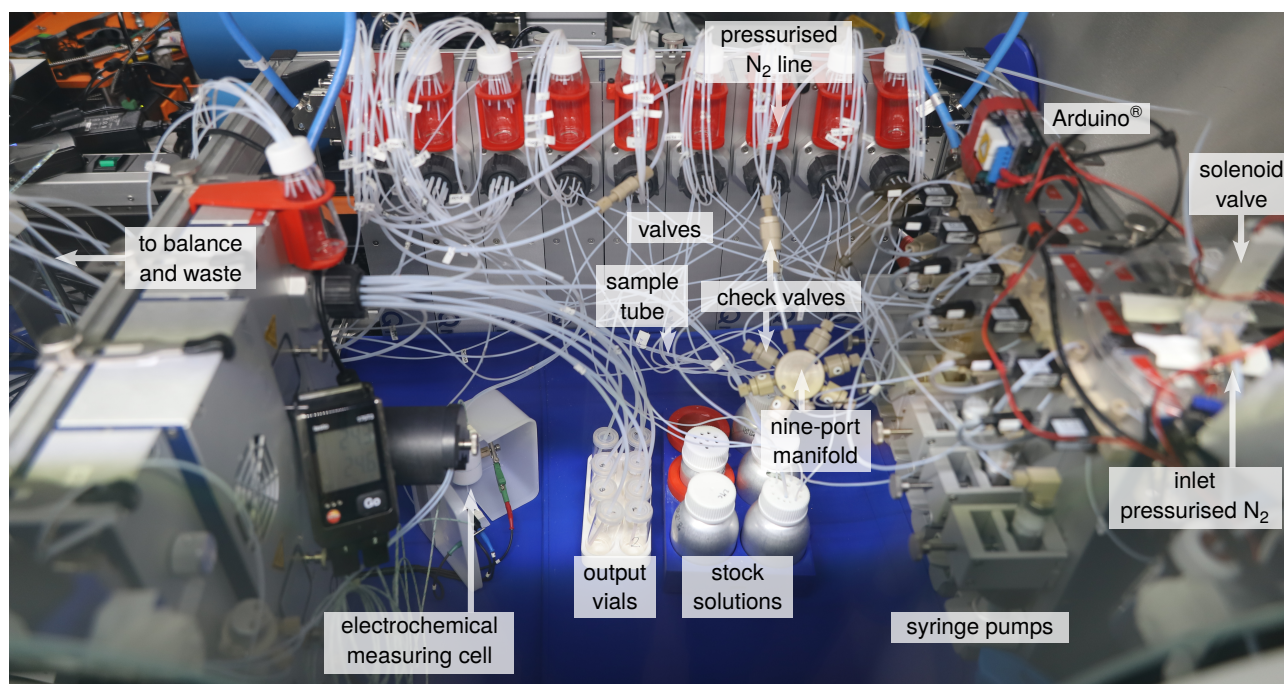


Figure 4.2 The formulation unit of the ASAB setup comprising six syringe pump modules, ten eleven-port valve modules, and additional modules for UV-VIS, heating and cooling on the left, which are not used in this work. Further, the electrochemical measuring cell and the *Arduino®* with the associated solenoid valve are shown. The Manifold used to merge the flows created by the pumps, the vials for the stock solutions and the output vials are presented. Different versions of this setup were used in [13] and [14].

All components of the ASAB setup are physically connected using PTFE tubes either with an inner diameter of 0.3 mm and 1.6 mm outer diameter or 1.6 mm inner diameter and an outer diameter of 3.2 mm. The thinner inner diameter tubing is predominantly used to reduce the volume of the tubing to a minimum. Where larger volume of the tubes is advantageous or dead volume is not relevant, the tubing with the larger inner diameter is used.

Each of the syringe pumps is connected to one of the stock solutions and can pump them at various flow rates. To formulate a sample, the flow rate for each syringe pump needs to be set according to the volume fraction of the respective stock solution in the sample [13, 14]. The thus generated flows are subsequently merged in a nine-port manifold to obtain an electrolyte sample for analysis or transfer to other devices [13]. Check valves block dispensed fluids from being pressed back into the syringes, reservoirs or the gas line. Samples for analysis by one of the instruments connected to the ASAB setup can directly be pumped to the respective device [13, 14]. In case the formulated electrolyte shall be used for a different purpose, the ASAB setup can output them in the output vials, where they can be collected by a human researcher [14].

4.1.2 The analysis instrumentation

The connected analysis instruments include a *DMA 4100* (Anton Paar GmbH, Graz, Austria) densimeter with an attached *Lovis 2000 ME* (Anton Paar GmbH, Graz, Austria) rolling ball microviscometer presented in Figure 3B in the publication included in chapter 6.1 [13]. The latest software version of the *DMA 4100* instrument used for this work is 2.98.22703.320. An ethernet connection includes the instrument into the local network enabling it to be interfaced by the *AP Connect* software [143] (Anton Paar GmbH, Graz, Austria).

Further, an *Oxford Instruments X-Pulse* (Oxford Instruments plc, United Kingdom) benchtop NMR instrument equipped with an *X-band* probe including an external D_2O -lock as shown in Figure 4.3a is connected to the ASAB setup. The design of the *Oxford Instruments X-Pulse* includes the possibility for a flow-through configuration, which allows to provide samples directly from the formulation unit to the measurement region of the NMR instrument. Figure 4.3b shows the 900 mm long FEP tube used to transport the samples through the probe of the NMR instrument. The tube has an inner diameter of 3.2 mm (1/8 in) and an outer diameter of 4.8 mm (3/16 in). Its ends are equipped with fittings to enable the connection to the formulation unit. This setup is simple and yields reproducible results when combined with the external lock of the probe. The NMR instrument is operated using the *SpinFlow* software [144] (Oxford Instruments plc, United Kingdom). The processing and analysis of the recorded spectra in chapter 5 [13] and 6.2 [14] is done using the software *MestReNova* [94] (Mestrelab Research S.L., Spain).

An in-house designed two-electrode electrochemical measuring cell shown in Figure SI-5a in the publication included in chapter 6.2 [14] enables the electrochemical analysis of the formulated electrolytes. It consists of a PTFE body with two stainless steel screws mounted as symmetrical electrodes on either side of the measuring chamber. [14] To avoid excessive wear due to the contact between the PTFE and stainless steel threads and to enable disassembly of the cell for cleaning purposes, the screws are fitted and glued into fittings. To achieve a planar surface of the electrodes used in this work, the ends of the fitted screws are sanded and subsequently polished with a 9 μm polishing paste (*MetaDiTM Monocrystalline Diamond Suspension Oil based* (Buehler, ITW Test & Measurement GmbH, Leinfelden-Echterdingen, Germany)). Deviations from parallelism of the electrodes are included in the cell constant obtained *via* calibration. The potentiostat controlling the electrochemical measurements is a *PalmSens4* (PalmSens B.V., Houten, Netherlands) [14]. Together with it, the software *PSTrace* [145] (PalmSens B.V., Houten, Netherlands) is used. The software control is realized using the *PalmSens SDK for Python* [56] (PalmSens B.V., Houten, Netherlands). The MADAP package in version 1.1.0 [85, 146] is used in this work to automatically analyse data obtained from EIS measurements performed using the electrochemical cell integrated with the ASAB setup. [14]

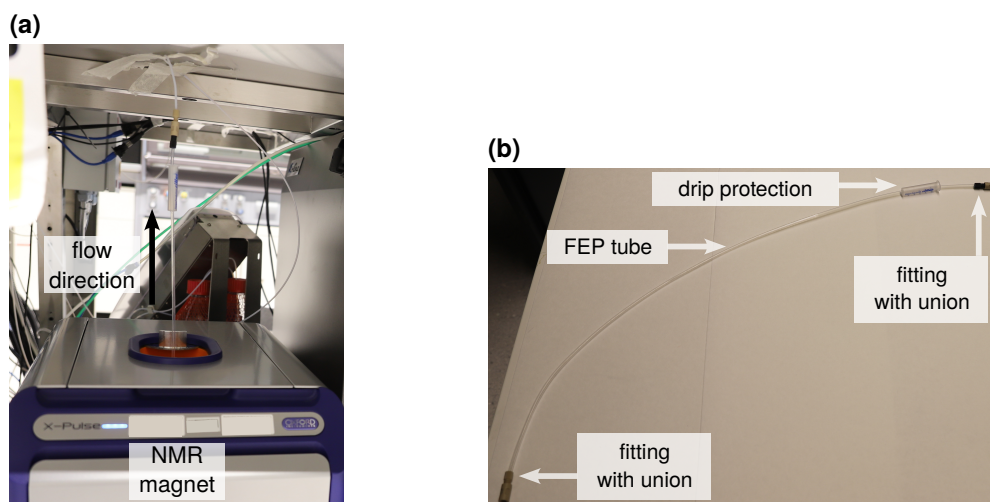


Figure 4.3 (a) The flow-through configuration of the NMR instrument with the FEP tube installed in the probe of the NMR magnet. The direction of the flow is indicated. (b) The FEP tube used to transport the sample through the probe of the NMR instrument. The fittings and unions used to connect the tube to the ASAB setup at either end are shown. Also, a drip protection is installed to hinder fluid from flowing along the tube into the probe in case of leakage.

4.2 The software package

A *ThinkCentre M720q* (Lenovo (Deutschland) GmbH, Stuttgart, Deutschland) running *Windows 10 Education* (Microsoft Corporation, Redmond, USA) is used to develop and run the ASAB software [140]. The ASAB hardware and software follow a modular design, which enables the facile integration of new experimental or analysis methods. The ASAB software package is implemented in the Python programming language version 3.9 and implements a hierarchical architecture based on drivers and actions as proven valuable in the HELAO framework [58] (latest version available at <https://github.com/helgestein/helao-pub>). The latest version of the ASAB software is available on GitHub <https://github.com/Helge-Stein-Group/ASAB>. The version v1.0.1 of the code used in the study presented in chapter 6.1 [13] can be found in [139] and the version v2.0.1 used in the publication presented in chapter 6.2 [14] is published in [140]. By the year 2024, drivers and actions for the formulation unit, the densimeter and viscometer, the PalmSens potentiostat for operating the electrochemical measuring cell, the balance, and the Arduino[®] including the valve connected to it are implemented and demonstrated. The drivers provide the basic functionality of the respective module, while the actions encapsulate these functionalities in more complex tasks to simplify the usage [13].

The ASAB setup works with two configuration files, which render it flexible towards the research task at hand. One of the configuration files specifies the software environment of the ASAB package defining the directories of the various SDKs. The second configuration file determines parameters relevant for the respective experiment like the total flow rate, the connections of tubes, edges and nodes and the provided stock solutions among many more parameters. This second configuration file further offers settings to simulate the balance and Arduino[®] functionalities. These options are inspired by the respective functionality offered in the commercial *Cetoni Elements* [142] software and are useful for testing purposes.

To facilitate the navigation through the network of tubing, valves and other components, the ASAB hardware setup is represented as a directed graph [13] using the *NetworkX* [147] Python package and defining the tubes as the edges. By assigning a dead volume to each of the tubes, it is possible to deploy the Dijkstra algorithm [148] as implemented in the *NetworkX* [147] package to determine the path between two nodes, which has the minimum dead volume and is therefore preferred in most cases. Based on the tubing

configuration and a dictionary relating nodes to positions of valves, the path found as a list of edges can be used to switch the valves accordingly. This significantly facilitates the switching of the valves, which is a very frequent task and performing it with manual control is very time consuming and error-prone. Further features offered by the *NetworkX* [147] package are deployed in the ASAB software [140] for example in the automated cleaning routine or the visualisation of the graph representing the hardware setup.

Besides the hardware functionalities, the ASAB framework is equipped with a logging capability to enable trouble shooting and traceability of the processes executed by the setup [14]. Additional to the definition of formulations in units of volume fractions, the ASAB setup also accepts molar fractions as the input and transforms them to volume fractions prior to formulating the respective electrolyte. This is important to allow for the integration into MAPs incorporating experimental and computational capabilities. The transformation is necessary, because the ASAB setup controls the formulation based on the volumetric flow rates of the used stock solutions and merges the flows to obtain the sample. This procedure corresponds to a volumetric dosing of the stock solutions. [13, 14]

4.3 A typical experiment

In a typical experiment, the configuration of the hardware and the software is followed by the manual preparation of the stock solutions required for the experiment. Up to five stock solutions and one cleaning solvent can be connected to the syringe pump modules, because each syringe transports one solution. The composition of the stock solutions must be chosen such that the chemical space of interest is accessible while maintaining reasonably low viscosity of the stock solutions [13, 14]. The maximum tolerable viscosity values depend on the hardware setup and especially the inner diameter of the tubing. Among other parameters, the composition and density of the stock solutions must be provided in the configuration file of the experiment to allow for the determination of the flow rates required to achieve the defined formulations of the samples [14]. The ASAB software version 2.0.1 [140] is able to process specifications of formulations given in mole fractions of chemical components or volume fractions of stock solutions. Once these preparations are done, the experimental procedure can be defined in a script. It typically involves the formulation of a sample based on a given composition. When starting the ASAB system with empty syringes, they are in a first step filled with their respective stock solution [13]. In this process, the stock solution is iteratively aspirated and dispensed to the waste container on the balance. Once the balance reading increases for a predefined number of readings, it is assumed that no more gas is contained in the syringe and it is consequently completely filled with the stock solution. After filling the syringes, the formulation process starts by setting the volume flows of the stock solutions [13, 14]. The flows generated by the syringe pumps are merged in a manifold and the formulated sample may subsequently be output to a specified node for further use, e.g. in the assembly of coin cells using the AutoBASS [41, 60] system, or supplied to one of the connected analysis instruments. For density and viscosity or EIS measurements, the ASAB setup can automatically trigger the measurement and retrieve the data. [13, 14] In the case of EIS data, the MADAP package [85, 146] can be deployed to fully automatically analyse the raw data and obtain the ionic conductivity of the sample [14]. The raw data and the processed data are saved locally on the machine running the ASAB package in a directory configured by the user. Subsequent to a measurement, the sample can be drained from the measuring instrument by pumping gas aspirated from the ambient of the formulation unit through the device, which is usually followed by an intermediate cleaning using the cleaning solvent and subsequent draining of the solvent and drying using ambient gas [13] or pressurised gas. After the last measurement, the setup can run an automatic cleaning routine using cleaning solvent, ambient gas or the pressurised gas to remove residues of the samples and avoid damage to the equipment. If controlled manually, the cleaning of the device and all of its components takes several hours. Therefore, the automation saves a significant amount of human labour although the last residues need to be manually removed from the syringes. In case the ASAB setup encounters an error during operation or the operator cancels the execution of the experiment, the setup stops all pumps

and exits the procedure. This is essential since the setup otherwise finishes a pumping step although the ASAB software is no longer responsive, which is critical in case the operator has to stop the setup due to leakage or similar issues.

4.4 Modes of operation

The degree of automation achieved with the setup and software version 2.0.1 [140] enables three modes of operation for the setup. The first option is to use the manufacturer's software to operate the setup and the associated instruments individually with manual control. This mode of operation is referred to as the conventional mode of operation in this thesis and it is deployed in the study presented in chapter 5 [95]. A similar way of operation can be achieved by scripting the experiment and executing the code in a step-by-step manner in the command line. Further, it is possible to choose a semi-automated approach by creating a script for an experiment defining a single formulation, executing it, and subsequently altering the script to define the next experiment. Of course, the script can also be designed to include a predefined list of formulations to process. Eventually, there is the fully autonomous mode of operation not relying on predefined formulations. In this mode, an ML model or a human researcher provides the definition of the formulation and the results output from the ASAB setup may be directly processed to identify a promising follow-up formulation. This last mode of operation using an ML model to guide the process is demonstrated in the publications shown in the chapters 6.1 [13], deploying the density and viscosity measurement capabilities of the ASAB setup, and 6.2 [14], making use of the two-electrode electrochemical measuring cell to determine the ionic conductivity.

4.5 The connection to FINALES

For the connection to the FINALES framework [13, 14, 141, 149], a so-called *tenant* is created, which serves as an interface between the ASAB setup and an instance of FINALES. The code of version 1.0.1 of the tenant used in the publication included in chapter 6.2 can be found in [86]. The tenant establishes an interface to FINALES and manages the login and status updates for pulled requests. It further can transform the requests collected from FINALES into the inputs required by the ASAB setup. Once a request is processed and results are available, it assigns a quality rating (for details see chapters 6.1 [13] and 6.2 [14]), formats the results according to the structures imposed by FINALES and posts the result. [13, 14] Just as the ASAB setup, the tenant is also configurable to be able to connect to different instances of FINALES running on different IP addresses and ports [14]. Additionally, the software versions of the FINALES [141], FINALES schemas [150], MADAP [85], and ASAB [140] packages can be provided in the configuration file for documentation purposes. In the study presented in chapter 6.2 [14], this was done by specifying the branch and the identifier of the relevant commit in the respective GitHub repositories, because this also enables traceability of local changes that do not correspond to a release. Furthermore, the configuration allows to define a time, at which the setup will stop checking FINALES for new requests. This functionality may be used to respect the working hours of the operator or introduce maintenance intervals e.g. to refill the stock solutions or empty waste containers.

Since the software for the ASAB tenant [86] is fully separate from the software required to run the ASAB setup [140] itself, the tenant can be stopped at any time to use the ASAB setup with another instance of FINALES or switching to one of the other modes of operation.

5 Investigation of Hückel-type conducting salts for battery electrolytes

This section presents the publication [95]

A. Szczęsna-Chrzan, M. Vogler, P. Yan, G. Z. Żukowska, C. Wölke, A. Ostrowska, S. Szymańska, M. Marcinek, M. Winter, I. Cekic-Laskovic, W. Wieczorek, and H. S. Stein, “Ionic conductivity, viscosity, and self-diffusion coefficients of novel imidazole salts for lithium-ion battery electrolytes,” *Journal of Materials Chemistry A*, vol. 11, no. 25, pp. 13 483–13 492, 2023. doi: 10.1039/d3ta01217d

submitted in February 2023 and published after peer-review in May 2023. The open access publication is available under the terms of the Creative Commons Attribution 3.0 Unported (CC BY 3.0) (<https://creativecommons.org/licenses/by/3.0/>) license.

Monika Vogler presented this work online in a virtual poster at the *16th International conference on materials chemistry (MC16)* in Dublin, Ireland in July 2023 (poster ID: mc16.01e0039), in a poster at the annual project meeting of the BIG-MAP project in Brussels, Belgium in October 2023 and partially in a poster at the *POLiS Annual Conference 2024* in Karlsruhe, Germany in June 2024.

Author contributions

The following author contributions are given as a literal quotation from [95]:

"AS planned, performed and analyzed conductivity measurements; PY planned, conducted and analyzed the viscosity and conductivity measurements; MV planned, conducted and analyzed J-PGSE NMR measurements; GZZ planned and performed NMR, IR and FTIR measurements and analyzed the results; AO and SS synthesized the Hückel-type salts; AS, PY, MV and HSS wrote the initial manuscript; CW, ICL, WW, MW, and HSS revised the manuscript. AS, MV and PY contributed equally."

For information regarding the reprint permission see Annex A.1.

In this publication, we present a comprehensive analysis of ionic conductivity, viscosity and anionic self-diffusion coefficients of battery electrolytes using novel Hückel-type salts that among other advantages can be synthesised in a single-stage process [52, 54] and tolerate moisture [53, 54]. The salts under investigation were LiTDI, LiPDI, and LiHDI, which differ in the length of their perfluorinated alkyl side chain. LiPF₆ served as a reference. Electrolyte solutions with various salt concentrations were investigated using a mixed solvent containing EC:EMC in a weight ratio of 3:7. [95]

The ionicity of the Hückel-type salts are found to be lower than that of LiPF₆ and the viscosity-dependence of the ionic motion is the least in the reference electrolytes. The strongest influence of viscosity is found for LiTDI, which might indicate a stronger aggregation of the ionic species in electrolytes using LiTDI compared to those containing the other salts investigated in this study. As expected, electrolytes with higher salt concentration are observed to show higher viscosity than their more dilute counterparts. Unsurprisingly, the increased viscosity is found to correlate with decreased self-diffusion coefficients of the anions in the respective electrolytes. Among the samples containing Hückel-type salts, the highest ionic conductivity is found for electrolytes containing LiPDI. These observations together with spectroscopic findings hint towards different solvation structures in the electrolytes based on Hückel-type salts compared to those using LiPF₆ and suggest possible differences in the aggregation of the ions depending on the conducting salt used. [95]

By the time the work for this study took place, the initial installation of the hardware components and the implementation of the software for the ASAB setup was in progress. Therefore, the entirety of the ASAB setup could not yet be used in its automated mode of operation. However, the modularity of the ASAB setup enabled the use of the NMR device in its conventional mode of operation without impairing the installation and automation of the other components. In this way, the author of this work performed J-PGSE NMR measurements and analysed the data to determine the anionic self-diffusion coefficients [95]. Performing the experiments for this study by deploying the conventional mode of operation allowed the author of this thesis to become accustomed to the electrolyte formulation process and the use of the NMR device. Alongside the experiments performed in contribution to this publication, first trials with the densimeter and viscometer devices were performed. The experience gained from manually performing the relevant tasks enabled the conceptualisation of a workflow for the performed tasks that was beneficial for the automation of the processes and their connection to the ASAB setup. In the context of the publication presented in this chapter, the author further contributed to the overall interpretation of the results gathered in this study [95].

The remainder of this chapter shows a reprint of [95] and the corresponding Supplementary Information.

Cite this: *J. Mater. Chem. A*, 2023, 11, 13483

Ionic conductivity, viscosity, and self-diffusion coefficients of novel imidazole salts for lithium-ion battery electrolytes†

Anna Szczęśna-Chrzan,^{‡a} Monika Vogler,^{‡bc} Peng Yan,^{‡d} Grażyna Zofia Żukowska,^a Christian Wölke,^{‡d} Agnieszka Ostrowska,^a Sara Szymańska,^a Marek Marcinek,^a Martin Winter,^d Isidora Cekić-Lasković,^{‡*d} Władysław Wiczorek^{*a} and Helge S. Stein^{‡*bc}

Lithium-ion battery performance and longevity depend critically on the conducting salt utilized in the electrolyte. With new avenues for multifunctional integration and optimization of functional properties, conducting salts beyond lithium hexafluorophosphate (LiPF₆) need to be studied. Herein we elucidate on viscosity, ionicity, anion self-diffusion and ionic conductivity through variation of the length of the perfluoroalkyl side chain present in the anions of the used lithium imidazole salts. Specifically, we study LiPF₆ in comparison with lithium 4,5-dicyano-2-(trifluoromethyl)imidazolide (LiTDI), lithium 4,5-dicyano-2-(pentafluoroethyl)imidazolide (LiPDI), and lithium 4,5-dicyano-2-(*n*-heptafluoropropyl)imidazolide (LiHDI). We find that the ion mobility of LiPF₆ depends the least on viscosity and its ionicity is the highest among the electrolytes investigated here. LiTDI shows the strongest correlation between ion mobility and viscosity and the lowest ionicity. LiPDI and LiHDI range between these two regarding their ionicity and the correlation of mobility with viscosity. The previously rarely studied anion self-diffusion coefficients exhibit a strong correlation with viscosity as it was to be expected. Differences between the LiTDI, LiPDI and LiHDI salts are minute.

Received 26th February 2023
Accepted 30th May 2023

DOI: 10.1039/d3ta01217d

rsc.li/materials-a

Introduction

Liquid battery electrolytes fulfill a multitude of functional properties, like high ionic conductivity,^{1,2} the formation of an effective solid electrolyte interphase (SEI),³ low viscosity at low temperatures, flame inhibition, overcharge protection, dendrite prevention^{4,5} and others. Tailoring of the conductivity is for instance performed through controlled variation of the formulation like adjustment of the solvent to co-solvent ratio⁶ and conducting salt concentration. The governing factor for electrolyte conductivity is the chemical nature and the concentration of the conducting salt, following newly discovered and well established theories.^{7,8}

Through modern machine learning applications, it is even possible to predict the optimal electrolyte formulation at various temperatures for commonly used organic carbonate-based solvents and co-solvents such as ethylene carbonate (EC), propylene carbonate (PC), ethyl methyl carbonate (EMC) and the state-of-the-art lithium conducting salt lithium hexafluorophosphate (LiPF₆).² The outstanding electrochemical stability and thus resulting longevity of cell chemistries containing LiPF₆-based electrolytes have made it a widely studied system.^{9,10} However, thermally unstable LiPF₆ can decompose and lead to the formation of hydrofluoric acid (HF), which can initiate harmful processes that jeopardize the overall performance and safety of a battery.¹¹ Recently there has been an increased interest in studying other, non-phosphorous containing salts, which, among other benefits, are often more stable against hydrolysis.^{9,10} For example, the presence of lithium 4,5-dicyano-2-(trifluoromethyl)imidazolide (LiTDI) prolongs the lifetime of the cell by stabilizing LiPF₆-based electrolytes due to its HF and H₂O scavenging ability.^{9,10} Further, LiTDI improves the SEI stability formed with conventional organic carbonates or film-forming additives like fluoroethylene carbonate (FEC) or vinylene carbonate (VC).^{9,10} For example, metallic lithium anodes could benefit from different solvation characteristics⁸ while silicon-graphite anodes could benefit from lower viscosity of highly concentrated salts at low temperatures.^{12,13} In addition, the LiTDI is reported to be capable of preventing the aluminum current

^aFaculty of Chemistry Warsaw University of Technology, Noakowskiego 3, Warsaw 00-664, Poland. E-mail: wladyslaw.wiczorek@pw.edu.pl^bApplied Electrochemistry, Helmholtz Institute Ulm, Helmholtzstr. 11, 89081 Ulm, Germany. E-mail: helge.stein@kit.edu^cKarlsruhe Institute of Technology, Institute of Physical Chemistry, Fritz-Haber-Weg 2, 76131 Karlsruhe, Germany^dHelmholtz Institute Münster (IEK-12), Forschungszentrum Jülich GmbH, Corrensstraße 46, 48149 Münster, Germany. E-mail: i.cekic-laskovic@fz-juelich.de† Electronic supplementary information (ESI) available: Further information about the formulation of the electrolytes, exemplary visualization of the deviation from theory in J-PGSE NMR measurements, values of the deviation from the ideal KCl line and slopes of the Walden plot. See DOI: <https://doi.org/10.1039/d3ta01217d>

‡ AS, MV and PY contributed equally.



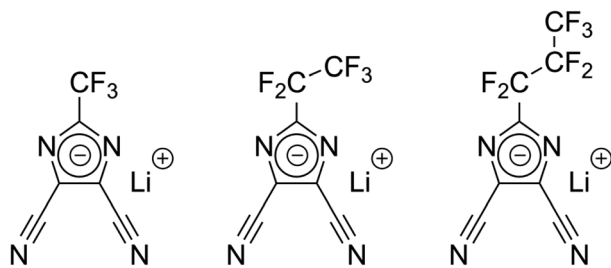


Fig. 1 Chemical structures of LiTDI (left), LiPDI (middle) and LiHDI (right).

collector up to 5.0 V vs. Li/Li^+ .^{14,15} Due to the structural similarity between LiTDI, LiPDI, and LiHDI, a similar behavior regarding the attack of the aluminum current collector could be expected. Besides electrochemical performance, the proliferation of batteries on the TWh scale will necessitate millions of tons of material⁶ such that facile and sustainable synthesis paths are of paramount interest for academia and industry alike.

Herein we report on the physicochemical and electrochemical characterization of lithium 4,5-dicyano-2-(trifluoromethyl)imidazolide (LiTDI), lithium 4,5-dicyano-2-(pentafluoroethyl)imidazolide (LiPDI), and lithium 4,5-dicyano-2-(*n*-heptafluoropropyl)imidazolide (LiHDI). The structures of the conducting salts are shown in Fig. 1. Furthermore, seldomly studied anion self-diffusion coefficients that are *e.g.* important for *ab initio* modelling of these novel electrolyte formulations are included in the study.

Methods

Synthesis of imidazole salts

Lithium 4,5-dicyano-2-(trifluoromethyl)imidazolide (LiTDI). Trifluoroacetic anhydride (550 mL, 3.90 mol) was added dropwise into diaminomaleonitrile (366.2 g, 3.39 mol) solution in 1,4-dioxane (2 L). The reaction mixture was refluxed for 4 h until the substrate disappeared (TLC monitoring; eluent: toluene-ethyl acetate (1:1)). Thereafter, the resulting mixture was evaporated under vacuum (approx. 3 h) to remove solvent and the acid produced in the reaction. Solid residue was dissolved in water (700 mL) and the resulting solution was heated to a temperature of 70 °C. Lithium carbonate (247.4 g, 3.35 mol) was dosed stepwise, followed by the addition of decolorizing activated charcoal. The mixture was heated for 2 h at 70 °C. After filtering off the charcoal on filter paper, the water was evaporated under vacuum (approx. 2 h) using a rotary evaporator. The resulting solid was dried on the vacuum line (1 h, 90 °C) and the residue was dissolved in anhydrous acetonitrile. The impurities were filtered off and the solvent was evaporated under vacuum (approx. 1 h). Twofold crystallization from acetonitrile gave colorless crystals, which were dried in the vacuum drier (48 h, 130 °C) to give lithium salt of 4,5-dicyano-2-(trifluoromethyl)imidazolide (320 g, 49% yield).

Lithium 4,5-dicyano-2-(pentafluoroethyl)imidazolide (LiPDI). Pentafluoropropionic anhydride (130 mL, 0.66 mol) was added dropwise into diaminomaleonitrile (65.2 g, 0.60 mol) solution in 1,4-dioxane (1100 mL). The obtained mixture was

refluxed until the substrate disappeared (approx. 8 h; TLC monitoring; eluent: toluene-ethyl acetate (1:1)). After evaporating the solvent and the acid produced in the reaction under vacuum (approx. 2 h), the resulting oily brown residue was dissolved in a mixture of acetonitrile and water (500 mL + 50 mL). Thereafter, lithium carbonate (70.5 g, 0.95 mol) was dosed stepwise, followed by the addition of decolorizing activated charcoal. The mixture was heated for 2 h at 70 °C. After filtering off the charcoal on filter paper, the water was evaporated under vacuum (approx. 2 h) using a rotary evaporator. The residue was dissolved in anhydrous acetonitrile. The impurities were filtered off and the solvent was evaporated under vacuum (approx. 1 h). Multiple crystallization (3–4 times) from acetonitrile gave colorless crystals, which were dried in the vacuum drier (48 hours, 130 °C) to give lithium salt of 4,5-dicyano-2-(pentafluoroethyl)imidazolide (94 g, 64% yield).

Lithium 4,5-dicyano-2-(*n*-heptafluoropropyl)imidazolide (LiHDI). Heptafluorobutyric anhydride (60 mL, 0.24 mol) was added dropwise into diaminomaleonitrile (21.2 g, 0.20 mol) solution in 1,4-dioxane (240 mL). The mixture was refluxed until the substrate disappeared (approx. 10 h; TLC monitoring; eluent: toluene-ethyl acetate (1:1)). Then, the resulting mixture was evaporated under vacuum (approx. 1 h) to remove the solvent and the acid produced in the reaction. The solid residue was dissolved in diethyl ether (250 mL) and the resulting mixture was extracted three times with lithium carbonate (17.5 g, 0.24 mol) suspension in water (450 mL). The water solution of a salt was washed three times with ether (3 × 100 mL). The decolorizing activated charcoal was added to the water solution and the mixture was heated for 1 h at 70 °C. After filtering off the charcoal on filter paper, the water was evaporated under vacuum (approx. 1 h) using a rotary evaporator. Then the residue was dissolved in anhydrous acetonitrile. The impurities were filtered off and the solvent was evaporated under vacuum (approx. 1 h). Multiple crystallization (3–4 times) from acetonitrile gave colorless crystals, which were dried in the vacuum drier (48 h, 130 °C) to give lithium salt of 4,5-dicyano-2-(*n*-heptafluoropropyl)imidazolide (13.4 g, 23% yield).

NMR structure verification by means of ¹³C NMR and ¹⁹F NMR spectroscopy in CD₃CN for LiTDI, LiPDI, and LiHDI is in agreement with literature.¹⁶

IR and Raman spectroscopy

Raman spectra were recorded on a Nicolet Almega Raman dispersive spectrometer. A diode laser with excitation line 532 nm was used. The exposure time was set to 10 s and integrated such that each spectrum is the sum of two independent scans. The spectral resolution for all experiments was around 2 cm⁻¹.

FTIR spectra were collected on a Nicolet Avatar 370 spectrometer with a wavenumber resolution of 2 cm⁻¹. Spectra were recorded for samples in form of a thin film sandwiched between two NaCl plates (high salt concentration) or placed in a cuvette with a 0.1 mm spacer.

Electrolyte formulations

The electrolytes used in this work were formulated starting from commercially available ethylene carbonate (EC), ethyl methyl



carbonate (EMC), lithium hexafluorophosphate (LiPF₆) and commercial, pre-mixed 1 M LiPF₆ in EC : EMC (3 : 7 by weight). All these components were ordered from E-Lyte Innovations GmbH in battery grade quality and used as received. The Hückel-type salts, LiTDI, LiPDI, and LiHDI, were synthesized and characterized at the Warsaw University of Technology (WUT) as described in the *Synthesis of imidazole salts* section. The Helmholtz Institute Münster (FZJ) and Karlsruhe Institute of Technology (KIT) received the materials from WUT.

The nominal concentrations of the Hückel-type salts in the formulated electrolytes were chosen to be 0.05 M, 0.6 M and 1.0 M for the electrolytes, while 1.0 M LiPF₆ concentration was used as a reference electrolyte. For all electrolytes, EC : EMC (3 : 7 by weight) was used as the solvent mixture.

Electrolytes used for the measurements were formulated in an oxygen and water free inert gas-filled glovebox. The formulation was based on the mixing of the former prepared solvents mixture and gravimetrically dosed salts to obtain the concentrations mentioned above. In this work, the samples are designated based on their nominal compositions. An overview of the electrolytes used in this study, the formulation methods and the measurements is compiled in Table SI-1.†

Conductivity measurements

All experiments were carried out under an inert atmosphere inside a glovebox (MBraun, H₂O and O₂ < 1 ppm). Conductivity cells were filled with the various electrolyte formulations as previously described.⁶ Cell constants were determined by using a 0.01 M solution of KCl in H₂O at 20 °C (VWR, known conductivity of 1.276 mS cm⁻¹) and averaging over five measurements. Disposable 2 mL Eppendorf Safe-Lock Tubes were used as sample containers and filled with 750 μL of electrolyte each. Impedance measurements were conducted on a Metrohm Autolab/M204 potentiostat/galvanostat with 12 channels and an 8-channel multiplexer for a total of 96 channels in the frequency range of 50–20 000 Hz using in-house developed electrodes.¹⁷ The conductivity cells were placed in a temperature chamber (Memmert TTC256, 0.1 °C temperature setting accuracy) and each temperature was held for 2 h prior to measurement for equilibration. The ionic conductivity of the considered electrolytes was measured in the temperature range from –30 °C to 60 °C in 10 °C steps. Impedance spectra were fitted using a model specified with set parameters for resistors R_s and R_p , as well as for the constant phase element (CPE) with the Metrohm Nova software. Fitting was carried out after each additional measuring point by using the fitting model $R_s(\text{CPE} - R_p)$. Electrolyte conductivity values were obtained from the quotient of the cell constant and the determined electrolyte resistance.

Viscosity and density measurements

For the viscosity and density measurements, a manually filled viscometer (Anton Paar SVM 3001, Austria) was used. Measurements were performed at the following temperatures: –20 °C, 0 °C, 20 °C, 30 °C, 40 °C and 60 °C. Acetone was used to clean the instrument between the measurements to avoid contamination of the samples.

PGSE-NMR measurements

In preparation of the NMR measurements, each electrolyte was filled in a standard NMR tube inside a nitrogen filled glovebox. The tubes were closed using standard NMR caps and sealed with Parafilm. The formulated electrolytes were removed from the nitrogen-filled glovebox and transferred to the NMR device, which was operated in the regular laboratory environment. Care was taken to keep the time span between filling the electrolytes into the NMR tubes and starting the measurement as short as possible to avoid reactions with the glass, air, and/or humidity. The NMR instrument used in this study is an Oxford Instruments X-Pulse benchtop NMR comprising a 1.4 T (60 MHz) permanent magnet operating at 40 °C. The device was equipped with a probe head capable of detecting ¹H and ¹⁹F nuclei. In this study, ¹⁹F NMR spectra were recorded to determine the self-diffusion coefficients of the anions. A J-PGSE pulse sequence developed at Oxford Instruments GmbH was used to perform J-compensated pulsed field gradient spin echo (PGSE) measurements. Since the focus of this study was not on structure elucidation, the chemical shift of the individual signals was not primarily relevant. Therefore, the addition of a reference was omitted and the soft-lock procedure provided by the device was used to record spectra. The assignment of the signal groups to the respective nuclei was performed based on the multiplet structures observed in the spectra. In the case of overlapping signals, these signals were excluded from the integration and the evaluation of the self-diffusion coefficients. The maximum gradient, G_{max} , obtained from calibration with water was 0.315 T m⁻¹ with a standard deviation of 2.9 10⁻⁵ T m⁻¹ determined by three measurements. The duration of the gradient pulses, δ , was set to 4 ms, the diffusion time, Δ , is set to 25 ms and a relaxation delay of 30 s was used. The gradient strength was varied from 0% to 100% in 10% steps. The spectra were zero filled, phased, baseline corrected and apodized prior to integration. For the analysis, the Stejskal–Tanner equation¹⁸ as given in eqn (3.1) was used. The term $2/\pi$ was required due to the sinusoidal shape of the pulses.

$$\ln\left(\frac{I}{I_0}\right) = -2D\gamma^2\left(\delta\frac{2}{\pi}\right)^2 G^2\left(\frac{\Delta}{2} - \frac{\left(\delta\frac{2}{\pi}\right)}{3}\right) \quad (3.1)$$

Based on theory, the maximum intensity of the signals, I_0 , should be obtained from spectra recorded at zero gradient. However, in this study, the values for the smallest non-zero gradient, yielded higher values than no gradient in most cases (cf. Fig. SI-1†). Therefore, a linear fit of the Stejskal–Tanner plot with zero intercept yielded a bad fit for most of the data and did not result in a meaningful trend. This behavior persisted even for gradients below the lowest applied in this study. Therefore, the intensity obtained for the smallest gradient set in this study, i.e. 10% of G_{max} , was used to reference the Stejskal–Tanner equation and the value at zero gradient was excluded from the evaluation. This resulted in R^2 values between 0.88 and 0.99.



The errors of the self-diffusion coefficients were determined from the errors of the integrals combined with those of the input quantities. Integration errors were estimated by integrating three regions without signals and the width corresponding to the integral of interest in each spectrum and averaging their values. This error was assigned to the respective integral of interest. Based on this integration error and the standard deviation of G_{\max} , an error propagation yielded the maximum absolute error for the self-diffusion coefficients.

Results and discussion

Raman and IR spectroscopy

The conducting Hückel-type salts used in this study, LiTDI, LiPDI, and LiHDI, differing only in the length of their perfluorinated alkyl chains, are found to be characterized by very

similar coordinating properties. The most widely used and best described conducting salt from this family is LiTDI. Coordination modes of the TDI^- anion were found on the basis of extensive studies on LiTDI solvates^{19–22} and the corresponding characteristic bands in the Raman spectra further served in the analysis of the conducting salt dissociation in liquid and solid electrolytes.

For the present work, we used data obtained from solvates with various solvents, which served as models for free ions, ionic pairs and dimers. The solvates of 12-crown-4 ether (12C4) with lithium salts usually have a structure with cations fully isolated from anions, corresponding to *spectroscopically free* anions (SSIP). Solutions with triglyme (G3) and 15-crown-5 ether (15C5) may serve as models for ionic pairs (CIP) and solutions with diglyme (G2) for dimers and chains. Acetonitrile (AN) can serve as another model system for dimers. Fig. 2 shows the coordination modes of the ions observed in the model solutions, obtained on the basis of structural studies on LiTDI solvates.

Table 1 summarizes the position of the characteristic bands for the solvates in the Raman spectra. A comparison of the properties of these LiPDI and LiTDI solutions in oligoethers²³ and cyclic carbonates²⁴ would suggest that the length of the chain has only a limited effect on the viscosity and thermal properties of the electrolyte. Only at the highest salt/solvent ratio in oligoethers (Li:G3 ratio higher than 5) one may observe that the viscosities of LiPDI based systems were slightly higher.²³

The increase of the conducting salt concentration is reflected by similar changes in the spectral pattern of the salt, *i.e.* (i) shift of the maximum of the ν_{CN} towards higher wavenumbers, from 2224 cm^{-1} to 2230 cm^{-1} , and formation of a shoulder at approx. 2245 cm^{-1} ; (ii) broadening of the band and formation of the shoulder at higher wavenumber for $\nu_{\text{CN Im}}$ and $\delta_{\text{NCN Im}}$.

Fig. 3 presents a comparison of ν_{CN} spectral range in FTIR spectra of LiHDI-based electrolytes and the exemplary

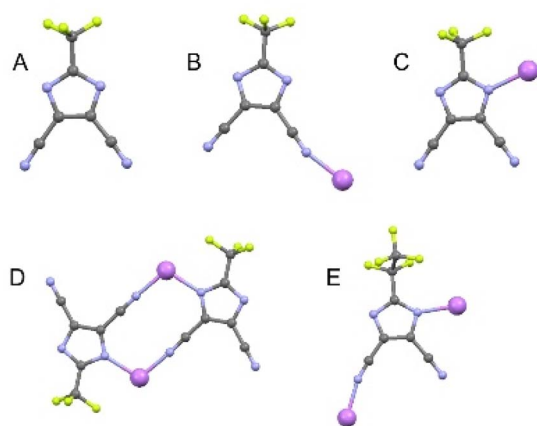


Fig. 2 Coordination modes of the TDI^- , PDI^- and HDI^- anions found in adducts with aprotic solvents: (A) "free" anions (SSIP); (B) contact ion pairs (CIP I); (C) contact ion pairs (CIP II); (D) dimer; (E) chain. Molecules: pink – Li, blue – N, yellow – F, gray – C.

Table 1 Relevant data from Raman spectra of LiTDI, LiPDI and LiHDI solvates representing various types of anion coordination. The acronyms are used as in Fig. 2

Formula	ν_{CN} [cm^{-1}]	$\nu_{\text{CN Im}}$ [cm^{-1}]	$\delta_{\text{NCN Im}}$ [cm^{-1}]	Coordination mode
LiTDI				
$[\text{Li}^+(12\text{C}4)_2]\text{TDI}$	2225	1307	977	SSIP
$\text{Li}(15\text{C}5)\text{TDI}$	2228; 2239	1302	979	CIP I
$\text{Li}(\text{G}3)\text{TDI}$	2230	1320	991	CIP II
$[\text{Li}(\text{G}2)]_2\text{TDI}_2$	2250; 2233	1313	988; 976	Dimer
LiPDI				
$[\text{Li}^+(12\text{C}4)_2]\text{PDI}^-$	2229	1300	943	SSIP
$[\text{Li}(15\text{C}5)]\text{PDI}$	2244; 2234	1311	948	CIP I
$[\text{Li}(\text{G}2)]_2\text{PDI}_2$	2257; 2233	1308	951	Dimer
$[\text{Li}(\text{G}2)\text{PDI}]_n$	2255	1312	948	Chain
$[\text{Li}(\text{AN})]_2\text{PDI}_2$	2256; 2238	1309	954	Dimer
LiHDI				
$[\text{Li}^+(12\text{C}4)_2]\text{HDI}^-$	2226; 2216	1299	993	SSIP
$\text{Li}(15\text{C}5)\text{HDI}$	2228	1308	1002; 992	CIP II
$[\text{Li}(\text{G}2)]_2\text{HDI}_2$ or $[\text{Li}(\text{G}2)\text{HDI}]_n$	2254; 2232	1310	992	Dimer or chain



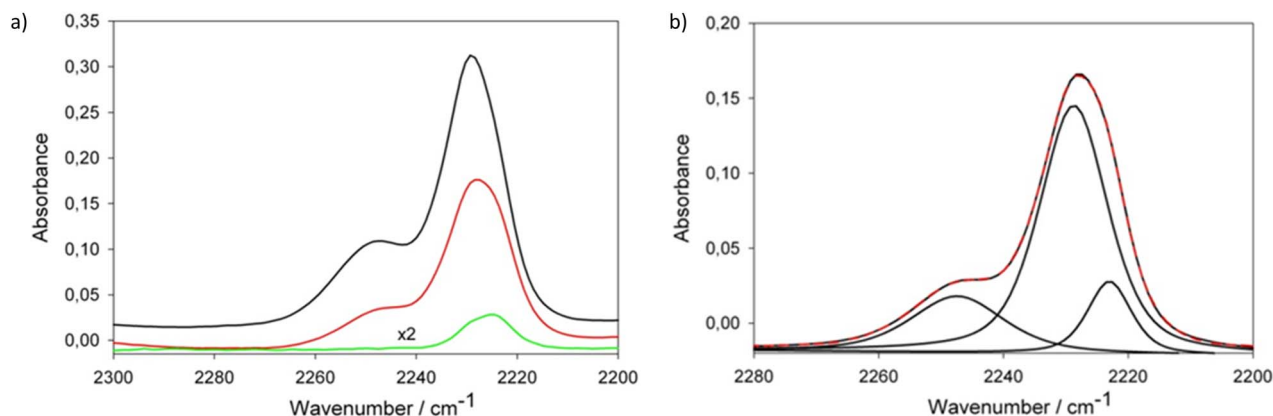


Fig. 3 (a) Spectral range of the ν_{CN} vibrations in FTIR spectra of electrolytes containing LiHDI in a solvent mixture of EC and DEC with different salt concentration: 1 M (black line), 0.63 M (red line) and 0.1 M (green line) and (b) the exemplary deconvolution of the ν_{CN} band for the 0.63 M solution.

deconvolution of this range. The attribution of the peaks was made on the basis of previous studies²³ as follows: 2224 cm^{-1} for free ions (SSIP), 2230 cm^{-1} for ionic pairs (CIP), and 2247 cm^{-1} for aggregates (AGG. *e.g.* dimers/chains).

Table 2 presents the estimated percentage of ionic species obtained on the basis of the deconvolution of ν_{CN} band in FTIR spectra of electrolyte solutions containing LiHDI in a solvent mixture of EC and diethyl carbonate (DEC). The results are very close to that obtained for LiTDI-based electrolytes containing mixtures of organic carbonates²⁵ which supports the conclusion, that HDI⁻ and TDI⁻ anions are characterized by similar donor properties and exhibit similar dissociation mechanisms. Due to the similarity between the dielectric constants of DEC ($\epsilon_r = 2.8$ at 25 °C (ref. 26)) and EMC ($\epsilon_r = 2.9$ at 25 °C (ref. 26)), it is to be expected, that electrolytes based on LiTDI and LiHDI dissolved in solvent mixtures containing EC and EMC show similar dissociation behavior as such containing EC and DEC in their solvent mixtures.

The results from FTIR and Raman analysis, indicate a strong influence of the concentration of the conducting salt on the ionic arrangement, as expected. For LiHDI an increased concentration results in a larger percentage of ionic pairs and aggregates in a solvent mixture containing EC and DEC. Assuming transferability of this behavior to the EC and EMC containing solvent mixture and other Hückel-type salts used herein, this is in agreement with the observed correlation between the anionic self-diffusion coefficients and the viscosity shown in Fig. 8. A higher fraction of paired or aggregated ions is

expected to result in decreased ionic self-diffusion coefficient and conductivity as compared to fully dissociated salt. Both observations are evident in the NMR and conductivity measurements. Table 2 shows, that for LiHDI based-electrolytes, the increase in the number of aggregates is stronger than the one of the number of ionic pairs for increasing concentration.

Conductivity and viscosity of the considered electrolytes

To investigate the influence of the dissociation processes on the performance of electrolytes containing the Hückel-type salts, the conductivity was determined. As shown in Fig. 4, our results show a strong dependence of the ionic conductivity on the salt concentration and temperature, as expected.^{2,7} With increasing temperature, an increase of the conductivity can be observed for all electrolyte formulations. In this work we keep the solvent type and ratio fixed, to only consider the influence of salt concentration and solvation structure on conductivity. For the LiTDI-based electrolyte, the maximum conductivity is observed at an 0.6 M concentration for temperatures up to 20 °C. Above 20 °C, 1 M concentration yields the maximum conductivity. As for LiPDI, which contains a larger anion, the maximum conductivity could also be observed at 0.6 M concentration up to 40 °C. For larger anions as in LiHDI, the conductivity maximum is observed at 0.6 M in the temperature range considered here. The reason why the 0.6 M Hückel-type salt-based electrolyte would have a larger conductivity than the respective 1 M electrolyte formulation could be explained by the formation of ion pairs and aggregates at higher concentration as observed by IR measurement.

Comparing the conductivity of electrolytes based on the different salts at the same salt concentration in Fig. 4d–f, no difference in the conductivity is observed at low salt concentrations of 0.05 M and 0.1 M, but when the salt concentration is increased up to 0.6 M, the LiPDI containing-electrolyte shows the highest ionic conductivity while the electrolyte containing LiTDI has the lowest. When further increasing the salt concentration to 1 M, the LiPDI containing electrolyte retains

Table 2 Data resulting from the deconvolution of the ν_{CN} band in FTIR spectra of electrolytes containing LiHDI dissolved in a solvent mixture composed of EC and DEC

LiHDI conc. [M]	Free ions [%]	Ionic pairs [%]	Aggregates [%]
0.1	62.5	37.5	0
0.63	30.5	51.5	18.0
1.0	15.5	57.5	27.0



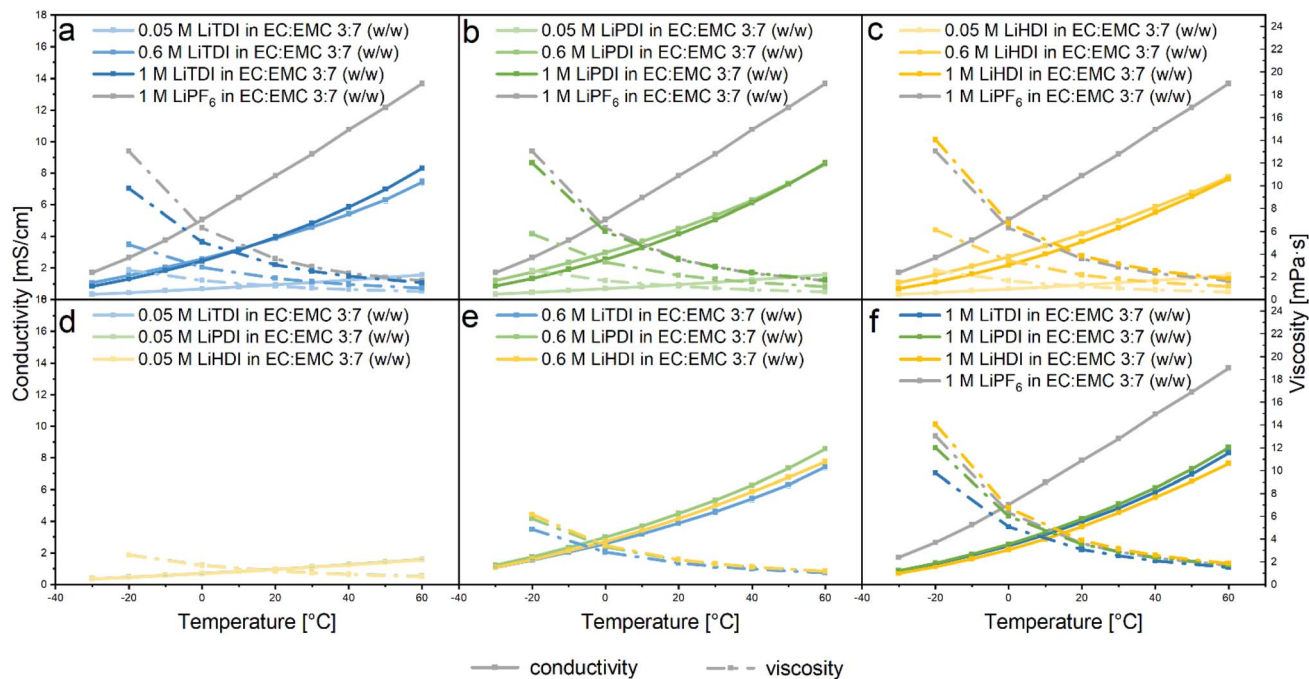


Fig. 4 (a–c) Conductivity vs. viscosity at different temperatures for Hückel-type salt-based electrolytes with different salt concentration (d–f) conductivity vs. viscosity at different temperatures for Hückel-type salt-based electrolytes with the same conducting salt concentration. Solid lines show the conductivity vs. temperature and the dashed-dotted lines represent the viscosity vs. temperature.

the highest ionic conductivity but the electrolyte based on LiHDI gives the lowest one.

For all solutions investigated in this study, the ionic conductivity of electrolytes shows a strong correlation to viscosity. For all considered electrolytes, decreasing viscosity caused the increase of the conductivity, which was strongly

correlated with the increase of the temperature. The changes of the viscosity and conductivity are similar for all the electrolytes as shown in Fig. 4a–c. However, changes are smaller for lower concentrations of the conducting salt in the electrolyte as can be seen in Fig. 4d–f.

Based on the conductivity and viscosity data, a Walden plot²⁷ was compiled. The graph presented in Fig. 5 shows the molar conductivity with respect to the conducting salt concentration plotted vs. the inverse viscosity including 1 M LiPF₆-based electrolyte as a reference. For all formulations, a linear correlation between the molar conductivity and the inverse viscosity is found for increasing temperature. The slopes determined for the formulations presented here are shown in Fig. 6. The slope of $0.80 \log(\text{S cm}^2 \text{ mol}^{-1}) \log(\text{P}^{-1})$ obtained for 1 M LiPF₆ is lower than the ones obtained for the Hückel-type salts, which are closer to unity. Since slopes close to unity indicate a strong interrelation of the ion mobility and viscosity,²⁸ this suggests a less viscosity-controlled ion movement in 1 M LiPF₆ than in any of the other electrolyte formulations investigated here.

The 0.05 M formulations containing Hückel-type salts and the 1 M LiPF₆ electrolyte formulation yield values closest to the ideal KCl line. The vertical deviations from the ideal KCl line, $\Delta \log(\sigma_m)$ are used as indicators for the degree of dissociation.^{27,28} All the 0.05 M formulations range from $-0.64 \log(\text{S cm}^2 \text{ mol}^{-1})$ to $-0.67 \log(\text{S cm}^2 \text{ mol}^{-1})$ at 20 °C suggesting the highest relative ionicity. This is not surprising since 0.05 M electrolyte formulations containing Hückel-type salts yield the lowest viscosities reported herein. Based on the slopes of the Walden plot, the ion mobility in these samples appears to be strongly correlated with viscosity. Furthermore, the low concentration

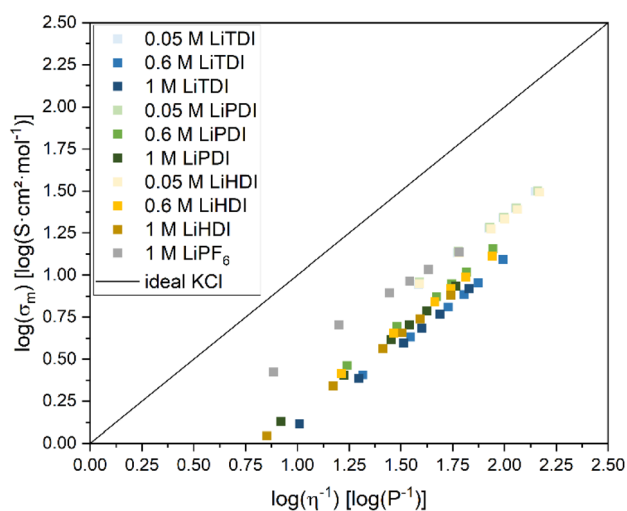


Fig. 5 Walden plot²⁸ for the electrolyte formulations investigated in this study. The formulations having the lowest conducting salt concentration reveal the highest ionicity. For the concentrations higher than 0.05 M, the differences in ionicity are not very pronounced. The data points for 0.6 M LiTDI and 1 M LiTDI are the lowest in this graph.



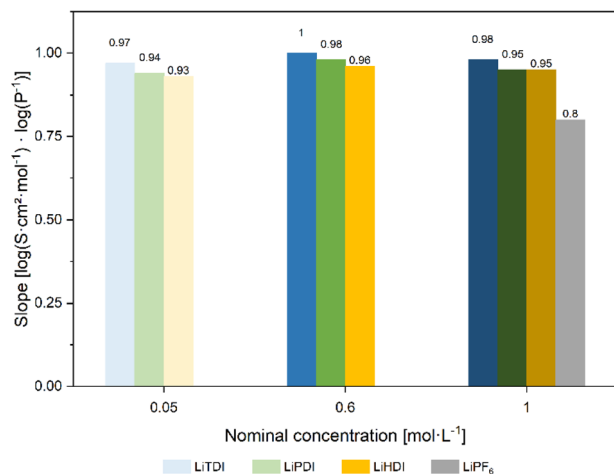


Fig. 6 Slopes determined from the Walden plot for the considered electrolyte formulations.

favoring dissociation of the salts can be expected to support a degree of dissociation in these electrolyte formulations.

The electrolyte formulations containing Hückel-type salts in concentrations higher than 0.05 M are located in a narrow band in the Walden plot. No significant differences are observed between LiPDI and LiHDI containing formulations with respect to ionicity. The $\Delta \log(\sigma_m)$ values for LiPDI are $-0.80 \log(\text{S cm}^2 \text{ mol}^{-1})$ and $-0.83 \log(\text{S cm}^2 \text{ mol}^{-1})$ for 0.6 M and 1 M concentration, respectively, while those for LiHDI are $-0.82 \log(\text{S cm}^2 \text{ mol}^{-1})$ for 0.6 M and $-0.85 \log(\text{S cm}^2 \text{ mol}^{-1})$ for the 1 M solution at 20 °C. The formulations with 0.6 M LiTDI and 1 M LiTDI yield values at the lower end of this band with $\Delta \log(\sigma_m)$ being $-0.92 \log(\text{S cm}^2 \text{ mol}^{-1})$ at 20 °C for both concentrations indicating the lowest ionicity for these electrolyte formulations. The minor differences between 0.6 M and 1 M concentrations for all Hückel-type conducting salts investigated here might indicate a dissociation limit of the formulations at concentrations close to 1 M. The position in the Walden plot of LiTDI at concentrations of 0.6 M and 1 M might indicate a stronger tendency towards ion pairing or aggregation for the LiTDI salt compared to the other Hückel-type salts. This is in agreement with Niedzicki *et al.*,²⁹ who reported a lower association constant for LiHDI compared to LiTDI and LiPDI in electrolytes using propylene carbonate (PC) as a solvent. Niedzicki *et al.*²⁹ suggest the higher volume of the HDI⁻ anion due to the longer perfluoroalkyl side chain as a possible cause for this behavior.

Overall, the electrolyte formulations presented here are located at a significant distance from the ideal KCl line and, therefore, they need to be regarded as only partially dissociated and the presence of ion pairs and aggregates needs to be considered which is in agreement with the IR data discussed in the *IR and Raman spectroscopy* section for LiHDI. Similar structures were found in LiTDI and LiPDI containing formulations in various ethers and glycols as reported by Jankowski *et al.*,¹⁹ who performed XRD investigations. They report a significant number of ionic aggregates at higher salt concentration, mostly dimers and chains for LiTDI and LiPDI.

Unpublished data using the same approach indicates the presence of dimers and chains also for LiHDI in the concentration ranges investigated in our study.

Anion self-diffusion coefficients

Further insights into the dynamics of the electrolyte formulations on a molecular level can be obtained by determining self-diffusion coefficients. In this study, we focus on the anion self-diffusion coefficients. Fig. 7 shows the correlation between the self-diffusion coefficients and the viscosities of the considered electrolyte formulations. Increased viscosity is related to a lower self-diffusion coefficient and higher concentration of the conducting salt. Among the electrolyte formulations of approximately 1 M concentration, the highest self-diffusion coefficient is observed for the PF_6^- anion. The Hückel-type anions show a lower self-diffusion coefficient and a spread in viscosity values. Minor differences in the self-diffusion coefficients between the electrolytes containing the different Hückel-type salts are observed. This is in agreement with the similar dissociation behavior of the Hückel-type salts as reported in the section *IR and Raman spectroscopy*.

Fig. 8 shows the plot of the self-diffusion coefficients obtained as described in the *PGSE-NMR measurements* section *vs.* the molality of the conducting salt. The self-diffusion coefficient for all considered conducting salts in this study decrease with higher salt concentration. Furthermore, Fig. 8 shows, that the self-diffusion coefficient of LiPF₆ is towards the higher end of the range for all molalities of the conducting salt. The Hückel-type salts yield lower self-diffusion coefficients over the whole range of molalities. For electrolytes containing LiTDI and LiPF₆ in a solvent mixture of EC and DMC (1 : 1 by weight), a higher degree of dissociation of LiPF₆ compared to LiTDI is reported.³⁰

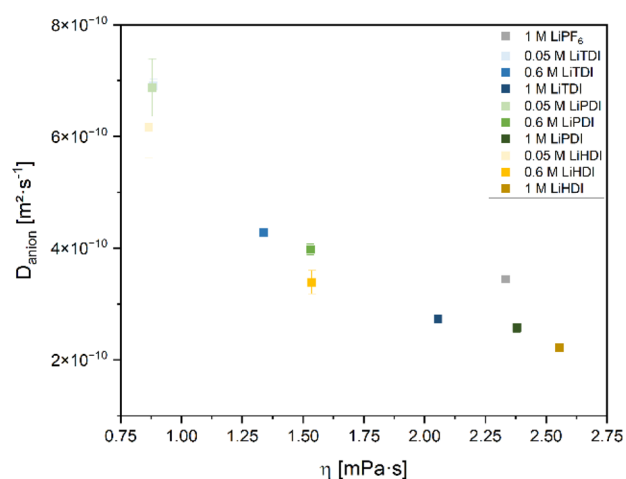


Fig. 7 Self-diffusion coefficients of the anions of the conducting salts contained in the electrolytes plotted *versus* viscosity. The data presented here covers various concentrations of the salts in the solvent mixture EC : EMC 3 : 7 by weight investigated in this study. The electrolyte containing 1 M LiPF₆ is given as a reference. The data is obtained from ¹⁹F NMR using a J-PGSE pulse sequence and evaluation using the Stejskal–Tanner eqn (3.1). The magnet of the used benchtop NMR device operates at 40 °C.



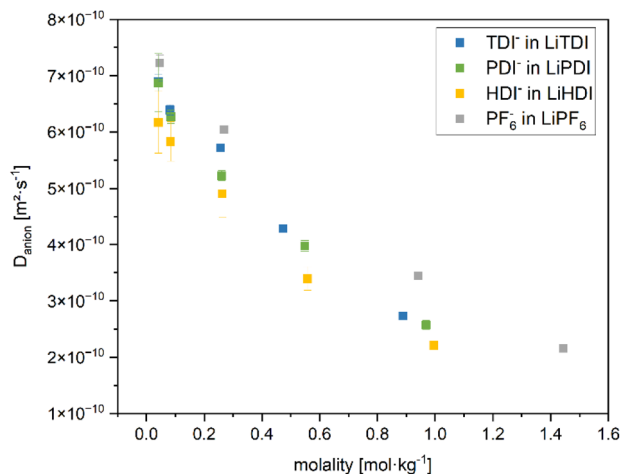


Fig. 8 Self-diffusion coefficients of the anions of the conducting salts in the EC : EMC (3 : 7 by weight) solvent mixture at various molalities determined from ¹⁹F NMR spectra using a J-PGSE pulse sequence. The diffusion coefficients are determined by applying the Stejskal–Tanner eqn (3.1) to the measured spectra. The molalities are calculated from the masses of each component and stock solution recorded during the formulation of the electrolytes. The values for the electrolyte containing 1 M LiPF₆ are given as a reference. The magnet of the used benchtop NMR device operates at 40 °C.

Based on the Walden plot presented in Fig. 5, the degrees of dissociation of LiPDI and LiHDI lie in between LiTDI and LiPF₆. The solvent mixture containing EC and EMC (3 : 7 by weight) used in our study should be expected to result in a tendency towards lower degrees of dissociation due to the slightly lower dielectric constant of EMC ($\epsilon_r = 2.9$ at 25 °C (ref. 31)) compared to DMC ($\epsilon_r = 3.1$ at 25 °C (ref. 31)) and the lower fraction of EC ($\epsilon_r = 95.3$ at 25 °C (ref. 31)) in these mixtures.²⁸ Due to the larger size of associated ions, their mobility is expected to be reduced compared to free ions. Therefore, the lower self-diffusion coefficients for the Hückel-type salt anions compared to the PF₆⁻ anions found for the considered electrolytes indicate a stronger tendency towards ion association for Hückel-type salt anions than for LiPF₆. Differences across Hückel-type salts are minute. The errors of the diffusion coefficients for LiHDI are the largest among the considered formulations, which is most likely due to the splitting of the signals leading to a lower signal-to-noise ratio, which results in higher uncertainties upon integration.

The decrease in self-diffusion coefficient correlates well with the increase in viscosity upon higher concentration of the electrolyte formulations and the decrease in conductivity for increasing concentration above 0.6 M as shown and discussed in the *Conductivity and viscosity of the considered electrolytes* section.

Conclusions

Non-conventional electrolytes need to be selected to incorporate multiple fundamental properties. Here we investigate electrolyte systems containing the Hückel-type salts LiTDI, LiPDI and LiHDI in a solvent mixture of EC and EMC (3 : 7 by weight). FTIR and Raman spectroscopy results reveal the presence of ion

pairs, dimers, chains and aggregates. Values regarding the ionic conductivity, viscosity and anion self-diffusion coefficients of the investigated electrolytes are reported. An analysis of a Walden plot generated based on the conductivity and viscosity data provided insights into the ionicity of the considered electrolytes. LiPF₆ showed the highest ionicity, while LiTDI was found to have the lowest ionicity among the considered Hückel-type conducting salts.

Author contributions

AS planned, performed and analyzed conductivity measurements; PY planned, conducted and analyzed the viscosity and conductivity measurements; MV planned, conducted and analyzed J-PGSE NMR measurements; GZZ planned and performed NMR, IR and FTIR measurements and analyzed the results; AO and SS synthesized the Hückel-type salts; AS, PY, MV and HSS wrote the initial manuscript; CW, ICL, WW, MW, and HSS revised the manuscript.

Conflicts of interest

There are no conflicts to declare.

Acknowledgements

This project received funding from the European Union's Horizon 2020 research and innovation programme under grant agreement No. 957189. The authors acknowledge BATTERY 2030PLUS funded by the European Union's Horizon 2020 research and innovation program under Grant Agreement No. 957213. The work of HSS and MV contributes to the research performed at CELEST (Center for Electrochemical Energy Storage Ulm-Karlsruhe) and was funded by the German Research Foundation (DFG) under Project ID 390874152 (POLIS Cluster of Excellence). MV acknowledges the KIT Graduate School Enabling Net Zero – ENZO.

Notes and references

- 1 A. Benayad, D. Diddens, A. Heuer, A. N. Krishnamoorthy, M. Maiti, F. L. Cras, M. Legallais, F. Rahmanian, Y. Shin, H. Stein, M. Winter, C. Wölke, P. Yan and I. Cekic-Laskovic, High-Throughput Experimentation and Computational Freeway Lanes for Accelerated Battery Electrolyte and Interface Development Research, *Adv. Energy Mater.*, 2022, 12(17), 1–30, DOI: [10.1002/aenm.2021102678](https://doi.org/10.1002/aenm.2021102678).
- 2 F. Rahmanian, M. Vogler, C. Wölke, P. Yan, M. Winter, I. Cekic-Laskovic and H. S. Stein, One-Shot Active Learning for Globally Optimal Battery Electrolyte Conductivity, *Batteries Supercaps*, 2022, 5(10), 1–9, DOI: [10.1002/batt.202200228](https://doi.org/10.1002/batt.202200228).
- 3 S. J. An, J. Li, C. Daniel, D. Mohanty, S. Nagpure and D. L. Wood, The State of Understanding of the Lithium-Ion-Battery Graphite Solid Electrolyte Interphase (SEI) and



- Its Relationship to Formation Cycling, *Carbon*, 2016, **105**, 52–76, DOI: [10.1016/j.carbon.2016.04.008](https://doi.org/10.1016/j.carbon.2016.04.008).
- 4 M. Fichtner, K. Edström, E. Ayerbe, M. Bercibar, A. Bhowmik, I. E. Castelli, S. Clark, R. Dominko, M. Erakca, A. A. Franco, A. Grimaud, B. Horstmann, A. Latz, H. Lorrmann, M. Meeus, R. Narayan, F. Pammer, J. Ruhland, H. Stein, T. Vegge and M. Weil, Rechargeable Batteries of the Future—The State of the Art from a BATTERY 2030+ Perspective, *Adv. Energy Mater.*, 2022, **12**(17), 1–25, DOI: [10.1002/aenm.202102904](https://doi.org/10.1002/aenm.202102904).
 - 5 J. Amici, P. Asinari, E. Ayerbe, P. Barboux, P. Bayle-Guillemaud, R. J. Behm, M. Bercibar, E. Berg, A. Bhowmik, S. Bodoardo, I. E. Castelli, I. Cekic-Laskovic, R. Christensen, S. Clark, R. Diehm, R. Dominko, M. Fichtner, A. A. Franco, A. Grimaud, N. Guillet, M. Hahlin, S. Hartmann, V. Heiries, K. Hermansson, A. Heuer, S. Jana, L. Jabbour, J. Kallo, A. Latz, H. Lorrmann, O. M. Løvik, S. Lyonnard, M. Meeus, E. Paillard, S. Perraud, T. Placke, C. Punckt, O. Raccurt, J. Ruhland, E. Sheridan, H. Stein, J.-M. Tarascon, V. Trapp, T. Vegge, M. Weil, W. Wenzel, M. Winter, A. Wolf and K. Edström, A Roadmap for Transforming Research to Invent the Batteries of the Future Designed within the European Large Scale Research Initiative BATTERY 2030+, *Adv. Energy Mater.*, 2022, **12**(17), 1–42, DOI: [10.1002/aenm.202102785](https://doi.org/10.1002/aenm.202102785).
 - 6 A. Narayanan Krishnamoorthy, C. Wölke, D. Diddens, M. Maiti, Y. Mabrouk, P. Yan, M. Grünebaum, M. Winter, A. Heuer and I. Cekic-Laskovic, Data-Driven Analysis of High-Throughput Experiments on Liquid Battery Electrolyte Formulations: Unraveling the Impact of Composition on Conductivity, *Chem.: Methods*, 2022, **2**(9), 1–8, DOI: [10.1002/cmtd.202200008](https://doi.org/10.1002/cmtd.202200008).
 - 7 E. Flores, C. Wölke, P. Yan, M. Winter, T. Vegge, I. Cekic-Laskovic and A. Bhowmik, Learning the Laws of Lithium-Ion Transport in Electrolytes Using Symbolic Regression, *Digit. Discovery*, 2022, **1**(4), 440–447, DOI: [10.1039/D2DD00027J](https://doi.org/10.1039/D2DD00027J).
 - 8 E. Flores, G. Åvall, S. Jeschke and P. Johansson, Solvation Structure in Dilute to Highly Concentrated Electrolytes for Lithium-Ion and Sodium-Ion Batteries, *Electrochim. Acta*, 2017, **233**, 134–141, DOI: [10.1016/j.electacta.2017.03.031](https://doi.org/10.1016/j.electacta.2017.03.031).
 - 9 F. Lindgren, C. Xu, L. Niedzicki, M. Marcinek, T. Gustafsson, F. Björefors, K. Edström and R. Younesi, SEI Formation and Interfacial Stability of a Si Electrode in a LiTDI-Salt Based Electrolyte with FEC and VC Additives for Li-Ion Batteries, *ACS Appl. Mater. Interfaces*, 2016, **8**(24), 15758–15766, DOI: [10.1021/acsami.6b02650](https://doi.org/10.1021/acsami.6b02650).
 - 10 C. Xu, S. Renault, M. Ebadi, Z. Wang, E. Björklund, D. Guyomard, D. Brandell, K. Edström and T. Gustafsson, LiTDI: A Highly Efficient Additive for Electrolyte Stabilization in Lithium-Ion Batteries, *Chem. Mater.*, 2017, **29**(5), 2254–2263, DOI: [10.1021/acs.chemmater.6b05247](https://doi.org/10.1021/acs.chemmater.6b05247).
 - 11 K. Xu, Nonaqueous Liquid Electrolytes for Lithium-Based Rechargeable Batteries, *Chem. Rev.*, 2004, **104**(10), 4303–4418, DOI: [10.1021/cr030203g](https://doi.org/10.1021/cr030203g).
 - 12 B. Zhang, L. Merker, A. Sanin and H. S. Stein, Robotic Cell Assembly to Accelerate Battery Research, *Digit. Discovery*, 2022, **1**(6), 755–762, DOI: [10.1039/D2DD00046F](https://doi.org/10.1039/D2DD00046F).
 - 13 J. Hu, B. Wu, S. Chae, J. Lochala, Y. Bi and J. Xiao, Achieving Highly Reproducible Results in Graphite-Based Li-Ion Full Coin Cells, *Joule*, 2021, **5**(5), 1011–1015, DOI: [10.1016/j.joule.2021.03.016](https://doi.org/10.1016/j.joule.2021.03.016).
 - 14 L. Niedzicki, S. Grugeon, S. Laruelle, P. Judeinstein, M. Bukowska, J. Prejzner, P. Szczeciński, W. Wiczorek and M. Armand, New Covalent Salts of the 4+V Class for Li Batteries, *J. Power Sources*, 2011, **196**(20), 8696–8700, DOI: [10.1016/j.jpowsour.2011.06.030](https://doi.org/10.1016/j.jpowsour.2011.06.030).
 - 15 I. A. Shkrob, K. Z. Pupek, J. A. Gilbert, S. E. Trask and D. P. Abraham, Chemical Stability of Lithium 2-Trifluoromethyl-4,5-Dicyanoimidazolide, an Electrolyte Salt for Li-Ion Cells, *J. Phys. Chem. C*, 2016, **120**(50), 28463–28471, DOI: [10.1021/acs.jpcc.6b09837](https://doi.org/10.1021/acs.jpcc.6b09837).
 - 16 L. Niedzicki, G. Z. Żukowska, M. Bukowska, P. Szczeciński, S. Grugeon, S. Laruelle, M. Armand, S. Panero, B. Scrosati, M. Marcinek and W. Wiczorek, New Type of Imidazole Based Salts Designed Specifically for Lithium Ion Batteries, *Electrochim. Acta*, 2010, **55**(4), 1450–1454, DOI: [10.1016/j.electacta.2009.05.008](https://doi.org/10.1016/j.electacta.2009.05.008).
 - 17 H.-D. Wiemhöfer, M. Grünebaum and M. Hiller, Mikro-Elektrodenflüssigkeitsmesszelle, WO2014/139494A1, 2014.
 - 18 E. O. Stejskal and J. E. Tanner, Spin Diffusion Measurements: Spin Echoes in the Presence of a Time-Dependent Field Gradient, *J. Chem. Phys.*, 1965, **42**(1), 288–292, DOI: [10.1063/1.1695690](https://doi.org/10.1063/1.1695690).
 - 19 P. Jankowski, M. Dranka, G. Z. Żukowska and J. Zachara, Structural Studies of Lithium 4,5-Dicyanoimidazolate-Glyme Solvates. 1. From Isolated Free Ions to Conductive Aggregated Systems, *J. Phys. Chem. C*, 2015, **119**(17), 9108–9116, DOI: [10.1021/acs.jpcc.5b01352](https://doi.org/10.1021/acs.jpcc.5b01352).
 - 20 P. Jankowski, M. Dranka and G. Z. Żukowska, Structural Studies of Lithium 4,5-Dicyanoimidazolate-Glyme Solvates. 2. Ionic Aggregation Modes in Solution and PEO Matrix, *J. Phys. Chem. C*, 2015, **119**(19), 10247–10254, DOI: [10.1021/acs.jpcc.5b01826](https://doi.org/10.1021/acs.jpcc.5b01826).
 - 21 M. Dranka, P. Jankowski and G. Z. Żukowska, Snapshots of the Hydrolysis of Lithium 4,5-Dicyanoimidazolate-Glyme Solvates. Impact of Water Molecules on Aggregation Processes in Lithium-Ion Battery Electrolytes, *J. Phys. Chem. C*, 2018, **122**(6), 3201–3210, DOI: [10.1021/acs.jpcc.7b11145](https://doi.org/10.1021/acs.jpcc.7b11145).
 - 22 M. Dranka, L. Niedzicki, M. Kasprzyk, M. Marcinek, W. Wiczorek and J. Zachara, An Insight into Coordination Ability of Dicyanoimidazolate Anions toward Lithium in Presence of Acetonitrile. Crystal Structures of Novel Lithium Battery Electrolyte Salts, *Polyhedron*, 2013, **51**, 111–116, DOI: [10.1016/j.poly.2012.12.022](https://doi.org/10.1016/j.poly.2012.12.022).
 - 23 M. Broszkiewicz, A. Zaleska and L. Niedzicki, Comparison of LiTDI and LiPDI Salts and Influence of Their Perfluoroalkyl Side-Chain on Association and Electrochemical Properties in Triglyme, *Ionics*, 2019, **25**(8), 3651–3660, DOI: [10.1007/s11581-019-02905-w](https://doi.org/10.1007/s11581-019-02905-w).



- 24 L. Niedzicki, M. Kasprzyk, K. Kuziak, G. Z. Żukowska, M. Armand, M. Bukowska, M. Marcinek, P. Szczeciński and W. Wieczorek, Modern Generation of Polymer Electrolytes Based on Lithium Conductive Imidazole Salts, *J. Power Sources*, 2009, **192**(2), 612–617, DOI: [10.1016/j.jpowsour.2009.03.050](https://doi.org/10.1016/j.jpowsour.2009.03.050).
- 25 L. Niedzicki, E. Karpierz, A. Bitner, M. Kasprzyk, G. Z. Żukowska, M. Marcinek and W. Wieczorek, Optimization of the Lithium-Ion Cell Electrolyte Composition through the Use of the LiTDI Salt, *Electrochim. Acta*, 2014, **117**, 224–229, DOI: [10.1016/j.electacta.2013.11.134](https://doi.org/10.1016/j.electacta.2013.11.134).
- 26 A. B. McEwen, S. F. McDevitt and V. R. Koch, Nonaqueous Electrolytes for Electrochemical Capacitors: Imidazolium Cations and Inorganic Fluorides with Organic Carbonates, *J. Electrochem. Soc.*, 1997, **144**(4), L84, DOI: [10.1149/1.1837561](https://doi.org/10.1149/1.1837561).
- 27 W. Xu, E. I. Cooper and C. A. Angell, Ionic Liquids: Ion Mobilities, Glass Temperatures, and Fragilities, *J. Phys. Chem. B*, 2003, **107**(25), 6170–6178, DOI: [10.1021/jp0275894](https://doi.org/10.1021/jp0275894).
- 28 D. Farhat, D. Lemordant, J. Jacquemin and F. Ghamouss, Alternative Electrolytes for Li-Ion Batteries Using Glutaronitrile and 2-Methylglutaronitrile with Lithium Bis(Trifluoromethanesulfonyl) Imide, *J. Electrochem. Soc.*, 2019, **166**(14), A3487–A3495, DOI: [10.1149/2.1261914jes](https://doi.org/10.1149/2.1261914jes).
- 29 L. Niedzicki, M. Kasprzyk, K. Kuziak, G. Z. Żukowska, M. Marcinek, W. Wieczorek and M. Armand, Liquid Electrolytes Based on New Lithium Conductive Imidazole Salts, *J. Power Sources*, 2011, **196**(3), 1386–1391, DOI: [10.1016/j.jpowsour.2010.08.097](https://doi.org/10.1016/j.jpowsour.2010.08.097).
- 30 C. L. Berhaut, D. Lemordant, P. Porion, L. Timperman, G. Schmidt and M. Anouti, Ionic Association Analysis of LiTDI, LiFSI and LiPF₆ in EC/DMC for Better Li-Ion Battery Performances, *RSC Adv.*, 2019, **9**(8), 4599–4608, DOI: [10.1039/C8RA08430K](https://doi.org/10.1039/C8RA08430K).
- 31 A. B. McEwen, S. F. McDevitt and V. R. Koch, Nonaqueous Electrolytes for Electrochemical Capacitors: Imidazolium Cations and Inorganic Fluorides with Organic Carbonates, *J. Electrochem. Soc.*, 1997, **144**(4), L84, DOI: [10.1149/1.1837561](https://doi.org/10.1149/1.1837561).



Supplemental Information

Ionic conductivity, viscosity, and self-diffusion coefficients of novel imidazole salts for lithium-ion battery electrolytes

Anna Szczęśna-Chrzan^{a,*}, Monika Vogler^{b,c,*}, Peng Yan^{d,*}, Grażyna Zofia Żukowska^a, Christian Wölke^d, Agnieszka Ostrowska^a, Sara Szymańska^a, Marek Marcinek^a, Martin Winter^d, Isidora Cekic-Laskovic^{d,†}, Władysław Wiczorek^{a,†}, and Helge S. Stein^{b,c,†}

^a Faculty of Chemistry, Warsaw University of Technology, Noakowskiego 3, Warsaw 00-664, Poland

^b Helmholtz Institute Ulm, Applied Electrochemistry, Helmholtzstr. 11, 89081 Ulm, Germany

^c Karlsruhe Institute of Technology, Institute of Physical Chemistry, Fritz-Haber-Weg 2, 76131 Karlsruhe, Germany

^d Helmholtz Institute Münster (IEK-12), Forschungszentrum Jülich GmbH, Corrensstraße 46, 48149 Münster, Germany

* AS, MV and PY contributed equally

1 Electrolyte formulation and conducted measurements

This section presents a table summarizing the electrolyte formulations used in this study, their preparation procedure and the selected measurements, for which they were used.

The procedures applied to formulate the electrolytes used in our study are described in the following. Commercially available 1 M LiPF₆ in EC:EMC (3:7 by weight) is used as a reference in EIS and viscosimetry since it is an established industry standard and to mitigate deviations between the references at different laboratories. For NMR, a 1.5 M LiPF₆ solution is diluted by pre-mixed EC:EMC (3:7 by weight) to ensure the same treatment of all electrolytes including the reference.

- Automated gravimetric dispensing of all components using the robotic system described in¹.
- Manual formulation of stock solutions by gravimetric dosing followed by manual volumetric dosing of the stock solutions controlled by weighing after the addition of each stock solution.

Table SI-1: Overview of the electrolytes used in this study, the respective formulation method and performed measurements. All the electrolyte formulations contain EC:EMC (3:7 by weight) as a solvent mixture. The electrolyte formulation labels report the nominal concentration of the conducting salt in mol·L⁻¹ and the respective conducting salt.

Electrolyte formulation label	Formulation method	Measurements
1 M LiPF ₆ (benchmark)	purchased	EIS, viscosimetry
1 M LiPF ₆ (benchmark)	B	NMR
0.05 M LiTDI	A	EIS, viscosimetry
0.05 M LiPDI	A	EIS, viscosimetry
0.05 M LiHDI	A	EIS, viscosimetry
0.6 M LiTDI	A	EIS, viscosimetry
0.6 M LiPDI	A	EIS, viscosimetry
0.6 M LiHDI	A	EIS, viscosimetry
1 M LiTDI	A	EIS, viscosimetry
1 M LiPDI	A	EIS, viscosimetry
1 M LiHDI	A	EIS, viscosimetry
0.05 M LiTDI	B	NMR
0.05 M LiPDI	B	NMR
0.05 M LiHDI	B	NMR

0.1 M LiTDI	B	NMR
0.1 M LiPDI	B	NMR
0.1 M LiHDI	B	NMR
0.3 M LiTDI	B	NMR
0.3 M LiPDI	B	NMR
0.3 M LiHDI	B	NMR
0.6 M LiTDI	B	NMR
0.6 M LiPDI	B	NMR
0.6 M LiHDI	B	NMR
1 M LiTDI	B	NMR
1 M LiPDI	B	NMR
1 M LiHDI	B	NMR

2 Deviation from theoretical behavior in J-PGSE

Figure SI-1 shows exemplarily the intensities of the two signals of the PF_6^- doublet in the ^{19}F J-PGSE measurement plotted versus the gradient strength for the electrolyte containing 0.3 M LiPF_6 in EC:EMC (3:7 by weight). It can be seen, that the initial intensity in the absence of a gradient is not the maximum intensity for both of the signals. This is observed for several other single salt electrolytes in this study as well.

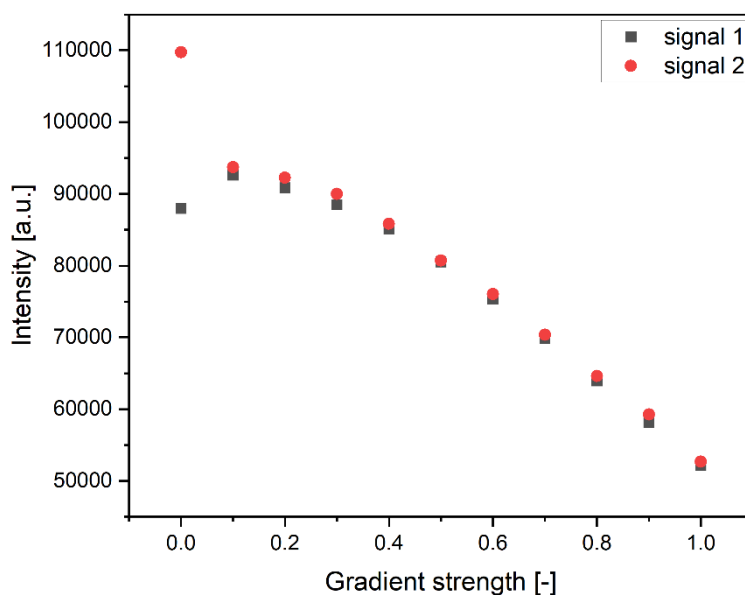


Figure SI-1: The intensity of the two signals of the PF_6^- doublet in the fluorine J-PGSE measurement plotted vs. the gradient strength for the electrolyte containing 0.3 M LiPF_6 in EC:EMC (3:7 by weight). The maximum intensity is observed at zero gradient only for one of the two signals.

3 Analysis of the Walden plot

Deviations from the ideal KCl line determined from the Walden plots presented in the manuscript are presented in Table SI-2 for 20 °C and Table SI-3 for 40 °C, respectively.

Table SI-2: Deviations from the ideal KCl line at 20 °C for electrolyte formulations containing considered conducting salts in EC:EMC (3:7 by weight). The electrolyte formulations are labelled as in Table SI-1.

20 °C			
Electrolyte formulation label	$\log(\sigma_m)_{ideal}$ [$\log(S \cdot cm^2 \cdot mol^{-1})$]	$\log(\sigma_m)_{actual}$ [$\log(S \cdot cm^2 \cdot mol^{-1})$]	Vertical deviation from ideal KCl [$\log(S \cdot cm^2 \cdot mol^{-1})$]
0.05 M LiTDI	1.92526	1.27784	-0.65
0.05 M LiPDI	1.92893	1.28375	-0.65
0.05 M LiHDI	1.93449	1.27323	-0.66
0.6 M LiTDI	1.72688	0.81057	-0.92
0.6 M LiPDI	1.67117	0.87322	-0.80
0.6 M LiHDI	1.66298	0.84126	-0.82
1 M LiTDI	1.51412	0.59737	-0.92
1 M LiPDI	1.45192	0.61784	-0.83
1 M LiHDI	1.41355	0.56419	-0.85
1 M LiPF ₆	1.44434	0.89387	-0.55

Table SI-3: Deviations from the ideal KCl line at 40 °C for electrolyte formulations containing considered conducting salts in EC:EMC (3:7 by weight). The electrolyte formulations are labelled as Table SI-1.

40 °C			
Electrolyte formulation label	$\log(\sigma_m)_{ideal}$ [$\log(S \cdot cm^2 \cdot mol^{-1})$]	$\log(\sigma_m)_{actual}$ [$\log(S \cdot cm^2 \cdot mol^{-1})$]	Vertical deviation from ideal KCl [$\log(S \cdot cm^2 \cdot mol^{-1})$]
0.05 M LiTDI	2.05308	1.39655	-0.66
0.05 M LiPDI	2.05552	1.39967	-0.66
0.05 M LiHDI	2.0625	1.38952	-0.67
0.6 M LiTDI	1.87345	0.95545	-0.92
0.6 M LiPDI	1.81508	1.01939	-0.80
0.6 M LiHDI	1.81364	0.98975	-0.82
1 M LiTDI	1.68715	0.76708	-0.92
1 M LiPDI	1.62357	0.78661	-0.84
1 M LiHDI	1.59295	0.74092	-0.85
1 M LiPF ₆	1.63209	1.03197	-0.60

The slopes determined from the Walden plots for the individual electrolyte formulations investigated in this study are presented in Table SI-4

Table SI-4: Slopes for all considered electrolyte formulations as obtained from the Walden plots. All electrolyte formulations contain EC:EMC (3:7 by weight) as the solvent mixture.

Electrolyte formulation label	Slope [$\log(S \cdot cm^2 \cdot mol^{-1}) \log(P^{-1})$]
0.05 M LiTDI	0.97
0.05 M LiPDI	0.94
0.05 M LiHDI	0.93
0.6 M LiTDI	1.00
0.6 M LiPDI	0.98
0.6 M LiHDI	0.96
1 M LiTDI	0.98
1 M LiPDI	0.95
1 M LiHDI	0.95
1 M LiPF ₆	0.80

4 NMR-spectra of the salts under investigation

This section presents the NMR spectra obtained for the salts under investigation. The ^1H , ^{19}F , and ^{13}C NMR spectra were recorded in CD_3CN , with a Varian VNMR5 spectrometer, operating at 500 MHz. The ^{19}F and ^{13}C NMR spectra confirm the structures of the lithium salts. The ^7Li NMR spectra were recorded for a concentration of 0.63 M salt in EC:EMC (3:7 by weight) without a deuterated solvent using LiCl in D_2O as an external reference.

4.1 ^1H -NMR

4.1.1 LiTDI

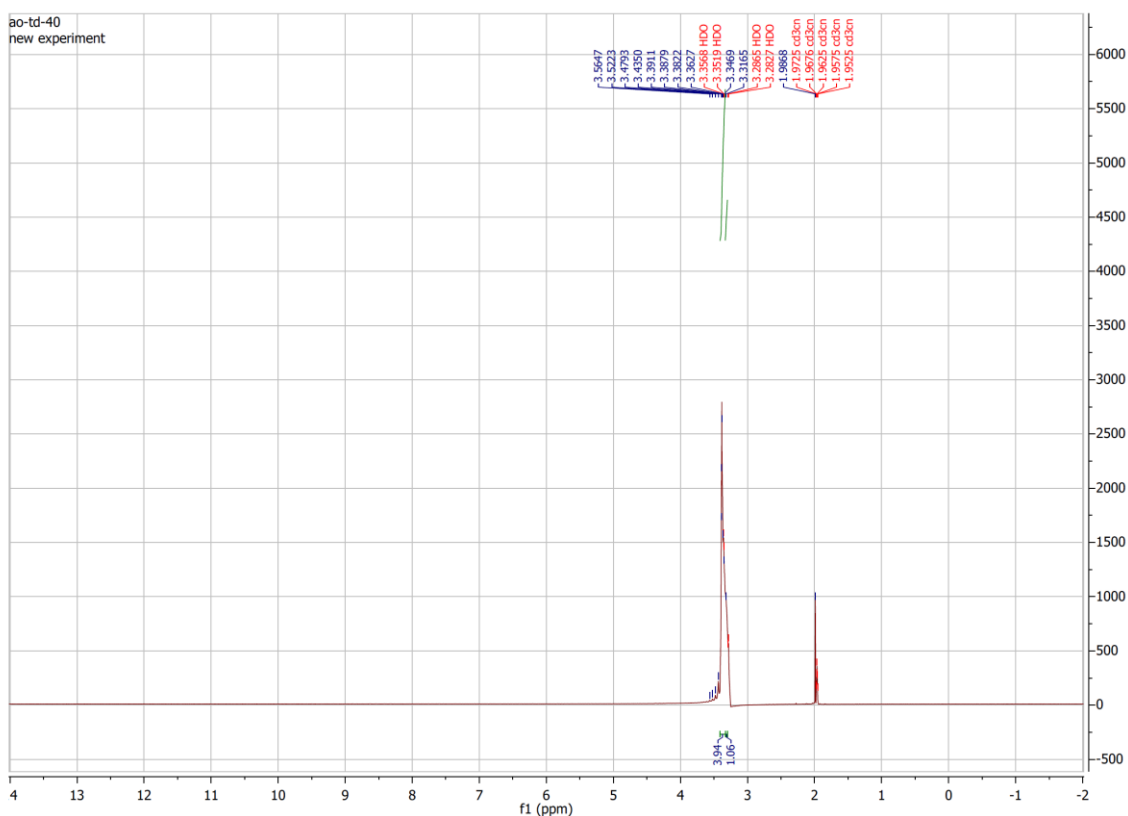


Figure SI-2: ^1H -NMR spectrum of LiTDI

4.1.2 LiPDI

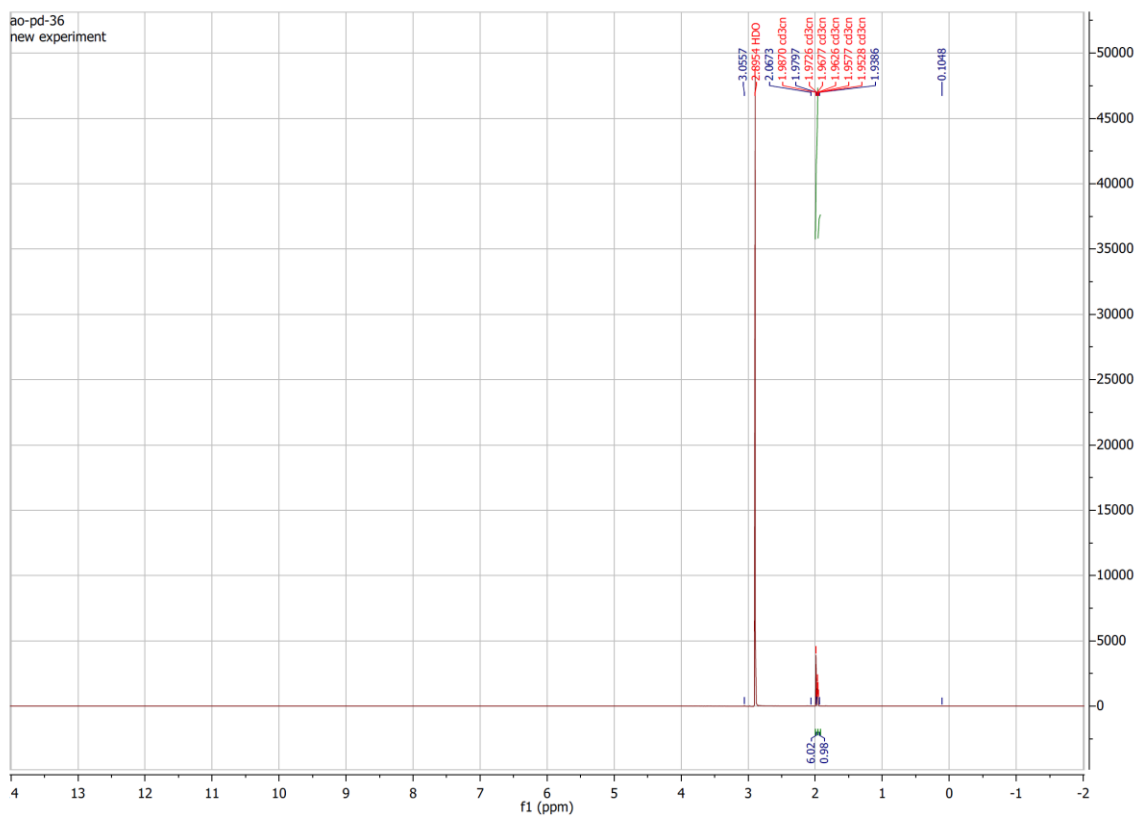


Figure SI-3: $^1\text{H-NMR}$ spectrum of LiPDI

4.1.3 LiHDI

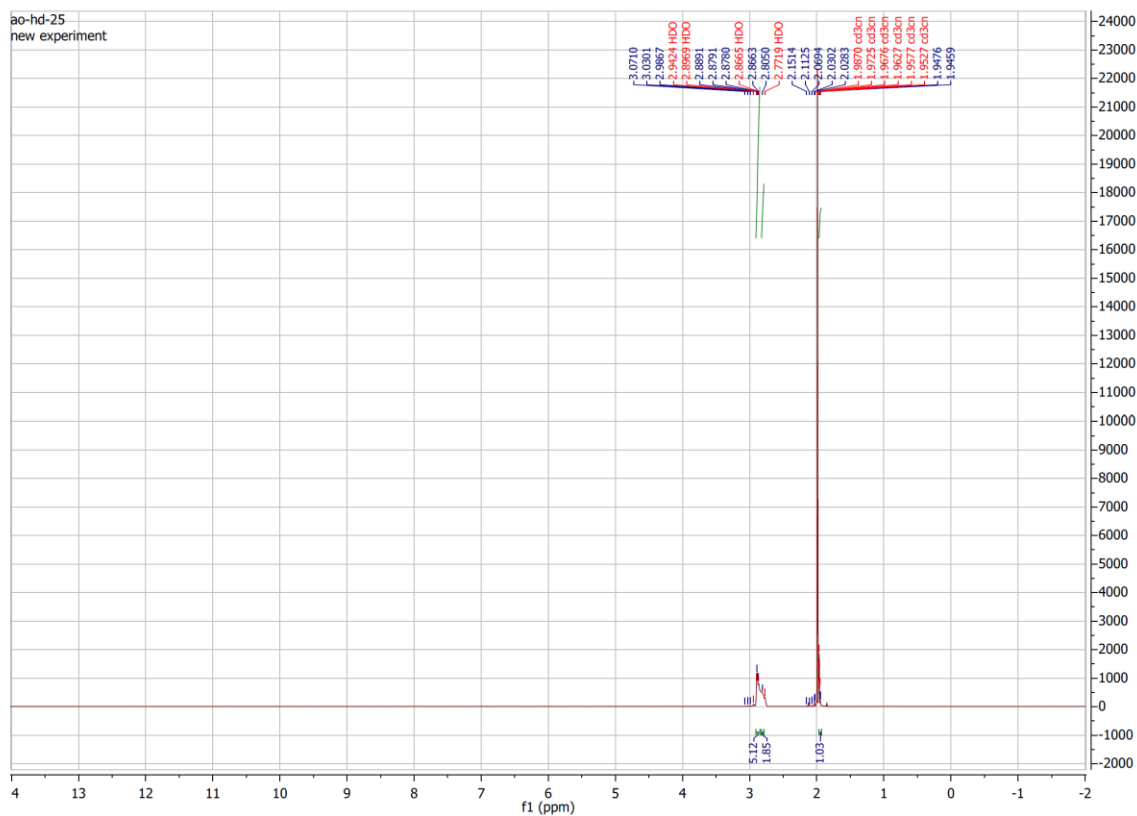


Figure SI-4: $^1\text{H-NMR}$ spectrum of LiHDI

4.2 ^{19}F -NMR

4.2.1 LiTDI

In the ^{19}F NMR spectrum for LiTDI shown in Figure SI-5, a diagnostic signal at $\delta = -64.24$ ppm originating from the $-\text{CF}_3$ group was observed.

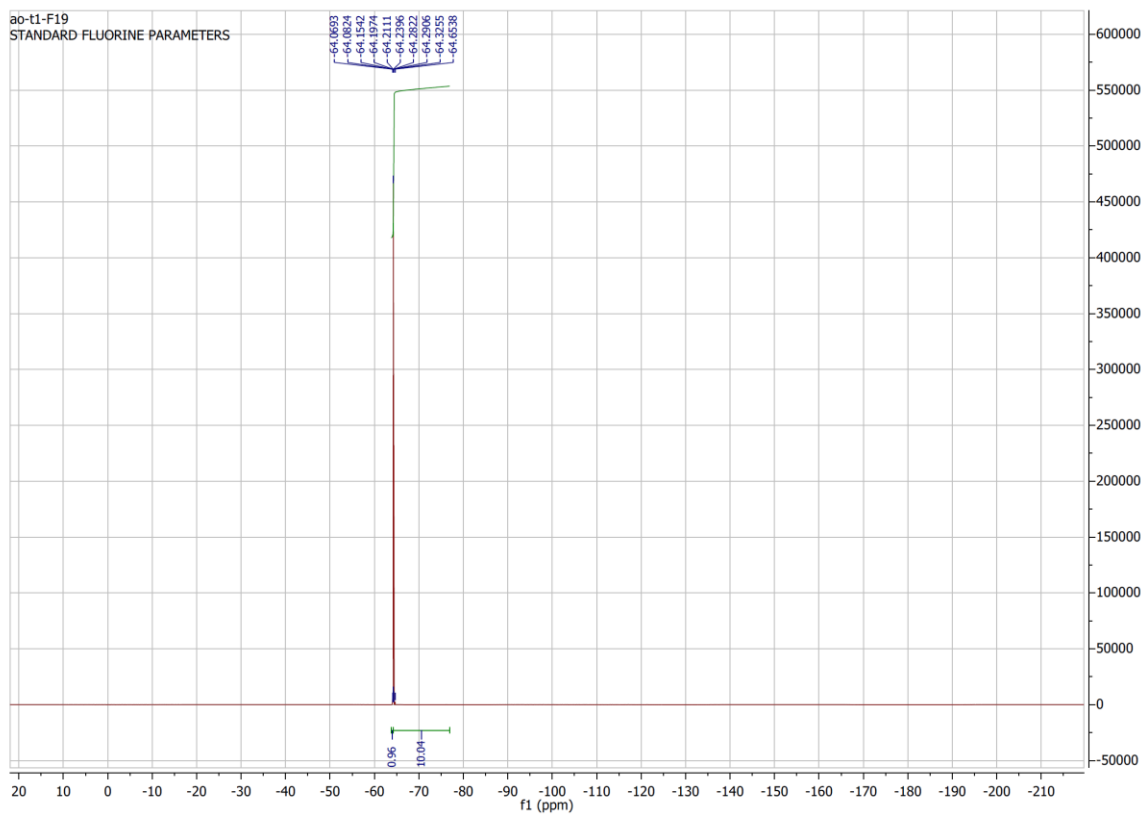


Figure SI-5: ^{19}F -NMR spectrum of LiTDI.

4.2.2 LiPDI

In the ^{19}F NMR spectrum for LiPDI presented in Figure SI-6, we observed two diagnostic signals at $\delta = -84.24$ ppm originating from the $-\text{CF}_3$ group and at $\delta = -112.31$ ppm corresponding to the $-\text{CF}_2$ group of the molecule.

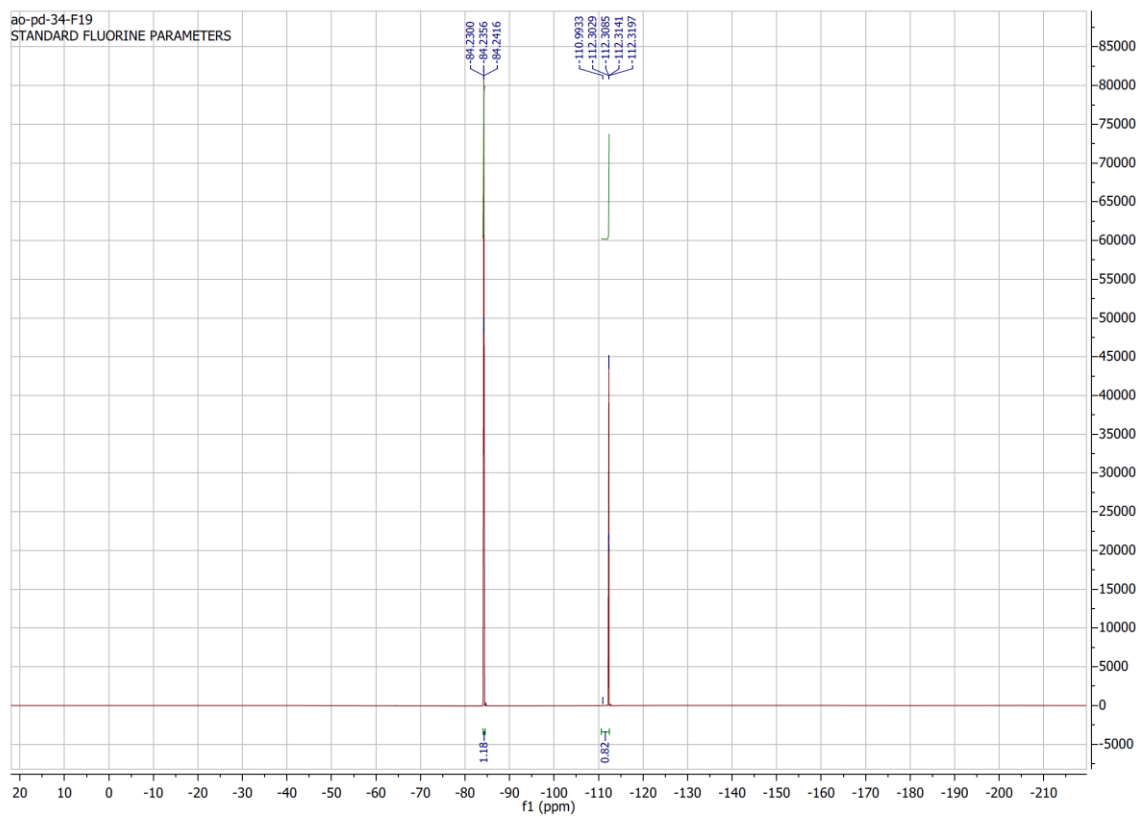


Figure SI-6: ^{19}F -NMR spectrum of LiPDI.

4.2.3 LiHDI

For LiHDI, we observed three diagnostic signals in the ^{19}F spectrum presented in Figure SI-7 at $\delta = -81.31$ ppm originating from the $-\text{CF}_3$ group, $\delta = -111.22$ ppm, and at $\delta = -127.39$ ppm with the latter two corresponding to the $-\text{CF}_2$ groups present in the molecule.

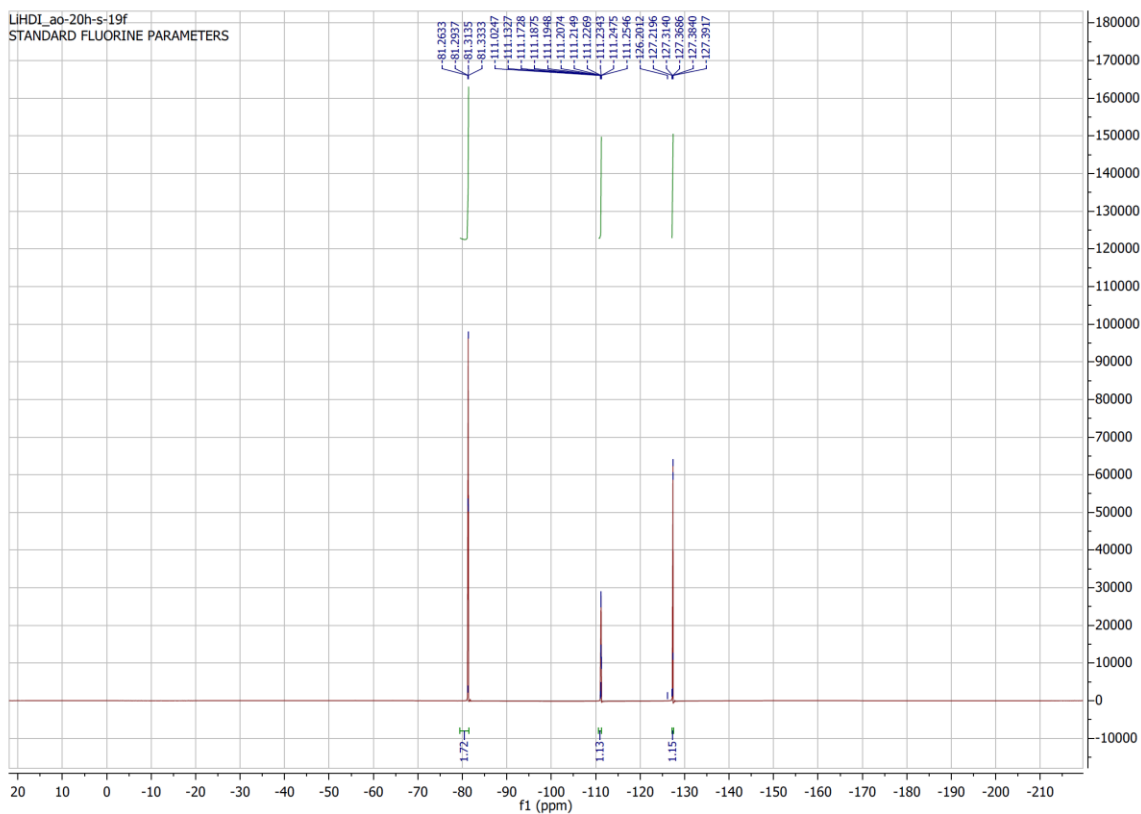


Figure SI-7: Total view of the ^{19}F -NMR spectrum of LiHDI.

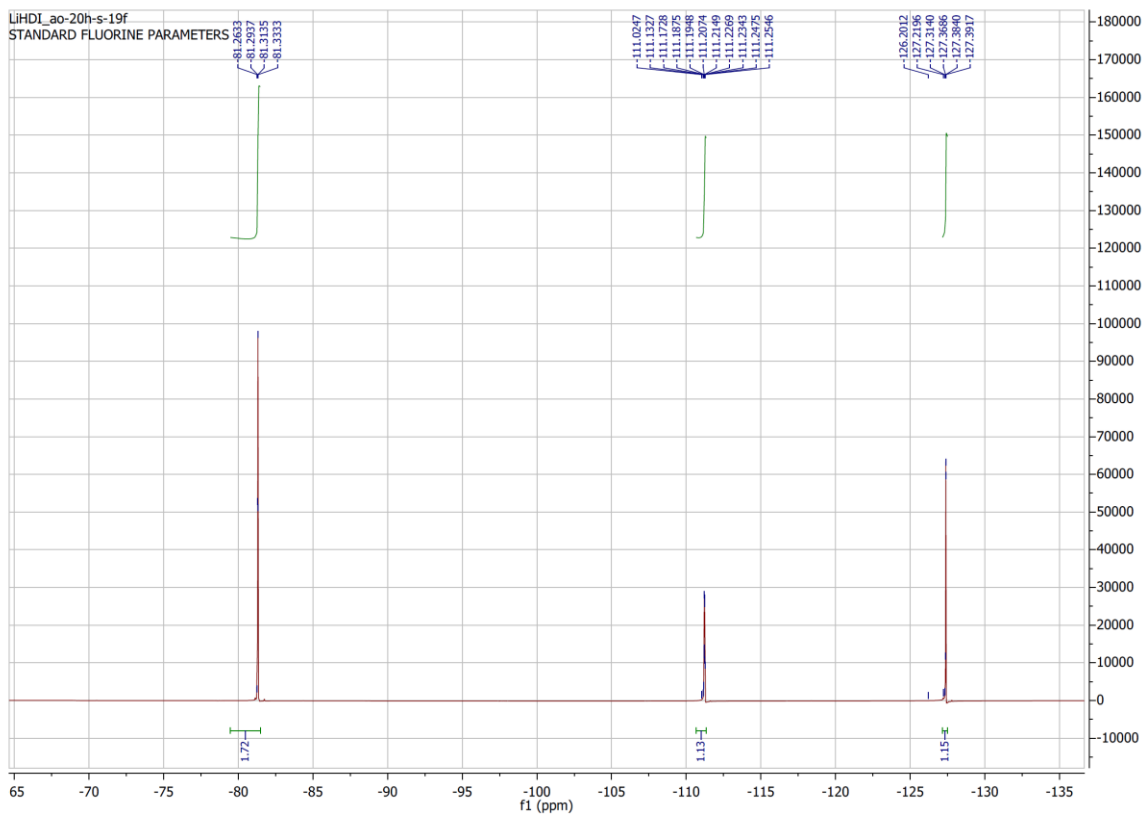


Figure SI-8: Enlarged view of the ^{19}F -NMR spectrum of LiHDI in the range from approx. -137 ppm to 65 ppm.

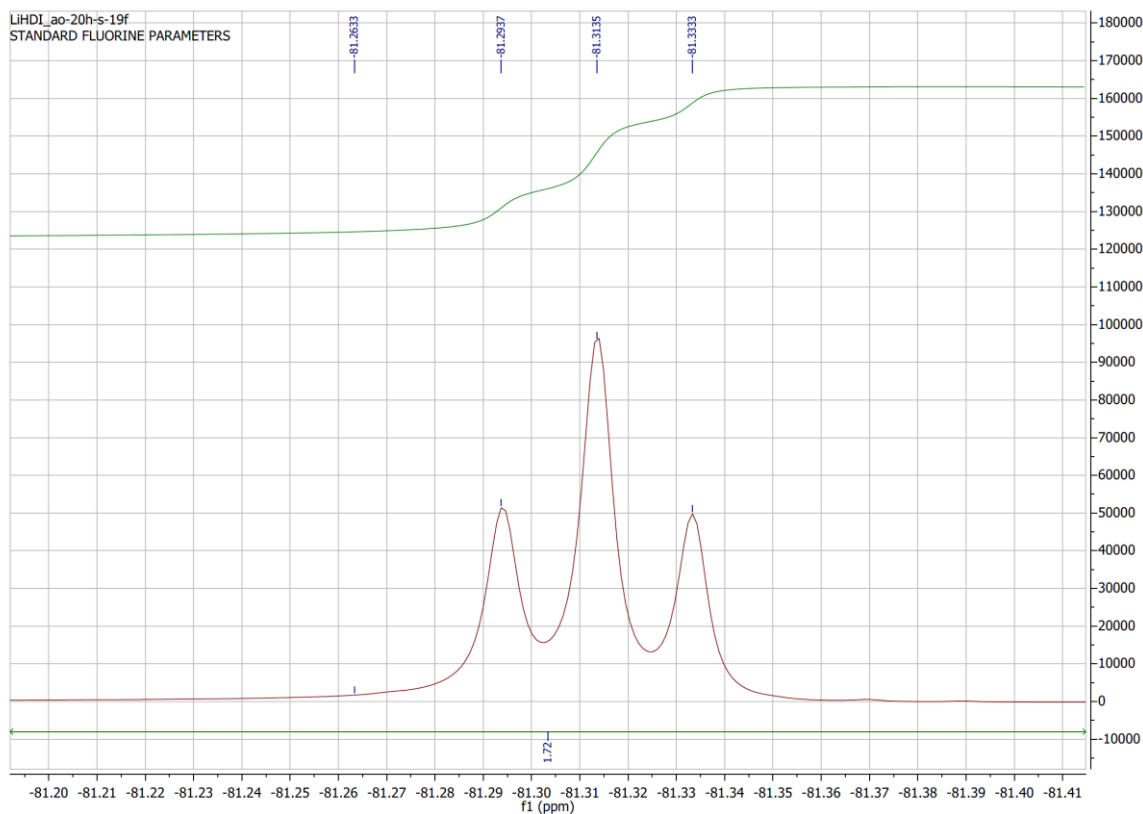


Figure SI-9: Enlarged view of the ^{19}F -NMR spectrum of LiHDI in the range from approx. -81.5 ppm to -81.2 ppm.

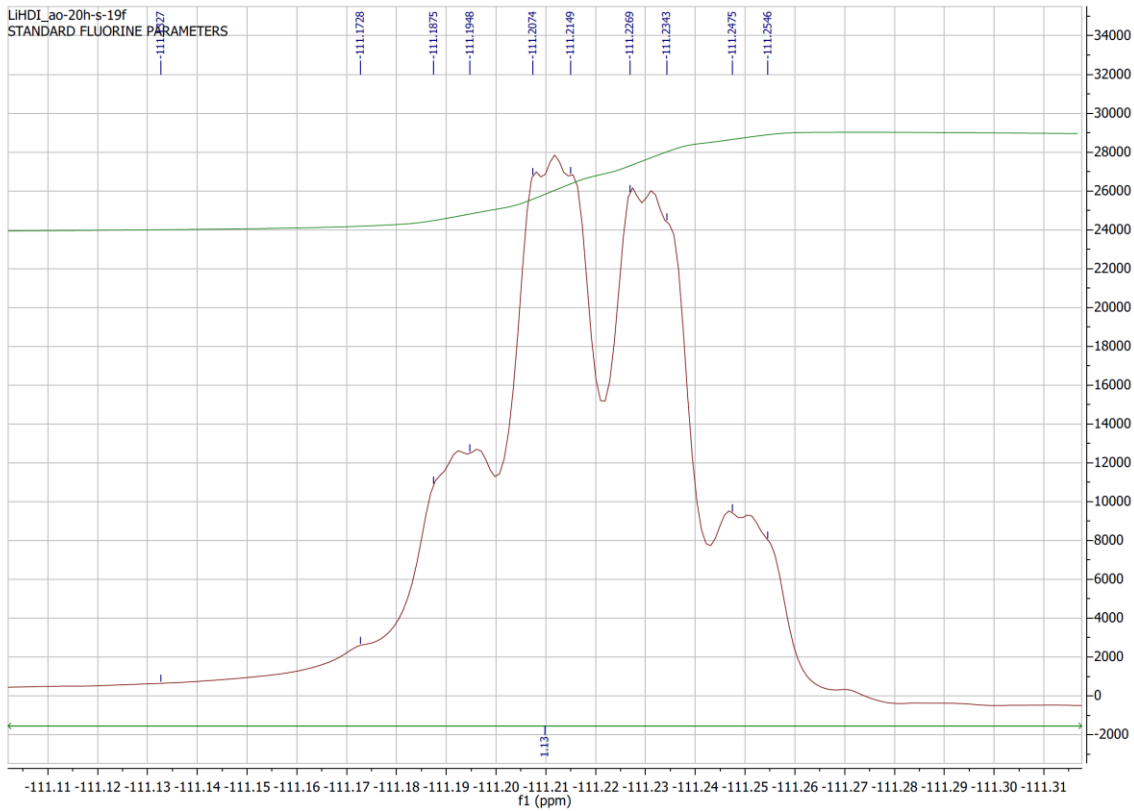


Figure SI-10: Enlarged view of the ^{19}F -NMR spectrum of LiHDI in the range from approx. -111.32 ppm to -111.10 ppm.

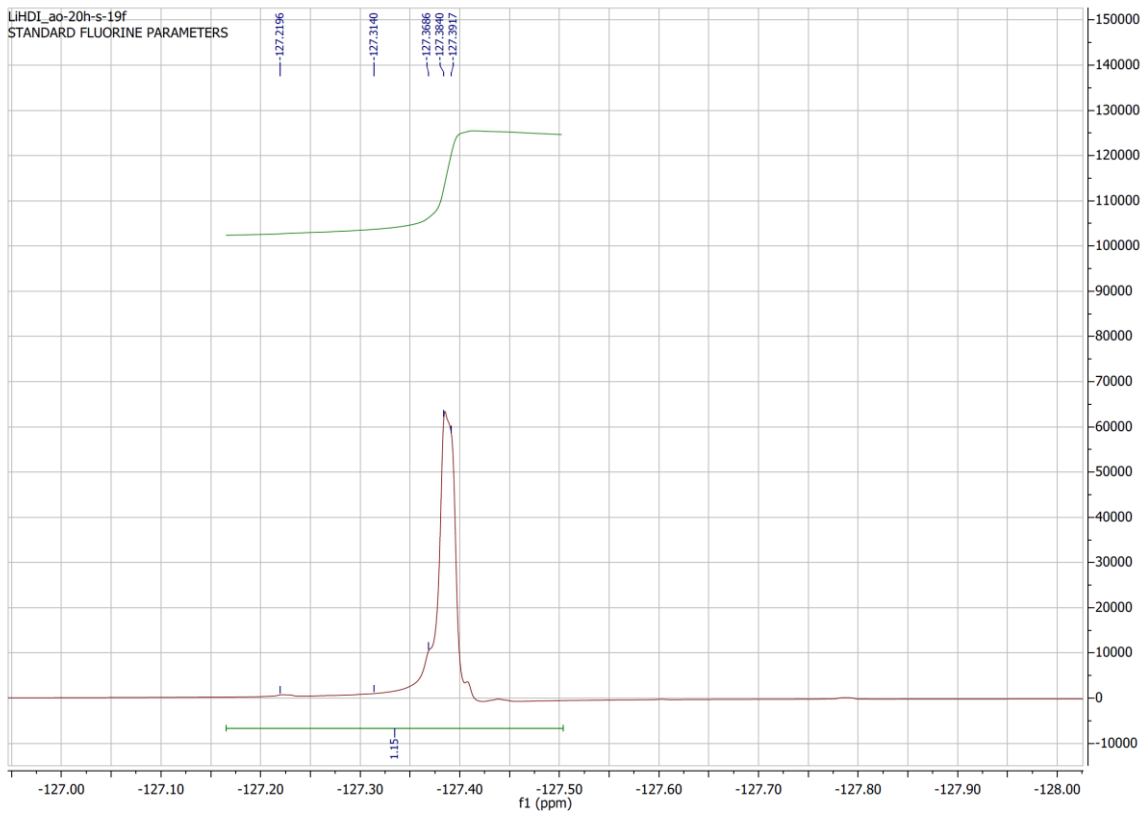


Figure SI-11: Enlarged view of the ^{19}F -NMR spectrum of LiHDI in the range from approx. -128.03 ppm to -126.95 ppm.

4.3 ^{13}C -NMR

All ^{13}C NMR spectra for LiTDI, LiPDI, and LiHDI were in agreement with those published in literature².

4.3.1 LiTDI

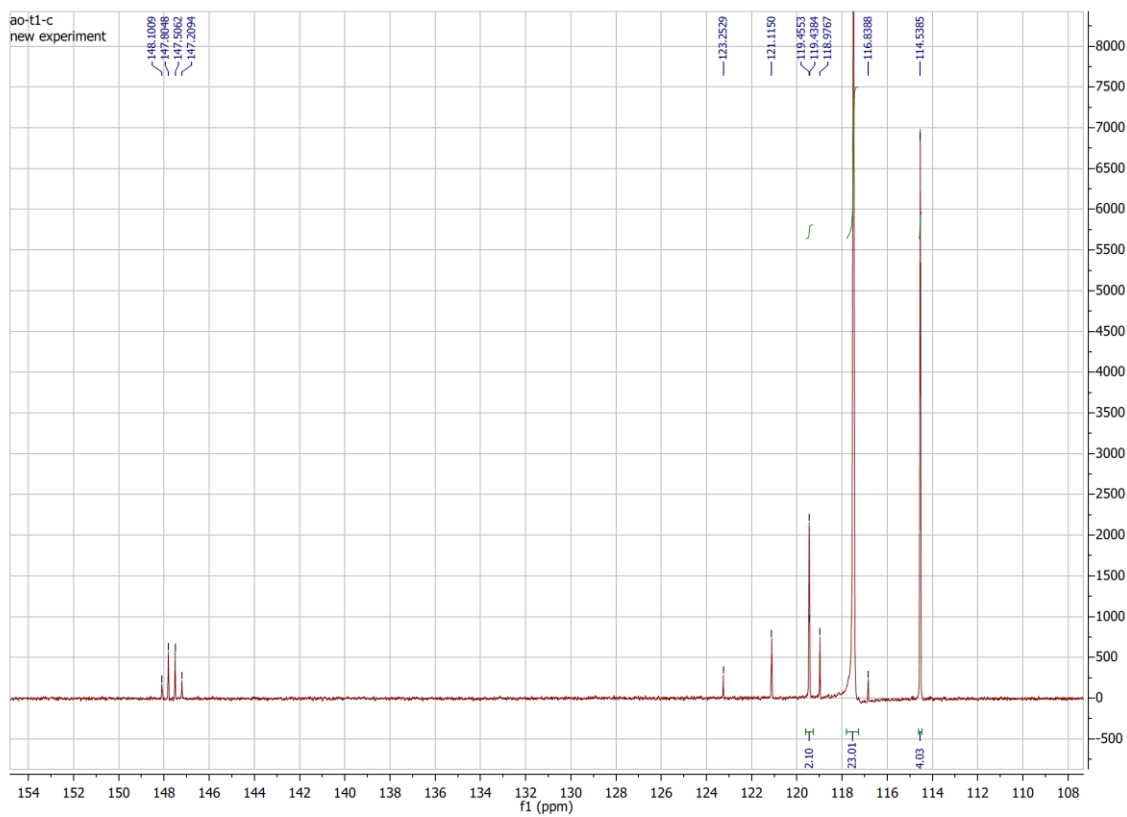


Figure SI-12: Total view of the ^{13}C -NMR spectrum of LiTDI.

4.3.2 LiPDI

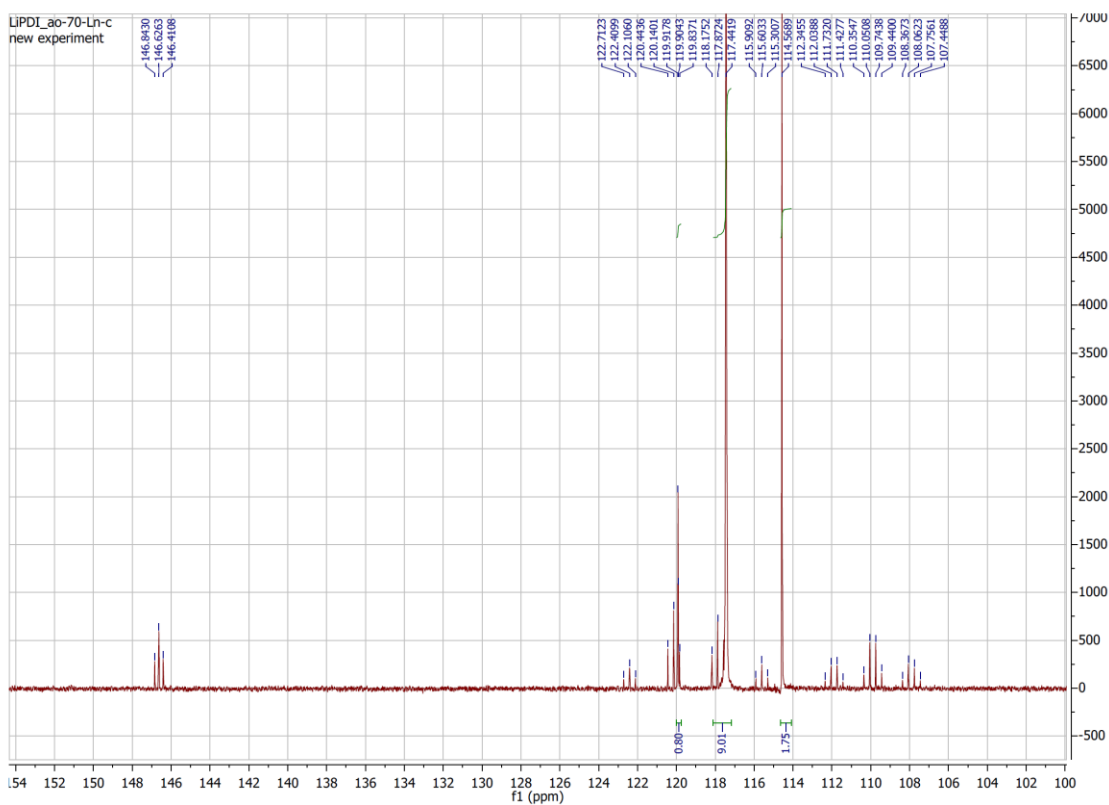


Figure SI-13: Total view of the ^{13}C -NMR spectrum of LiPDI.

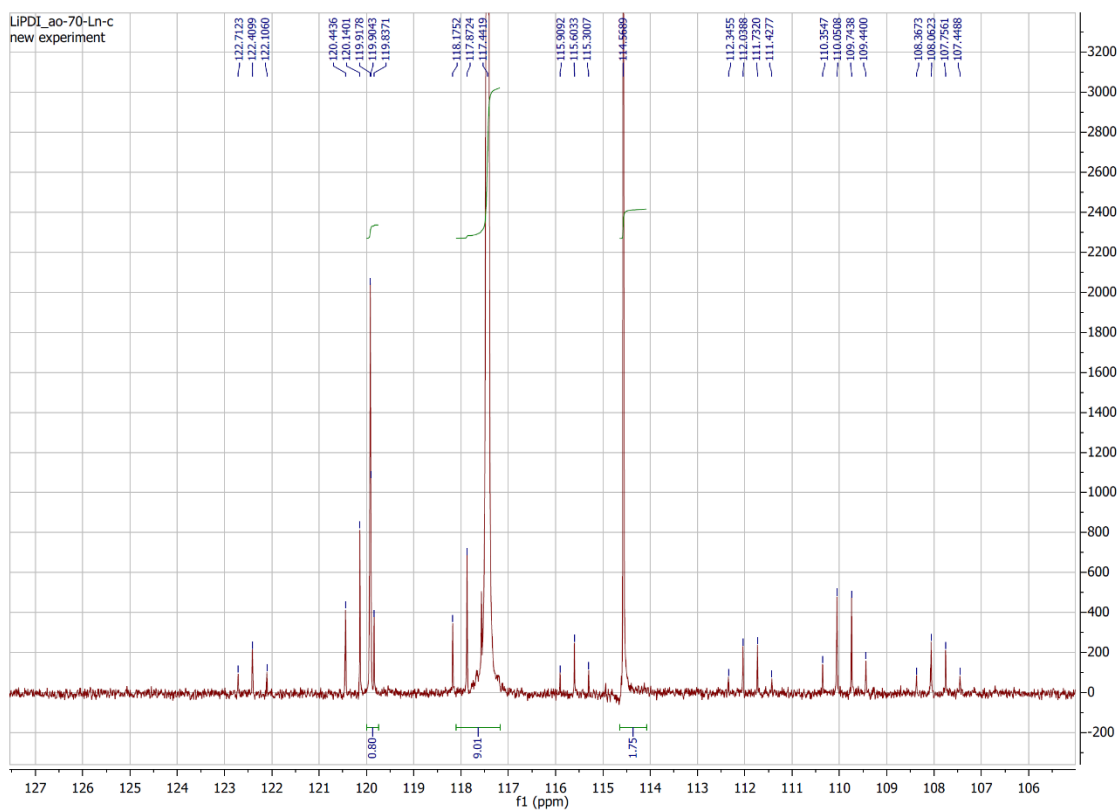


Figure SI-14: Enlarged view of the ^{13}C -NMR spectrum of LiPDI in the range between approx. 105 ppm and 127.5 ppm.

4.3.3 LiHDI

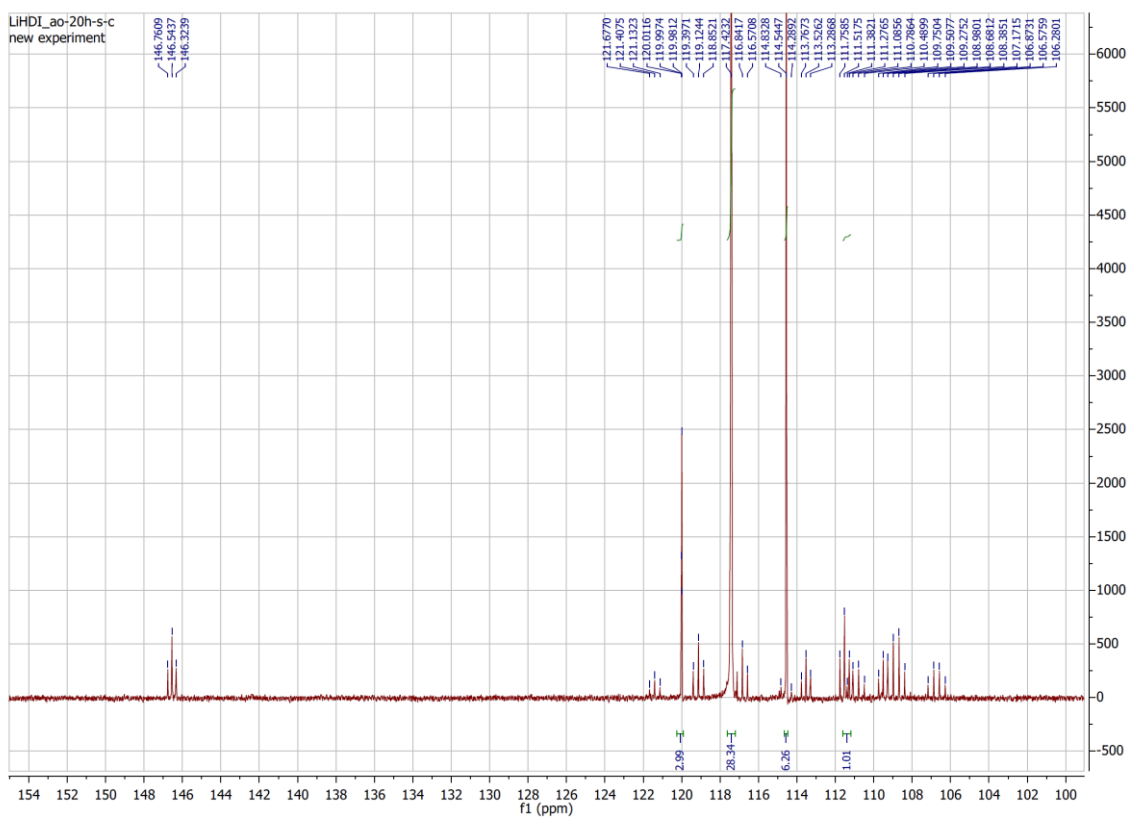


Figure SI-15: ^{13}C -NMR spectrum of LiHDI.

4.4 ^7Li -NMR

Some of the lithium spectra show signals additional to the main signal.

4.4.1 LiTDI

Parameter	Value
1 Title	LiTDI_Li7
2 Origin	Varian
3 Spectrometer	nmr5
4 Solvent	d2o
5 Temperature	25.0
6 Pulse Sequence	s2pul
7 Number of Scans	540
8 Acquisition Time	0.1990
9 Spectrometer Frequency	194.27
10 Nucleus	7Li

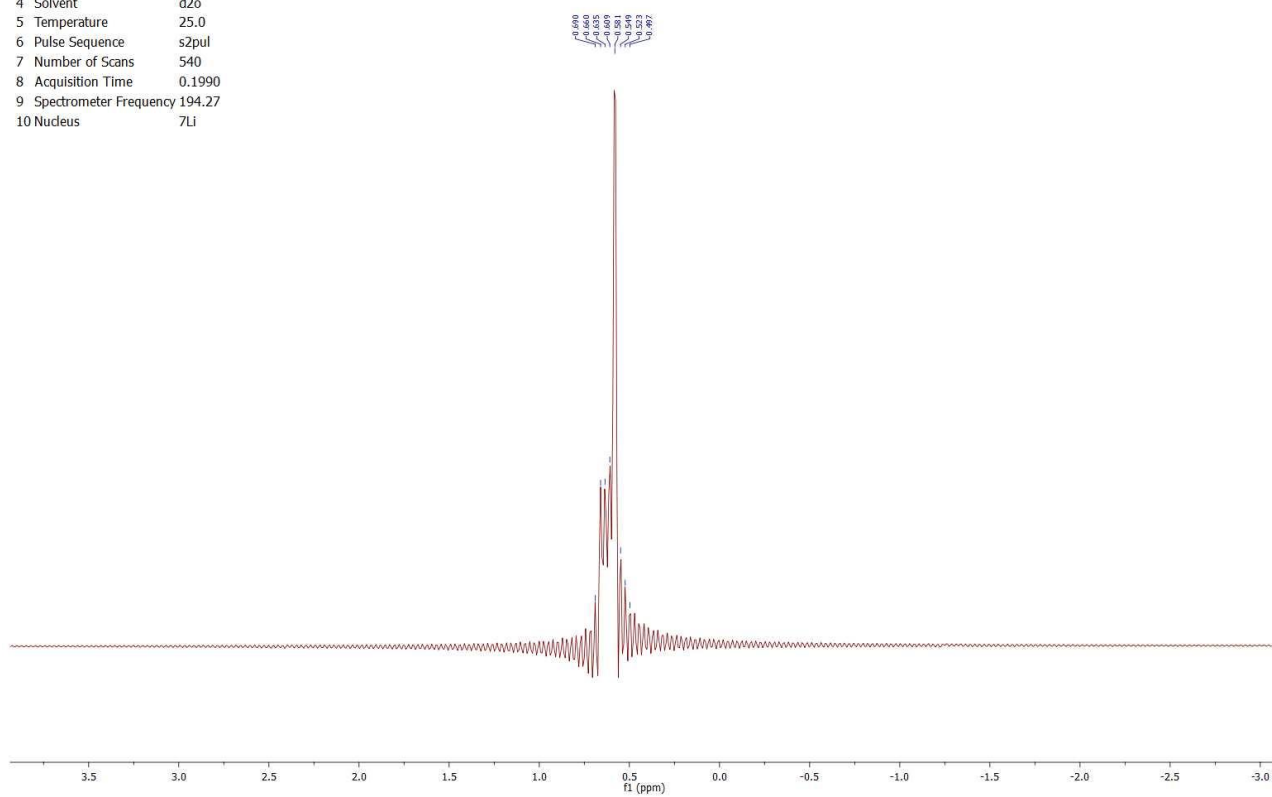


Figure SI-16a: ${}^7\text{Li}$ -NMR spectrum of LiTDI.

4.4.2 LiPDI

Parameter	Value
1 Title	niebieski_Li7
2 Origin	Varian
3 Spectrometer	nmrns
4 Solvent	d2o
5 Temperature	25.0
6 Pulse Sequence	s2pul
7 Number of Scans	680
8 Acquisition Time	0.1990
9 Spectrometer Frequency	194.27
10 Nucleus	⁷ Li

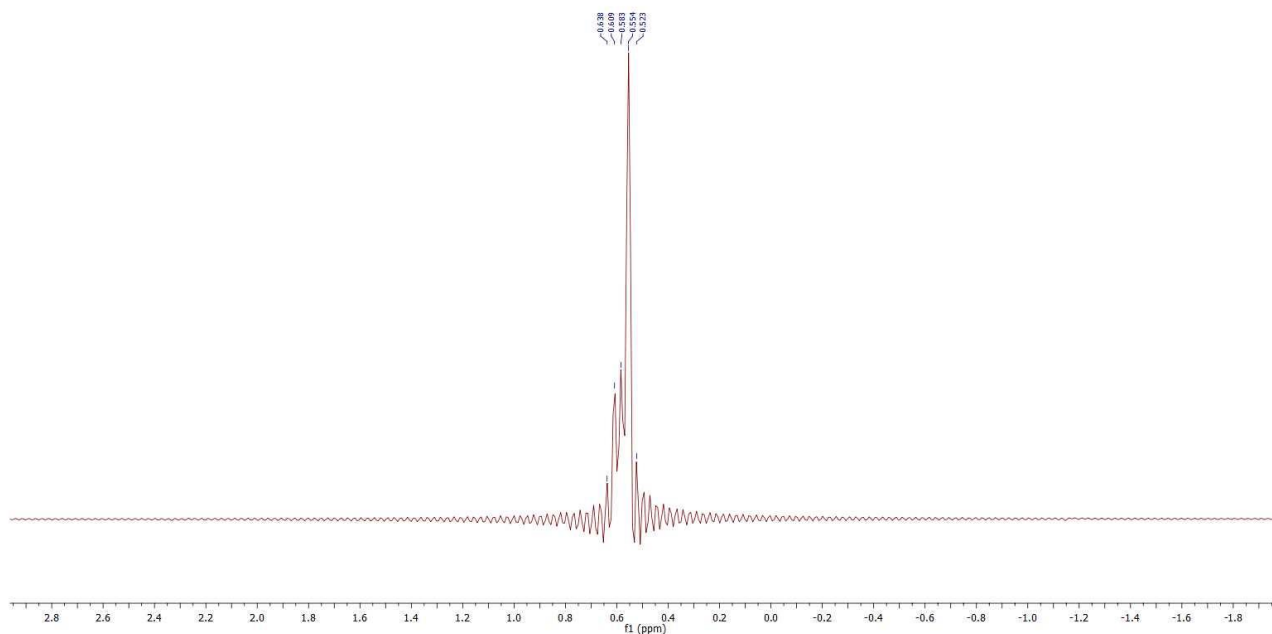


Figure SI-16b: ⁷Li-NMR spectrum of LiPDI.

4.4.3 LiHDI

Parameter	Value
1 Title	zoly_Li7
2 Origin	Varian
3 Spectrometer	nmrs
4 Solvent	d2o
5 Temperature	25.0
6 Pulse Sequence	s2pul
7 Number of Scans	480
8 Acquisition Time	0.1990
9 Spectrometer Frequency	194.27
10 Nucleus	⁷ Li

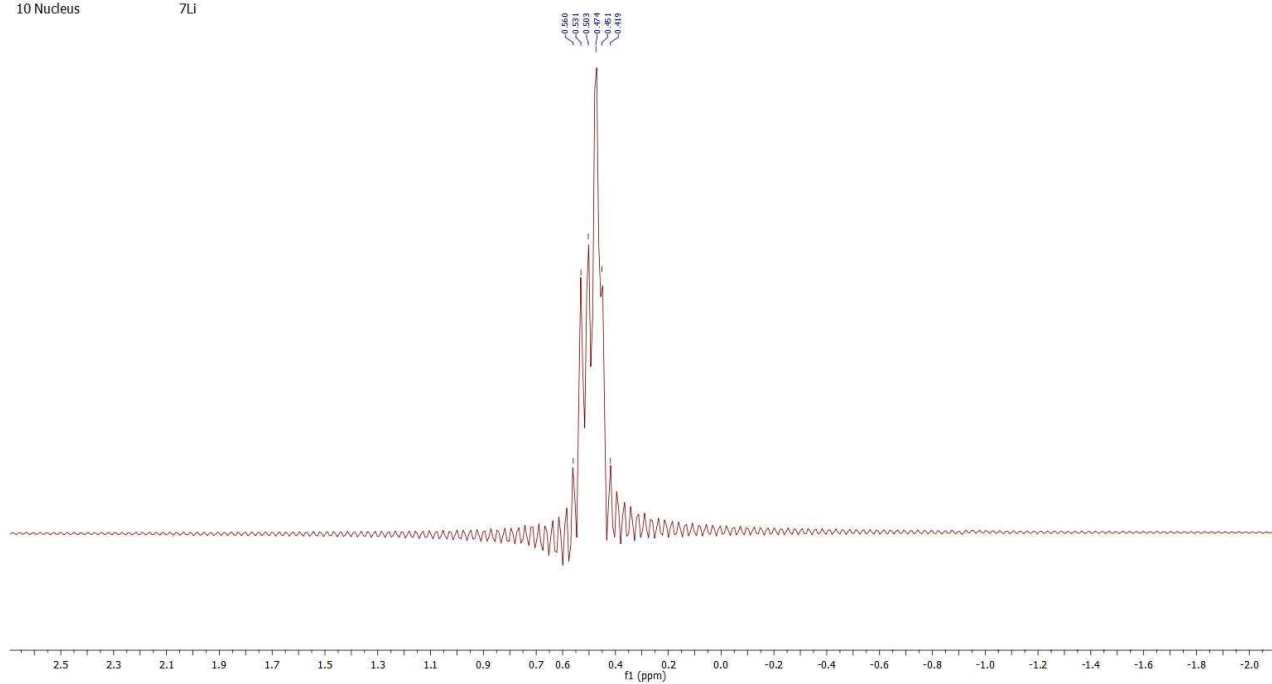


Figure SI-16c: ⁷Li-NMR spectrum of LiHDI.

4.4.4 LiPF₆

Parameter	Value
1 Title	niebieski_Li7
2 Origin	Varian
3 Spectrometer	nmrs
4 Solvent	d2o
5 Temperature	25.0
6 Pulse Sequence	s2pul
7 Number of Scans	680
8 Acquisition Time	0.1990
9 Spectrometer Frequency	194.27
10 Nucleus	⁷ Li

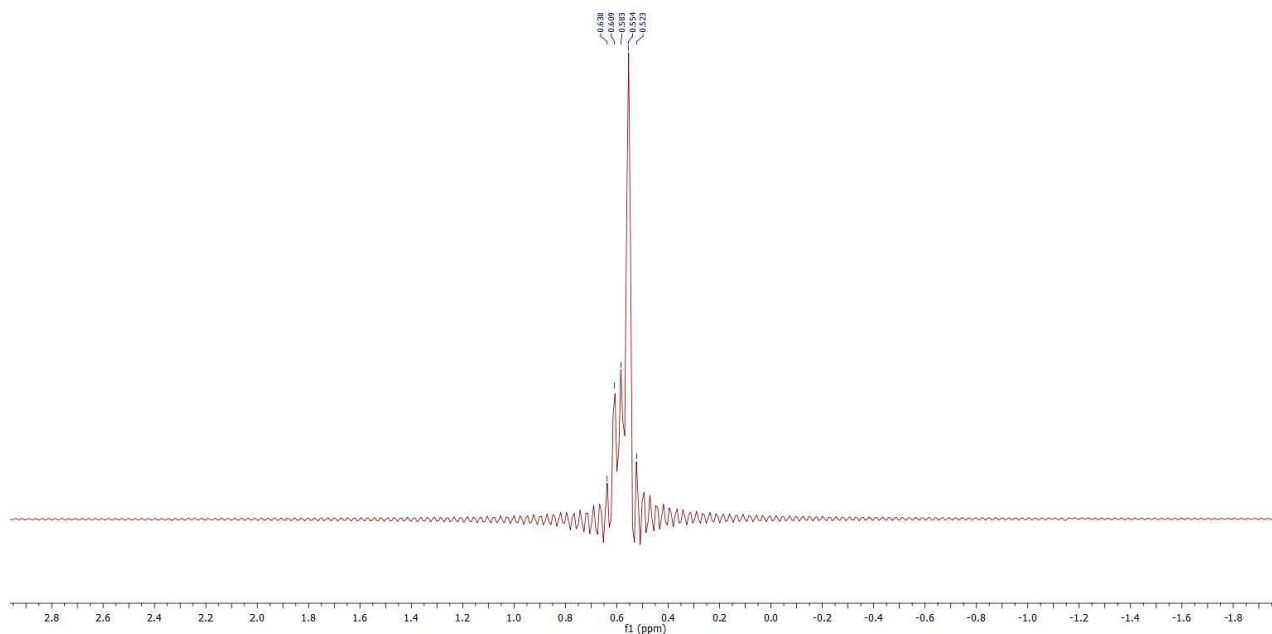


Figure SI-16d: ⁷Li-NMR spectrum of LiPF₆.

5 FTIR and Raman spectra of the pure salts

For each salt three spectral ranges, the full spectrum and the ranges of ring vibrations (1550 cm⁻¹ – 650 cm⁻¹) and vibrations of the CN nitrile groups were applied to present a deep analysis of LiPDI and LiHDI salts using Raman and FTIR methods. The CN stretching vibration band in spectra of the crystalline LiPDI and LiHDI solvates with 12C₄ exhibits a split, with a separation between the bands equal to ~8 cm⁻¹. Such an effect was not found for the previously studied LiTDI solvates and may arise due to the longer alkylchain of the -C₂F₅ and -C₃F₇ substituents as compared with -CF₃ in the TDI⁻ anion. Increasing temperature results in merging of the bands in the spectra of the melted solvate, with the position of the resulting peak averaged between the positions of the peaks in the crystalline state, e.g. 2225 cm⁻¹ for LiHDI-12C₄ melt as compared with 2227 cm⁻¹ and 2218 cm⁻¹ in the crystal. Bands originating from ring stretching and bending vibrations were not split and their position was almost the same before and after melting.

The analysis of the spectra of 15C₅ complexes revealed significant difference between LiPDI and LiHDI. The spectral characteristic of the LiPDI-15C₅ complex, with the position of the γCN band significantly shifted as compared with LiPDI-12C₄, 2242 cm⁻¹ and 2233 cm⁻¹ vs 2227 cm⁻¹ and 2219 cm⁻¹, but similar for the ring bending and stretching vibrations, points on the formation of the complex making use of the nitrile group. After melting, the positions of the anion bands is characteristic for the non-coordinated anion.

In spectra of LiHDI-15C5, bands characteristic for ring stretching and bending vibrations are either split, as in the case of δNCN vibration, or exhibit asymmetry, while the maximum of γCN band is shifted compared with molten LiHDI-12C4 (2230 cm^{-1} vs 2225 cm^{-1}), but the band is only slightly asymmetric. Such spectral features are characteristic for ionic pairs formed with use of the imidazolium nitrogen. After melting, the positions of the bands shift to values characteristic for ionic pairs, but the formation of a shoulder $\sim 2240\text{ cm}^{-1}$, clearly visible in Raman spectrum, is an evidence of partial aggregation of the salt.

5.1 LiPDI

5.1.1 In 12C4 crown ether

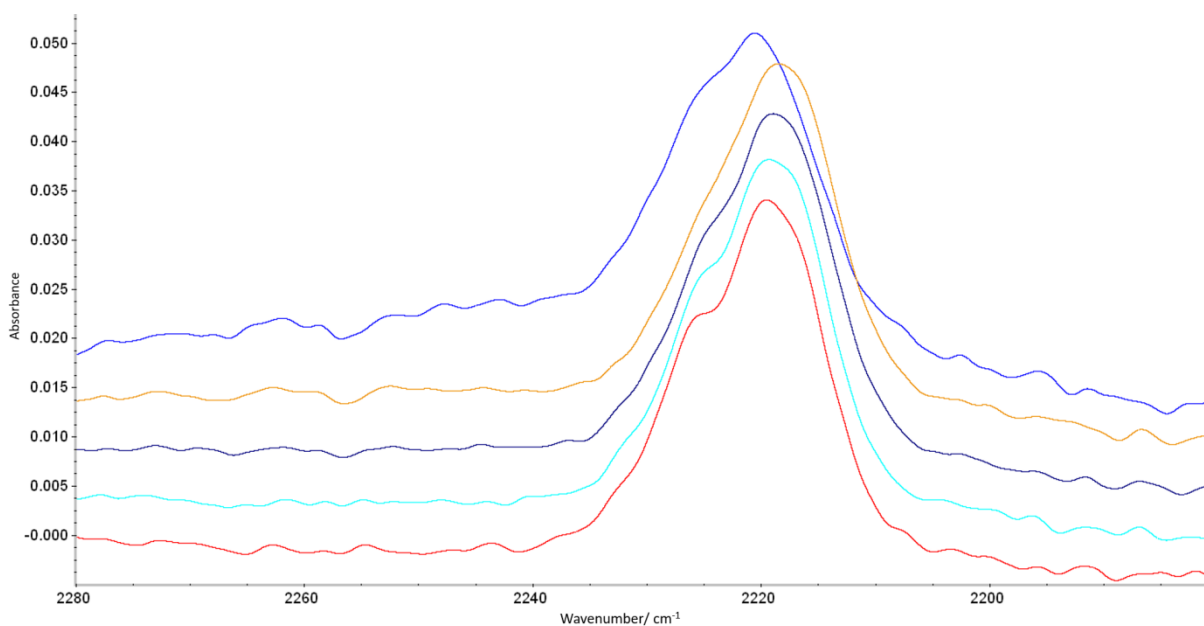


Figure SI-17: CN stretching vibration range in FTIR spectra of LiPDI-12C4 solvate in different temperatures: red - 30 °C, light blue - 50 °C, purple - 70 °C, yellow - 90 °C and blue - 120 °C.

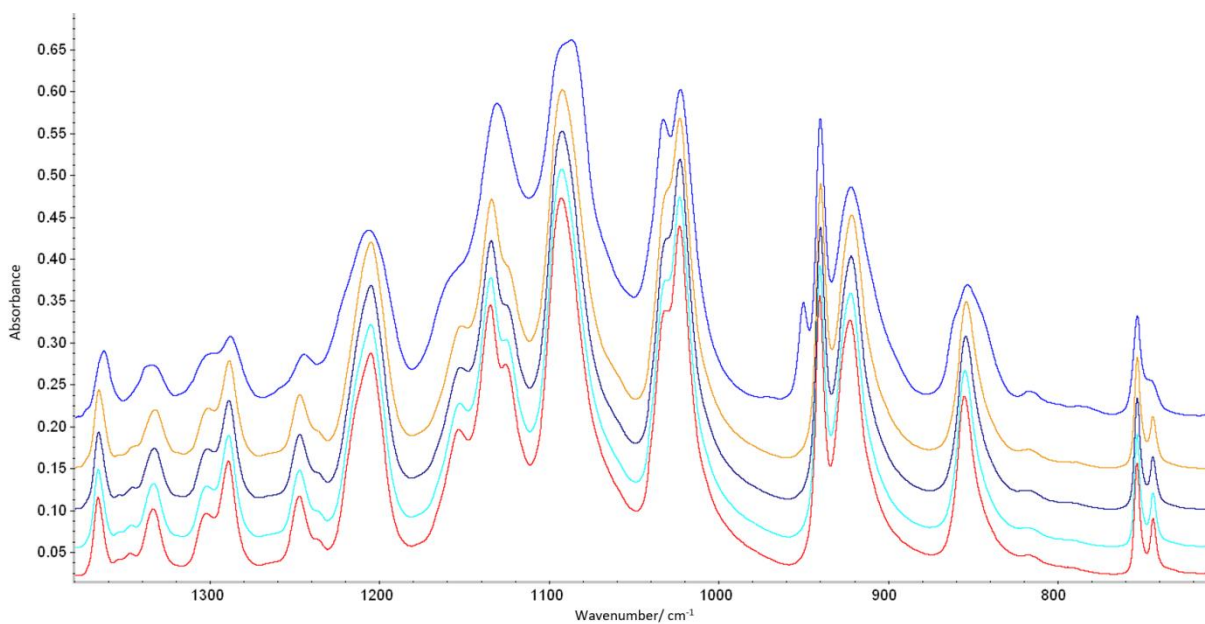


Figure SI-18: Imidazole ring bending ($\sim 940\text{ cm}^{-1}$), C-O stretching and CH_2 rocking (900 cm^{-1} - 800 cm^{-1}) vibration range in FTIR spectra of LiPDI-12C4 solvate in different temperatures: red - $30\text{ }^\circ\text{C}$, light blue - $50\text{ }^\circ\text{C}$, purple - $70\text{ }^\circ\text{C}$, yellow - $90\text{ }^\circ\text{C}$ and blue - $120\text{ }^\circ\text{C}$.

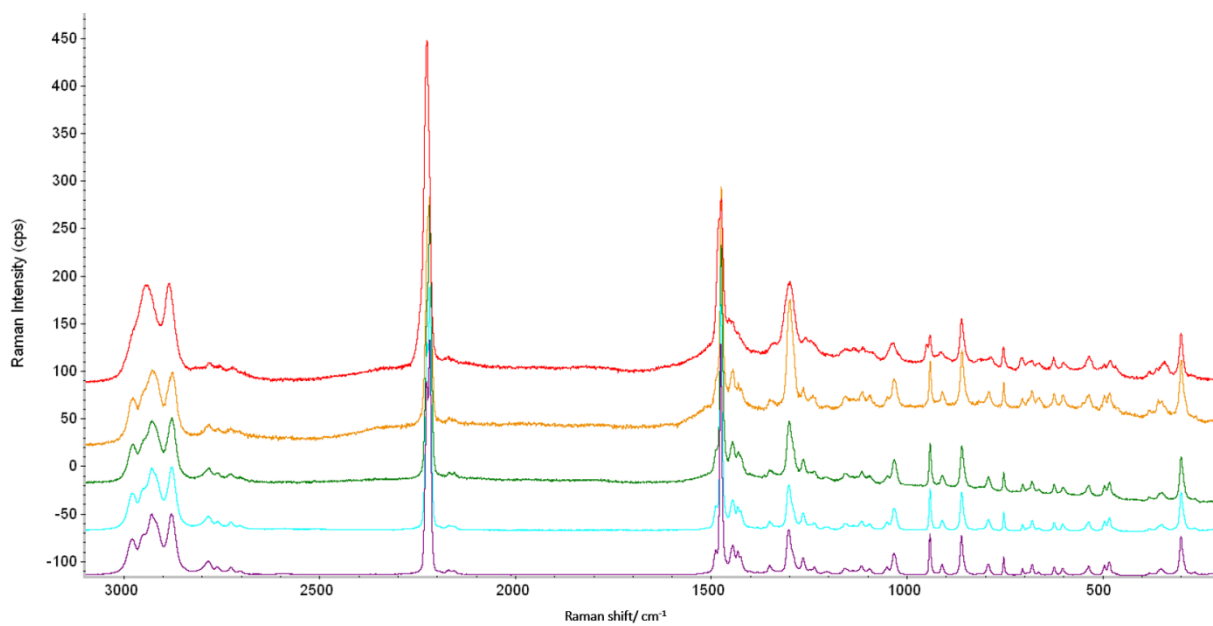


Figure SI-19: Raman spectra of LiPDI-12C4 solvate in different temperatures: purple - $30\text{ }^\circ\text{C}$, light blue - $50\text{ }^\circ\text{C}$, green - $60\text{ }^\circ\text{C}$ (solution), orange - $90\text{ }^\circ\text{C}$ (melted), red - $100\text{ }^\circ\text{C}$ (aggregation).

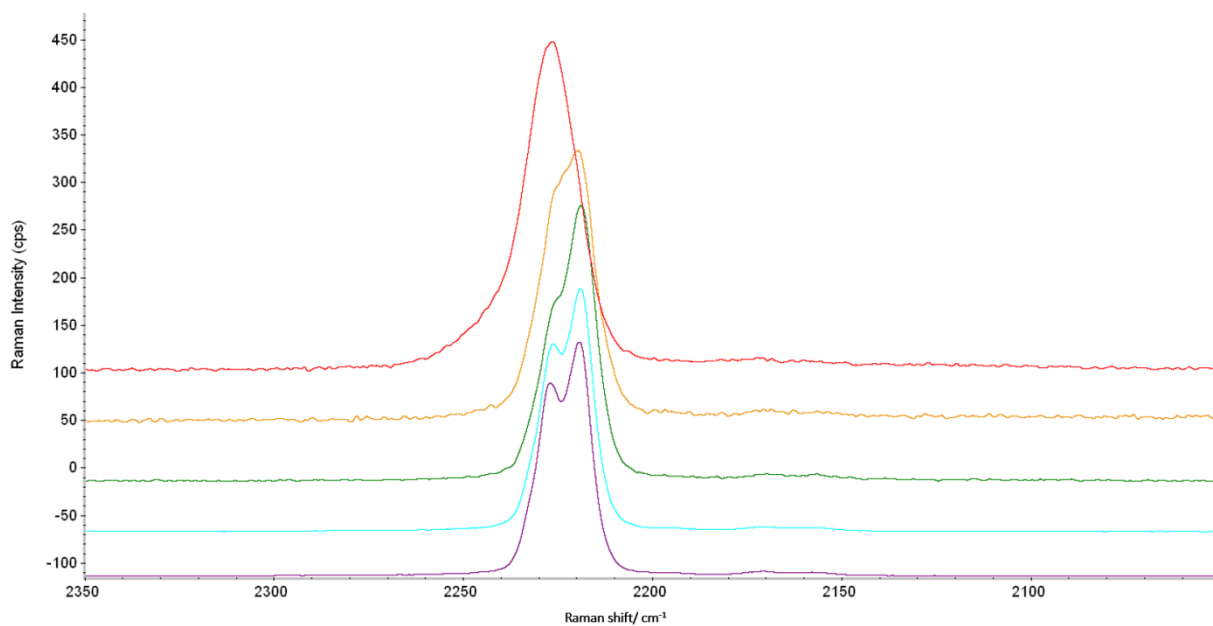


Figure SI-20: CN stretching vibration range in Raman spectrum of LiPDI-12C4 solvate in different temperatures: purple - 30 °C, light blue - 50 °C, green - 60 °C (solution), orange - 90 °C (melted), red - 100 °C (aggregation).

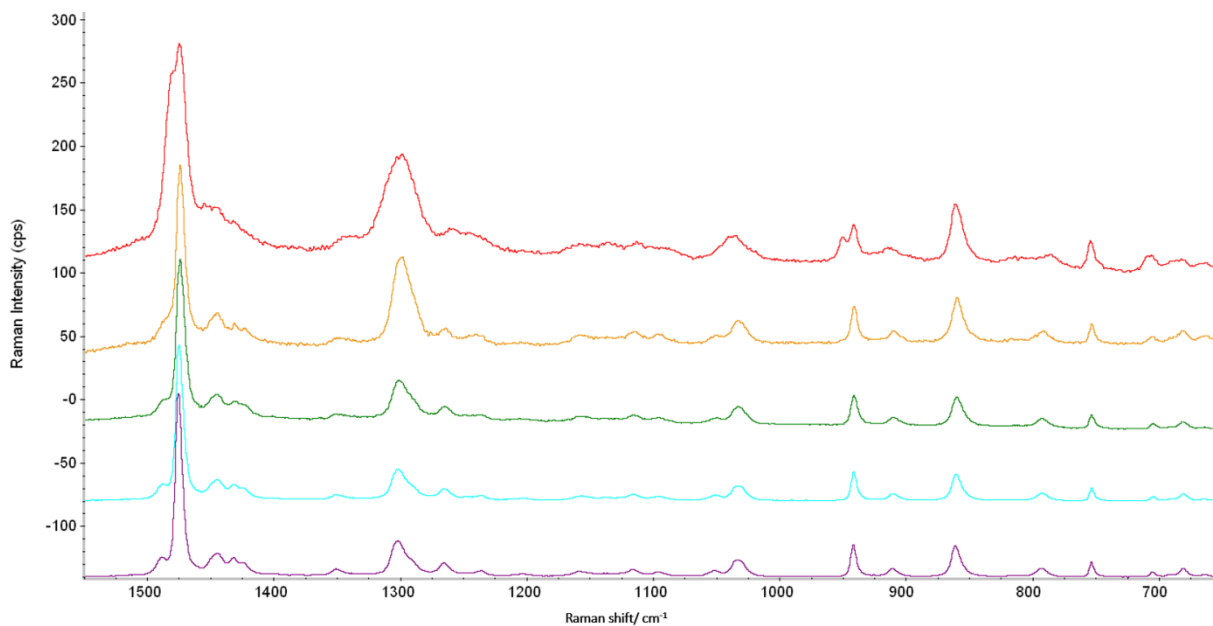


Figure SI-21: Imidazole ring stretching (1500 cm^{-1} - 1200 cm^{-1}), ring bending ($\sim 943\text{ cm}^{-1}$) and CH_2 rocking (900 cm^{-1} - 800 cm^{-1}) vibration range in Raman spectra of LiPDI-12C4 in different temperatures: purple - 30 °C, light blue - 50 °C, green - 60 °C (solution), orange - 80 °C (melted), red - 100 °C (aggregation).

5.1.2 In 15C5 crown ether

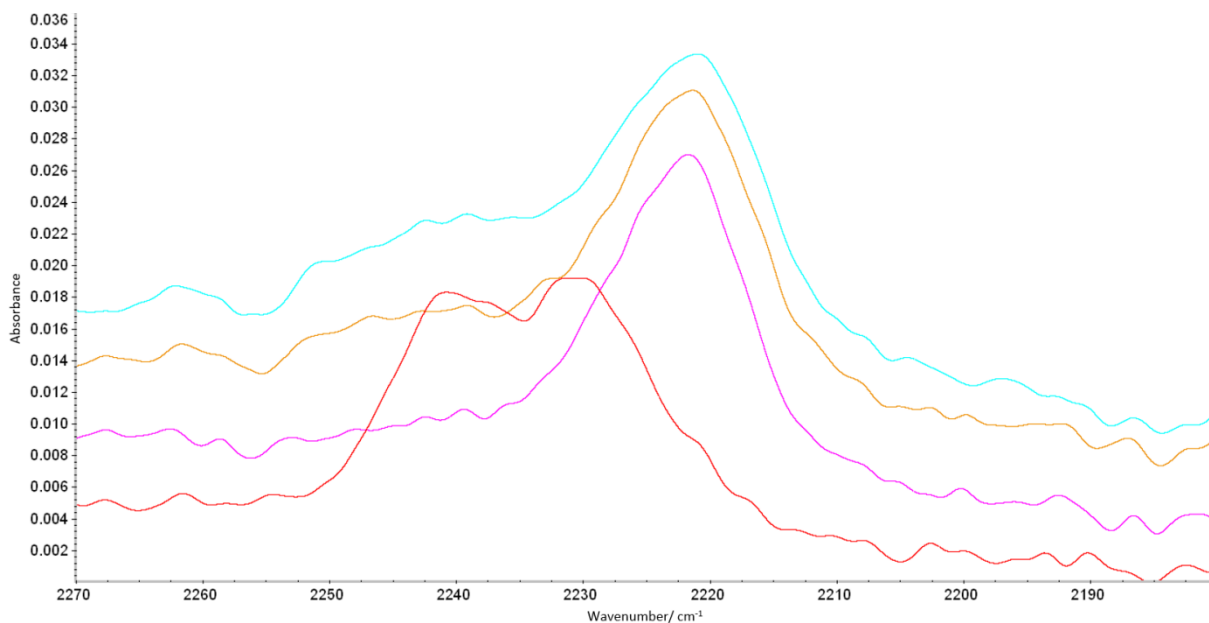


Figure SI-22: CN stretching vibration range in FTIR spectra of LiPDI-15C5 in different temperatures: red - 30 °C, pink - 40 °C, orange - 50 °C, and light blue - 60 °C (melted).

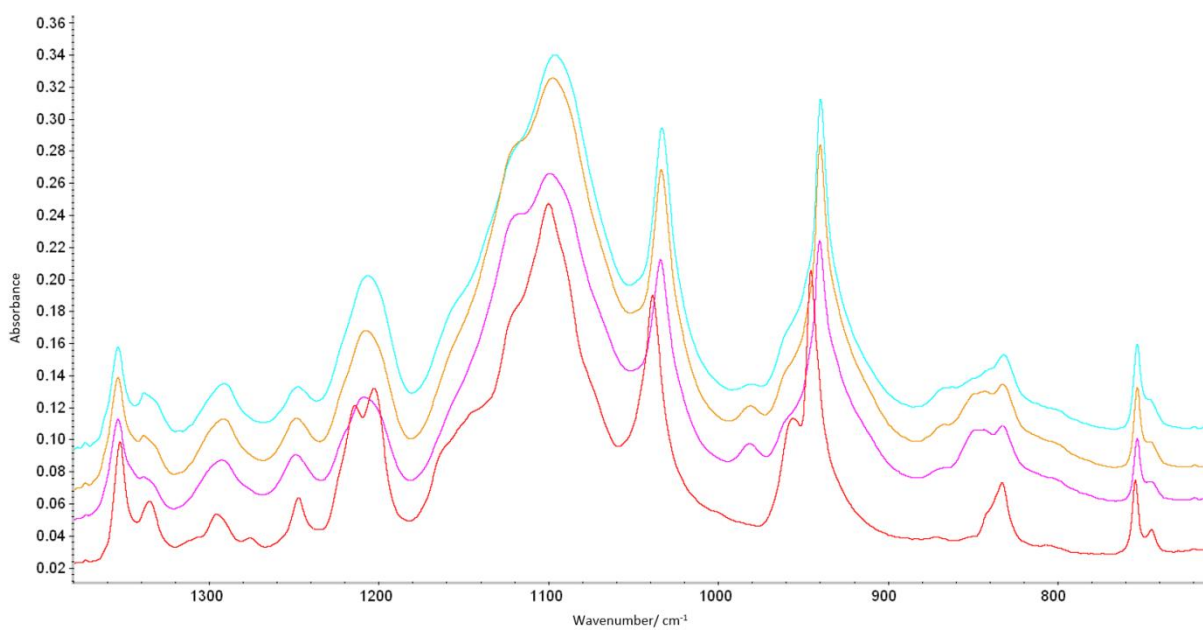


Figure SI-23: Imidazole ring bending ($\sim 940\text{ cm}^{-1}$), C-O stretching and CH₂ rocking ($900\text{ cm}^{-1} - 800\text{ cm}^{-1}$) vibration range in FTIR spectra of LiPDI-15C5 solvate in different temperatures: red - 30 °C, pink - 40 °C, orange - 50 °C, and light blue - 60 °C (melted).

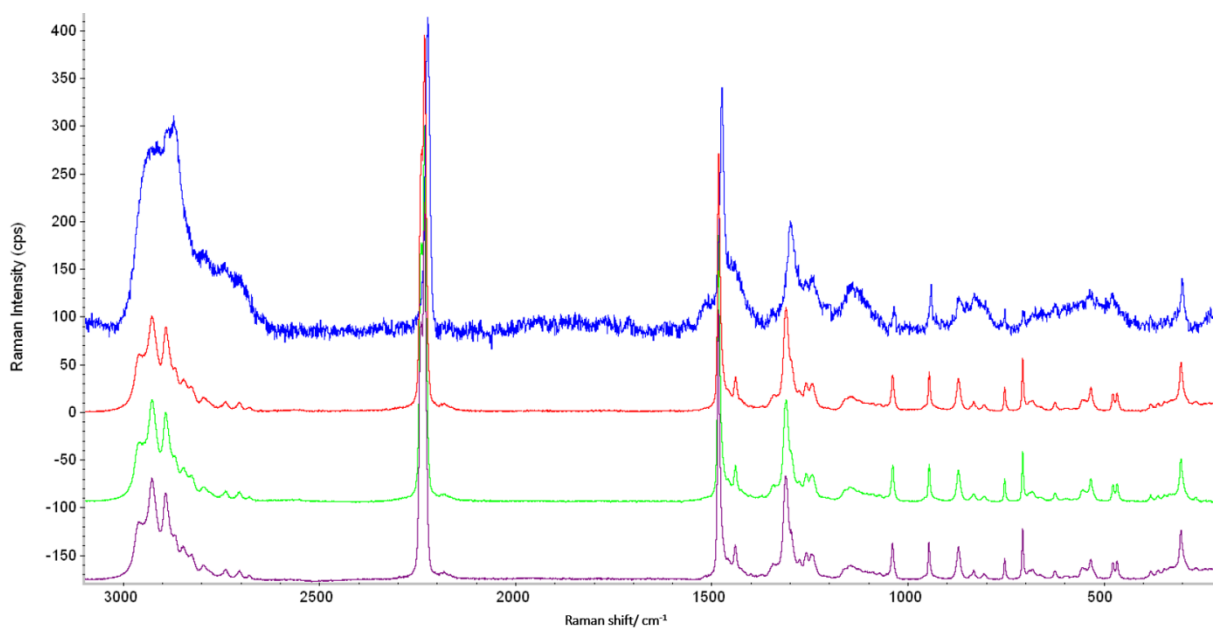


Figure SI-24: Raman spectra of LiPDI-15C5 in different temperatures: purple - 30 °C, green - 40 °C, red - 50 °C and blue - 60 °C (melted).

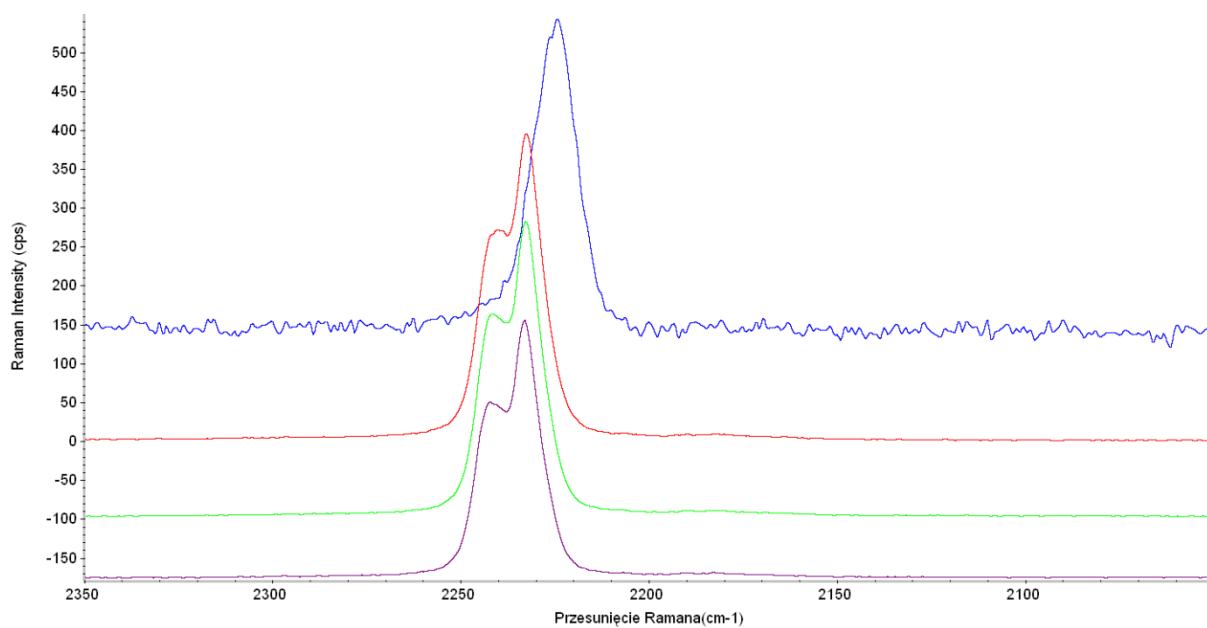


Figure SI-25: CN stretching vibration range in Raman spectra of LiPDI-15C5 in different temperatures: purple - 30 °C, green - 40 °C, red - 50 °C and blue - 60 °C (melted).

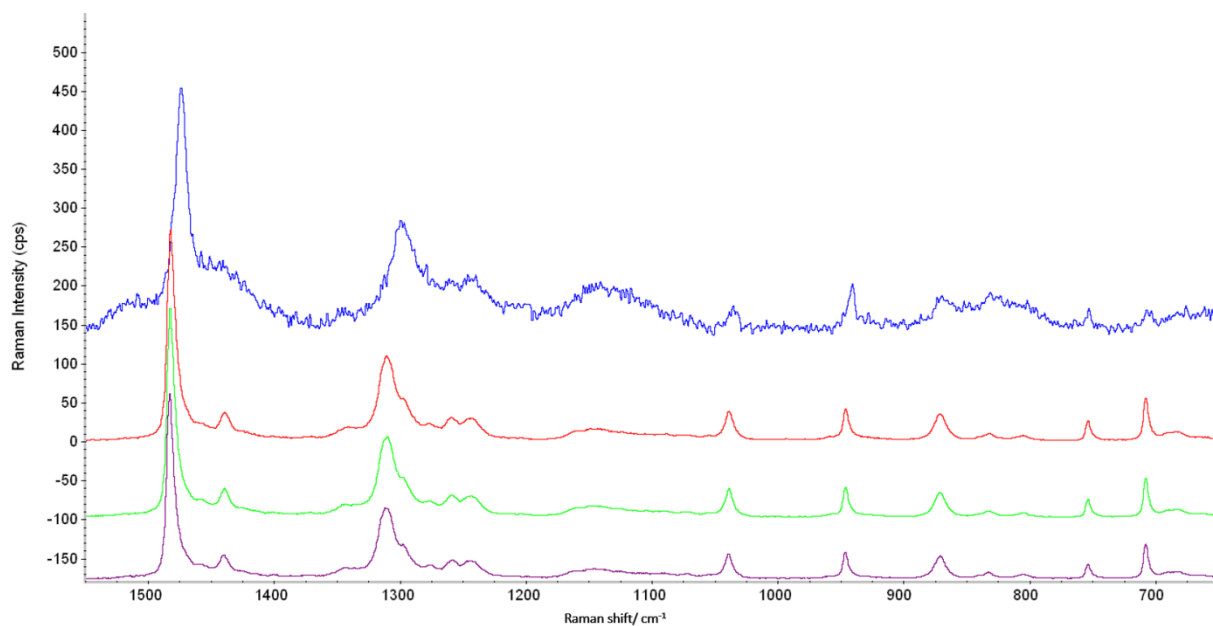


Figure SI-26: Imidazole ring stretching ($1500\text{ cm}^{-1} - 1200\text{ cm}^{-1}$), ring bending ($\sim 948\text{ cm}^{-1}$) and CH_2 rocking ($900\text{ cm}^{-1} - 800\text{ cm}^{-1}$) vibration range in Raman spectra of LiPDI-15C5 in different temperatures: purple - $30\text{ }^\circ\text{C}$, green - $40\text{ }^\circ\text{C}$, red - $50\text{ }^\circ\text{C}$ and blue - $60\text{ }^\circ\text{C}$ (melted).

5.2 LiHDI

5.2.1 In 12C4 crown ether

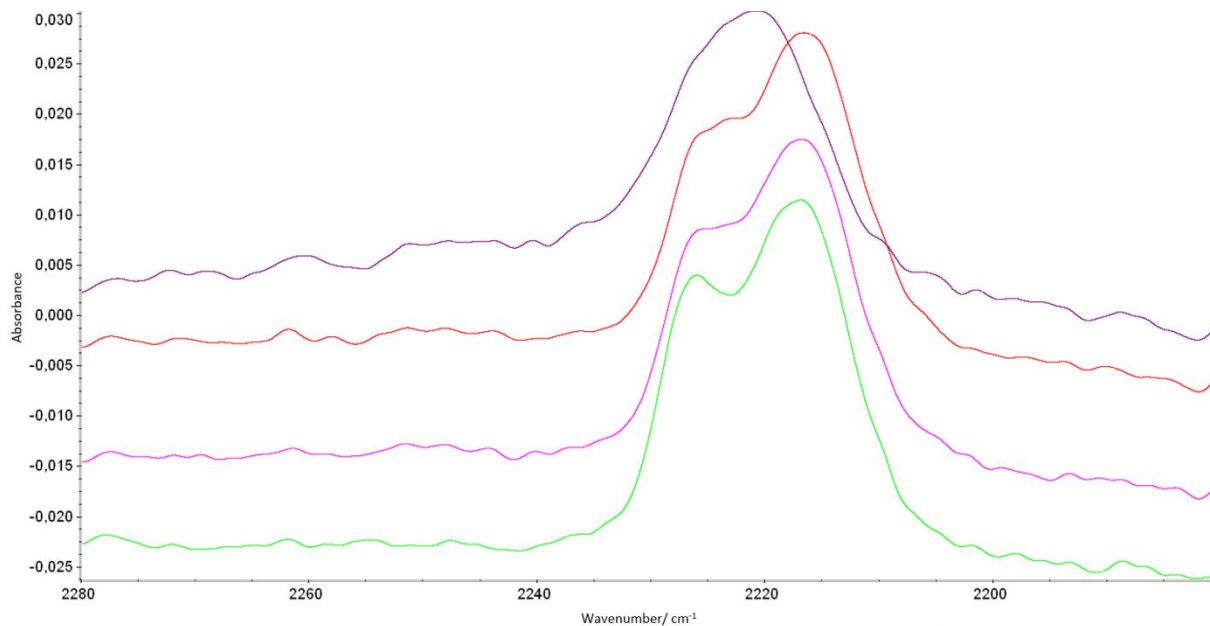


Figure SI-27: CN stretching vibration range in FTIR spectra of LiHDI-12C4 solvate in different temperatures: green - $40\text{ }^\circ\text{C}$, pink - $60\text{ }^\circ\text{C}$, red - $90\text{ }^\circ\text{C}$, and purple - $120\text{ }^\circ\text{C}$.

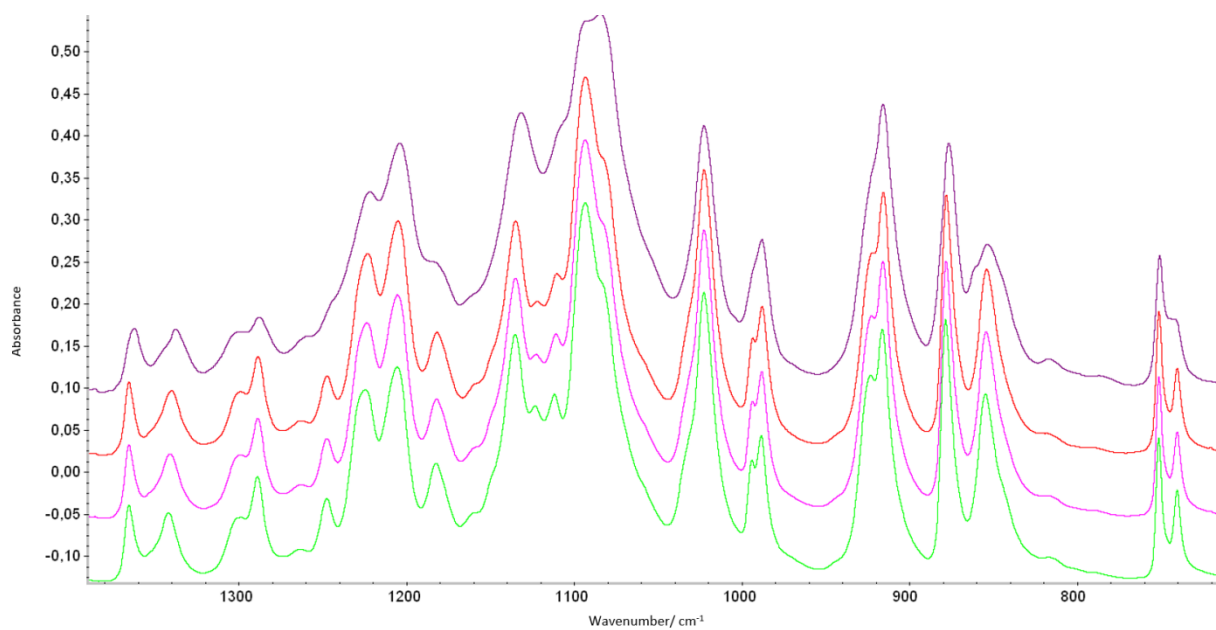


Figure SI-28: Imidazole ring bending ($\sim 990\text{ cm}^{-1}$), C-O stretching and CH_2 rocking ($900\text{ cm}^{-1} - 800\text{ cm}^{-1}$) vibration range in FTIR spectra of LiHDI-12C4 in different temperatures: green - $40\text{ }^\circ\text{C}$, pink - $60\text{ }^\circ\text{C}$, red - $90\text{ }^\circ\text{C}$, and purple - $120\text{ }^\circ\text{C}$.

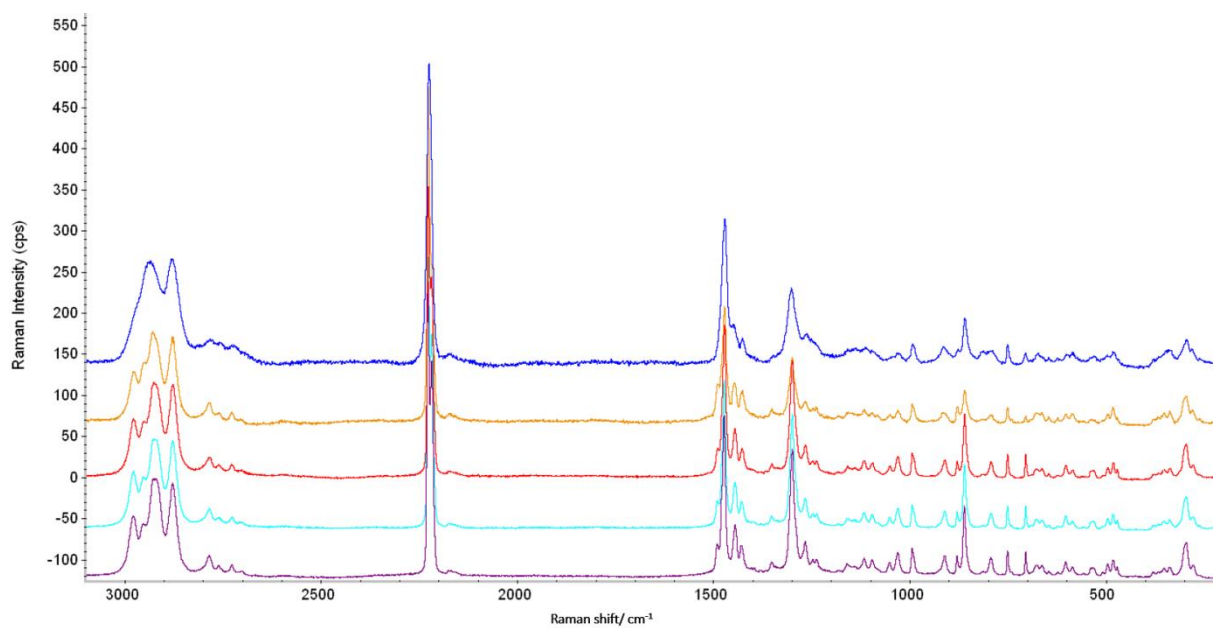


Figure SI-29: Raman spectra of LiHDI-12C4 solvate in different temperatures: purple - $30\text{ }^\circ\text{C}$, light blue - $50\text{ }^\circ\text{C}$, red - $70\text{ }^\circ\text{C}$, orange - $90\text{ }^\circ\text{C}$ (melting started), and blue - $120\text{ }^\circ\text{C}$ (melted).

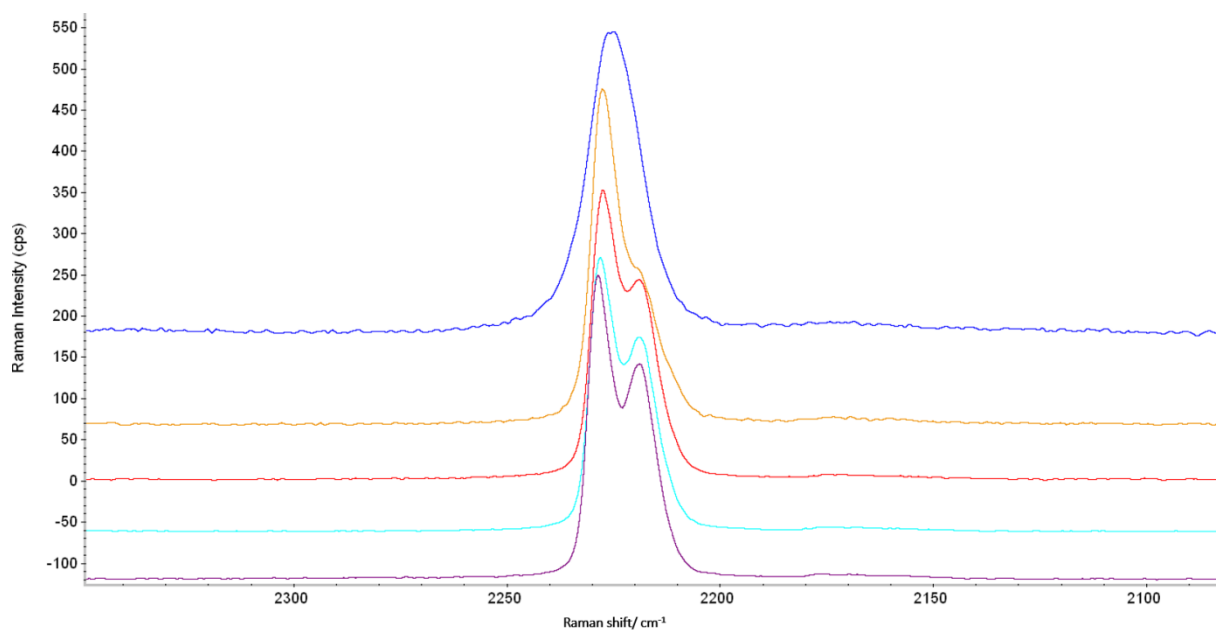


Figure SI-30: CN stretching vibration range in Raman spectra of LiHDI-12C4 solvate in different temperatures: purple - 30 °C, light blue - 50 °C, red - 70 °C, orange - 90 °C (melting started), and blue - 120 °C (melted).

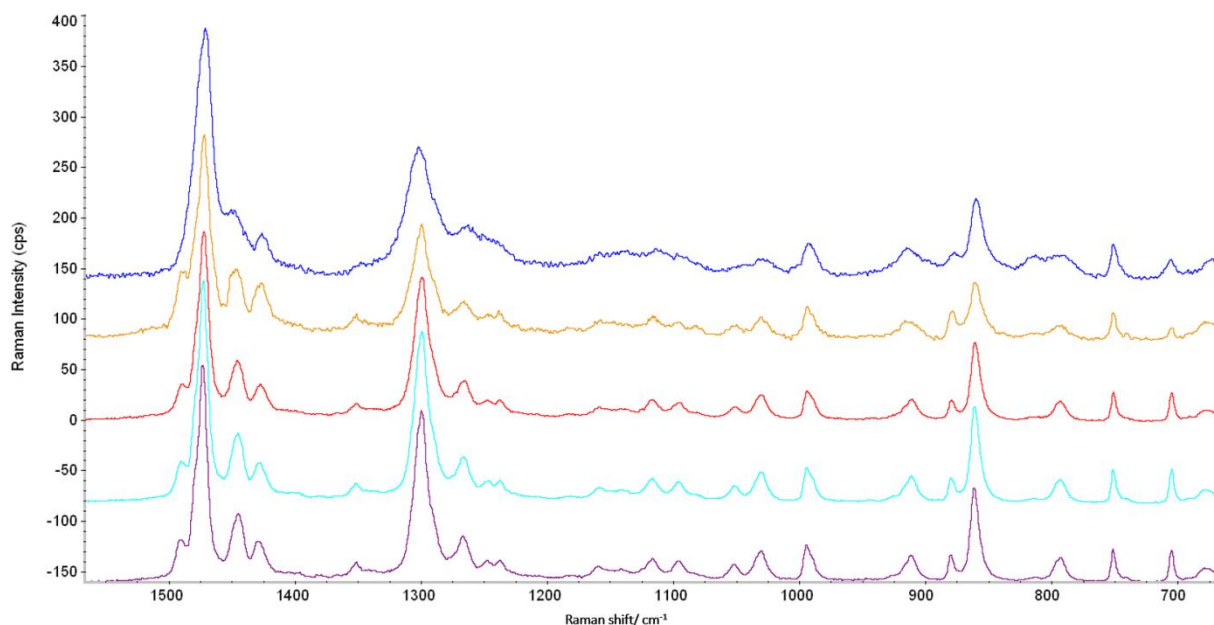


Figure SI-31: Imidazole ring stretching (1500 cm^{-1} - 1200 cm^{-1}), ring bending ($\sim 943 \text{ cm}^{-1}$) and CH_2 rocking (900 - 800 cm^{-1}) vibration range in Raman spectra of LiHDI-12C4 solvate in different temperatures: purple - 30 °C, light blue - 50 °C, red - 70 °C, orange - 90 °C (melting started), and blue - 120 °C (melted).

5.2.2 In 15C5 crown ether

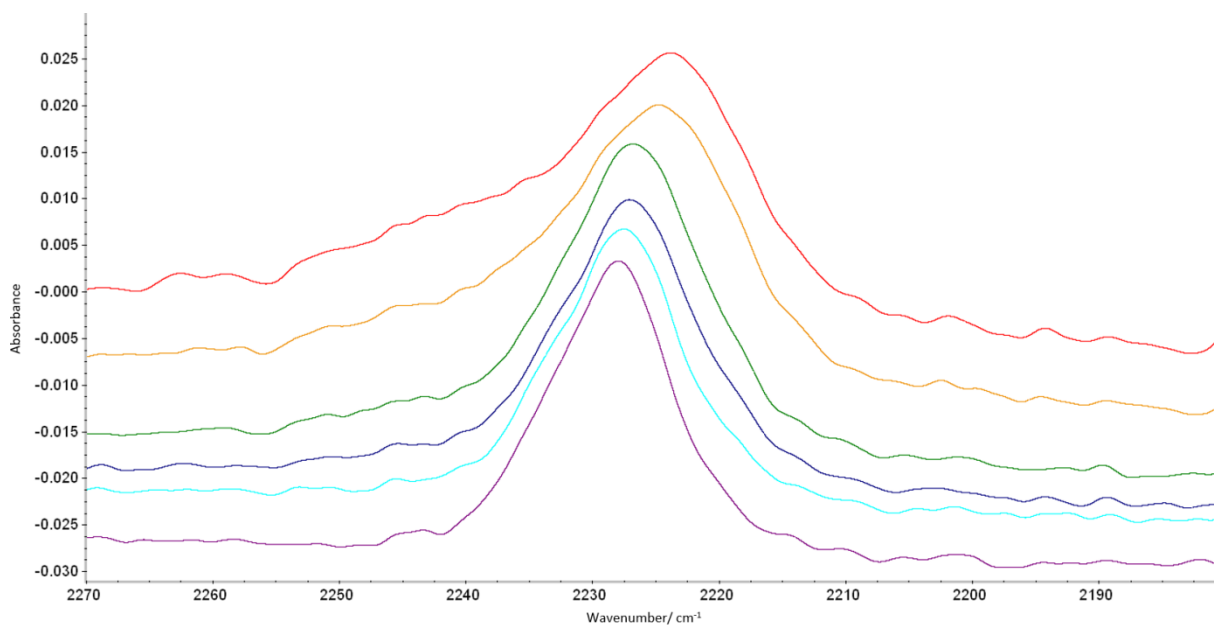


Figure SI-32: CN stretching vibration range in spectra of LiHDI-15C5 solvate in different temperatures: purple - 30 °C, light blue - 50 °C, blue - 70 °C, green - 80 °C (solution), yellow - 80 °C (crystal), and red - 110 °C.

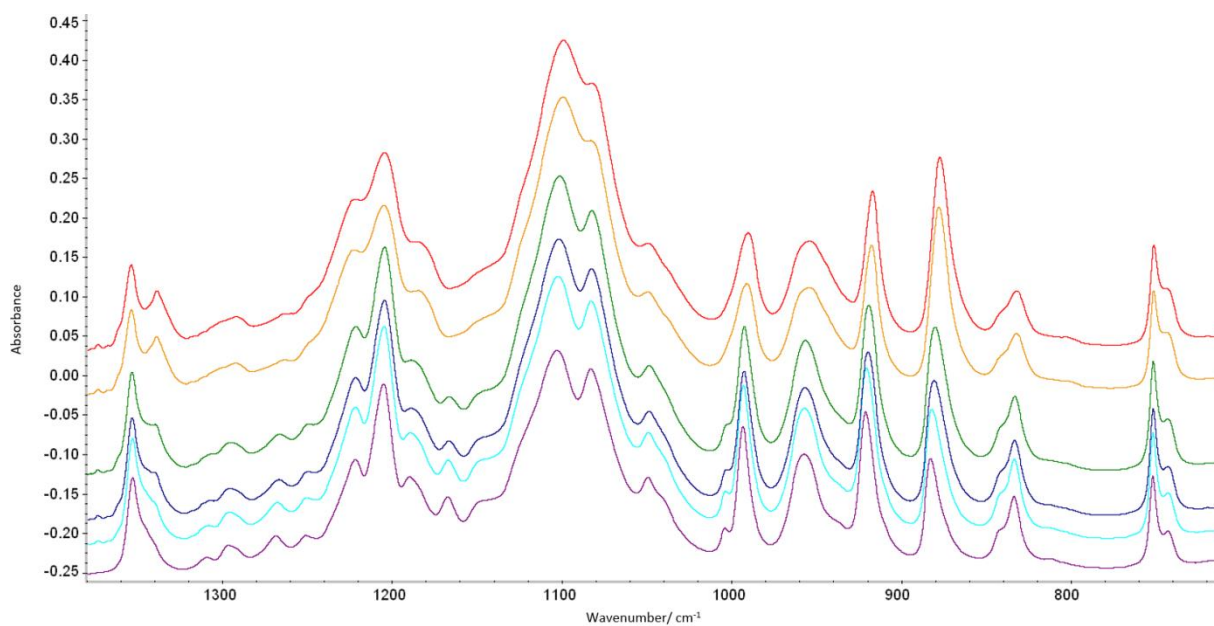


Figure SI-33: Imidazole ring bending (~1000 cm⁻¹), C-O stretching and CH₂ rocking (900 cm⁻¹ - 800 cm⁻¹) vibration range in FTIR spectra of LiHDI-15C5 in different temperatures: purple - 30 °C, light blue - 50 °C, blue - 70 °C, green - 80 °C (solution), yellow - 80 °C (crystal), and red - 110 °C.

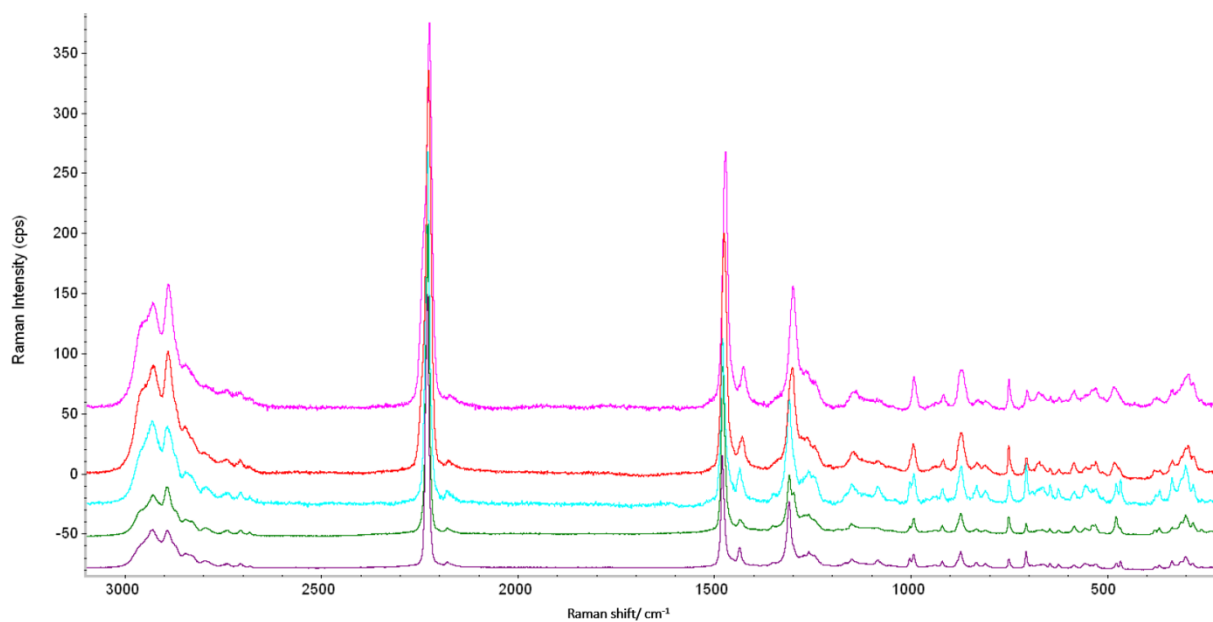


Figure SI-34: Raman spectra of LiHDI-15C5 solvate in different temperatures: purple - 30 °C, green - 50 °C, light blue - 70 °C, red- 80 °C (solution), and pink - 110 °C.

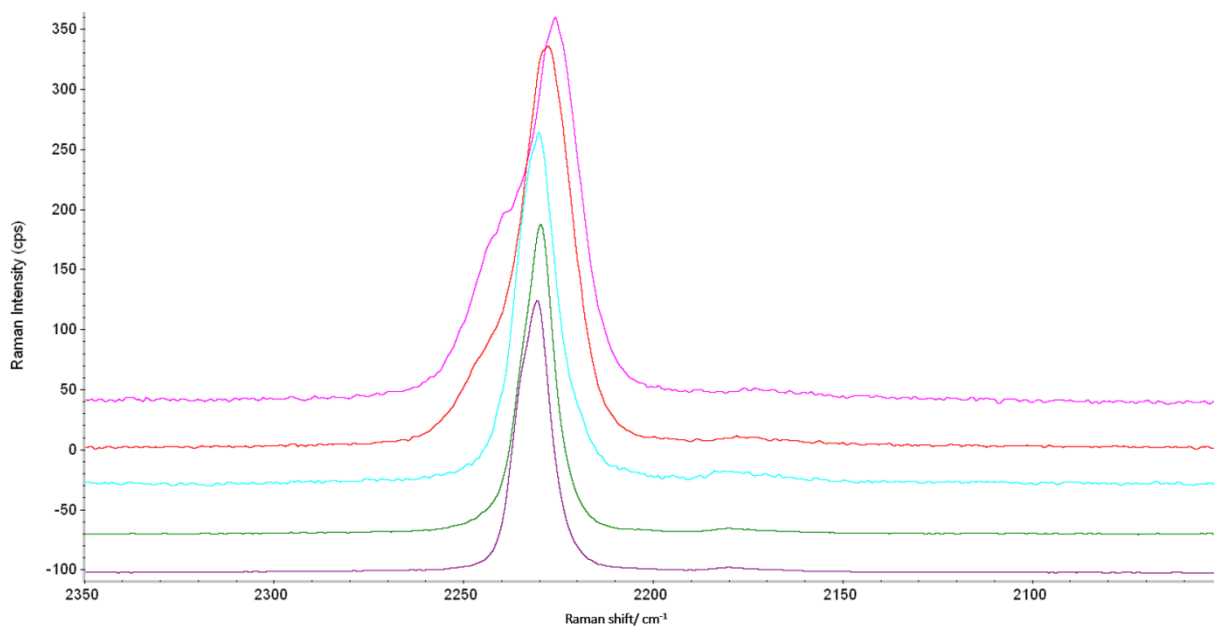


Figure SI-35: CN stretching vibration range in Raman spectra of LiHDI-15C5 in different temperatures: purple - 30 °C, green - 50 °C, light blue - 70 °C, red- 80 °C (solution), and pink - 110 °C.

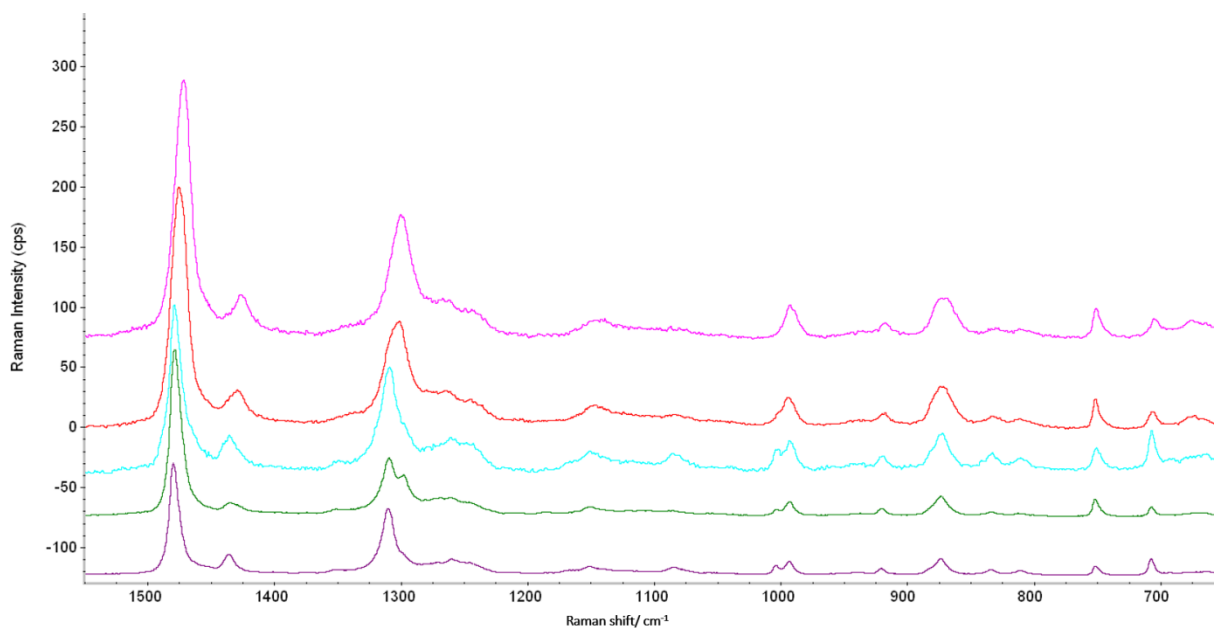


Figure SI-36: Imidazole ring stretching (1500 cm^{-1} - 1200 cm^{-1}), ring bending ($\sim 1000\text{ cm}^{-1}$) and CH_2 rocking (900 cm^{-1} - 800 cm^{-1}) vibration range in Raman spectra of LiHDI-15C5 in different temperatures: purple - $30\text{ }^\circ\text{C}$, green - $50\text{ }^\circ\text{C}$, light blue - $70\text{ }^\circ\text{C}$, red - $80\text{ }^\circ\text{C}$ and pink - $110\text{ }^\circ\text{C}$.

References

- 1 A. Narayanan Krishnamoorthy, C. Wölke, D. Diddens, M. Maiti, Y. Mabrouk, P. Yan, M. Grünebaum, M. Winter, A. Heuer and I. Cekic-Laskovic, Data-Driven Analysis of High-Throughput Experiments on Liquid Battery Electrolyte Formulations: Unraveling the Impact of Composition on Conductivity, *Chemistry–Methods*, 2022, **2**, 1–8.
- 2 L. Niedzicki, G. Z. Żukowska, M. Bukowska, P. Szczeciński, S. Grugeon, S. Laruelle, M. Armand, S. Panero, B. Scrosati, M. Marcinek and W. Wieczorek, New type of imidazole based salts designed specifically for lithium ion batteries, *Electrochimica Acta*, 2010, **55**, 1450–1454.

6 Geographically distributed autonomous MAPs

6.1 Autonomous operation as part of a MAP

This section presents the publication [13]

M. Vogler, J. Busk, H. Hajiyani, P. B. Jørgensen, N. Safaei, I. E. Castelli, F. F. Ramirez, J. Carlsson, G. Pizzi, S. Clark, F. Hanke, A. Bhowmik, and H. S. Stein, “Brokering between tenants for an international materials acceleration platform,” *Matter*, vol. 6, no. 9, pp. 2647–2665, 2023. doi: 10.1016/j.matt.2023.07.016

submitted in September 2022 and published after peer-review in August 2023. The open access publication is available under the terms of the Creative Commons Attribution 4.0 International (CC BY 4.0) (<https://creativecommons.org/licenses/by/4.0/>) license.

Monika Vogler presented this work in a contributed talk at the *11th International Workshop on Combinatorial Materials Science and Technology* in Golden, Colorado, USA in September 2022 (contributed talk #5) and at the *2023 Spring Meeting of the European Materials Research Society* in Strasbourg, France in May 2023 (contributed talk 1317), at the *LMS Seminars* in Villigen, Switzerland in October 2024, and in several oral presentations in the context of the BIG-MAP project. Further, the results presented in this chapter were parts of deliverables and a demonstrator for the BIG-MAP project.

Author contributions

The following author contributions are given as a literal quotation from [13]:

"M.V. built and designed ASAB and organized the FINALES run; J.B. and P.B.J. programmed and ran the optimizer tenant; H.H., N.S., J.C., and F.H. programmed and ran the Pipeline Pilot tenant; F.H. organized and J.B., H.H., and M.V. implemented regression tests; I.E.C. and S.C. developed the DMP and ontology link; F.F.R. and G.P. developed the AiiDA tenant; A.B. and H.S.S. wrote the first draft of the manuscript; H.S.S. developed the FINALES software, hosted and maintained the FINALES broker server, and conceived the initial idea and MAP design."

For information regarding the reprint permission see Annex A.2.

In this publication, we report a demonstration of a decentralised MAP. This concept conceived by Prof. Dr.-Ing. Helge S. Stein is implemented in a modular fashion including experimental and computational tenants, as the clients in the MAP are called. While the tenants of the MAP are geographically distributed, the communication is centralised in the in-house developed brokering server called FINALES, which maintains a *Structured Query Language* (SQL) database tracking requests, results and user information. One of the distinctive design features of FINALES is its permissive append-only operation of the database to mitigate data loss and enable maximum traceability of the data. Since the status of requests and results need to be updated to inform the tenants in the MAP about which of them are already processed, the append-only mechanism is not strict in this case. Additionally, the tenants assign a quality rating to the results they post, which can be used for filtering the data. This quality rating can for example be low, if an error occurred while running an experiment that may have affected the reliability of the result. Moreover, FINALES requires commitment to defined data structures as realised in the demonstration to enable unambiguous communication, which is inevitable for the autonomous operation of such a MAP. Another special feature of FINALES is its passive operation. This means, that it does not control any of the connected tenants, which allows the tenants to operate according to their respective schedule. Hence, tenants with significantly different rates of data generation can be connected to the MAP. Furthermore, due to this feature, FINALES does not pose any requirements on the internal workings of its tenants rendering it independent of the specific hardware or software of tenants, which contributes to its flexibility and versatility. Another key feature of MAPs based on FINALES is the concept of *multitenancy* meaning, that the design of the MAP explicitly allows for several tenants providing the same capabilities enabling an enhancement of fault-tolerance by redundancy. [13]

The demonstration described in this publication comprised an optimiser tenant deploying a machine learning model implemented and operated at the Technical University of Denmark (DTU) (Denmark) to guide the study. Experiments were performed by the ASAB system connected as the experimental tenant and computational results were contributed by the computational tenant running *molecular dynamics* (MD) simulations developed and operated by Dassault Systèmes (Germany and UK). The experimental and the computational tenants were agnostic towards the intention of the study and executed requests, which they were capable to serve. Solely the machine learning model was aware of the aim of the optimisation, which was chosen to be the maximisation of viscosity and the minimisation of density to demonstrate the operability of the MAP. For this, density and viscosity data was used and data regarding the ionic conductivity, heat capacity, diffusion coefficients, transference numbers, and radial distribution functions were obtained as side results contributed by the computational tenant. The MAP operated for approximately 4.5 h without human intervention. [13]

We report on the lessons learned from this demonstration covering experimental and hardware aspects as well as insights regarding the data management in distributed MAPs. Overall, the design of our MAP based on FINALES is shown to be operable and functional. [13]

The study presented in this publication made use of the autonomous operation of the formulation unit and the density and viscosity measurements implemented in the ASAB system developed in the context of this thesis. It was integrated into the MAP as the experimental tenant [13]. The automation of the experimental procedures benefited from the experience gained during the initial work presented in chapter 5 using the conventional mode of operation and enabled the autonomous operation of the MAP.

The remainder of this chapter shows a reprint of [13].

Perspective

Brokering between tenants
for an international materials
acceleration platform

Monika Vogler,^{1,2} Jonas Busk,³ Hamidreza Hajiyani,⁴ Peter Bjørn Jørgensen,³ Nehzat Safaei,⁴ Ivano E. Castelli,³ Francisco Fernando Ramirez,^{5,6} Johan Carlsson,⁴ Giovanni Pizzi,^{5,6,8} Simon Clark,⁷ Felix Hanke,^{9,*} Arghya Bhowmik,^{3,*} and Helge S. Stein^{1,2,10,*}

SUMMARY

The efficient utilization of resources in accelerated materials science necessitates flexible, reconfigurable software-defined research workflows. We demonstrate a brokering approach to modular and asynchronous research orchestration to integrate multiple laboratories in a cooperative multitenancy platform across disciplines and modalities. To the best of our knowledge, this constitutes the first internationally distributed materials acceleration platform (MAP) linked via a passive brokering server, which is demonstrated through a battery electrolyte workflow capable of determining density, viscosity, ionic conductivity, heat capacity, diffusion coefficients, transference numbers, and radial distribution functions that ran in five countries over the course of 2 weeks. We discuss the lessons learned from multitenancy and fault tolerance and chart a way to a universal battery MAP with fully ontology-linked schemas and cost-aware orchestration.

INTRODUCTION

Scientists have continuously innovated on the efficiency improvements of the research process¹ with notable driving accelerators such as automation of research tasks² and their integration with data lineage tracking^{3,4} in biotechnology and materials science.⁵ This research automation created the field of combinatorial materials science (CMS),⁶ which utilizes the paradigm of well-defined composition and processing variation to unravel the underlying physicochemical relationships at a greater pace.^{7,8} The combinatorial nature of chemical space does, however, render any brute force exploration for discovery ineffective. Efficient research therefore necessitates approaches that can predict how to design materials according to a target functional property. This inverse design^{9–11} approach is rooted in the idea of descriptors based on rational design^{12,13} that define composition-structure-property relationships. Recent advancements in research instrumentation¹⁴ and user interfaces have lowered the entrance barrier for high-throughput experimentation (HTE). Abundance of searchable data, enabled by data management,^{3,15} then sparked the proliferation of data-driven methods in synthesis,¹⁶ characterization,¹⁷ performance evaluation,¹⁸ and interpretation.¹⁹ The integration of accelerated research tasks in workflows² guided by data-driven methods was then conceived as the next evolutionary step in a 2018 workshop initiated by the UN Mission Innovation Initiative and was called the materials acceleration platform (MAP).²⁰

PROGRESS AND POTENTIAL

New developments in modern technology often rely on specifically designed materials. Tailoring materials properties to meet the requirements of an application is a key task in materials research. The increasing pace of technology development requires faster discovery of optimized materials. Materials acceleration platforms (MAPs) automate materials optimization and therefore allow for a considerable acceleration of materials discovery. MAPs allow for a more efficient use of research infrastructure like laboratories, devices, and computational resources. We demonstrate a modular MAP design, which allows us to include automated as well as non-automated units. It can hence be used in the current research landscape already. Future development is envisioned to promote comprehensive recording of data and metadata and to expose laboratories as a service. This is expected to result in the usage of research equipment to capacity, maximizing the return on invest of research funding.



Here, we define MAPs as platforms that enable multiple units, which we call tenants, to connect using standardized communication schemas. A MAP should combine tenants providing physical services, like, e.g., experimental capabilities using multi-tenant instruments for measurements and simulations, as well as digital services for, e.g., data processing or machine learning. In the field of computer science, there is a nomenclature for multitenancy that relates to shared digital services serving multiple customers from a shared resource. We would like to avoid the competing nomenclature of an agent, as it semantically implies an entity with hidden or potentially malicious features as well as a hierarchy. To express a collaborative and community spirit, we choose to refer to all units within a MAP as tenants. MAPs should be designed such that tenants providing the same capabilities can be exchanged on the fly without affecting the platform. This implies that an operator or optimizer cannot *a priori* know who is going to fulfill a request at what time, requiring all tenants to be asynchronous. This asynchronous operation of tenants and the platform itself means that processing requests and result communication function independently. While the sharing of data should be as open as possible, resources need to be protected against malicious input, which renders security aspects a vital part of the MAP design.

The concept of connecting distributed resources through networking instances is well established in the field of computer science. In materials science, applications of this concept are, however, often focused on the processing and management of generated research data^{21,22} or automation on a lab bench,²³ in a building,²⁴ or at a single research institution.²⁵ An example is large-scale research infrastructures and their data-processing pipelines and visions to integrate these into so-called superfacilities.²⁶ Using, for instance, the Globus²¹ framework, single experimental setups are integrated into computational fabrics that enable the transfer and analysis of data at rates of gigabytes per second.

Going beyond a single materials property or even transcending the laboratory is necessary for a true battery MAP,²⁷ as there are multiple functional properties to optimize,^{28,29} e.g., lifetime, energy capacity, energy density, voltage range, cost, power density, safety, embodied energy, etc. All these critically depend on high-dimensional parameter spaces comprising the chemistry, structure, and processing of the materials as well as the assembly, composition, and environmental conditions during operation of the cell system. The optimization of battery materials is therefore a truly multiscale challenge ranging from atoms to systems and from nanoseconds to years and therefore cannot be mastered by a single institution or domain alone. A complicating factor in all of this is the mutual exclusion of certain methods, i.e., high-throughput density functional theory (DFT) calculations are challenging to run on the month scale,^{9,30} and manufactured batteries cannot easily be analyzed by, e.g., X-ray photoelectron spectroscopy (XPS). This is in stark contrast to all of the early MAP-inspired demonstrations from other fields,^{31–33} where the entire research life cycle can be covered either using a single robotic setup or a single research group. A comprehensive MAP in battery research therefore needs to be distributed across different domains, spanning the entire set of battery research processes.³⁴

Here, we describe the design of a cooperative MAP that is spatially distributed across multiple countries and involves scientists from the experimental and modeling domains. A graphical representation of our MAP concept is shown in [Figure 1](#). The development involved partners across Europe associated with the BIG-MAP project.¹⁵ A brokering software system called FINALES (fast intention-agnostic

¹Helmholtz Institute Ulm, 89073 Ulm, Germany

²Institute for Physical Chemistry, Karlsruhe Institute of Technology, 76131 Karlsruhe, Germany

³Department of Energy Conversion and Storage, Technical University of Denmark (DTU), 2800 Kgs. Lyngby, Denmark

⁴Dassault Systèmes, 51063 Cologne, Germany

⁵Theory and Simulation of Materials (THEOS), École Polytechnique Fédérale de Lausanne, 1015 Lausanne, Switzerland

⁶National Centre for Computational Design and Discovery of Novel Materials (MARVEL), École Polytechnique Fédérale de Lausanne, 1015 Lausanne, Switzerland

⁷SINTEF Industry, Battery and Hydrogen Technologies, 7034 Trondheim, Norway

⁸Laboratory for Materials Simulations (LMS), Paul Scherrer Institut (PSI), 5232 Villigen, Switzerland

⁹Dassault Systèmes, 334 Science Park, Cambridge CB4 0WN, UK

¹⁰Present address: Department of Chemistry, School of Natural Sciences, Technical University of Munich, Lichtenbergstraße 4, 85748 Garching bei München, Germany

*Correspondence: felix.hanke@3ds.com (F.H.), arbh@dtu.dk (A.B.), helge.stein@tum.de (H.S.S.)
<https://doi.org/10.1016/j.matt.2023.07.016>

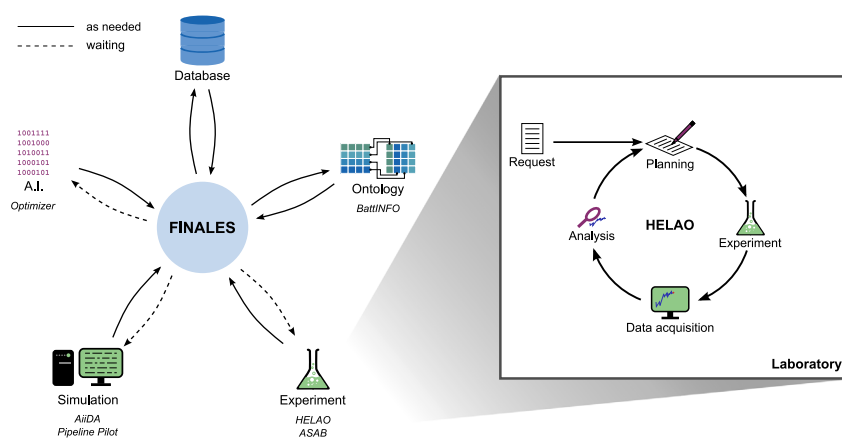


Figure 1. Schematics of conventional accelerated research labs and brokered multitenant MAPs

The left part of the figure shows the general layout of the FINALES paradigm to research orchestration in which multiple tenants, i.e., optimizers, experiments, simulations, and databases, exist in a cooperative environment in which each participant can be located anywhere on the globe. The communication within the MAP is based on pulling from the server in timed intervals, labeled “waiting,” and pushing information to the server, labeled “as needed.” The inset presents an emblematic workflow of a HELAO²⁵ run in which multiple instruments can be pooled together, but typically a run is limited to a single laboratory. The design of our MAP allows for the integration of a HELAO workflow as one of its tenants.

learning server) was developed and hosted at the Karlsruhe Institute of Technology (KIT, Germany), laboratory experiments were performed at the Helmholtz Institute Ulm (HIU, Germany), computer simulations were performed at Dassault Systèmes (3DS, Germany and UK), a machine-learning optimizer was developed and run at the Technical University of Denmark (DTU, Denmark), and ontology and data interfaces were prepared at DTU, Stiftelsen for industriell og teknisk forskning (SINTEF, Norway), and École polytechnique fédérale de Lausanne (EPFL, Switzerland).

We demonstrate the communication in our MAP during an explorative deployment using a setup consisting of the brokering software, the laboratory experiments, the computer simulations, and the machine-learning-based optimizer. This MAP can thus determine the density, viscosity, ionic conductivity, heat capacity, diffusion coefficients, transference numbers, and radial distribution functions for various formulations of lithium-ion battery electrolytes. To the best of our knowledge, this is the first demonstration of an internationally distributed MAP in the field of battery research.

The lessons learned from the development and real-world deployment of our MAP involving many partners are summarized in a separate section at the end of this perspective. We believe that sharing not only the success but also the shortcomings of these design considerations of this new paradigm of performing research will help to accelerate the progression toward truly autonomous and globally interconnected materials discovery.

METHODS AND TENANTS

Our MAP concept comprises various units collaborating via the MAP. We call each participating unit in our MAP a tenant and differentiate between intention-aware and intention-agnostic tenants. The optimization task, and hence the intention of the resulting requests, is known to intention-aware tenants, which act actively and thereby “inject intent” into the workflow. In contrast, intention-agnostic tenants

are not aware of the reasoning behind requests. They fulfill requests matching their capabilities without considering any optimization or experimental campaigns. In this context, it is essential that the brokering server FINALES is not just intention agnostic but purely passive to fully enable the communication in our MAP.

In this section, we will introduce the different tenants, which provide interfaces compatible with our broker server FINALES, namely the brokering server itself; the experimental setup for density and viscosity measurements ASAB (autonomous synthesis and analysis of battery electrolytes); the simulation orchestrator implemented in Pipeline Pilot; the AiiDA interface for data storage and machine-learning-based conductivity predictions; and the machine-learning optimizer based on a Gaussian process optimizer in combination with Chimera³⁵ to enable multiobjective optimization.

Broker server: FINALES

The FINALES tenant is designed as a broker server mediating between all the tenants in the MAP. It accepts requests from all the tenants through a web application programming interface (API), which requires requests and replies to be structured in defined Pydantic³⁶ schemas in JSON format. This structured representation of the data and requests facilitates the integration of an ontology such as BattINFO.³⁷ Furthermore, the type checking promoted by Pydantic improves the security of FINALES. The formalized and human-readable communication protocols allow us to include non-automated data acquisition in autonomously orchestrated loops, maximizing the inclusiveness and versatility of FINALES.

Tenants use the requests to order or report a measurement or a simulation or to retrieve data from the database connected to FINALES. The requests for measurements and simulations as well as reported results are stored in the FINALES database in an append-only scheme preserving all generated data. FINALES provides methods to request data from the database by its origin, meaning whether it was generated from an experiment or a simulation, or by the measured or simulated quantity. The respective request by the tenant contains a field specifying the method to use. The queries from the database are implemented as functions in FINALES, which take an element of an enumeration as an input. This way of working allows for type checking and enhances the security of the MAP against malicious database queries. FINALES performs all its actions in an asynchronous manner, allowing the MAP to continue its operation while requests are pending. The core functionality of FINALES is to act as a communication hub between the tenants while not actively controlling any tenant. This means that it is not actively triggering actions of individual tenants but rather keeps track of a queue of requests and replies, which can be queried by the various tenants in the MAP at any time. This passivity renders FINALES independent of the state of the individual tenants and distinguishes it from many other automation frameworks like HELAO,²⁵ Bluesky,³⁸ or ChemOS.²³ By design, instruments operated by these other frameworks or Globus²¹ flows could be connected to FINALES as tenants.

A further difference between FINALES and HELAO is FINALES's hardware-independent operation by abstracting away from a sequence of hardware events to requesting desired outcomes. FINALES allows for maximum flexibility and redundancy by explicitly allowing the integration of several intention-agnostic tenants with the same capabilities as well as multiple intention-aware tenants, like optimizers, operating simultaneously and in parallel. This multitenancy design allows for several intention-aware tenants to explore and exploit the data and services available through FINALES.

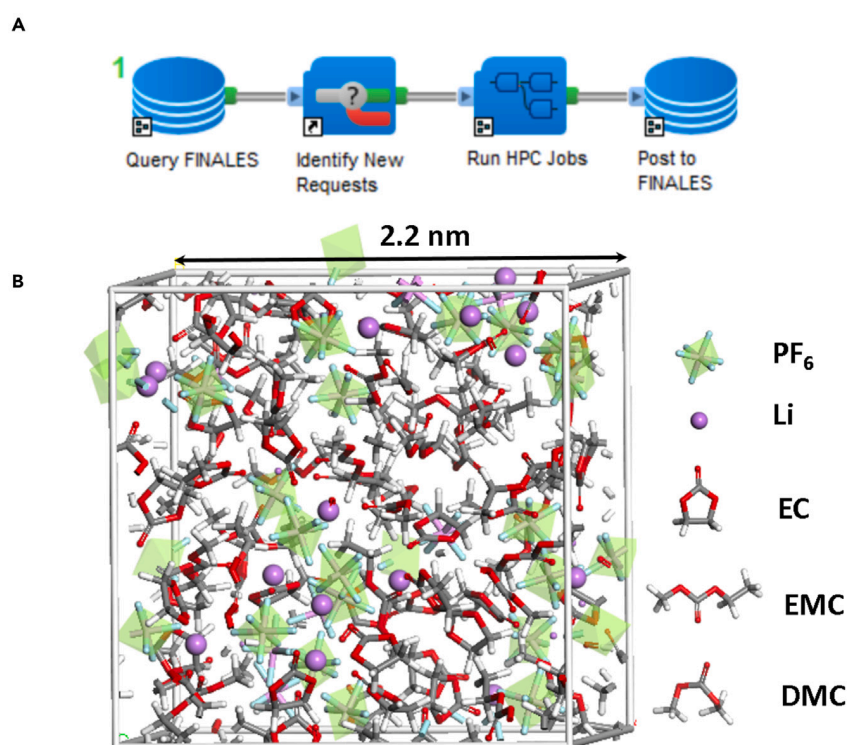


Figure 2. The workflow and the atomistic unit cell used by the simulation tenant

(A) The workflow architecture for automated simulations using BIOVIA Pipeline Pilot. The first component queries the FINALES broker server for simulation requests, which are read and input parameters to perform MD simulations, are extracted. The complete workflow for the MD simulations is contained in the “run HPC job” subprotocol. The results of the MD simulations are obtained asynchronously and posted back onto FINALES upon convergence via the “post to FINALES” component.

(B) The atomistic supercell model of an electrolyte. The ethylene carbonate (EC), ethyl methyl carbonate (EMC), and dimethyl carbonate (DMC) molecules are shown in a stick representation, the lithium ions are shown as large violet balls, and the hexafluorophosphate (PF_6^-) ions are represented as a stick model enclosed by a light green octahedron.

Simulation orchestrator: Pipeline Pilot

The intention-agnostic simulation tenant provides simulation capabilities to the MAP and is created using BIOVIA Pipeline Pilot.³⁹ This is a workflow engine and data analysis tool, which enables reading and writing of data from and to databases and the automation of simulations and experiments as well as the analysis, model building, visualization, and reporting of results. The manipulation of data is executed by components, which are connected via data pipelines into workflows called protocols. Figure 2A shows how the protocol used as the simulation tenant in our demonstration may be graphically represented. The first component in the protocol periodically queries the broker server for pending simulation requests using the FINALES API. The relevant input parameters required to set up a molecular dynamics (MD) simulation are extracted once a new simulation request is received and passed on to a high-performance computing (HPC) cluster for execution.

The core calculations of the protocol are performed in the “run HPC job” subprotocol component, which contains a complete workflow to calculate the ionic transport coefficients of a given electrolyte composition^{40,41} at a given temperature. Briefly, this calculation starts by building an Amorphous Cell model of the molecular liquid

as shown in [Figure 2B](#). This model is the starting configuration to run a sequential MD workflow containing an initialization stage MD run under constant volume and temperature (NVT-MD) followed by an MD run under constant pressure and temperature (NPT-MD) for 250 ns each to thermalize the system and to obtain an estimate for the density. This equilibrated amorphous model is used as a starting configuration for a 2,000 ns production MD simulation run. An automatic analysis of the MD trajectory provides diffusion coefficients, conductivities, and transference numbers for all ionic species in the system as described in detail by Hanke et al.⁴⁰ In addition, the radial distribution function (RDF) is computed, which provides detailed information about the ordering of the molecules in the liquid.

Finally, the results of the MD simulations are collected and formatted for reporting back to FINALES in the last component called “post to FINALES.” The metadata, such as trajectories, can also be sent simultaneously to the Materials Cloud Archive. This protocol runs asynchronously in specific time intervals, and each request is treated independently for querying, simulation, and posting.

Experimental setup: ASAB

The ASAB system used to perform the experiments described in this study is shown in [Figure 3](#). In the demonstration, it serves as an intention-agnostic tenant that comprises a base module for power supply, six syringe pumps, and ten eleven-port valve modules including a matching API commercially available from CETONI. Furthermore, an Entris II laboratory balance from Sartorius AG and a DMA 4100 M densimeter with an additional Lovis 2000 viscometer by Anton Paar Germany are connected to the system. A computer is used to control the system via an in-house-implemented Python package. The software package comprises servers for the densimeter and viscometer, the pump and valve system, and the balance, all based on the FastAPI framework.⁴² These servers call functions in an actions level within the in-house-developed software, which run more complex tasks by calling functions in the driver level. The tubing and interconnections of pumps, valves, vials, and connected devices are digitally represented by a graph. This allows searching for the shortest connection between two nodes or paths passing defined nodes in a given order. Its graph implementation makes ASAB flexible regarding the tubing interconnections and enables processing of high-level requests even after reconfiguring the hardware. Prior to any mixing step, the system fills every syringe related to a reservoir containing a component included in the formulation to avoid gas being located at the top of the syringes, which results in flawed mixing ratios. The hardware layout is loaded from a configuration file, which needs to be supplied by the operator prior to starting an experiment. Requests are pulled from FINALES, and the corresponding functionality is triggered on the device requested. The setup offers functionalities to request mixing, providing a sample to a device, retrieving data, and draining the sample from the device. The deduction of detailed step-by-step procedures from these high-level requests is performed within the ASAB actions and drivers, exploiting its internal flexibility.

Since the simulations work on a molecular representation of the system, the optimizer is chosen to represent formulations as a set of molar fractions. Requests for formulations therefore need to be transformed to volume fractions by the ASAB software to enable volumetric dosing of the stock solutions. In case there is no exact solution to the transformation, the system selects the closest accessible formulation using a gradient descent method provided in the SciPy⁴³ Python package.

Based on the volume fractions calculated according to this procedure, the volume flow of each stock solution is determined by multiplication of the targeted total

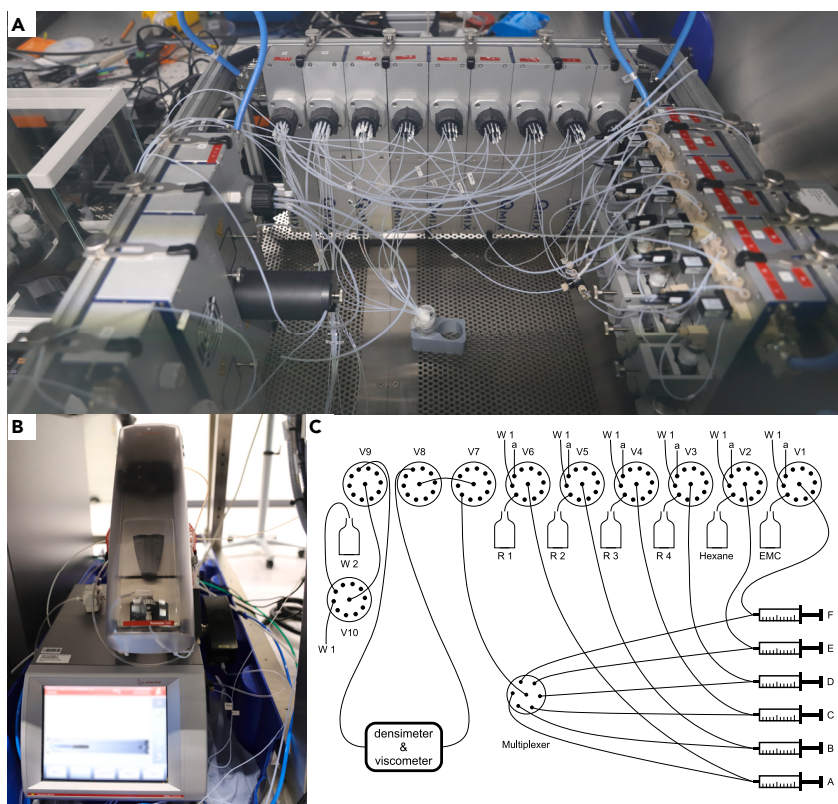


Figure 3. The hardware setup and a schematic overview of the ASAB tenant

(A) The pump and valve system of the experimental ASAB setup used to perform the experiments relevant for this study.

(B) The densimeter and the attached viscometer device used for the measurements.

(C) A schematic drawing showing the connections within the system.

The valves, reservoirs containing the stock solutions (R1–R4), cyclohexane, and EMC for cleaning are shown. Further, the syringes (A–F), the multiplexer for mixing, and the densimeter and viscometer device are displayed.

flow with the volume fraction of the respective stock solution. The flows of the stock solutions are merged in the multiplexer before a valve determines whether the flow is directed toward the waste while stabilizing the flows or toward the measuring device. After the measurement ends, the sample is drained to the waste using gas aspirated from the atmosphere in the glovebox, in which the pumps and valves are located. Prior to the subsequent experiment, gas is pumped through the measuring cells of the densimeter and viscometer several times to remove large residues of sample material.

Optimizer tenant

The intention-aware optimizer tenant software is designed in a modular and configurable way using the Python programming language. One module is responsible for all communication with FINALES, including authentication, data retrieval, and sending new measurement or simulation requests. Another module is responsible for data preprocessing and collating data in a table format appropriate for data analysis. A third module contains the optimizer algorithm, responsible for analyzing data and suggesting new measurement inputs. In the current version of the optimizer tenant, the optimizer algorithm is a Gaussian process optimizer based on the widely

used GP-UCB algorithm⁴⁴ extended for multiobjective optimization with the Chimera³⁵ scalarizing function. Finally, a central application module binds the other modules together in a main loop by continuously checking the current state of FINALES's database, retrieving available data, fitting the machine-learning model with the data, and using the optimizer algorithm to generate new measurement and simulation requests, which are finally sent to FINALES. The optimizer tenant can be configured to specify what to optimize, which quantities to request, and how to reach the broker server.

Low-fidelity conductivity predictor integrated through an AiiDA tenant

AiiDA^{4,45,46} is a general-purpose workflow management platform for computational research projects, with a plugin interface to support external codes. Currently, the vast majority of the plugins cover simulations in the field of materials science. AiiDA provides a framework to codify and automate the different tasks involved in computational workflows and is able to seamlessly integrate with simulation codes running on HPC clusters. A generic intention-agnostic AiiDA tenant can thus grant FINALES users access to a wide variety of simulation tools without needing to implement specific infrastructure to interact with the computational server, similar to those offered by the Pipeline Pilot simulation orchestrator discussed earlier. Furthermore, it can also significantly simplify the management of the computing resources used to run these calculations, as well as the coordination between multiple simulation codes required to produce a given figure of merit (FOM), i.e., the implementation of a complete workflow.

The AiiDA-FINALES tenant demonstrates the interaction of a simulation managed by AiiDA with FINALES. A command line interface is also implemented to simplify the process of starting the tenant, and also provides an easy way of populating requests in the server, which is particularly useful for testing. Here, we demonstrate the use of the AiiDA tenant to estimate a low-fidelity value for the conductivity, based on the model reported by Rahmanian et al.⁴⁷ developed using one-shot active learning, in order to provide multifidelity data to the MAP. The model was designed for solutions of lithium hexafluorophosphate (LiPF₆) in mixtures of ethylene carbonate (EC), ethyl methyl carbonate (EMC), and propylene carbonate (PC), in a range of temperatures reaching from -30°C to 60°C . The original model was expressed as a polynomial on the mass ratios of the participating species, in which the coefficients were determined for specific temperatures within the range provided in increments of 10°C . In the implementation used here, any temperature is accepted, but processing is only possible for temperatures within -30°C to 60°C . The parameters are interpolated from those corresponding to the two nearest multiples of ten. A filter is implemented that only processes requests from the AiiDA internal queue, which are within the temperature range of the model. Once the tenant is started, it connects to the server, pulls any request for conductivity simulations, and submits any simulation that is not already queued to the AiiDA internal queuing system. It then monitors the state of the submitted calculations in the internal queue of AiiDA, and when they finish, it submits back the measurement results to FINALES. The overall data and process flow is analogous to the one discussed for the Pipeline Pilot simulation orchestrator in [Figure 2A](#).

Our implementation serves to demonstrate AiiDA's capabilities that can be enabled by connecting AiiDA as a tenant to FINALES. Further features, such as a persistence mechanism to allow the tenant to be restarted or error handling, will be implemented in the future, also leveraging future features of the FINALES broker.

In the following sections, we describe the design of our MAP, the reduced setup used to demonstrate the operability of the communication, the results obtained from the demonstration run, the lessons learned, and future goals.

MAP design

Current implementations of MAPs often limit themselves to loops^{48–50} optimizing for a specific target by using workflows, which are predefined to a certain degree, i.e., a fixed sequence of events is given, and instrument or research actions are predetermined. Battery research, or energy conversion research in a broader sense, is, however, intrinsically multimodal and multitarget. Consequently, our MAP allows us to combine hardware and software components, providing complementary capabilities and aiming to minimize error-prone human interventions while increasing the experimental and computational efficiency and maximizing information generation in a time- and cost-efficient manner.

A defining design decision, which is specific to our approach, is to disable direct communication between tenants and to channel all communication through a brokering service, which we implemented. FINALES constitutes an open interface brokering between hardware and software as well as humans. Simulations and experiments can be requested as a service through the FINALES API. By implementing an interface to the FINALES API, new tenants can easily be connected to our MAP without necessitating alterations of existing workflows in the MAP or the tenant.

Further, it is designed to be highly modular with respect to possible workflows, which, in the future, is expected to allow for various independent optimizations running simultaneously on a common MAP. For this to work, the design and mode of operation of our MAP must be independent of the target of any optimization running on the MAP. This necessitates a separation of concerns among all the tenants, which results in the aforementioned distinction between intention-aware and intention-agnostic tenants. Moreover, FINALES is prepared to allow for multitenancy. Several intention-agnostic tenants offering the same physical or computational capabilities and multiple intention-aware tenants with different intentions are planned to operate in the same MAP. This will allow the MAP to be utilized for multiple purposes at once and may dramatically increase its utility as a general research framework.

This concept requires the central instance, here FINALES, to be passive, i.e., it does not actively trigger actions in the MAP. This allows for asynchronous operation of the individual tenants by enabling them to fetch new tasks from the server according to their own schedule. This passive operation of FINALES allows us to continue optimization independent of any single tenant's online availability or load. If any equipment or compute cluster is removed from or added to the MAP, the queuing system of FINALES remains unaffected. Requests, which cannot be served by any tenant in the MAP, will remain in the queue until a tenant with the required capabilities connects to the MAP and picks up the request. This behavior allows for the handling of errors on the tenant level without affecting the further operation of the remaining MAP. If a tenant does not report results due to an internal error, the request remains pending, and the MAP will proceed its operation. Hence, there is no need for FINALES to deal with tenant-internal errors. Errors in tenants, which can occur and still allow for results to be reported, need to trigger an entry in the quality field of the response to enable intention-aware tenants to withdraw the data to treat these data according to their standards. Fault tolerance toward a failure of FINALES can be achieved in principle by running redundant servers and to switch to another instance as soon as one instance cannot be reached.

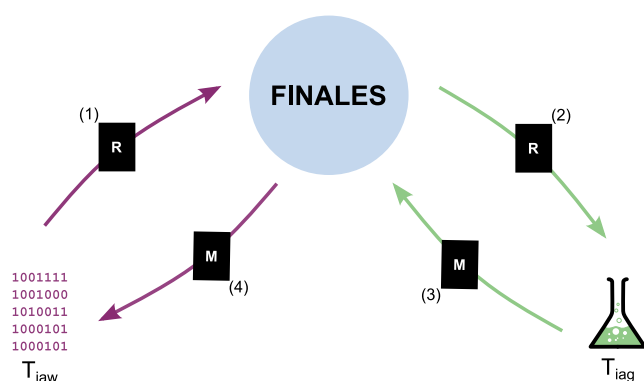


Figure 4. The workflow for performing an experiment or a simulation in our MAP

The intention-aware tenant (T_{iaw}) posts a request (R) to FINALES (1), where it is picked up by the intention-agnostic tenant (T_{iag}) (2), which processes the request and posts back the results (M) to FINALES (3). The intention-aware tenant collects the data from FINALES (4) and operates on them according to its task. Links to the BattINFO³⁷ ontology are prepared for all applicable fields in the JSON-formatted schema.

The general workflow of the MAP is shown in Figure 4. Initially, an intention-aware tenant (T_{iaw}) posts a request to FINALES. From there, an intention-agnostic tenant (T_{iag}) can pick it up and process it according to its own schedule. Hence, the requests are processed asynchronously within the MAP, and different durations of experimental, simulation, or other processes do not block the whole MAP. Once results are available, the T_{iag} posts them back to FINALES, from which the T_{iaw} can withdraw them by posting an appropriate request to FINALES. This request will be served by FINALES itself, and the results matching the request will be sent.

Figure 5 exemplarily shows the structure of a request for a density measurement and a corresponding reply. The two schemas are identical except that the field “pending” must be “true” to identify a request or “false” for reported results, and the field “fom_data” may not be empty for reported results. The field “failed” is used to mark failed measurements or simulations. The “message” field allows us to freely add additional information. In the example, this contains the composition in a volumetric representation and in the molar representation resulting from this. In the example, it is further used to convey a rating of the fidelity of the data by the tenant providing it, e.g., according to the success or the failure of the measurement. In this example, the system reported viscosity and density in the reply, as these two quantities are measured in a single measurement.

DEMONSTRATION OF OPERABILITY

To demonstrate the operability of the current implementation of our MAP, we deployed a minimal configuration for the task of optimizing the composition of a battery electrolyte by maximizing viscosity while minimizing density. The primary aim of the demonstration was to show the basic operability of the MAP design in an actual physical manifestation rather than drawing any scientific conclusions regarding battery electrolytes from the generated data.

The setup included the ASAB system and the simulation orchestrator created using Pipeline Pilot for performing the experiments and simulations, respectively. The optimizer tenant was used to guide the optimization procedure and send requests to FINALES based on the experimental and simulated density, viscosity and ionic conductivity data available in the database and retrieved through FINALES. The

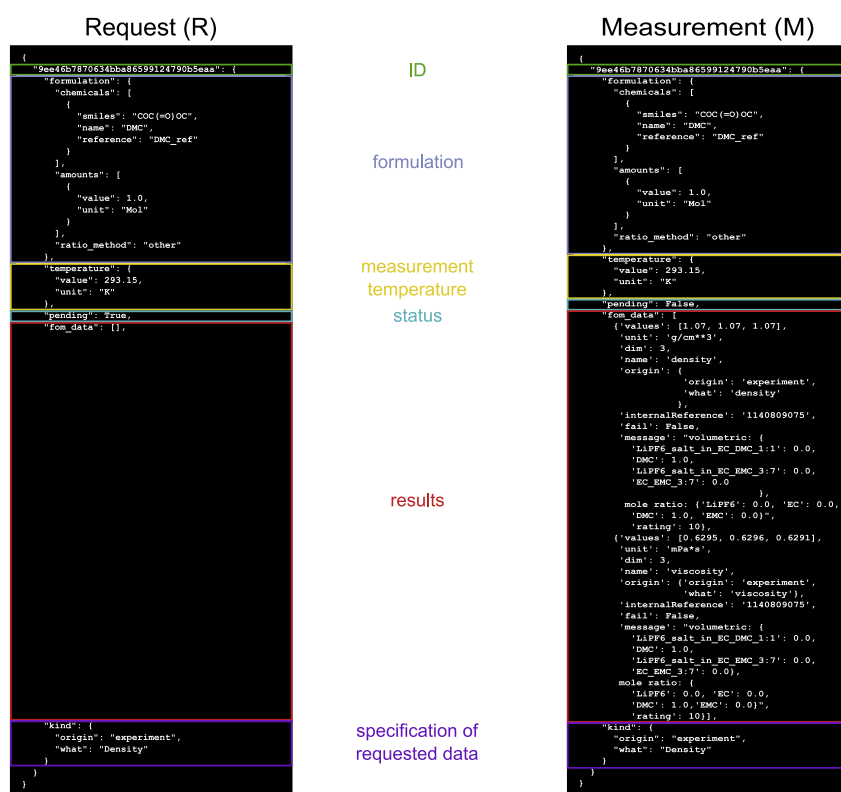


Figure 5. The format of a request and a measurement

The schemas for requests (R) and measurements (M) is the same. For measurements, the field “fom_data” must not be empty, while it may be empty for requests. The main difference is the field “pending,” which is “true” for the request and “false” for the measurement.

distributed MAP was tested incrementally in several trials during development. During periods in which the optimizer was not running, requests were generated manually, demonstrating FINALES’s ability for human-in-the-loop operation. Most recently, an autonomous run of the MAP, in which FINALES orchestrated the optimizer tenant, the Pipeline Pilot-based simulation orchestrator, and ASAB, ran successfully for approximately 4.5 h without any human intervention and performed several iterations of requests, simulations, and measurements. The current version of the optimizer did not distinguish whether the data originated from experiments or from simulations and treated all values provided by both methods the same. The data presented in the following section were retrieved from the database after the end of the demonstration. It therefore contains the results requested by manual input as well as the results obtained during the autonomous period of the run.

In the experimental setup, the electrolyte samples were formulated based on stock solutions provided in vials prior to the start of the experiment. For the purpose of the demonstration reported here, commercial solutions of 1 M LiPF₆ in EC:EMC 3:7 by weight and 1 M LiPF₆ in EC:dimethyl carbonate (DMC) 1:1 by weight, as well as EC:EMC 3:7 by weight and DMC, all ordered from E-Lyte Innovations, were used as received and provided as stock solutions to the experimental setup. In preparation of the demonstration run, density measurements for each stock solution needed to be performed, as these values were required as inputs to calculate the volume fractions from the molar fractions. Each measurement originating from the experimental setup comprised three individual measurements. The value for each

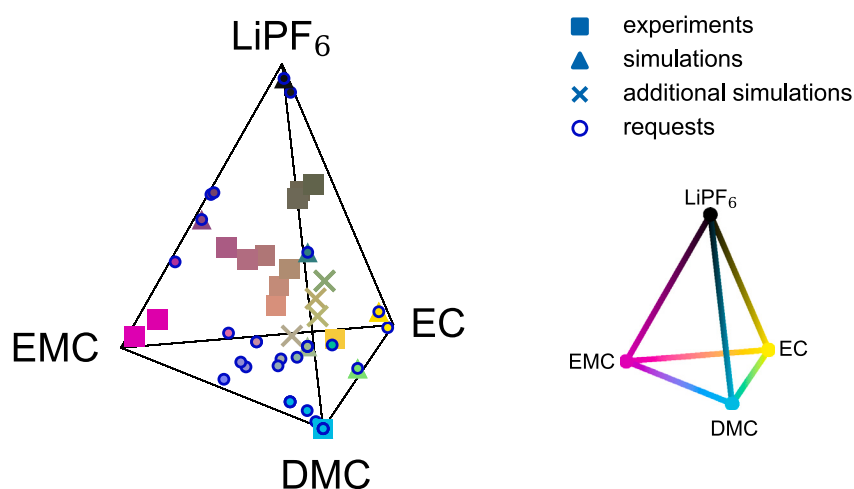


Figure 6. The compositional space covered during the demonstration run

Squared markers represent calculated target formulations of the experiments, triangles mark formulations covered by simulations, and the circles with blue outlines represent the requested formulations. Markers in an x shape denote additional simulations performed during test runs and saved to an instance of FINALES not connected to the optimizer. The set composition in molar fractions is represented by the color. This color scheme is also used in the following figures. A severe deviation between the requested and experimentally targeted formulations is observed. This is likely to be caused by the limitations due to the stock solutions and the approximation of the requested molar fractions by volume fractions.

individual measurement was reported to FINALES within one measurement object. Hence, it is left to the user of the data whether the data shall be averaged or used as is.

RESULTS

The chemical space covered during the entire run is shown in Figure 6. The squared markers represent experimentally measured data, and triangles indicate results obtained from simulations. The round markers with blue outlines represent requested formulations. Simulations for formulations marked by x were added to the server after the demonstration run, as they were saved during testing to a second instance of the server not connected to the optimizer. A significant deviation between the molecular formulations requested by the optimizer and the formulations resulting from the calculated volume fractions targeted in the experiments can be observed. This most probably depends on the stock solutions, which are not allowed to cover the full chemical space spanned by the individual chemicals. Furthermore, the approximation required during the transition from molar fractions to volume fractions and back during the experiment adds another contribution to the deviation if no exact transformation is possible.

Figure 7 shows a plot of the ionic conductivity obtained from simulation results versus the concentration of LiPF_6 . The values shown originate from simulations requested manually as well as optimizer-requested simulations, and it is also important to note that the LiPF_6 content is not the only compositional variation between the data points. The formulations corresponding to the conductivity data presented in this figure also differ in the composition of the solvent. However, the strongest correlation in our data seems to be observed for the LiPF_6 content, which is in line with the literature reporting a stronger influence on conductivity by the salt concentration than the composition of the solvent in various electrolyte systems.^{47,51,52} Figure 7

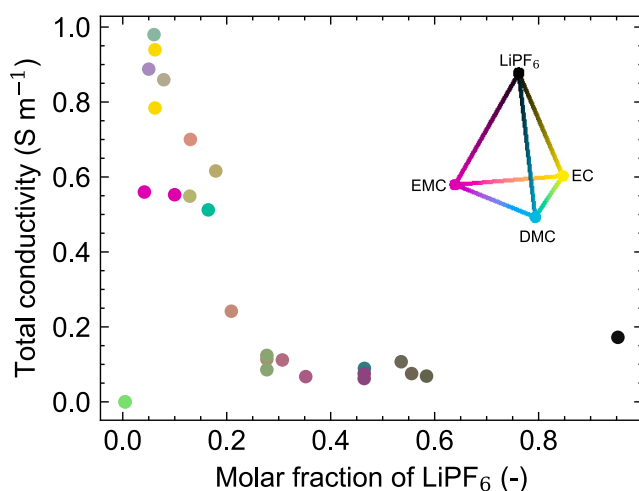


Figure 7. The ionic conductivity data calculated in the course of the MD workflow

The color scheme of Figure 6 was used to denote the composition. The graph comprises data points, which were requested for simulation during the demonstration run and, as such, were generated for the formulations requested for experimental measurement during the demonstration. The simulations for the latter were run after the demonstration was finished. It must be noted that the data points correspond to formulations differing not only in their salt content but also in the composition of the solvent. Further, data originating from simulations triggered by manually posted requests as well as optimizer-generated requests are presented. It seems that a maximum in conductivity for a certain LiPF_6 concentration is found, assuming no significant influence of the solvent composition on conductivity.

shows an increase of ionic conductivity for small concentrations of LiPF_6 up to a maximum followed by a decrease. The presence of a maximum with respect to the salt concentration is reported in the literature based on experimental results^{47,51,53,54} and calculations⁴⁰ for similar electrolyte systems. These correlations to the literature suggest that the simulations triggered during this demonstration captured some general trends regarding the ion conductivity in the electrolyte system that has been investigated.

The RDF presented in Figure 8 shows the interatomic distances of lithium ions to relevant atoms within molecules contained in the electrolyte mixture. The peaks at 2 and 4 Å in the Li-O RDF denote oxygen atoms in the carbonate groups of the electrolyte, with corresponding peaks in the Li-C function. Together, these peaks indicate the first solvation shell around the lithium ions. The ordering becomes stronger with increasing EMC content as the relative height of peaks increases compared to the liquid background. In contrast, the RDF between lithium ions shows multiple peaks at very high EMC content. This suggests long-range ordering of the lithium ions, which is likely to be related to the low dielectric constant of pure EMC ($\epsilon = 2.5\text{--}3$)⁵⁵ and the short screening length arising from it.

Our experimental results show a strong correlation between the viscosity and the density averaged per measurement in the system under investigation with a Pearson correlation coefficient of approximately 0.91. The correlation can also be seen in Figure 9. Due to this strong correlation, the density and viscosity cannot be truly individually optimized, which renders the minimization of the density and the maximization of the viscosity non-ideal targets for multiobjective optimization in this formulation space.

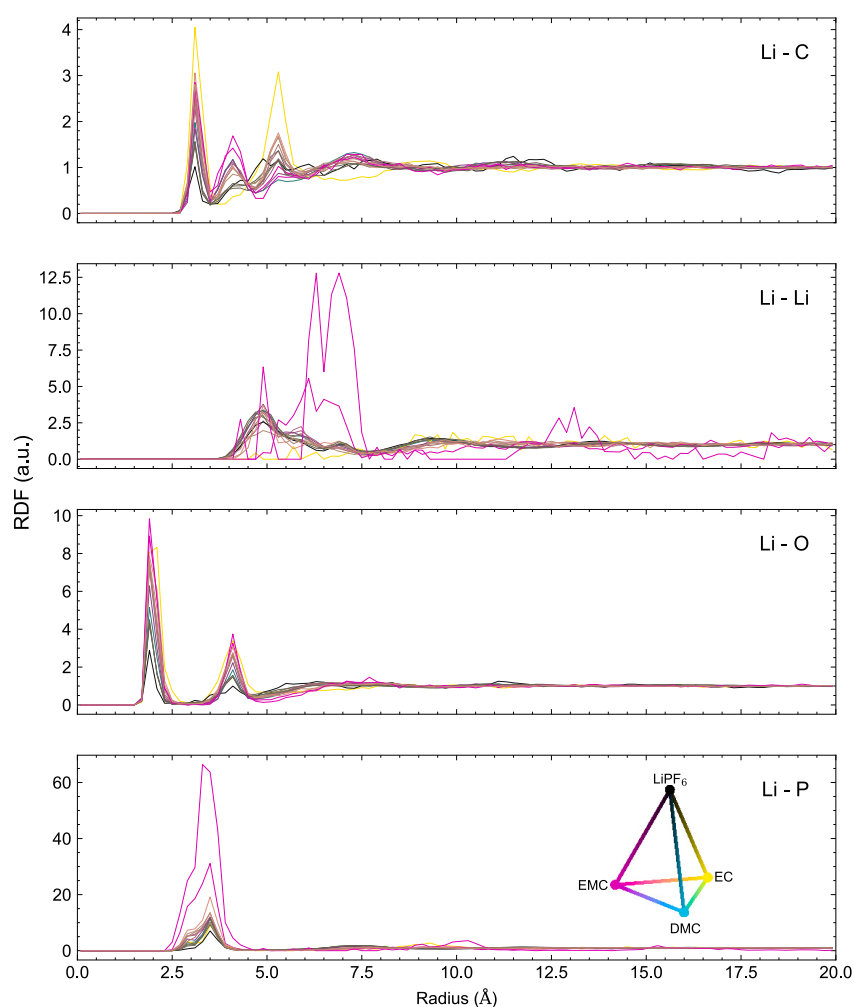


Figure 8. The radial distribution function for lithium ions as obtained from the simulations run on the data generated during the demonstration run based on manual and optimizer-generated requests

The solvation shell of the lithium ions can be observed. The color coding representing the various formulations corresponds to that used in Figure 6.

LESSONS LEARNED

The first run of our international MAP with a passive FINALES brokering instance generated some valuable lessons, which we believe are of great interest for the community and of impact for MAP design.

Data structures

A general insight from this deployment is the realization that the actual implementation of a truly autonomous platform is critically dependent on binding, well-documented, and interoperable data structures. Our MAP requires unambiguous communication. In order to be applicable to such MAPs, data management plans (DMPs)¹⁵ need very strict structures and definitions. During the development of our MAP, a lot of communication between the scientists was required to agree on how to correctly and usefully populate the fields in the schemas due to the various needs of different tenants. Schemas developed for future MAPs need clear

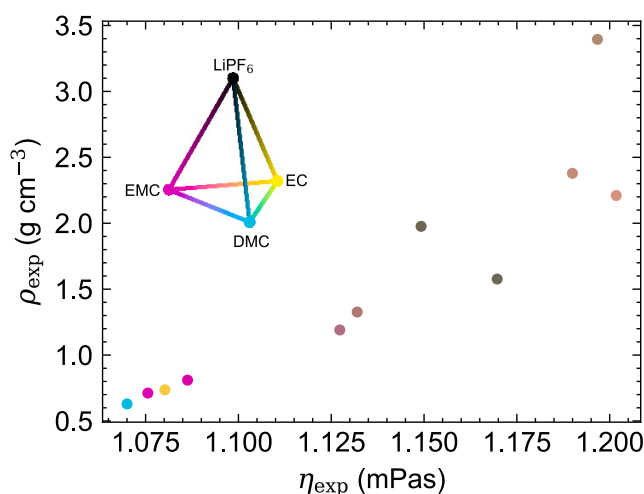


Figure 9. The correlation between the density ρ_{exp} and the viscosity η_{exp} as observed from the formulations yielding both successful density and viscosity measurements

The formulations are colored according to the coloring scheme introduced in Figure 6. A correlation between ρ_{exp} and η_{exp} can be seen. The Pearson correlation coefficient amounts to approximately 0.91.

definitions of the type and format of data contained in each field, which go well beyond the FAIR criteria.⁵⁶ A strong mapping from the fields in the schemas to an ontology can help to precisely describe the information conveyed with each field. Further, an ontology can provide a common semantic for the MAP, enabling specific requests and replies.

Data quality

Due to the multimodality of our map, it turned out to be important to rate the quality of data reported to FINALES on the level of the tenant providing them. If, e.g., a measurement with several subsamples is requested, it is valuable information how many data points were valid and can be included in the analysis. This information enables, e.g., an optimizer to decide whether data with a certain rating should be included in the training of the machine-learning model or not. This concept also applies to other tenants, which could rate the fidelity based on different measures. Hence, there is a need for a tangible and measurable data quality rating for all possible data types and tenants.

Sharing limitations, costs, and units

The demonstration revealed the significance of the limitations of individual tenants on the effective operation of our MAP. In the experimental setup, the range of feasible formulations is mainly limited by the stock solutions provided to the system. Requests by the optimizer can exceed these limitations because the current implementation of the optimizer defines formulations on a molecular level without consideration of the stock solutions. In several cases, this results in rough approximations of the formulation when determining the volume fractions of the stock solutions. Analogously, limitations in the simulation tenant arise due to the limited number of molecules, which can be simulated with reasonable use of computational resources. In the case of our demonstration, a molar fraction of the salt exceeding 0.5 is the limit due to the size of the unit cell. These examples emphasize the necessity of dealing with the limitations of each tenant. We suggest sharing the limitations upon connection of a tenant to the MAP so that other tenants can adjust their requests

accordingly. For costs arising for the use of tenants, this concept of sharing can be extended to include the price, which can be used to enforce a budget on optimizations. This does not mean restricting the search space to the limits of the most restrictive tenant but rather installing a preventive measure for cost-excessive or impossible-to-fulfill requests. The implementation of a billing system could further add a new direction to research by offering laboratories as a service like existing biotechnology services.

The example of the formulations also shows the importance of finding a common way of specifying crucial quantities shared by several tenants and transforming them according to the specific needs of a tenant, where necessary. Such common representations and units need to be defined for the whole MAP during setup.

MAP design

In our demonstration, asynchronicity and the append-only way of saving requests and results proved to be valuable features in orchestrating our MAP. As each tenant processes its tasks independently from the MAP, no tenant is being blocked by the state of another. This fulfills the requirement of a modular and hardware-independent operation. The intention-agnostic operation of some tenants also proved beneficial regarding the flexible selection of the optimization targets. The T_{iaw} is able to access all the data available in the database of the MAP and to exploit the full dataset while pursuing its objective.

For future development, the implementation of full data lineage tracking including timestamps and the complete collection of metadata for the exploitation of additional results will be targeted. Full data lineage tracking requires each tenant to provide the data lineage tracking for its workflow and to report it to the MAP or at least to save it in tenant-specific storage for future reference. Overall, we recommend not restricting data recording solely to the quantities of primary interest but to record all data and metadata possible.

Our proposed MAP architecture, including the centralized passive FINALES brokering service, fulfills the requirements of interchangeability of tenants, asynchronous and distributed operation, and inclusion of experimental and computational setups. This constitutes a significant portion of our definition of a MAP. Hence, we regard this as a possible concept for the future development of international MAPs.

Improvements need to be made to the standardization of the schemas, the user authentication, and the communication of limitations of tenants. Further development and a demonstration of multitenancy and data lineage tracking are part of the future work.

CONCLUSION

The demonstration reported here showed an operation principle for a distributed MAP on an international scale. We believe that this orchestration paradigm of implementing a marketplace of requests to be fulfilled by available tenants could be a universal approach to the acceleration of research. This first run of our internationally distributed MAP allowed us to identify a variety of challenges, which need to be addressed in the further development and integration of an increasing number of tenants. We believe that efforts toward the further development and deployment of MAPs are worth undertaking, as building shared MAPs, where instruments are no

longer used solely by a single group, allows the simultaneous usage of research equipment for a variety of research questions and fields. This is important for ensuring fault tolerance and around-the-clock operation and, simultaneously, creates incentives for cost reduction and efficiency enhancement. By the collaborative nature of MAPs, community building is an integral part of the design process. The current funding schemes in, e.g., the European Union (EU) and associated national or bilateral funding agencies in fact foster this collaborative approach to research, and we believe that there is a need to create more cross-country funding lines that can help in building global research workflows. We believe that MAPs can improve the efficient utilization of equipment in new innovative workflows with little additional effort to ultimately enable a more efficient allocation of funding. We hope that our insights shared in this perspective will support the further development of international MAPs and the acceleration of research to overcome the material limited challenges of our time.

EXPERIMENTAL PROCEDURES

Resource availability

Please refer to the "[Methods and tenants](#)" section to obtain information about the experimental procedures and how to reproduce them.

Lead contact

Requests for further information should be directed to the lead contact, Helge S. Stein (helge.stein@tum.de).

Materials availability

This study did not generate new unique reagents.

Data and code availability

All data reported in this perspective will be shared by the lead contact upon request. All original code regarding the FINALES broker server has been deposited at <https://github.com/BIG-MAP/finale> under <https://zenodo.org/record/8009625> and is publicly available under the MIT license as of the date of publication. Any additional information required to reanalyze the data reported in this perspective is available from the [lead contact](#) upon request.

ACKNOWLEDGMENTS

This work contributes to the research performed at CELEST (Center for Electrochemical Energy Storage Ulm-Karlsruhe) and was funded by the German Research Foundation (DFG) under Project ID 390874152 (POLiS Cluster of Excellence). This project received funding from the European Union's Horizon 2020 research and innovation program under grant agreement no. 957189. The authors acknowledge BATTERY 2030PLUS, funded by the European Union's Horizon 2020 research and innovation program under grant agreement no. 957213. M.V. acknowledges the KIT Graduate School Enabling Net Zero - ENZo.

AUTHOR CONTRIBUTIONS

M.V. built and designed ASAB and organized the FINALES run; J.B. and P.B.J. programmed and ran the optimizer tenant; H.H., N.S., J.C., and F.H. programmed and ran the Pipeline Pilot tenant; F.H. organized and J.B., H.H., and M.V. implemented regression tests; I.E.C. and S.C. developed the DMP and ontology link; F.F.R. and G.P. developed the AiiDA tenant; A.B. and H.S.S. wrote the first draft of the

manuscript; H.S.S. developed the FINALES software, hosted and maintained the FINALES broker server, and conceived the initial idea and MAP design.

DECLARATION OF INTERESTS

H.H., N.S., J.C., and F.H. may be beneficiaries of shares in Dassault Systèmes through an employer scheme.

INCLUSION AND DIVERSITY

We support inclusive, diverse, and equitable conduct of research.

REFERENCES

- Maier, W.F. (2019). Early Years of High-Throughput Experimentation and Combinatorial Approaches in Catalysis and Materials Science. *ACS Comb. Sci.* 21, 437–444. <https://doi.org/10.1021/acscmbosci.8b00189>.
- Stein, H.S., Gregoire, J.M., and Gregoire, M. (2019). Progress and prospects for accelerating materials science with automated and autonomous workflows. *Chem. Sci.* 10, 9640–9649. <https://doi.org/10.1039/C9SC03766G>.
- Soedarmadji, E., Stein, H.S., Suram, S.K., Guevarra, D., and Gregoire, J.M. (2019). Tracking materials science data lineage to manage millions of materials experiments and analyses. *npj Comput. Mater.* 5, 79. <https://doi.org/10.1038/s41524-019-0216-x>.
- Pizzi, G., Cepellotti, A., Sabatini, R., Marzari, N., and Kozinsky, B. (2016). AiiDA: Automated Interactive Infrastructure and Database for Computational Science. *Comput. Mater. Sci.* 111, 218–230. <https://doi.org/10.1016/j.commatsci.2015.09.013>.
- Amis, E.J., Xiang, X.-D., and Zhao, J.-C. (2002). Combinatorial Materials Science: What's New Since Edison? *MRS Bull.* 27, 295–300. <https://doi.org/10.1557/mrs2002.96>.
- Koinuma, H., and Takeuchi, I. (2004). Combinatorial solid-state chemistry of inorganic materials. *Nat. Mater.* 3, 429–438. <https://doi.org/10.1038/nmat1157>.
- Ludwig, A., Zarnetta, R., Hamann, S., Savan, A., and Thienhaus, S. (2008). Development of multifunctional thin films using high-throughput experimentation methods. *J. Mater. Chem.* 19, 1144–1149. <https://doi.org/10.1039/b714610a>.
- Ludwig, A. (2019). Discovery of new materials using combinatorial synthesis and high-throughput characterization of thin-film materials libraries combined with computational methods. *npj Comput. Mater.* 5, 70–77. <https://doi.org/10.1038/s41524-019-0205-0>.
- Bhowmik, A., Castelli, I.E., Garcia-Lastra, J.M., Jørgensen, P.B., Winther, O., and Vegge, T. (2019). A perspective on inverse design of battery interphases using multi-scale modelling, experiments and generative deep learning. *Energy Storage Mater.* 21, 446–456. <https://doi.org/10.1016/j.ensm.2019.06.011>.
- Sanchez-Lengeling, B., and Aspuru-Guzik, A. (2018). Inverse molecular design using machine learning: Generative models for matter engineering. *Science* 361, 360–365.
- Noh, J., Kim, J., Stein, H.S., Sanchez-Lengeling, B., Gregoire, J.M., Aspuru-Guzik, A., and Jung, Y. (2019). Inverse Design of Solid-State Materials via a Continuous Representation. *Matter* 1, 1370–1384. <https://doi.org/10.1016/j.matt.2019.08.017>.
- Isayev, O., Oses, C., Toher, C., Gossett, E., Curtarolo, S., and Tropsha, A. (2017). Universal fragment descriptors for predicting properties of inorganic crystals. *Nat. Commun.* 8, 15679–15712. <https://doi.org/10.1038/ncomms15679>.
- Peterson, A.A., and Nørskov, J.K. (2012). Activity Descriptors for CO₂ Electroreduction to Methane on Transition-Metal Catalysts. *J. Phys. Chem. Lett.* 3, 251–258. <https://doi.org/10.1021/jz201461p>.
- Curtarolo, S., Hart, G.L.W., Nardelli, M.B., Mingo, N., Sanvito, S., and Levy, O. (2013). The high-throughput highway to computational materials design. *Nat. Mater.* 12, 191–201. <https://doi.org/10.1038/nmat3568>.
- Castelli, I.E., Arismendi-Arrieta, D.J., Bhowmik, A., Cekic-Laskovic, I., Clark, S., Dominko, R., Flores, E., Flowers, J., Ulvskov Frederiksen, K., Friis, J., et al. (2021). Data Management Plans: the Importance of Data Management in the BIG-MAP Project. *Batter. Supercaps* 4, 1803–1812. <https://doi.org/10.1002/batt.202100117>.
- Ling, J., Hutchinson, M., Antono, E., Paradiso, S., and Meredig, B. (2017). High-Dimensional Materials and Process Optimization using Data-driven Experimental Design with Well-Calibrated Uncertainty Estimates. *Integr. Mater. Manuf. Innov.* 6, 207–217. <https://doi.org/10.1007/s40192-017-0098-z>.
- Ament, S.E., Stein, H.S., Guevarra, D., Zhou, L., Haber, J.A., Boyd, D.A., Umehara, M., Gregoire, J.M., and Gomes, C.P. (2019). Multi-component background learning automates signal detection for spectroscopic data. *npj Comput. Mater.* 5, 1–7. <https://doi.org/10.1038/s41524-019-0213-0>.
- Schwarting, M., Siol, S., Talley, K., Zakutayev, A., and Phillips, C. (2017). Automated algorithms for band gap analysis from optical absorption spectra. *Mater. Discov.* 10, 43–52. <https://doi.org/10.1016/j.md.2018.04.003>.
- Umehara, M., Stein, H.S., Guevarra, D., Newhouse, P.F., Boyd, D.A., and Gregoire, J.M. (2019). Analyzing machine learning models to accelerate generation of fundamental materials insights. *npj Comput. Mater.* 5, 34. <https://doi.org/10.1038/s41524-019-0172-5>.
- Mission Innovation (2018). *Materials Acceleration Platform—Accelerating Advanced Energy Materials Discovery by Integrating High-Throughput Methods with Artificial Intelligence (Mission Innovation)*.
- Vescovi, R., Chard, R., Saint, N.D., Blaiszik, B., Pruyne, J., Bicer, T., Lavens, A., Liu, Z., Papka, M.E., Narayanan, S., et al. (2022). Linking scientific instruments and computation: Patterns, technologies, and experiences. *Patterns* 3, 100606. <https://doi.org/10.1016/j.patter.2022.100606>.
- Chard, R., Pruyne, J., McKee, K., Bryan, J., Raumann, B., Ananthakrishnan, R., Chard, K., and Foster, I.T. (2023). Globus automation services: Research process automation across the space-time continuum. *Future Generat. Comput. Syst.* 142, 393–409. <https://doi.org/10.1016/j.future.2023.01.010>.
- Roch, L.M., Häse, F., Kreisbeck, C., Tamayo-Mendoza, T., Yunker, L.P.E., Hein, J.E., and Aspuru-Guzik, A. (2018). ChemOS: Orchestrating autonomous experimentation. *Sci. Robot.* 3, eaat5559. <https://doi.org/10.1126/scirobotics.aat5559>.
- Burger, B., Maffettone, P.M., Gusev, V.V., Aitchison, C.M., Bai, Y., Wang, X., Li, X., Alston, B.M., Li, B., Clowes, R., et al. (2020). A mobile robotic chemist. *Nature* 583, 237–241. <https://doi.org/10.1038/s41586-020-2442-2>.
- Rahmanian, F., Flowers, J., Guevarra, D., Richter, M., Fichtner, M., Donnelly, P., Gregoire, J.M., and Stein, H.S. (2022). Enabling Modular Autonomous Feedback-Loops in Materials Science through Hierarchical Experimental Laboratory Automation and Orchestration. *Adv. Mater. Interfac.* 9, 2101987. <https://doi.org/10.1002/admi.202101987>.
- Antypas, K., Canon, S., Dart, E., Fagnan, K., Gerhardt, L., Jacobsen, D., Lockwood, G.K., Monga, I., Nugent, P., Ramakrishnan, L., et al. (2020). Superfacility: The Convergence of Data, Compute, Networking, Analytics and Software. In *Handbook on Big Data and Machine Learning in the Physical Sciences (World Scientific Series on Emerging Technologies)*, pp. 361–386. https://doi.org/10.1142/9789811204579_0017.
- Amici, J., Asinari, P., Ayerbe, E., Barboux, P., Bayle-Guillemaud, P., Behm, R.J., Berecibar, M., Berg, E., Bhowmik, A., Bodoardo, S., et al. (2022). A Roadmap for Transforming Research to Invent the Batteries of the Future Designed

- within the European Large Scale Research Initiative BATTERY 2030+. *Adv. Energy Mater.* **12**, 2102785. <https://doi.org/10.1002/aenm.202102785>.
28. Fichtner, M. (2022). Recent Research and Progress in Batteries for Electric Vehicles. *Batter. Supercaps* **5**, e202100224. <https://doi.org/10.1002/batt.202100224>.
 29. Fichtner, M., Edström, K., Ayerbe, E., Berecibar, M., Bhowmik, A., Castelli, I.E., Clark, S., Dominko, R., Erakca, M., Franco, A.A., et al. (2021). Rechargeable Batteries of the Future—The State of the Art from a BATTERY 2030+ Perspective. *Adv. Energy Mater.* **12**, 2102904. <https://doi.org/10.1002/aenm.202102904>.
 30. Bhowmik, A., Berecibar, M., Casas-Cabanas, M., Csanyi, G., Dominko, R., Hermansson, K., Palacin, M.R., Stein, H.S., and Vegge, T. (2022). Implications of the BATTERY 2030+ AI-Assisted Toolkit on Future Low-TRL Battery Discoveries and Chemistries. *Adv. Energy Mater.* **12**, 2102698. <https://doi.org/10.1002/aenm.202102698>.
 31. Nikolaev, P., Hooper, D., Perea-López, N., Terrones, M., and Maruyama, B. (2014). Discovery of Wall-Selective Carbon Nanotube Growth Conditions via Automated Experimentation. *ACS Nano* **8**, 10214–10222. <https://doi.org/10.1021/nn503347a>.
 32. Kusne, A.G., Gao, T., Mehta, A., Ke, L., Nguyen, M.C., Ho, K.-M., Antropov, V., Wang, C.-Z., Kramer, M.J., Long, C., and Takeuchi, I. (2014). On-the-fly machine-learning for high-throughput experiments: search for rare-earth-free permanent magnets. *Sci. Rep.* **4**, 6367. <https://doi.org/10.1038/srep06367>.
 33. Li, Y.J., Savan, A., Kostka, A., Stein, H.S., Ludwig, A., and Ludwig, A. (2018). Accelerated atomic-scale exploration of phase evolution in compositionally complex materials. *Mater. Horiz.* **5**, 86–92. <https://doi.org/10.1039/C7MH00486A>.
 34. Stein, H.S., Sanin, A., Rahmanian, F., Zhang, B., Vogler, M., Flowers, J.K., Fischer, L., Fuchs, S., Choudhary, N., and Schroeder, L. (2022). From materials discovery to system optimization by integrating combinatorial electrochemistry and data science. *Curr. Opin. Electrochem.* **35**, 101053. <https://doi.org/10.1016/j.coelec.2022.101053>.
 35. Häse, F., Roch, L.M., and Aspuru-Guzik, A. (2018). Chimera: enabling hierarchy based multi-objective optimization for self-driving laboratories. *Chem. Sci.* **9**, 7642–7655. <https://doi.org/10.1039/C8SC02239A>.
 36. Colvin, S. (2022). Contributors to pydantic (pydantic). <https://github.com/pydantic/pydantic>.
 37. Clark, S., Bleken, F.L., Stier, S., Flores, E., Andersen, C.W., Marcinek, M., Szczesna-Chrzan, A., Gaberscek, M., Palacin, M.R., Uhrin, M., and Friis, J. (2022). Toward a Unified Description of Battery Data. *Adv. Energy Mater.* **12**, 2102702. <https://doi.org/10.1002/aenm.202102702>.
 38. Allan, D., Caswell, T., Campbell, S., and Rakin, M. (2019). Bluesky's Ahead: A Multi-Facility Collaboration for an *la Carte* Software Project for Data Acquisition and Management. *Synchrotron Radiat. News* **32**, 19–22. <https://doi.org/10.1080/08940886.2019.1608121>.
 39. Dassault Systèmes Americas Corporation (2022). BIOVIA Pipeline Pilot release 2022. <https://www.3ds.com/products-services/biovia/products/data-science/pipeline-pilot/>.
 40. Hanke, F., Modrow, N., Akkermans, R.L.C., Korotkin, I., Mocanu, F.C., Neufeld, V.A., and Veit, M. (2019). Multi-Scale Electrolyte Transport Simulations for Lithium Ion Batteries. *J. Electrochem. Soc.* **167**, 013522. <https://doi.org/10.1149/2.0222001JES>.
 41. Schaarschmidt, J., Yuan, J., Strunk, T., Kondov, I., Huber, S.P., Pizzi, G., Kahle, L., Bölle, F.T., Castelli, I.E., Vegge, T., et al. (2022). Workflow Engineering in Materials Design within the BATTERY 2030+ Project. *Adv. Energy Mater.* **12**, 2102638. <https://doi.org/10.1002/aenm.202102638>.
 42. Ramírez, S. Contributors to FastAPI FastAPI. <https://fastapi.tiangolo.com/>.
 43. Virtanen, P., Gommers, R., Oliphant, T.E., Haberland, M., Reddy, T., Cournapeau, D., Burovski, E., Peterson, P., Weckesser, W., Bright, J., et al. (2020). SciPy 1.0: fundamental algorithms for scientific computing in Python. *Nat. Methods* **17**, 261–272. <https://doi.org/10.1038/s41592-019-0686-2>.
 44. Srinivas, N., Krause, A., Kakade, S., and Seeger, M. (2010). Gaussian Process Optimization in the Bandit Setting: No Regret and Experimental Design. In *Proceedings of the 27th International Conference on Machine Learning ICML, 10Proceedings of the 27th International Conference on Machine Learning ICML (Omnipress)*, pp. 1015–1022.
 45. Huber, S.P., Zoupanos, S., Uhrin, M., Talirz, L., Kahle, L., Häuselmann, R., Gresch, D., Müller, T., Yakutovich, A.V., Andersen, C.W., et al. (2020). AiIDA 1.0, a scalable computational infrastructure for automated reproducible workflows and data provenance. *Sci. Data* **7**, 300. <https://doi.org/10.1038/s41597-020-00638-4>.
 46. Uhrin, M., Huber, S.P., Yu, J., Marzari, N., and Pizzi, G. (2021). Workflows in AiIDA: Engineering a high-throughput, event-based engine for robust and modular computational workflows. *Comput. Mater. Sci.* **187**, 110086. <https://doi.org/10.1016/j.commatsci.2020.110086>.
 47. Rahmanian, F., Vogler, M., Wölke, C., Yan, P., Winter, M., Cekic-Laskovic, I., and Stein, H.S. (2022). One-Shot Active Learning for Globally Optimal Battery Electrolyte Conductivity. *Batter. Supercaps* **5**, e202200228. <https://doi.org/10.1002/batt.202200228>.
 48. Flores-Leonar, M.M., Mejía-Mendoza, L.M., Aguilar-Granda, A., Sanchez-Lengeling, B., Tribukait, H., Amador-Bedolla, C., and Aspuru-Guzik, A. (2020). Materials Acceleration Platforms: On the way to autonomous experimentation. *Curr. Opin. Green Sustain. Chem.* **25**, 100370. <https://doi.org/10.1016/j.cogsc.2020.100370>.
 49. Saikin, S.K., Kreisbeck, C., Sheberla, D., Becker, J.S., and Aspuru-Guzik, A. (2019). Closed-loop discovery platform integration is needed for artificial intelligence to make an impact in drug discovery. *Expert Opin. Drug Discov.* **14**, 1–4. <https://doi.org/10.1080/17460441.2019.1546690>.
 50. Häse, F., Roch, L.M., and Aspuru-Guzik, A. (2019). Next-Generation Experimentation with Self-Driving Laboratories. *Trends Chem.* **1**, 282–291. <https://doi.org/10.1016/j.trechm.2019.02.007>.
 51. Ding, M.S., Xu, K., Zhang, S.S., Amine, K., Henriksen, G.L., and Jow, T.R. (2001). Change of Conductivity with Salt Content, Solvent Composition, and Temperature for Electrolytes of LiPF₆ in Ethylene Carbonate-Ethyl Methyl Carbonate. *J. Electrochem. Soc.* **148**, A1196. <https://doi.org/10.1149/1.1403730>.
 52. Chen, H.P., Fergus, J.W., and Jang, B.Z. (2000). The Effect of Ethylene Carbonate and Salt Concentration on the Conductivity of Propylene Carbonate/Lithium Perchlorate Electrolytes. *J. Electrochem. Soc.* **147**, 399. <https://doi.org/10.1149/1.1393209>.
 53. Nyman, A., Behm, M., and Lindbergh, G. (2008). Electrochemical characterisation and modelling of the mass transport phenomena in LiPF₆-EC-EMC electrolyte. *Electrochim. Acta* **53**, 6356–6365. <https://doi.org/10.1016/j.electacta.2008.04.023>.
 54. Kondo, K., Sano, M., Hiwara, A., Omi, T., Fujita, M., Kuwae, A., Iida, M., Mogi, K., and Yokoyama, H. (2000). Conductivity and Solvation of Li⁺ Ions of LiPF₆ in Propylene Carbonate Solutions. *J. Phys. Chem. B* **104**, 5040–5044. <https://doi.org/10.1021/jp000142f>.
 55. Hall, D.S., Self, J., and Dahn, J.R. (2015). Dielectric Constants for Quantum Chemistry and Li-Ion Batteries: Solvent Blends of Ethylene Carbonate and Ethyl Methyl Carbonate. *J. Phys. Chem. C* **119**, 22322–22330. <https://doi.org/10.1021/acs.jpcc.5b06022>.
 56. Wilkinson, M.D., Dumontier, M., Aalbersberg, I.J., Appleton, G., Axton, M., Baak, A., Blomberg, N., Boiten, J.-W., da Silva Santos, L.B., Bourne, P.E., et al. (2016). The FAIR Guiding Principles for scientific data management and stewardship. *Sci. Data* **3**, 160018. <https://doi.org/10.1038/sdata.2016.18>.

6.2 Integration into a workflow in parallel to direct contribution to a MAP

This section presents the publication [14]

M. Vogler, S. K. Steensen, F. F. Ramírez, L. Merker, J. Busk, J. M. Carlsson, L. H. Rieger, B. Zhang, F. Liot, G. Pizzi, F. Hanke, E. Flores, H. Hajiyani, S. Fuchs, A. Sanin, M. Gaberšček, I. E. Castelli, S. Clark, T. Vegge, A. Bhowmik, and H. S. Stein, “Autonomous Battery Optimization by Deploying Distributed Experiments and Simulations,” *Advanced Energy Materials*, vol. 14, no. 46, p. 2403263, 2024. doi: 10.1002/aenm.202403263

submitted in May 2024 and published after peer-review in October 2024. The open access publication is available under the terms of the Creative Commons Attribution 4.0 International (CC BY 4.0) (<https://creativecommons.org/licenses/by/4.0/>) license.

Monika Vogler presented this work in a poster at the *Battery2030+ Annual Conference 2024* in Grenoble, France in May 2024, in a poster at the *POLiS Annual Conference 2024* in Karlsruhe, Germany in June 2024, at the *LMS Seminars* in Villigen, Switzerland in October 2024, and contributed to several presentations in the context of the BIG-MAP project. Further, the results presented in this chapter were parts of deliverables and a demonstrator for the BIG-MAP project.

Author contributions

The following author contributions are given as a literal quotation from [14]:

"M.V. and S.K.S. contributed equally to this work. Conceptualization: A.B., H.S.S.; Data curation: J.B., S.K.S, E.F., M.V., F.L.; Formal analysis: J.B., M.V., J.C., H.H., F.H., L.M., A.B.; Funding acquisition: I.E.C., G.P., J.C., H.H., F.H., H.S.S., T.V., A.B.; Investigation: J.B., M.V., L.M., B.Z., S.K.S.; Methodology: J.B., S.K.S., M.V., F.F.R., J.C., H.H., F.H., M.G., L.H.R., A.S., S.F., S.C., H.S.S., A.B.; Project administration: S.K.S., M.V.; Resources: BZ; Software: J.B., S.K.S., E.F., M.V., F.F.R., F.L., G.P., J.C., H.H., F.H., L.M., L.H.R., B.Z., S.C., H.S.S.; Supervision: I.E.C., G.P., J.C., H.H., F.H., H.S.S., T.V., A.B.; Validation: J.B., M.V., M.G., A.S., S.F.; Visualization: J.B., S.K.S., M.V., J.C., H.H., F.H.; Writing – original draft: J.B., S.K.S., E.F., M.V., F.L., J.C., H.H., F.H., L.H.R., H.S.S., T.V., A.B.; Writing – review & editing: J.B., I.E.C., S.K.S., E.F., M.V., F.F.R., G.P., J.C., H.H., F.H., M.G., L.M., L.H.R., B.Z., A.S., S.F., S.C., H.S.S., T.V., A.B."

For information regarding the reprint permission see Annex A.3.

This publication presents the further development of the FINALES framework presented in chapter 6.1 [13]. It describes a new implementation of the framework with significant improvements in the structure of the database and its versatility towards new research goals while keeping the aspects of passive operation, permissive append-only data management, quality ratings, intention-agnosticism, and multitenancy. The improved structure of the communication schemas is based on *capabilities*, which are defined as a pair of a *quantity* and a *method* required to obtain a result for the respective quantity. Capabilities must be unique in an instance of a FINALES-based MAP and are registered in the FINALES database with their associated input and output data structures. The improved data structures used in the second implementation are composed of high-level generic structures, which are augmented with use case-specific data formats. Data structures inherent to FINALES are generic to maintain flexibility while enabling the verification of postings. The use case-specific data structures provided to FINALES configure the server for a certain study. Reconfiguration of this second set of data structures is possible without stopping and restarting the server rendering it even more flexible. Traceability is maintained by registering capabilities and tenants in the FINALES database, which keeps a history of their respective evolution. The reimplementations equips requests and results with a status field, for which a history is maintained to add traceability. [14]

The improved implementation of FINALES was demonstrated in a use case significantly more advanced than the one presented in chapter 6.1 [13] by including two instances of an optimiser working on two independent optimisation tasks. One of the optimisers aimed for maximum ionic conductivity of electrolytes and the other targeted the maximisation of the EOL of coin cells. Both optimiser instances varied the electrolyte formulation to reach their goal. The assembly and testing of coin cells required the implementation of a workflow in the MAP without violating the centralisation of the communication. For this purpose, the *Overlooking Orchestrating Tenant* (OVERLORT) was implemented, which broke down requests for e.g. cycling data of a coin cell into a request for each step necessary to obtain the requested data, which it posted to FINALES one after the other. Once all individual steps were completed, it collected all the results in a single result and posted it in response to the initial request. Since an iteration of the workflow used in this demonstration took several days to complete, the OVERLORT was designed such that it could handle several instances of the workflow in parallel. [14]

The results of the study show, that the FINALES-based MAP was able to identify the area of maximum ionic conductivity as a narrow band of LiPF_6 concentrations. A trend in the composition of the solvent was not captured, which was likely due to its less pronounced effect on the ionic conductivity compared to that of the salt concentration. The optimum ionic conductivity was observed for LiPF_6 concentrations around 1 mol kg^{-1} . The median values of the experimentally obtained EOL seem to also show a maximum at approximately 1 m LiPF_6 . However, the latter requires verification by further studies. Overall, in this publication, we demonstrated the parallel operation of several optimisers on the same infrastructure and the ability of our MAP concept to not only target the optimisation of bulk material properties but to also include the investigation of the performance in devices like the coin cells in this study. [14]

In the context of this publication, the ASAB system was equipped with the in-house assembled two electrode electrochemical cell described in chapter 4 [14]. Since leakage issues were observed during the demonstration described in chapter 6.1, vials were added to each valve to collect the liquid in case of a leakage and avoid spillage. Additionally, check valves were added to hinder the formulated electrolyte to be pressed back into the bottles containing the stock solutions. Further improvements were achieved by implementing a connection to a pressurised gas line and making use of it in an automated cleaning routine. Moreover, a new ASAB tenant was implemented to ensure compatibility with the new FINALES instance [14]. Since both optimisation tasks relied on formulated electrolytes, the ASAB tenant was associated with two capabilities, one being to provide ionic conductivity data by means of EIS and the second being to prepare electrolytes for the assembly of coin cells by means of the formulation unit. It was therefore shown in this demonstration, that the ASAB setup can serve as a tenant providing two capabilities to the MAP and it may easily be included into a workflow deploying its physical and digital outputs [14].

The remainder of this chapter shows a reprint of [14] and the corresponding Supporting Information.

Autonomous Battery Optimization by Deploying Distributed Experiments and Simulations

Monika Vogler, Simon Krarup Steensen, Francisco Fernando Ramírez, Leon Merker, Jonas Busk, Johan Martin Carlsson, Laura Hannemose Rieger, Bojing Zhang, François Liot, Giovanni Pizzi, Felix Hanke, Eibar Flores, Hamidreza Hajiyani, Stefan Fuchs, Alexey Sanin, Miran Gaberšček, Ivano Eligio Castelli, Simon Clark, Tejs Vegge, Arghya Bhowmik,* and Helge Sören Stein*

Non-trivial relationships link individual materials properties to device-level performance. Device optimization therefore calls for new automation approaches beyond the laboratory bench with tight integration of different research methods. This study demonstrates a Materials Acceleration Platform (MAP) in the field of battery research based on the problem-agnostic Fast INTention-Agnostic LEarning Server (FINALES) framework, which integrates simulations and physical experiments while leaving the active control of the hardware and software resources executing experiments or simulations with the partners running the respective units. This decentralization of control is a distinctive feature of MAPs using the FINALES framework. The connected capabilities entail the formulation and characterization of electrolytes, cell assembly and testing, early lifetime prediction, and ontology-mapped data storage provided by institutions distributed across Europe. The infrastructure is used to optimize the ionic conductivity of electrolytes and the End Of Life (EOL) of lithium-ion coin cells by varying the electrolyte formulation. Trends in ionic conductivity are rediscovered and the effect of the electrolyte formulation on the EOL is investigated. Further, the capability of this MAP to bridge diverse research modalities, scales, and institutions enabling system-level investigations under asynchronous conditions while handling concurrent workflows on the material- and system-level is shown, demonstrating true intention-agnosticism.

1. Introduction

The slow process of discovering new materials with enhanced properties, long term durability and ease of device integration is the critical bottleneck in the green transition. Automated materials discovery and optimization mark a breakthrough in this direction often captured by the general concept of a self-driving laboratory (SDL)^[1] and in a broader context as MAPs.^[2,3] This approach involves autonomous or closed-loop experimentation, integrating robotics and Artificial Intelligence (AI) to autonomously conduct, assess, and steer experiments using data analyzed through machine learning (ML). Such platforms transcend conventional lab automation by solving problems without the need for human interaction.

Conventional studies in battery research focus on the optimization of a preselected set of materials properties before finally testing the optimized

 The ORCID identification number(s) for the author(s) of this article can be found under <https://doi.org/10.1002/aenm.202403263>

[+]Present address: TUM School of Natural Sciences, Department of Chemistry, Chair of Digital Catalysis, Technical University of Munich, Lichtenbergstr. 4, 85748 Garching near Munich, Germany

[++]Present address: Munich Institute of Robotics and Machine Intelligence (MIRMI), Georg-Brauchle-Ring 60 - 62, 80992 München, Germany

[+++]Present address: Munich Data Science Institute (MDSI), Walther-von-Dyck Str. 10, 85748 Garching bei München, Germany

[Correction added on November 19, 2024, after first online publication: Affiliations has been updated.]

© 2024 The Author(s). Advanced Energy Materials published by Wiley-VCH GmbH. This is an open access article under the terms of the [Creative Commons Attribution](#) License, which permits use, distribution and reproduction in any medium, provided the original work is properly cited.

DOI: 10.1002/aenm.202403263

M. Vogler, L. Merker^{[+],[++],[+++]}, B. Zhang^{[+],[++],[+++]}, S. Fuchs, A. Sanin^{[+],[++],[+++]}

Helmholtz Institute Ulm (HIU)
Helmholtzstr. 11, 89081 Ulm, Germany

M. Vogler, H. S. Stein
TUM School of Natural Sciences

Department of Chemistry
Chair of Digital Catalysis
Technical University of Munich
Lichtenbergstr. 4, 85748 Garching near Munich, Germany
E-mail: helge.stein@tum.de

M. Vogler, H. S. Stein
Munich Institute of Robotics and Machine Intelligence (MIRMI)
Georg-Brauchle-Ring 60–62, 80992 München, Germany

M. Vogler, H. S. Stein
Munich Data Science Institute (MDSI)
Walther-von-Dyck Str. 10, 85748 Garching bei München, Germany

materials in cells. Due to the multitude of materials and interfaces in battery cells, this Edisonian one-variable-at-a-time method makes the discovery of new materials for high-performing batteries a time and resource intensive task, because the characteristics of the systems are not merely the aggregate of the components. For example, the performance and degradation resistance of a device (e.g., a battery) depend on the interplay of its constituent materials and resulting interfaces.^[4,5] Materials discovery therefore requires an optimization across all time and length scales, as well as among all involved materials. Directly targeting the optimization of the system has the potential to significantly shorten the time-to-market, while still gaining knowledge about the complex interplay between the materials and the interfaces.

Combining accelerated autonomous discovery capability with a device level perspective has very recently been introduced for opto-electronic systems,^[6] but has been out of reach for electrochemical system discovery. Electrochemical materials discovery and development is a complex, multi-pronged process spanning prediction, synthesis, characterization, and device testing processes. Related critical research tasks often hinge on the access to bespoke equipment, e.g., AI-supercomputers for generative design of new materials using foundation models,^[7] or high-fidelity synthesis and characterization equipment in large-scale facilities.^[8] Such resources often have limited and delayed access that requires peer-reviewed applications for compute resources or beamtime. Combining such infrastructure within a MAP requires a novel direction in MAP architecture in terms of distributed operation and decentralization by design. Surpassing pure acceleration^[9] and establishing reliability of discovery,^[10] such a MAP will encourage the thorough characterization and testing of full systems rather than individual materials or components. This also provides dual benefits of higher throughput

and better reproducibility by removing human error and providing improved automated documentation of experiments including negative results. The practice of publishing complete datasets from SDL operation alongside the adoption of standardized machine readable data formats, holds the promise of boosting data reusability and, consequently, further resource efficiency. By leveraging carefully designed autonomous experiments in conjunction with experiment planning algorithms, it is possible not only to reduce material usage but also enhance efficiency by minimizing downtime of the instruments.

To address the aforementioned challenges, we discuss here the versatile and ontology-linked FINALES framework capable of providing Application Programming Interface (API)-access to a distributed MAP enabling fully autonomous operation. The use of clearly defined data structures permits a unified and unambiguous communication without the need for human intervention. Since the framework passively enables the communication without actively triggering actions within the MAP, new clients (tenants) may be added without necessitating alterations in the internal processes and workflows. This agile construct leads us to expect facile scalability of MAPs based on the FINALES framework. Integrating patterns^[11] and automated analysis frameworks like the Modular and Autonomous Data Analysis Platform (MADAP)^[12] empowers even non-expert users to deploy the capabilities offered in the MAP. The link to the BattINFO^[13,14] ontology enables the datasets to be found by semantic searches while the connection to the Battery Interface Genome - Materials Acceleration Platform (BIG-MAP) Archive^[15] ensures a timely dissemination of the generated data using similar technology as the Materials Cloud Archive.^[16]

In this study, we demonstrate an internationally distributed MAP orchestrated by FINALES as shown in **Figure 1** working on two independent optimization tasks in parallel. Both optimization tasks vary the composition of a battery electrolyte composed of EC, EMC, and LiPF₆, but one targets the optimization of the ionic conductivity, while the other aims to maximize the End Of Life (EOL) of coin cells. We showcase the hierarchical acceleration in complex device level MAPs, both by intelligent sampling of the design space (here the chemical space of the electrolyte) as well as accelerating individual slow and resource-intensive tasks (here EOL testing) with ML. We further demonstrate the use of complementary methods for determining the ionic conductivity enlarging the chemical space accessible to the MAP as a whole. Moreover, we show the multi-tasking capability of our MAP by running the two optimization tasks in parallel on the same infrastructure. The setup was able to discover the correlation between the concentration of the salt and the ionic conductivity of the electrolyte and showed reasonable agreement between predicted and experimentally determined median EOL.

To perform the optimizations, the following tenants were registered in FINALES with capabilities stated in parenthesis: Autonomous Synthesis and Analysis of Battery electrolytes (ASAB) tenant (formulates electrolytes and measures ionic conductivity), Molecular Dynamics (MD) tenant (estimates ionic conductivity), Autonomous Battery Assembly System (AutoBASS) tenant (assembling coin cells), Cyclor tenant (battery cycling), Degradation model tenant (early lifetime prediction), Transportation tenant (transportation of physical samples), OVERLooking ORchestrating Tenant (OVERLORT) (workflow management),

S. K. Steensen, J. Busk, L. H. Rieger, I. E. Castelli, T. Vegge, A. Bhowmik
Department of Energy Conversion and Storage
Technical University of Denmark (DTU)
2800 Kgs., Lyngby, Denmark
E-mail: arbh@dtu.dk

F. F. Ramírez, F. Liot, G. Pizzi
Theory and Simulation of Materials (THEOS) and National Centre for
Computational Design and Discovery of Novel Materials (MARVEL)
École Polytechnique Fédérale de Lausanne (EPFL)
Lausanne CH-1015, Switzerland

J. M. Carlsson, H. Hajiyani
Dassault Systèmes Germany GmbH
Am Kabellager 11-13, D-51063 Cologne, Germany

G. Pizzi
Laboratory for Materials Simulations (LMS)
Paul Scherrer Institut (PSI)
CH-5232 Villigen PSI, Switzerland

F. Hanke
Dassault Systèmes
22 Science Park, Cambridge CB4 0FJ, UK

E. Flores, S. Clark
SINTEF Industry
Battery Technology
Trondheim 7034, Norway

M. Gaberšček
Department of Materials Chemistry
National Institute of Chemistry
Hajdrihova 19, Ljubljana 1000, Slovenia



Figure 1. The layout of the MAP centered around FINALES. The tenants involved in the workflow related to the optimization of the EOL orchestrated by the workflow management tenant OVERLORT are spanned by the turquoise arc. The communication is realized exclusively via FINALES. The flags indicate the country where the tenants were developed and located.

FINALES 2 Optimizer (F2Opt) (active learning optimizer). Additionally, the Archiving tenant (archiving results) interacted with FINALES. Further details on the tenants are provided in Section 4.

2. Results and Discussion

The study consist of two phases. In the *single-task* phase, only the tenants involved in the optimization of the ionic conductivity of the electrolytes are active. The *multi-task* phase starts with a new, empty database and includes the optimization of ionic conductivity in parallel to the optimization of the EOL with all the tenants listed in Section 4. Further details on the phases are reported in Section 4.

2.1. Ionic Conductivity and Chemical Space

Figure 2 presents the chemical space accessible to the MD and ASAB tenant including the requested formulations and the reported results. Additionally, predictions for the formulations providing maximum ionic conductivity are indicated for each of the tenants. These predictions are obtained from an optimizer model

after training it on the final data available in the database after completion of the data acquisition. The optima include a predicted global optimum (best predicted global), a predicted optimum respecting the limitations of the respective tenant (best predicted limited) and the highest mean ionic conductivity observed in the reported results (best observed). The numerical values of the identified optima are reported in Table S3 (Supporting Information). The top part of Figure 2 further shows a change of the limitations for the ASAB tenant, which was necessary because the initially included lower limit for EMC of 0.35 mol. – % (set based on the solubility limit reported by Ding, Xu, and Jow^[17]) was practically not accessible using the stock solutions chosen for this study.

The formulations with maximum ionic conductivity are found in the same band of LiPF₆ concentrations for the single-task phase and the multi-task phase, suggesting that the results and insights generated by the MAP are reproducible. The reproducibility is also evident from the value of maximum ionic conductivity, which is obtained for very similar formulations repeatedly tested in the high ionic conductivity region. Also, Figure 2 shows that the chemical space that can be explored by the MAP is significantly enlarged by using the MD tenant in addition to the ASAB tenant.

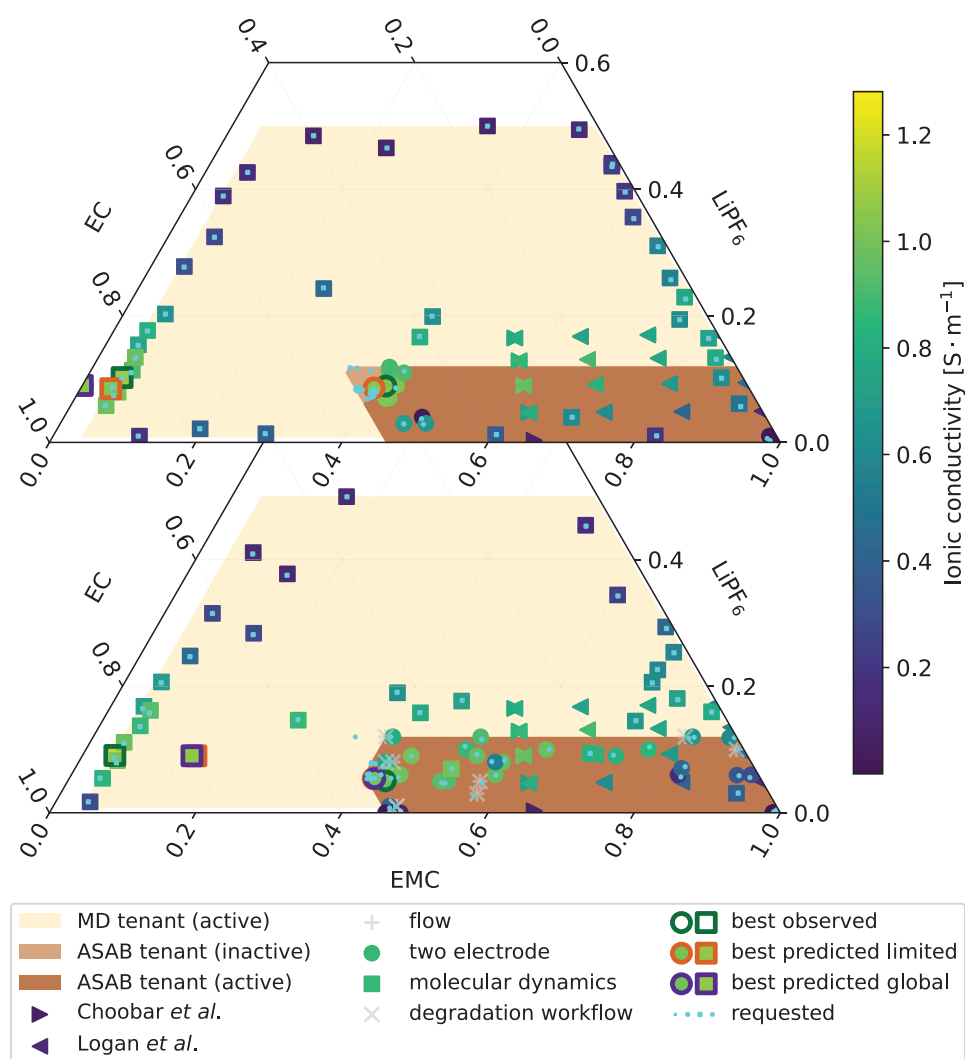


Figure 2. The chemical space accessible to the MD tenant and the ASAB tenant in the single-task phase (top) and the multi-task phase (bottom) of the study, including the formulations for which conductivity data was generated. The formulations requested in the context of the workflow associated with the EOL optimization are included, although no conductivity data are available for those samples. The coloring of the data points is based on the mean ionic conductivity. The colorbar and legend are valid for both graphs.

It also gets clear from the top part of Figure 2 that the optimizer explored more of the chemical space for the MD tenant than for the ASAB tenant. Possibly, this is due to the significantly larger region of the chemical space being accessible to the MD tenant than to the ASAB tenant. However, it also gets obvious that the optimizer requests a lot of formulations close to the edges of the chemical space of the MD tenant. This behavior likely occurs due to the model trained by the optimizer having a high uncertainty near the edges of the accessible chemical space. Regions with high predicted values and high uncertainty bear the potential for formulations with high ionic conductivity and are therefore sampled by the optimizer acquisition function. A larger number of randomly selected starting formulations (1 in the single-task phase vs 10 in the multi-task phase) seems to have resulted in a better initial model and consequently improved exploration of the chemical space in the multi-task phase of the campaign as can be seen in the bottom part of Figure 2.

2.2. Ionic Conductivity and EOL

A plot of the ionic conductivity versus the molality of LiPF_6 in the electrolyte formulation as shown in Figure 3a reveals an increasing ionic conductivity for increasing LiPF_6 concentration at low molalities. At approximately 1 m LiPF_6 , the ionic conductivity reaches a maximum at approximately 1.0 S m^{-1} prior to a decrease at higher molality. This observation matches with the behavior frequently reported in the literature.^[18–24] The data obtained from the empirical model published by Ding et al.^[18] used in this study for calibration of the conductivity measurement and simulation taking the molality of the salt, the mole fraction of EC in the solvent and the temperature into account is also shown in Figure 3a. Besides, data published by Choobar et al.^[23] and Logan et al.^[25] is presented in the graph, which is in good agreement with the data obtained from our MAP. It needs to be mentioned that the graphs shown in Figure 3a comprise averaged ionic

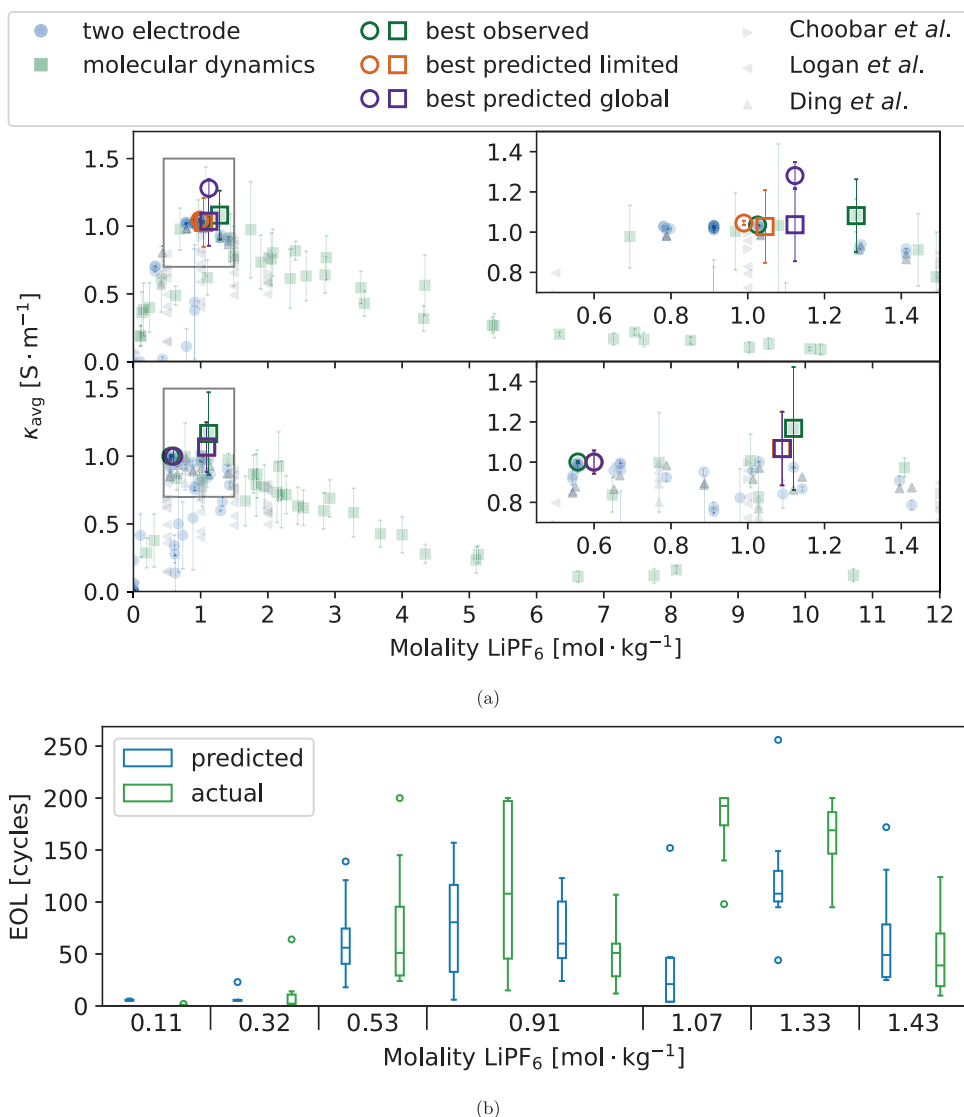


Figure 3. a) The average ionic conductivity (κ_{avg}) plotted against the molality of $LiPF_6$ as recorded during the single-task phase (top) and multi-task phase (bottom) of the campaign. Including the predicted optima globally (best predicted global) and respecting the limitations of the tenants (best predicted limited) as well as the highest observed value (best observed) for the MD and the ASAB tenant, respectively. Variations in temperature are not represented in this graph. The insets show a zoomed-in view of the region of maximum κ_{avg} . Literature data are obtained from the empirical model reported by Ding et al.^[18] and from the publications of Choobar et al.^[23] and Logan et al.^[25] b) EOL data generated in the multi-task phase of the campaign versus the molality of $LiPF_6$ in the electrolytes. Note that the composition of the solvent in the electrolyte also differs between the datapoints.

conductivity values for all the formulations, which are reported in Figure 2. Therefore, the composition of the solvent is varied besides the molality of the salt. However, the effect of changes of the salt concentration is reported to be significantly stronger than the influence of the solvent composition,^[18–20] which is also found in our data as visible in the Figures S16–S19 (Supporting Information). Variations in temperature are also not considered in Figure 3a, which is expected to cause some additional variation in the reported values for ionic conductivity. The observation of the same trend with molality in the single-task phase and the multi-task phase proves the reproducibility of the insights generated by our MAP.

Additional to the ionic conductivity, the EOL is investigated in the multi-task phase of the campaign. A second instance of the optimizer performs this fully independent optimization task on the same hardware and software infrastructure on which the single-task phase optimization was run previously. Since the early lifetime predictions require a complex, multi-step workflow involving hardware and software operations, the OVERLORT tenant is demonstrated to handle this workflow. The optimization of the EOL was started on 13th of November, 2023.

In the typical mode of operation, requests are posted by the optimizer. To investigate whether an electrolyte formulation optimized for ionic conductivity also yields an optimized EOL,

additional requests are manually posted to FINALES during the multi-task phase. These manually posted requests include the formulation optimized for ionic conductivity and two non-optimized formulations as identified in the single-task phase. It must be noted that the predicted optimized formulations used for the manual requests in the multi-task phase differ from the optimized formulations reported in Figure 2 and Table S3 (Supporting Information), since the model is retrained after each iteration and therefore the predictions based on a model trained later differ from earlier models. The electrolyte formulations included in the manually posted requests are reported in Table S4 (Supporting Information).

As shown in Figure 3b, the median EOL appears to show a slight trend toward higher values for increasing molality of the electrolyte formulation. Considering the distribution of the EOL data within and in between the batches, this trend does not persist due to the strong overlap of the distributions. The maximum experimentally determined median EOL is observed for 1.07 m LiPF₆.

From the comparison between Figure 3a and 3b higher ionic conductivity as well as median EOL are observed for increasing molality of LiPF₆ until 1 m LiPF₆ is reached. Further increasing molality is found to decrease both quantities. The data generated in this study suggest an agreement between the two optima around 1 m LiPF₆. Further investigation is, however, needed to validate this observation.

3. Conclusion

In this study, we demonstrated that an internationally distributed MAP based on the FINALES framework and composed of several software and hardware tenants can run two distinct optimization tasks while seamlessly integrating computational and experimental capabilities and bridging the gap between the material and system scales. The MAP was shown to reproducibly identify regions of high ionic conductivity within an electrolyte system composed of LiPF₆, EC, and EMC. Computational and experimental tenants connected to FINALES complemented each other, widening the chemical space accessible to the MAP as a whole. Furthermore, the communication of limitations for individual tenants, and the extensive use of identifiers and timestamps, allowed for improved data management and traceability in comparison to the previous version of FINALES.^[3]

The demonstrated MAP achieved a high degree of automation. The only manual tasks left during the operation of this MAP were the physical transport of electrolytes and cells between the experimental setups, maintenance tasks like restocking of consumables, and periodically monitoring the MAP and in case (re)starting of tenants. In the post-processing of the data, the mapping to the ontology and the upload of the mapping file alongside additional raw data, which was not posted to FINALES, were done manually. All other tasks related to the research campaign ran fully automated minimizing the need for human intervention.

Our study demonstrated ML acceleration of the electrolyte optimization and the cycling task by early prediction of the EOL. This shows that in MAPs centered around FINALES, the overall optimization task as well as the tasks of individual tenants can be accelerated using ML. Besides, this study demonstrated the

ability of our MAP to handle tenants with significantly different rates of data generation. To accommodate these differences, it is inevitable to allow each tenant to operate at its own schedule in an asynchronous fashion. Marking requests as reserved once they are processed enables a distribution of the tasks among faster and slower tenants providing the same quantity. The modular design of the FINALES-based MAP leads us to expect seamless connection of new tenants and, hence, scalability to larger MAPs. We anticipate that the multi-modal and multi-fidelity nature of the data generated in such MAPs benefits the robustness of models trained with the data. Future studies deploying our MAP concept will additionally benefit from the possibility to prepopulate a database with selected existing data. This is powered by FINALES accepting unsolicited results which do not reference to a request. Starting from existing data will reduce the need for initial random experiments and therefore accelerate optimization tasks.

We are convinced that this robust demonstration of an operating, distributed MAP centered around a passive brokering server with mostly *intention-agnostic* tenants proves our approach to be valid even for complex optimizations. Future optimization tasks for MAPs powered by FINALES will therefore encompass multi-objective optimizations requiring the identification of Pareto-optimal solutions. These approaches shall continue following the scale-bridging approach presented in this study by integrating tenants operating at different scales and post-mortem analysis technologies. Since FINALES is designed to impose only a minimum entry barrier for new tenants to join the MAP, it enables the generation of comprehensive yet consistently formatted datasets containing information about various materials and device properties, possibly even including variations of process parameters. Due to the standardized data structures, the obtained results can be analyzed to foster a profound understanding of effects across scales.

Although not yet demonstrated, the limitations included in the FINALES schemas could be used in the future to accommodate information regarding the accuracy and the approximate time required to generate a result of the tenants. This would allow for multi-fidelity optimizations, because requests could then be created such that they either request fast or more accurate results.

The further development of the schemas and their handling in FINALES could deal with enabling FINALES to enforce the tenants to provide certain limitations like e.g., information regarding the expected uncertainty of their results. It might be desired to accompany this by an enforced harmonization of uncertainty and quality metrics among tenants providing the same or similar capabilities. Since this study also included significant efforts in designing and developing tenants, we expect a further acceleration of data generation once more mature tenants are available.

4. Experimental Section

FINALES Brokering Framework: The FINALES architecture encompasses a server framework designed to provide communication protocols and access to a database to affiliated clients, referred to as *tenants*. Moreover, it hosts a centralized queue for task requests enabling the tenants to pull new tasks for processing and subsequently post the results. The tasks in this queue are presented in the order in which the requests were posted. A tenant may however implement a selection algorithm defining the next request to be processed. This allows tenants to deviate from the

first-come first-serve principle. Interactions with FINALES are possible via a web server interface through the implementation of the HTTP REST API protocol. The backend offers a well-structured relational database, where all incoming requests and results are stored. Alongside the scientific data, details about connected tenants as well as information about the quantities and methods available from the MAP are saved. Further, the database holds information about the data provenance and a history of the status of tenants, methods, quantities, requests and results. *Quantities* in the sense of the FINALES framework may be measurable quantities, but can also refer to a service like e.g., the transportation of a sample. The term *method* refers to a means of providing a value for a quantity, which may be an experimental or computational procedure. Since only combinations of quantities and methods are required to be unique in the FINALES setup, this combination is referred to as a *capability*. Tenants are therefore clients that provide one or more capabilities in the MAP. This means, they regularly call the server for requests related to their associated quantity and, after applying a computational or experimental method, return a result for that quantity. FINALES does not restrict its tenants regarding their source of data or the type of their method. Experimental setups and laboratories run by humans as well as data-driven models or physics-based simulations are accepted as tenants.

The modular approach of the framework allows for facile registration of new tenants while explicitly allowing for several tenants offering the same capabilities. We refer to this concept as *multitenancy*. FINALES enables modularity and diversity of the tenants by not actively triggering actions in the MAP, but passively providing access to the data to all the tenants. Since tenants pull requests for capabilities that they can serve from FINALES, the MAP operates asynchronously and each tenant may process the requests at its own schedule. This permits multi-task operation of the MAP with several optimizers sending requests related to their respective and potentially independent tasks. Depending on the degree of automation of the tenant, a MAP based on FINALES can operate fully autonomously exceeding the limitations of a single laboratory or institution. Furthermore, the modularity of MAPs based on FINALES provides the prerequisite for its adaptability to different research tasks and configurations of the MAP. Since the data structures internal to FINALES are designed as generic as possible, the adaption to a new study can easily be done by providing study-specific schemas for the capabilities and tenants. These new schemas can then be registered defining the potential of the MAP. The adaption of an existing MAP can be achieved in a similar way except that currently registered versions of affected schemas need to be deregistered first. Since changes in hardware or software configurations are mostly accompanied by changes in the limitations of a tenant, a re-registration of tenants with altered limitations serves as a means of accounting for changes in the setup of the MAP. As the JavaScript Object Notation (JSON) file containing the definition of a tenant required for its (re-)registration as well as the schemas associated with the capabilities are no internal part of the FINALES framework and they can be added, altered and removed by the FINALES administrator while FINALES is running, our framework provides full flexibility toward changes in the subject of a research campaign or alterations of tenant configurations. Moreover, optimization algorithms are connected to FINALES as tenants, which allows to easily switch to another algorithm or a different configuration by replacing or adding an optimizer tenant.

The communication within the MAP is based on JSON schemas, which are registered with FINALES and allow for the validation of submitted data structures. The overall schema design is developed to be problem-agnostic, allowing it to accommodate several capabilities, going beyond the specific implementation relevant for the optimization of electrolyte formulations that we demonstrate in this study. The flexibility of the design as described above allows for its application in various areas of research and for the optimization and discovery of diverse materials and systems. While different applications will require the development of tenants covering the requirements in the specific field, the functionalities of the FINALES framework itself are universally applicable. The JSON schemas developed for this study are detailed in Section 4.

In a typical iteration of an optimization task, an optimizer tenant posts a request for a certain quantity. Requests must specify only one quantity but may include a list of acceptable methods. According to the multitenancy

approach, several tenants may therefore be allowed to serve the request. This enables an improved use of instruments and resources as the earliest available tenant will process a request accepting its method. However, this requires the tenants to mark the request as *reserved* prior to start processing it, to hinder other tenants from picking up the same request. Once a tenant picked up the request and marked it as *reserved*, the relevant method of the tenant is executed and the results are posted to FINALES after formatting them according to the applicable output schema. An optimizer tenant may subsequently check for new results and generate a follow-up request starting the next iteration.

An earlier proof of concept (PoC) version of the framework^[3] demonstrated the basic concept of this MAP design. The present study utilizes a new implementation of the concept, and applies it to an optimization of a battery electrolyte system including the simultaneous operation of two optimizer instances. The completely redesigned framework has significantly updated communication schemas. The data structures implemented in the latest version of FINALES presented here are well defined but sufficiently generic to accommodate a variety of results for different quantities provided by diverse methods. These generic data structures are enhanced by external schemas, which are more specific to the use case of the FINALES instance. The specific schemas can be applied to the MAP by a human administrator, who registers them with FINALES and thus makes them binding for data related to the affected quantity and method. This composite design of the schemas significantly enhances the flexibility of the FINALES framework compared to the previous version, which based the communication on a single set of data structures. Outcomes from the earlier PoC implementation of FINALES^[3] helped us identify the improvements needed during our reimplementation of the code. We incorporated, among other improvements, a more robust database design, enhanced scalability, and implementation of generic rigid schemas for registration and communication. The changes make the new implementation of FINALES configurable with respect to the used schemas, which even allows for hot-swaps. Compared to the previous version this is a significant improvement as it externalizes the usecase-specific aspects from the framework, rendering it more universal. Additionally, the ubiquitous use of timestamps and Universally Unique Identifiers (UUIDs) in the new implementation improves the traceability of data and events in the MAP.

The repository with the source code of the redesigned FINALES framework can be found at <https://github.com/BIG-MAP/FINALES2> and the version 1.1.0 of the FINALES code used in this study is available at <https://doi.org/10.5281/zenodo.10987727>.

Database Design: The Python-based backend of FINALES deploys a relational database for data storage, whose design is visualized in Figure 4. The code is currently set up with the SQLite^[26] database engine, with all database interactions performed via SQLAlchemy.^[27] Utilizing SQLAlchemy allows for future deployments of the server using any of the alternative supported engines such as PostgreSQL (<https://www.postgresql.org/>), MySQL (<https://www.mysql.com/>), etc.

The database tables `quantity`, `tenant`, `request`, `result`, `link_quantity_request`, `link_quantity_result`, `status_log_request` and `status_log_result` depicted in Figure 4 all have a `uuid` column as a primary key, and `load_time` column time-stamping when the row is first appended to the table. This design, along with a backend logger, ensures traceability and reproducibility, which facilitates an exact tracing of the sequence of operations performed in the MAP at any point in time. The tables adhere to an append-only design, with only a few exceptions controlled through UPDATE interactions, e.g., for fields defining whether specific quantity and tenant entries are currently active in the MAP. A small expansion of the database schema allowing for a strict append-only design can be found in Figure S1 (Supporting Information), which will be implemented in the release of version 2.0.0. The database tables also include columns called `cost` and `budget` prepared to be used in studies involving partners being funded by different projects or institutions or subject to limitations regarding other resources, which shall be considered. The use of this field is not yet implemented in the current version of the API, but its implementation will be part of the future development. Users of FINALES are, however,

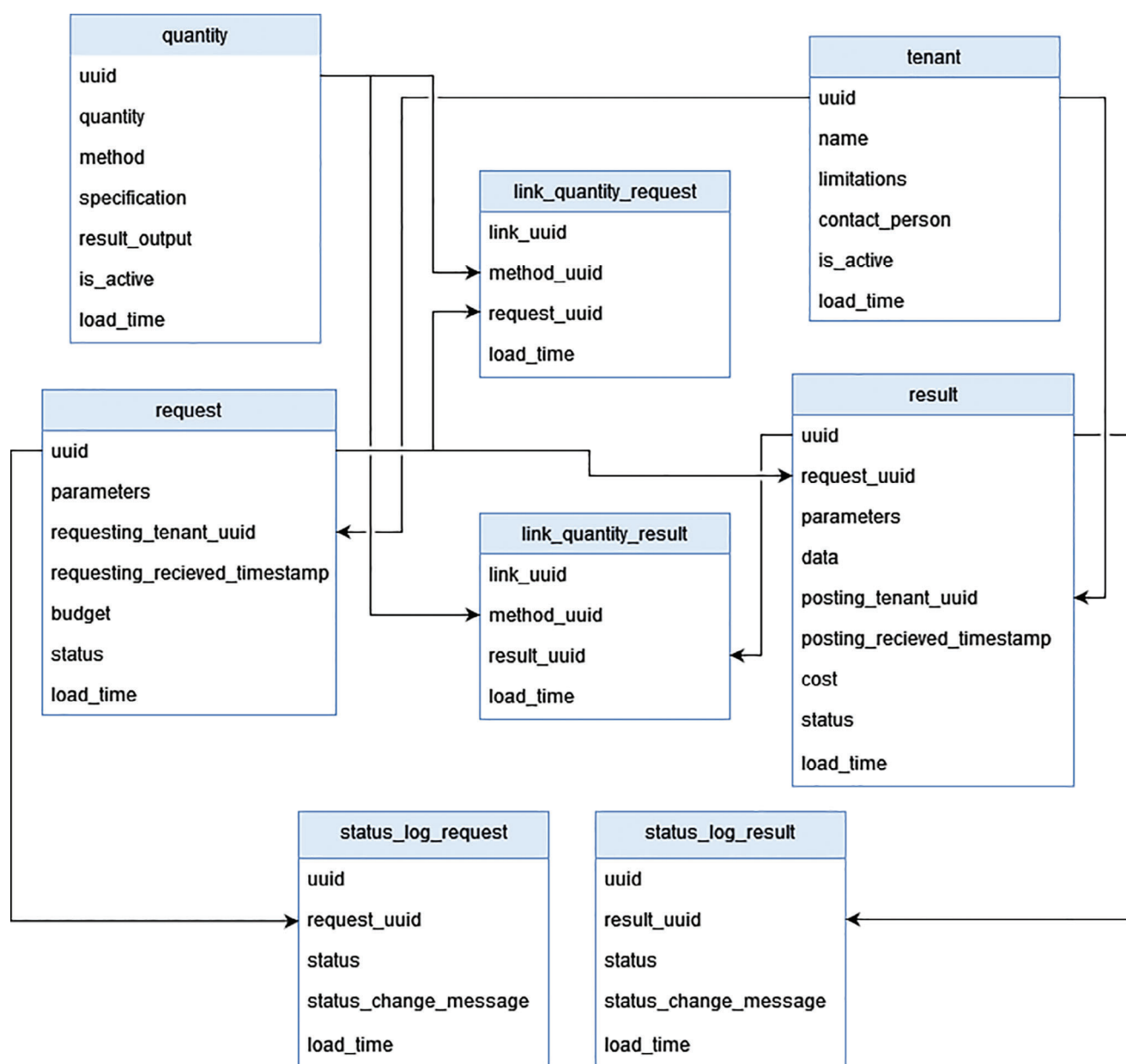


Figure 4. Database schema designed and implemented for FINALES. Arrows indicate table relationships with the direction defining the origin of the primary key mapped to a table as a foreign key. Besides this schema, a separate single table database is used for user credentials.

already now able to consider budget and cost in their studies by including them as fields in the schemas.

FINALES is designed to be easily installable in any computer and to be self-contained, so that a new independent installation (with its own independent database and secure access credentials for the tenants) can be used for a given campaign, thus preventing any risk of unwanted data leak and keeping different MAP studies fully independent. We call each installation a FINALES *instance*. Once capabilities and tenants are registered in an instance of FINALES, the tenants can communicate to the server through the web API endpoints. The Python framework FastAPI^[28] is utilized for constructing the RESTful API. In total, 17 endpoints are exposed to the tenants of which one handles the necessary user authentication protecting the other 16 endpoints. Several of the endpoints are however suited only for functionalities related to an optimizer and archiving tenant. A comprehensive explanation of all the API endpoints can be found in Section S1.2

(Supporting Information). The most relevant endpoints for an experimental or computational tenant are `pending_requests/` for retrieving the currently pending requests, `requests/object_id/update_status/` e.g., for changing the status of a request to `reserved` when it has been picked up by a tenant and `results/` for posting results based on a specific request. We stress that the exact parameters in the requests might not be directly applicable to a given tenant implementation. For example, in this study, the electrolyte formulation used in MD simulations may necessitate rounding ratios to achieve an integer number of molecules, resulting in slight deviations from the original formulation. An important design aspect is therefore that the parameters reported in requests and results are allowed to differ, and both are stored in the server.

A core design challenge is the need for the server to provide a rigid framework for brokering information, while remaining flexible to

unforeseen circumstances. The proposed solution is to allow the status of requests and results to be changed through endpoints. This accounts for scenarios such as a tenant not being able to fulfill a request, or e.g., leakage of a solution is discovered in an experimental setup after posting results, making the results unreliable. An additional embedded feature allows for prepopulating a database with previously generated results, which enables the deployment of an optimizer with initial training data for the specific optimization.

Schemas: The JSON schemas used to define the various quantities and methods involved in this study are available on GitHub with the URL https://github.com/BIG-MAP/FINALES2_schemas. Together with the data, most of the tenants also provide metadata, such as a success field reporting whether the method was executed successfully, and a rating providing information about the data quality as judged by the tenant generating the data on a scale from 1 (low quality) to 5 (high quality). An example for a definition of a quality rating is reported in the Section S1.3 (Supporting Information). These `success` and `rating` fields can be used by intention-aware tenants like optimizers to filter out unsuitable data. In this study, the instances of the optimizer were configured to only consider results with `success == True` and `rating >= 3`, if a rating is available. All entries, which do not fulfill either of these requirements or are marked as `deleted` in their status are considered invalid and therefore disregarded by the optimizer instances. Further metadata may include process parameters, laboratory or software environments or any other available parameters deemed relevant. Currently, the operators and developers of tenants are in charge of identifying the metadata, which they can provide considering technical limitations as well as confidentiality requirements.

The schemas also allow for the limitations of a tenant to be communicated in the `limitations` field. This field can be used to communicate the parameter space that a tenant in its current configuration can cover. At the same time, the limitations can also be used to provide information about the uncertainty and fidelity of the results provided by a tenant. The presence of a certain kind of limitation is currently not enforced by FINALES. However, the information about the limitations is included in the JSON file that needs to be provided to the administrator of the MAP when requesting the registration of a tenant. This gives the human administrator the chance to ensure the presence of certain information in the limitations or any other field in the definition of a tenant by inspection of the JSON file.

Tenants: As mentioned earlier, a tenant is a client connected to FINALES, which may be purely software-based, hardware or even a human researcher performing tasks. The tenants used in this study are described in the following subsections.

Optimizer Tenant (F2Opt): The Optimizer tenant F2Opt is a software tenant implementing a Bayesian optimization (BO) procedure. The role and responsibility of F2Opt in the MAP is to request new results from the data-producing methods available in the MAP, with the aim to optimize some predefined objective(s). In general, F2Opt is configured to iteratively consume previously reported results from the FINALES database, use the data to train a machine learning model, and apply a BO procedure to propose new electrolyte formulations which are then included in new requests submitted to FINALES. The specific optimization task, including what data to consume and which quantities to optimize, is specified in a configuration file and multiple configurations of F2Opt can be deployed in parallel to accommodate the specific objectives of the MAP. In this work, we deployed two instances of F2Opt configured to optimize conductivity (the OCond configuration) and EOL (the OEOL configuration), respectively.

To fully utilize the capabilities of the MAP, the optimizer tenant must be capable of considering measurements of different fidelity and from different data producing methods, including simulations and experiments. In general, data from different sources can have different noise and bias as well as different associated cost of evaluation which need to be considered. Additionally, it can be beneficial to co-optimize multiple objectives at the same time. Therefore, the optimizer tenant should be capable of multi-source multi-objective optimization to enable a diverse set of optimization tasks in the MAP. To meet these requirements, the BO procedure implemented in the F2Opt tenant applies a Gaussian process (GP) regression model, which is a smooth and highly flexible model that provides uncertainty estimates and can accommodate small datasets, which is of-

ten the starting point in optimization tasks. These properties make GPs a popular choice of model in BO. To handle data from multiple sources, we consider a multi-task GP^[29] and treat each data source as a separate output. This allows for separate predictions for each data source while utilizing correlations between data sources to improve the predictions.^[30] An acquisition function is then applied to propose new promising electrolyte formulations. In particular the widely used Expected Improvement (EI) function is used. Although not used in this work, multi-objective optimization can be achieved by transforming multiple objectives into a single objective with a scalarizing function,^[31] which can then be optimized using standard acquisition functions. Additionally, the optimizer can be configured to initially sample a number of random points before switching to the BO procedure when no initial data are available to fit a model. The implementation of F2Opt used in this demonstration does not consider cost or any hierarchy among the tenants with respect to their accuracy or speed. In our demonstration, these aspects are not considered, because the cost is more relevant for larger MAPs including tenants from different projects and the demonstration is aimed toward the joint use of simulated and experimental data rather than exploiting differences in the rate of data generation. The F2Opt code was developed in Python using the Pandas,^[32] PyTorch,^[33] and GPyTorch^[34] packages and is available online: <https://github.com/BIG-MAP/F2Opt>. The tenant was developed and situated in Denmark.

Molecular Dynamics (MD) Tenant: The Molecular Dynamics (MD) tenant for calculating lithium ion conductivity is using MD and it is implemented in BIOVIA Pipeline Pilot (BPP).^[35] The tenant is registered in FINALES as the `3DS_tenant` for the quantity conductivity and the method `molecular_dynamics`. A high-level outline of the workflow for the MD simulation tenant is shown in Figure S2a (Supporting Information). The workflow for the MD simulation tenant parses the requests from the optimizer tenant to convert the requested electrolyte formulation into an atomistic 3D model of the electrolyte. The molecular structure of each ingredient in the request is described by SMILES and the fractional concentrations are converted into integer numbers of molecules. The restriction to use complete molecules can lead to small differences to the real-valued concentrations requested by the optimizer. The simulation tenant handles up to a few hundred molecules, which places a lower limit on the concentration of each individual ingredient at 0.5 mol.-%. A physical limitation is that the lithium ions start to cluster and become immobile at high salt concentrations, which places an upper limit on the salt concentration around 50 mol.-%. However, this restriction is not significant as we are focused on solutions with high lithium ion mobility. The tenant creates 5 randomly generated amorphous cells for each formulation. These supercells of the type shown in Figure S2b (Supporting Information) are the starting points for a sequence of MD simulations^[36] using the COMPASSIII force field.^[37] The density is equilibrated in two steps by MD in the NVT ensemble (constant volume, temperature and number of molecules) with the velocity scale thermostat for 200 ps and NPT ensemble (constant pressure, temperature and number of molecules) for 200 ps using the Nose–Hoover–Langevin (NHL) thermostat^[38] and the Andersen barostat.^[39] The production run is performed by MD in the NVE ensemble (constant volume, total energy and number of molecules) for 2.5 ns. Diffusion coefficients are derived by an analysis of the mean square displacement via the Einstein relation. The conductivity is extracted using the Nernst–Einstein equation.^[40] Finally ionic conductivities, alongside the corresponding densities and temperatures for all five configurations, are collected and posted to FINALES. More details about the MD tenant are provided (Supporting Information). The tenant was developed collaboratively by developers situated in Germany and England and the calculations were prompted from Germany to a server based in England.

ASAB Tenant: The ASAB system serves as an experimental tenant providing the capability to formulate electrolytes and measure their ionic conductivity using a two electrode symmetric electrochemical cell. In FINALES it is registered with the quantities conductivity and electrolyte with the methods `two_electrode` and `flow`, respectively. The in-house developed electrochemical cell is made up from a polytetrafluoroethylene (PTFE) body equipped with two oppositely positioned stainless steel screws with sanded surfaces serving as the parallel

electrodes. The cell was calibrated using the results of repeated measurements of 1 M LiPF₆ in EC and EMC (EC:EMC 3:7 by weight) combined with data obtained from the empirical model reported by Ding et al.^[18] Electrochemical Impedance Spectroscopy (EIS) measurements are controlled by a PalmSens4 potentiostat (PalmSens B.V., Houten, Netherlands) and the data are automatically analyzed using the MADAP^[12] version 1.1.0. The six syringe pump modules and ten eleven-port rotary valve modules (Cetoni GmbH, Korbussen, Germany) integrated into the ASAB hardware are used to formulate electrolytes starting from stock solutions. Since the optimizer requests formulations in mole fractions, while ASAB doses the stock solutions in volume fractions, the specifications of the formulations need to be transformed. The resulting formulations may only be approximations of the requested one, which is why the ASAB tenant reports the mole fractions obtained from the transformed formulations rounded to two decimals together with the corresponding ionic conductivity results. The hardware of the system is operated inside a nitrogen-filled glovebox. Due to a lack of active temperature control inside the glovebox, the temperature is read manually from time to time and entered in a configuration file, from where it is loaded by the ASAB tenant and reported to FINALES together with the ionic conductivity results.

Details regarding the calibration procedure, the hardware setup, and the mode of operation of the ASAB tenant can be found in Section S2.2 (Supporting Information). The tenant was developed and situated in Germany.

AutoBASS Tenant: The AutoBASS^[41] is a modular automatic coin cell assembly system. Devices connected to this system comprise three six-axis robotic arms (Mecademic meca500 rev.3), a precision linear rail (Jenny Science Linax LXS 1800), a digital coin cell crimping machine (MTI MSK-160E, China), two cameras, and a 200 µL dispensing module (Sartorius rLine). The system has the capability to assemble CR2032 coin cells within a nitrogen-filled glovebox using lithium-nickel-oxide (LNO) cathodes with an areal capacity of 1 mAh/cm² coated on an aluminum current collector, graphite anodes with an areal capacity of 1 mAh/cm² coated on copper foil and the electrolytes formulated by the ASAB tenant. In the scope of the BIG-MAP project, cathode sheets were provided by BASF SE, Germany and the anode sheets were contributed by CIDETEC, Spain. The cathodes used are 14 mm in diameter, the diameter of the anodes is 15 mm and the 25 µm thick Celgard 2325 separator has a diameter of 16 mm. The AutoBASS tenant is registered with FINALES for the quantity `cell_assembly` and the method `autobass_assembly`.

The assembly process is carried out by orchestrated actions performed by the above-mentioned devices, including pick-and-place of cell components, image recognition for the auto-correction of the placement, dispensing of electrolyte, transfer, crimping and placement in the storage holder. Tracking of the process is realized by collecting visual information regarding the placement of components using an integrated camera, which is part of the data generated by AutoBASS. The tenant of AutoBASS is structured based on the reference tenant of FINALES, which is integrated into the interface of the local system. The limitations of the tenant are currently specified in terms of the maximum number of cells and the feasible battery chemistry.

Details regarding the AutoBASS tenant can be found in Section S2.3. The tenant was developed and situated in Germany.

Cycler Tenant: The Cycler tenant and the corresponding data analysis service are build up based on an already existing system of FastAPI^[28] servers. The implementation makes use of some features of the manufacturer's software, whereas the analysis is implemented in-house. The tenant is capable of processing reservation requests for cycling channels and handling the tests including the creation of a protocol, start and stop of the test, logging of errors, exporting and saving the data as well as performing selected analyses. To fulfill its tasks, it is registered in FINALES with the quantities `cycling_channel` and `capacity` with the corresponding methods `service` and `cycling`. The cycler saves the status, errors, parameters and the request of each individual channel in a JSON document and consequently is resistant to planned and unexpected stops. The tenant performs an intermediate export of the capacity trajectories after the duration estimated for at least 40 cycles elapsed. The exported data are subsequently processed by the analysis functionality and posted to FI-

NALES. The experiments continue and are stopped once 200 cycles are finished. A final export is triggered after the estimated time required for 200 cycles elapsed. Since the optimization of the EOL is based on the predicted EOL, the data obtained from the final export is not posted to FINALES, but stored locally. Details regarding the Cycler tenant can be found in Section S2.4 (Supporting Information). The tenant was developed and situated in Germany.

Degradation Model Tenant: The Degradation model tenant is a purely software-based tenant. It takes data from the first cycles of a cell as the input and outputs a prediction over the capacity trajectory and subsequent EOL along with the associated uncertainty early in the lifetime. It is therefore registered with FINALES as the `EOL_tenant` for the quantity `degradationEOL` and the method `degradation_model`. The underlying machine learning model, a Long Short-Term Memory (LSTM) neural network is based on previous work by Rieger et al.^[42] The tenant receives the capacity trajectory of at least the first 40 cycles along with the overpotential difference between the 10th and 40th cycle, the Coulombic efficiency, and the variance between charge and discharge capacities.^[43] Based on this input the model predicts the complete cell trajectory. The EOL is calculated as the point at which the cell capacity goes below 80 % of the initial capacity. To capture uncertainty, we use an ensemble of five models and extend the LSTM architecture to predict the variance of the output along with the mean. If the cell chemistry and format from which training data are obtained differ from the production data, the model predictions can become unreliable. Mitigating this risk, the model is trained with a dataset of 44 cells obtained from reference^[44] after filtering out outliers. This data was generated using the same cell type, hardware, and cycling protocol as the Cycler tenant. The uncertainty output gives an indication of the prediction accuracy. The code for this tenant was developed in PyTorch^[33] and is available online: https://github.com/BIG-MAP/eol_degradation_tenant. The tenant was developed and situated in Denmark.

Transportation Tenant: The Transportation tenant deals with the transport of physical samples between devices. In this study, electrolytes and coin cells need to be transported between different setups. The transport itself is done manually, but the Transportation tenant handles the communication with FINALES. It is set up as a chat service and registered in the FINALES database with the quantity `transport` and the method `transport_service`. Once it picks up a request from FINALES, it broadcasts the information regarding the physical location of the sample and the requested destination to the clients registered with the internal chat service. The humans monitoring the chat perform the transport and confirm it by a short, predefined chat message, which triggers the tenant to post a successful response to FINALES. The tenant was developed and situated in Germany.

OVERLORT: The OVERLORT is a purely software-based workflow tenant to enable requests for predicted EOL. In this study, the OVERLORT connects the hardware tenants of ASAB, AutoBASS and the Cycler, as well as the software-based Transportation and Degradation model tenants in a workflow. In FINALES, it is associated with the quantity `degradationEOL` and the method `degradation_workflow`. The limitations of the ASAB, AutoBASS, Cycler and Degradation model tenants determine its accessible parameter space. Details regarding the OVERLORT tenant can be found in Section S2.4 (Supporting Information). The tenant was developed and situated in Germany.

Archiving Tenant: The Archiving tenant is a command-line client capable of fetching data from FINALES and submitting the retrieved data to the API offered by the BIG-MAP Archive data repository.^[15] Since this tenant does not report results to FINALES and acts in the background, it is not registered as a tenant in the FINALES database, but is granted access to the data by specific credentials. It serves two specific purposes: 1) preventing data loss in the event of potential corruption of the FINALES database and 2) promptly disseminating results of calculations and experiments shortly after their submission to the server, to a broader consortium of researchers (in this case, the BIG-MAP project members). The archiving is executed periodically by means of a "cron" job scheduler. The tenant is optimized for efficient use of storage space and minimal upload time, by linking unchanged files between versions of the same entry, and only creating one new entry per campaign. Details regarding the Archiving

tenant can be found in Section S2.6 (Supporting Information). Overall the defined data structures and archiving tenant (including the ontological mapping) conform FINALES with the data management plan developed for the BIG-MAP project.^[45] The archiving tenant was developed and situated in Switzerland, with the following ontological mapping developed in collaboration between researchers based in Norway and Denmark.

The communication among tenants relies on the compliance to the commonly agreed exchange syntax underlying the structure of the requests and results posted for each method. As the number of tenants grows and their functions diversify, the data they exchange becomes structurally complex and susceptible to ambiguities. JSON keys might repeat but refer to different concepts depending on their location in the schema. E.g., *temperature* within a conductivity measurement might mean the internal temperature of an electrolyte solution, surface temperature of the cell, ambient temperature for the chamber, etc. In addition to ambiguity, the data exchanged by tenants might not be readily accessible. The exchange schemas are designed to support communication between tenants, but such flexibility comes at the expense of syntactic complexity. For instance, retrieving a conductivity result requires knowing the full data structure (albeit this can be retrieved and investigated directly from FINALES) to locate the relevant fields and values.

A remedy to ambiguity and accessibility is mapping data to controlled vocabularies of concepts. Such mapping effectively upgrades a syntactic data model into a semantic data model, where data fields are attributed an unambiguous meaning. As a *temperature* key in the schema is mapped to the concept of *SurfaceTemperature* in a controlled vocabulary, the intended meaning of the field becomes explicit and distinct to, e.g., *SampleTemperature*. Moreover, the association between a measurement (uniquely identified with a UUID), a vocabulary concept (e.g., Schema.org concept *dateCreated*), and a value (e.g., 2024-02-16) can be represented as a Node-Edge-Node connection in a network. Representing results as these *Triples*^[46] in a Graph Database makes data accessible irrespective of how it is syntactically encoded in the data model.

Identifiers should ideally be unique and resolve to a web resource that offers more information about the entity. For instance, the concept of Electrolyte is uniquely identified with an Internationalized Resource Identifier (IRI)^[47] that resolves in a web browser to a description of the concept: https://w3id.org/emmo/domain/electrochemistry#electrochemistry_fb0d9eef_92af_4628_8814_e065ca255d59. If the identifier cannot be resolved, we attempt using URL prefixes that resolve to some general information about the object. The implementation will facilitate search in a knowledge base. The ultimate purpose of this implementation is to make FINALES results available in a graph database that can be flexibly queried using structured languages, such as SPARQL^[48] or CYPHER.^[49]

To enrich the data with semantically well-defined concepts, we employ the recently developed ontology Battery Interface Ontology (BattINFO). BattINFO describes thousands of concepts related to electrochemistry and batteries. Concepts are linked to each other adhering to logically consistent relationships, thus rendering meaning machine-readable.^[13] The connections among data and concepts must be encoded using a standard method. In this work, JSON for Linked Data (JSON-LD) is used to link the results from the conductivity and EOL tasks to ontology concepts in BattINFO and Schema.org. BattINFO describes measurement fields related to batteries and electrochemistry, while the Schema.org vocabulary describes tenant metadata, software resources and other non-electrochemical concepts. For example, we enrich the descriptions of the request/result posting tenant with the ORCID of the responsible person linked to the <https://schema.org/author> schema:author type, and ROR-ID for the organization linked to <https://schema.org/creator> schema:creator type. These choices improve data consistency, since they avoid reliance on other identifiers (such as email addresses) that are subject to change. EOL and conductivity results in this study are all expressed in JSON-LD files mapped to ontology concepts. Details and an example of the semantic implementation of experimental results can be found in Section S2.6 (Supporting Information). Development of the knowledge graph representation of the data was done subsequently to the data collection. The graphs were therefore uploaded to the archive entries after the optimization phases had been completed.

The Structure of this Study: The campaign presented here comprises two optimization tasks with separate objectives. The first task is to identify an electrolyte formulation with maximum ionic conductivity by using data generated from experiments and simulations. As for the second task, the objective is to find an electrolyte formulation that maximizes the EOL of coin cells. Each of these tasks is associated with a separate instance and configuration of the F2Opt tenant, OCond and OEOL. We show, that the two optimizers can operate on the same MAP through a common FINALES instance, while pursuing fully independent tasks.

The tenants involved in the *single-task phase* are the optimizer (OCond), the MD tenant, the ASAB tenant, and the Archiving tenant. This phase is also used to confirm the limitations set for these tenants or adjust them, if needed. In the *multi-task phase*, a request with the conductivity-optimized formulation, as well as two non-optimized formulations identified from the results obtained in the single-task phase of the campaign are manually submitted to FINALES to investigate potential differences in the cycling performance. The electrolyte system chosen for this study is composed of LiPF₆ dissolved in EC and EMC, because this is a well-investigated electrolyte system for which references are available.^[12,18,20,23–25]

Single-Task Phase—Ionic Conductivity Only: The single-task phase of the campaign was run from the 26th of September 2023 to the 28th of October 2023. It included the ASAB tenant and MD tenant, which posted its first result 8 days after the first result was posted by the ASAB tenant.

After the end of the single-task phase, a total of 81 entries are stored in the FINALES database. 12 of these entries are invalid. 72 of the total entries have a quality rating of 4 or 5. Only 3 entries have a rating of 3, while 6 have a rating of 2. In total, 69 entries in the database are valid according to the requirements regarding the status and the rating configured in the OCond optimizer.

Multi-Task Phase—Ionic Conductivity and End-of-Life: The multi-task phase of the campaign included the optimization of the EOL and the ionic conductivity in parallel. The MD tenant and the ASAB tenant started their contribution of results to the database approximately 5 h apart, which is significantly shorter than 8 d in the single-task phase. Both optimizer instances, OCond and OEOL, were running at the same time, concurrently posting requests for their respective task. The multi-task phase was started on the 6th of November 2023 and lasted until the last result was posted on the 14th of December 2023. During this time, a total of 274 result entries were posted to FINALES. In the multi-task phase, 7 quantities and 9 methods were registered with FINALES. Out of the 274 results, 173 are valid.

Supporting Information

Supporting Information is available from the Wiley Online Library or from the author.

Acknowledgements

This project received funding from the European Union's Horizon 2020 research and innovation program under grant agreement no. 957189 (BIG-MAP). The authors acknowledge BATTERY2030PLUS, funded by the European Union's Horizon 2020 research and innovation program under grant agreement no. 957213. This work contributes to the research performed at CELEST (Center for Electrochemical Energy Storage Ulm-Karlsruhe) and was co-funded by the German Research Foundation (DFG) under Project ID 390874152 (POLiS Cluster of Excellence). H.S.S. acknowledges funding from DFG EXC 2089/1-390776260 (e-conversion). T.V. acknowledges funding from the Pioneer Center for Accelerating Materials Discovery (CAPeX), DNRF Grant P3. F.F.R., F.L., and G.P. acknowledge funding by the NCCR MARVEL, a National Centre of Competence in Research, funded by the Swiss National Science Foundation (grant number 205602). G.P. acknowledges funding by the Open Research Data Program of the ETH Board (project "PREMISE": Open and Reproducible Materials Science Research). F.L. and G.P. acknowledge useful discussions and support by Valeria Granata in the setup of the Archiving tenant. M.V. acknowledges

Table 1. The code availability for each of the tenants presented in this study.

Tenant	Version	Code availability
F2Opt	v1.0.0	https://github.com/BIG-MAP/F2Opt https://github.com/BIG-MAP/F2Opt/releases/tag/v1.0.0
ASAB	v2.0.1	https://github.com/Helge-Stein-Group/ASAB https://doi.org/10.5281/zenodo.11146699
ASAB tenant	v1.0.0, v1.0.1	https://github.com/BIG-MAP/FINALES_ASAB_tenant https://doi.org/10.5281/zenodo.11144341
OVERLORT	v1.0.0	https://github.com/BIG-MAP/FINALES_Overlort_tenant https://doi.org/10.5281/zenodo.11145783
AutoBASS	v1.0.1	https://github.com/BIG-MAP/FINALES_AutoBASS_tenant https://doi.org/10.5281/zenodo.11145983
Cycler	v1.0.0	https://github.com/BIG-MAP/FINALES_Cycler_tenant https://doi.org/10.5281/zenodo.11145850
Degradation model	v1.0.0	https://github.com/BIG-MAP/eol_degradation_tenant https://github.com/BIG-MAP/eol_degradation_tenant/releases/tag/v1.0.0
Archiving	v1.1.0	https://github.com/materialscloud-org/big-map-archive-api-client/blob/2511f86ec08c44fc8d32e5d96953eb72e3ac89d9/README.md#back-up-finales-databases https://zenodo.org/records/11184798
Transportation	v1.0.0	https://github.com/BIG-MAP/FINALES_Transportation_tenant https://doi.org/10.5281/zenodo.11120059

fruitful discussions with Jackson K. Flowers regarding the transformation of formulations in the ASAB tenant. L.M. and M.V. acknowledge effective discussions with Christian Wölke concerning the cycling data obtained from the pretests. The authors acknowledge BASF SE and CIDETEC for providing the electrode sheets.

Conflict of Interest

J.M.C. is beneficiary of an employee share plan at Dassault Systèmes.

Author Contributions

M.V. and S.K.S. contributed equally to this work. Conceptualization: A.B., H.S.S.; Data curation: J.B., S.K.S., E.F., M.V., F.L.; Formal analysis: J.B., M.V., J.C., H.H., F.H., L.M., A.B.; Funding acquisition: I.E.C., G.P., J.C., H.H., F.H., H.S.S., T.V., A.B.; Investigation: J.B., M.V., L.M., B.Z., S.K.S.; Methodology: J.B., S.K.S., M.V., F.F.R., J.C., H.H., F.H., M.G., L.H.R., A.S., S.F., S.C., H.S.S., A.B.; Project administration: S.K.S., M.V.; Resources: BZ; Software: J.B., S.K.S., E.F., M.V., F.F.R., F.L., G.P., J.C., H.H., F.H., L.M., L.H.R., B.Z., S.C., H.S.S.; Supervision: I.E.C., G.P., J.C., H.H., F.H., H.S.S., T.V., A.B.; Validation: J.B., M.V., M.G., A.S., S.F.; Visualization: J.B., S.K.S., M.V., J.C., H.H., F.H.; Writing - original draft: J.B., S.K.S., E.F., M.V., F.L., J.C., H.H., F.H., L.H.R., H.S.S., T.V., A.B.; Writing - review & editing: J.B., I.E.C., S.K.S., E.F., M.V., F.F.R., G.P., J.C., H.H., F.H., M.G., L.M., L.H.R., B.Z., A.S., S.F., S.C., H.S.S., T.V., A.B.

Data Availability Statement

The data generated in the course of this study is publicly available under the DOI <https://doi.org/10.24435/materialscloud-qt-1s>. The code for the version 1.1.0 of the FINALES framework is available under the DOI <https://doi.org/10.5281/zenodo.10987727> and on GitHub <https://github.com/BIG-MAP/FINALES2>. The code of the FINALES schemas version 1.0.1 is available under the DOI <https://zenodo.org/records/11142866> and the latest version of FINALES schemas can be found on GitHub https://github.com/BIG-MAP/FINALES2_schemas. The code associated with the individual tenants is available as stated in **Table 1**.

Keywords

battery research, Bayesian optimization, decentralized, electrolyte, materials acceleration platform, self-driving laboratory

Received: July 24, 2024
Revised: September 6, 2024
Published online: October 18, 2024

- [1] M. Abolhasani, E. Kumacheva, *Nature Synthesis* **2023**, 2, 483.
- [2] M. Seifrid, J. Hattrick-Simpers, A. Aspuru-Guzik, T. Kalil, S. Cranford, *Matter* **2022**, 5, 1972.
- [3] M. Vogler, J. Busk, H. Hajiyani, P. B. Jørgensen, N. Safaei, I. E. Castelli, F. F. Ramirez, J. Carlsson, G. Pizzi, S. Clark, F. Hanke, A. Bhowmik, H. S. Stein, *Matter* **2023**, 6, 2647.
- [4] A. Bhowmik, I. E. Castelli, J. M. Garcia-Lastra, P. B. Jørgensen, O. Winther, T. Vegge, *Energy Storage Mater.* **2019**, 21, 446.
- [5] W. A. Appiah, J. Busk, T. Vegge, A. Bhowmik, *Electrochim. Acta* **2023**, 439, 141430.
- [6] F. Strieth-Kalthoff, H. Hao, V. Rathore, J. Derasp, T. Gaudin, N. H. Angello, M. Seifrid, E. Trushina, M. Guy, J. Liu, X. Tang, M. Mamada, W. Wang, T. Tsagaantsooj, C. Lavigne, R. Pollice, T. C. Wu, K. Hotta, L. Bodo, S. Li, M. Haddadnia, A. Wołos, R. Roszak, C. T. Ser, C. Bozal-Ginesta, R. J. Hickman, J. Vestfrid, A. Aguilar-Granda, E. L. Klimareva, R. C. Sigerson, et al., *Science* **2024**, 384, eadk9227.
- [7] I. Batatia, P. Benner, Y. Chiang, A. M. Elena, D. P. Kovács, J. Riebesell, X. R. Advincula, M. Asta, M. Avaylon, W. J. Baldwin, F. Berger, N. Bernstein, A. Bhowmik, S. M. Blau, V. Cărare, J. P. Darby, S. De, F. Della Pia, V. L. Deringer, R. Elijošius, Z. El-Machachi, F. Falcioni, E. Fako, A. C. Ferrari, A. Genreith-Schriever, J. George, R. E. A. Goodall, C. P. Grey, P. Grigorev, S. Han, et al., *arXiv:2401.00096* **2024**.
- [8] J. Amici, P. Asinari, E. Ayerbe, P. Barboux, P. Bayle-Guillemaud, R. J. Behm, M. Bercibar, E. Berg, A. Bhowmik, S. Bodoardo, S. Bodoardo, I. E. Castelli, I. Cekic-Laskovic, R. Christensen, S. Clark, R. Diehm,

- R. Dominko, M. Fichtner, A. A. Franco, A. Grimaud, N. Guillet, M. Hahlin, S. Hartmann, V. Heiries, K. Hermansson, A. Heuer, S. Jana, L. Jabbour, J. Kallo, A. Latz, et al., *Adv. Energy Mater.* **2022**, *12*, 2102785.
- [9] N. J. Szymanski, B. Rendy, Y. Fei, R. E. Kumar, T. He, D. Milsted, M. J. McDermott, M. Gallant, E. D. Cubuk, A. Merchant, H. Kim, A. Jain, C. J. Bartel, K. Persson, Y. Zeng, G. Ceder, *Nature* **2023**, *624*, 86.
- [10] C. Chen, D. T. Nguyen, S. J. Lee, N. A. Baker, A. S. Karakoti, L. Lauw, C. Owen, K. T. Mueller, B. A. Bilodeau, V. Murugesan, M. Troyer, *arXiv preprint arXiv:2401.04070* **2024**.
- [11] L. H. Rieger, M. Wilson, T. Vegge, E. Flores, *Digital Discovery* **2023**, *2*, 1957.
- [12] F. Rahmanian, *Zenodo* **2023**.
- [13] S. Clark, F. L. Bleken, S. Stier, E. Flores, C. W. Andersen, M. Marcinek, A. Szczesna-Chrzan, M. Gaberscek, M. R. Palacin, M. Uhrin, J. Friis, *Adv. Energy Mater.* **2022**, *12*, 2102702.
- [14] S. Clark, J. Friis, F. L. Bleken, C. W. Andersen, E. Flores, H. Snijder, S. Stier, *Zenodo*, **2023**.
- [15] F. Liot, V. Granata, G. Pizzi, N. Marzari, Big-map archive, **2023**, <https://archive.big-map.eu/>.
- [16] L. Talirz, S. Kumbhar, E. Passaro, A. V. Yakutovich, V. Granata, F. Gargiulo, M. Borelli, M. Uhrin, S. P. Huber, S. Zoupanos, C. S. Adorf, C. W. Andersen, O. Schütt, C. A. Pignedoli, D. Passerone, J. VandeVondele, T. C. Schulthess, B. Smit, G. Pizzi, N. Marzari, *Sci. Data* **2020**, *7*, 299.
- [17] M. S. Ding, K. Xu, T. R. Jow, *J. Electrochem. Soc.* **2000**, *147*, 1688.
- [18] M. S. Ding, K. Xu, S. S. Zhang, K. Amine, G. L. Henriksen, T. R. Jow, *J. Electrochem. Soc.* **2001**, *148*, A1196.
- [19] F. Rahmanian, M. Vogler, C. Wölke, P. Yan, M. Winter, I. Cekic-Laskovic, H. S. Stein, *Batteries & Supercaps* **2022**, *5*, e202200228.
- [20] A. Narayanan Krishnamoorthy, C. Wölke, D. Diddens, M. Maiti, Y. Mabrouk, P. Yan, M. Grünebaum, M. Winter, A. Heuer, I. Cekic-Laskovic, *Chemistry-Methods* **2022**, *2*, e202200008.
- [21] J. Landesfeind, H. A. Gasteiger, *J. Electrochem. Soc.* **2019**, *166*, A3079.
- [22] E. Flores, C. Wölke, P. Yan, M. Winter, T. Vegge, I. Cekic-Laskovic, A. Bhowmik, *Digital Discovery* **2022**, *1*, 440.
- [23] B. Ghalami Choobar, H. Modarress, R. Halladj, S. Amjad-Iranagh, *J. Phys. Chem. C* **2019**, *123*, 21913.
- [24] A. Nyman, M. Behm, G. Lindbergh, *Electrochim. Acta* **2008**, *53*, 6356.
- [25] E. R. Logan, E. M. Tonita, K. L. Gering, L. Ma, M. K. G. Bauer, J. Li, L. Y. Beaulieu, J. R. Dahn, *J. Electrochem. Soc.* **2018**, *165*, A705.
- [26] R. D. Hipp, SQLite, **2023**, <https://www.sqlite.org/index.html> (accessed: July 2024).
- [27] M. Bayer, in *The Architecture of Open Source Applications Volume II: Structure, Scale, and a Few More Fearless Hacks* (Eds: A. Brown, G. Wilson), aosabook.org, **2012**.
- [28] S. Ramírez, FASTAPI, **2023**, <https://fastapi.tiangolo.com/> (accessed: July 2024).
- [29] E. V. Bonilla, K. Chai, C. Williams, in *Advances in Neural Information Processing Systems*, Vol. 20 (Eds.: J. Platt, D. Koller, Y. Singer, S. Roweis), Curran Associates, Inc, Glasgow **2007**.
- [30] K. Swersky, J. Snoek, R. P. Adams, in *Advances in Neural Information Processing Systems*, Vol. 26 (Eds: C. Burges, L. Bottou, M. Welling, Z. Ghahramani, K. Weinberger), Curran Associates, Inc, Glasgow **2013**.
- [31] T. Chugh, in *2020 IEEE Congress on Evolutionary Computation (CEC)*, **2020**, pp. 1–8.
- [32] W. McKinney, in *Proceedings of the 9th Python in Science Conference* (Eds: S. van der Walt, J. Millman), **2010** pp. 56–61.
- [33] A. Paszke, S. Gross, F. Massa, A. Lerer, J. Bradbury, G. Chanan, T. Killeen, Z. Lin, N. Gimelshein, L. Antiga, A. Desmaison, A. Kopf, E. Yang, Z. DeVito, M. Raison, A. Tejani, S. Chilamkurthy, B. Steiner, L. Fang, J. Bai, S. Chintala, in *Advances in Neural Information Processing Systems*, Vol. 32, Curran Associates, Inc, Glasgow **2019**, pp. 8024–8035.
- [34] J. R. Gardner, G. Pleiss, D. Bindel, K. Q. Weinberger, A. G. Wilson, in *Advances in Neural Information Processing Systems*, **2018**.
- [35] Dassault Systèmes Americas Corporation, Biovia pipeline pilot, **2022**, <https://www.3ds.com/products/biovia/pipeline-pilot> (accessed: July 2024).
- [36] Dassault Systèmes Americas Corporation, Biovia materials studio, **2022**, <https://www.3ds.com/products/biovia/materials-studio> (accessed: July 2024).
- [37] R. L. C. Akkermans, N. A. Spenley, S. H. Robertson, *Mol. Simul.* **2021**, *47*, 540.
- [38] A. A. Samoletov, C. P. Dettmann, M. A. J. Chaplain, *J. Stat. Phys.* **2007**, *128*, 1321.
- [39] H. C. Andersen, *J. Chem. Phys.* **1980**, *72*, 2384.
- [40] F. Hanke, N. Modrow, R. L. C. Akkermans, I. Korotkin, F. C. Mocanu, N. V. A. M. Veit, *J. Electrochem. Soc.* **2019**, *167*, 013522.
- [41] B. Zhang, L. Merker, A. Sanin, H. S. Stein, *Digital Discovery* **2022**, *1*, 755.
- [42] L. H. Rieger, E. Flores, K. F. Nielsen, P. Norby, E. Ayerbe, O. Winther, T. Vegge, A. Bhowmik, *Digital Discovery* **2023**, *2*, 112.
- [43] K. A. Severson, P. M. Attia, N. Jin, N. Perkins, B. Jiang, Z. Yang, M. H. Chen, M. Aykol, P. K. Herring, D. Fraggadakis, M. Z. Bazant, S. J. Harris, W. C. Chueh, R. D. Braatz, *Nat. Energy* **2019**, *4*, 383.
- [44] B. Zhang, L. Merker, A. Sanin, H. S. Stein, Zenodo, Cycling Data of 64 Cells manufactured by AutoBASS **2022**, <https://doi.org/10.5281/zenodo.7299473>.
- [45] I. E. Castelli, D. J. Arismendi-Arrieta, A. Bhowmik, I. Cekic-Laskovic, S. Clark, R. Dominko, E. Flores, J. Flowers, K. U. Frederiksen, J. Friis, A. Grimaud, K. V. Hansen, L. J. Hardwick, K. Hermansson, L. Königer, H. Lauritzen, F. Le Cras, H. Li, S. Lyonard, H. Lorrmann, N. Marzari, L. Niedzicki, G. Pizzi, F. Rahmanian, H. Stein, M. Uhrin, W. Wenzel, M. Winter, C. Wölke, T. Vegge, et al., *Batter. Supercaps* **2021**, *4*, 1803.
- [46] S. Powers, *Practical RDF: solving problems with the resource description framework*, “O’Reilly Media, Inc.”, **2003**.
- [47] M. J. Dürst, M. Suijnard, Internationalized Resource Identifiers (IRIs), RFC 3987, **2005**, <https://www.rfc-editor.org/info/rfc3987> (accessed: July 2024).
- [48] R. Angles, M. Arenas, P. Barceló, A. Hogan, J. Reutter, D. Vrgoč, *ACM Comput. Surv.* **2017**, *50*, 5.
- [49] N. Francis, A. Green, P. Guagliardo, L. Libkin, T. Lindaaker, V. Marsault, S. Plantikow, M. Rydberg, P. Selmer, A. Taylor, in *Proceedings of the 2018 International Conference on Management of Data, SIGMOD ’18*, Association for Computing Machinery, New York, NY, USA, ISBN 9781450347037, **2018**, pp. 1433–1445.

ADVANCED ENERGY MATERIALS

Supporting Information

for *Adv. Energy Mater.*, DOI 10.1002/aenm.202403263

Autonomous Battery Optimization by Deploying Distributed Experiments and Simulations

Monika Vogler, Simon Krarup Steensen, Francisco Fernando Ramírez, Leon Merker, Jonas Busk, Johan Martin Carlsson, Laura Hannemose Rieger, Bojing Zhang, François Liot, Giovanni Pizzi, Felix Hanke, Eibar Flores, Hamidreza Hajiyani, Stefan Fuchs, Alexey Sanin, Miran Gaberšček, Ivano Eligio Castelli, Simon Clark, Tejs Vegge, Arghya Bhowmik and Helge Sören Stein**

Autonomous battery optimization by deploying distributed experiments and simulations

Monika Vogler^{1,2,11}, Simon Krarup Steensen^{4,11}, Francisco Fernando Ramirez⁵, Leon Merker^{1,3}, Johan Martin Carlsson⁶, Laura Hannemose Rieger⁴, Bojing Zhang^{1,3}, François Liot⁵, Giovanni Pizzi^{7,5}, Felix Hanke⁸, Eibar Flores⁹, Hamidreza Hajiyani⁶, Stefan Fuchs¹, Alexey Sanin^{1,3}, Miran Gaberšček¹⁰, Ivano Eligio Castelli⁴, Simon Clark⁹, Tejs Vegge⁴, Arghya Bhowmik^{4,}, Helge Sören Stein^{2,*}*

¹ Helmholtz Institute Ulm (HIU), Helmholtzstr. 11, 89081 Ulm, Germany

² Technical University of Munich, Germany; TUM School of Natural Sciences, Department of Chemistry, Chair of Digital Catalysis; Munich Institute of Robotics and Machine Intelligence (MIRMI); Munich Data Science Institute MDSI

³ Present address: Technical University of Munich, Germany; TUM School of Natural Sciences, Department of Chemistry, Chair of Digital Catalysis; Munich Institute of Robotics and Machine Intelligence (MIRMI); Munich Data Science Institute MDSI

⁴ Technical University of Denmark (DTU), Department of Energy Conversion and Storage, 2800 Kgs. Lyngby, Denmark

⁵ Theory and Simulation of Materials (THEOS) and National Centre for Computational Design and Discovery of Novel Materials (MARVEL), École Polytechnique Fédérale de Lausanne (EPFL), CH-1015 Lausanne, Switzerland

⁶ Dassault Systèmes Germany GmbH, Am Kabellager 11-13, D-51063 Cologne, Germany

⁷ Laboratory for Materials Simulations (LMS), Paul Scherrer Institut (PSI), CH-5232 Villigen PSI, Switzerland

⁸ Dassault Systèmes, 22 Science Park, Cambridge CB4 0FJ, UK

⁹ SINTEF Industry, Battery Technology, 7034 Trondheim, Norway

¹⁰ Department of Materials Chemistry, National Institute of Chemistry, Hajdrihova 19, 1000, Ljubljana, Slovenia

¹¹ M. Vogler and S. K. Steensen contributed equally.

* Corresponding authors.

1 FINALES Framework

1.1 Append-only design

The current database design deployed in the Fast INTention-Agnostic LEarning Server (FINALES) uses the UPDATE interaction for the columns `is_active` and `status`. These are used to control the availability of quantities and tenants in the MAP, and states of requests and results, respectively. Since the UPDATE interaction is not part of the Append Only design, we plan to deal with these columns through separate tables as seen in Figure S1. While the current version of the server already deploys separate tables controlling the two `status` columns, the updated columns values are added back into the `request` and `result` tables for easing query implementation. A description of each table column can be found in the .py files defining each table in the folder <https://github.com/BIG-MAP/FINALES2/tree/main/src/FINALES2/db/tables>.

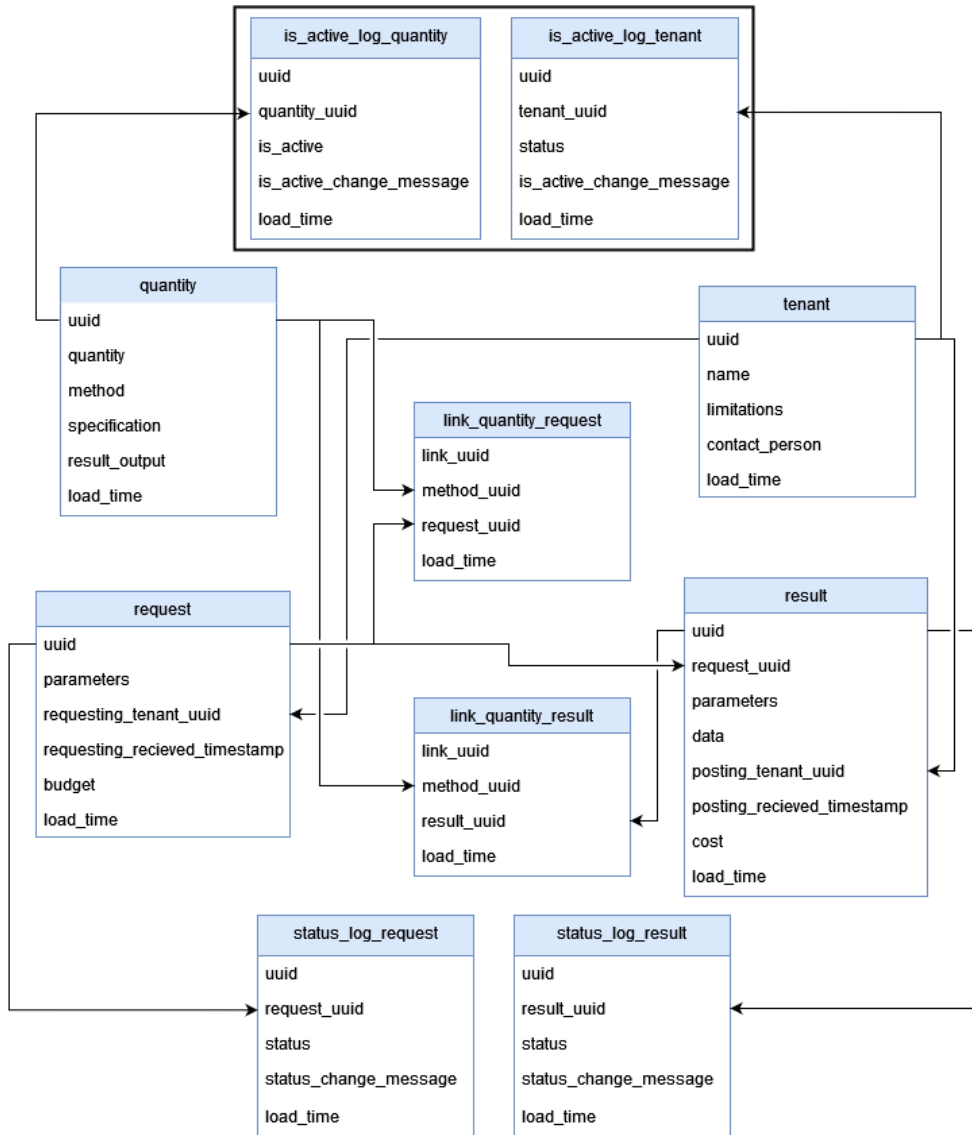


Figure S1: Future upgrade of the database table schematic enforcing an Append Only design for FINALES. Removing the `is_active` and `status` columns from the `quantity`, `tenant`, `request` and `result` tables into separate controlling log tables allows the server through chronological logic to adhere to the Append Only design. The additional log tables are enclosed in the black box. The backend update allowing for the extended table schema is planned for the release of v2.0.0.

1.2 Endpoints

An overview over the Application Programming Interface (API) endpoints in FINALES with explanation of their corresponding purpose divided into the POST and GET functionalities:

POST

- `/requests/` - Post new requests.
- `/results/` - Post new results.
- `/results/post_unsolicited_result` - Post new results to the server that are not prompted to an initial requests. This can be useful e.g. for prepopulating a database with already measured results.
- `/requests/{object_id}/update_status` - Updating the status of a specific request between the following possibilities: `pending`, `reserved`, and `retracted`. The other request status types `resolved` and `unsolicited` are handled internally by the engine and are assigned when a result is posted either linked to a request or not, respectively. In the case of a result being posted without an original request, a request with type `unsolicited` is automatically created. This is to keep a concise internal structure between the tables in the database. Additionally, when changing a status, it is possible and recommended to add a message defining why the change was needed.
- `/results/{object_id}/update_status` - Updating the status of a specific result between the following possibilities: `deleted` and `amended`. The final type `original` is internally defined to only be the initial result entry into the database. The status can therefore not be applied by a tenant. Just as for status changes of requests, a message can and should accompany the change.

GET

- `/requests/{object_id}` - Get a request with specific ID.
- `/results/{object_id}` - Get a result with specific ID.
- `/pending_requests/` - Get all the requests with status pending currently in the queue.
- `/all_requests/` - Get all requests irregardless of their status.
- `/results_requested/{request_id}` - Get result by using the corresponding ID of the request.
- `/results_requested/` - Get all results with the possibility of limiting retrieval to a specific quantity and/or method.
- `/capabilities/` - Get all the capabilities registered in FINALES. The default is to return all active tenants, but it is possible to remove this filter and return all tenants including the ones currently inactive.
- `/limitations/` - Get all limitations for all capabilities registered in FINALES. Possibility to retrieve limitations that are currently not active, which allow for traceability to understand requests that were within a set of limitations at an earlier point in time.
- `/capabilities/templates` - Get templates for the input/output schema defined for capabilities, easing the process of defining limitations for tenants.
- `/tenants/` - Get all tenants that are registered in FINALES.
- `/database_dump/{access_key}` - Download the entire database in FINALES (except for the separate user table) for archiving and backup purposes. The endpoint is accessed through an access key which is defined by the server administrator. The endpoint transfers the binary SQLite file with the correct database extension.

All endpoints are protected through user authentication. Another security aspect is the use of SQLAlchemy for database interactions, which protects the server from SQL injection attacks. Note that to utilize the provided protection, one must always avoid using raw SQL queries and e.g. adhere to the use of bound parameters when using the filter function of SQLAlchemy.

1.3 Example for a quality rating

As an example, we summarize here how the quality rating for the ionic conductivity results reported by the Autonomous Synthesis and Analysis of Battery electrolytes (ASAB) tenant are determined.

In this case, the quality rating considers two contributions. One is the deviation of the transformed formulation f_{act} from the requested one f_{req} : $|\Delta \vec{f}| = \left| \vec{f}_{\text{req}} \right| - \left| \vec{f}_{\text{act}} \right|$. The second one is the error of the average ionic conductivity $\Delta \kappa_{\text{avg}}$.

To obtain the contribution of the electrolyte formulation, the ratio $r_f = \left| \Delta \vec{f} \right| \cdot \left| \vec{f}_{\text{req}} \right|^{-1}$ is determined. The rating R_{form} is set to 0, if $r_f \geq 1$. Otherwise, the rating is assigned as $R_{\text{form}} = \lfloor (1.0 - r_f) \cdot 5.0 \rfloor$.

The contribution based on the Electrochemical Impedance Spectroscopy (EIS) results accounts for the influence of the number of successful individual measurements n out of the 3 performed ones: $r_n = 1.0 - (n/3)$. Additionally, the error of the average ionic conductivity $\Delta \kappa_{\text{avg}}$ is determined by error propagation and the ratio $r_\kappa = \Delta \kappa_{\text{avg}} \cdot \kappa_{\text{avg}}^{-1}$ is calculated. The quality rating of the EIS measurement R_{EIS} is set to 0, if $r_\kappa \geq 1$. Otherwise, it is obtained as $R_{\text{EIS}} = \lfloor (1.0 - r_n - r_\kappa) \cdot 5.0 \rfloor$.

The total quality rating of the result is obtained as $R = \lfloor 0.5 \cdot (R_{\text{form}} + R_{\text{EIS}}) \rfloor$.

2 Detailed Tenant Descriptions

This chapter presents in depth descriptions of the tenants involved in the study presented in the main article.

2.1 Molecular Dynamics (MD) tenant

The simulation tenant for calculating lithium ion conductivity is using Molecular Dynamics (MD) to simulate the movement of the molecules in the electrolyte formulation requested by the optimizer. MD simulations can handle any type of molecular electrolyte ingredient, restricted only by the requirement to use complete molecules which can lead to small differences to the real-valued concentrations requested by the optimizer.

The MD tenant is implemented in BIOVIA Pipeline Pilot (BPP), which is a general modular environment for data science and automation^[1]. The workflows in BPP are created by connecting computing components by data pipelines. Multiple components can be combined into a subroutine called subprotocol, such that a hierarchical workflow structure can be generated. The top level of the protocol for the MD tenant is shown in Figure S2a. The component *Query FINALES Database* starts the workflow by making an HTTP call to FINALES to inquire for pending requests for simulations of the ion conductivity. The FINALES request in JSON format is parsed in the subprotocol *Parse MD request* to extract the request ID, the amounts of the individual ingredients and the molecular structure of the ingredients described by SMILES or InChIKeys. The SMILES description of the ingredients gets converted into a 3D representation of the molecules.

The next step is to build an atomistic, pseudoamorphous model of the electrolyte with the *Construction (Amorphous Cell)* component from BIOVIA Materials Studio^[2]. The component creates 5 starting configurations using a Monte Carlo approach to randomly place the molecules into a supercell as shown in Fig. S2b. The number of molecules of each ingredient is calculated by converting the concentration ratios requested by the optimizer into fractions of integer numbers of molecules. The size of the supercell is determined by the volume required to fit the total number of molecules at a target starting density of 1.3 g cm^{-3} .

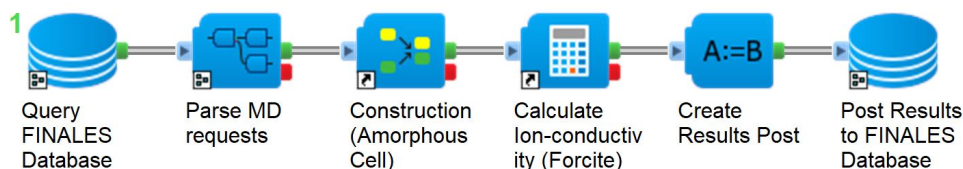
The subprotocol to calculate the ionic conductivity of the electrolyte model *Calculate ion-conductivity (Forcite)* uses a sequence of MD simulations with the MD component Forcite^[2] using the COMPASS-III forcefield^[3]. The density is equilibrated in two steps by MD in the NVT ensemble (constant

volume, temperature and number of molecules) with the velocity scale thermostat for 200 ps and NPT ensemble (constant pressure, temperature and number of molecules) for 200 ps using the Nose-Hoover-Langevin (NHL) thermostat^[4] and the Andersen barostat^[5]. The production run is performed by MD in the NVE ensemble (constant volume, total energy and number of molecules) for 2.5 ns to gather trajectories to calculate the diffusion coefficients of the charge carriers.

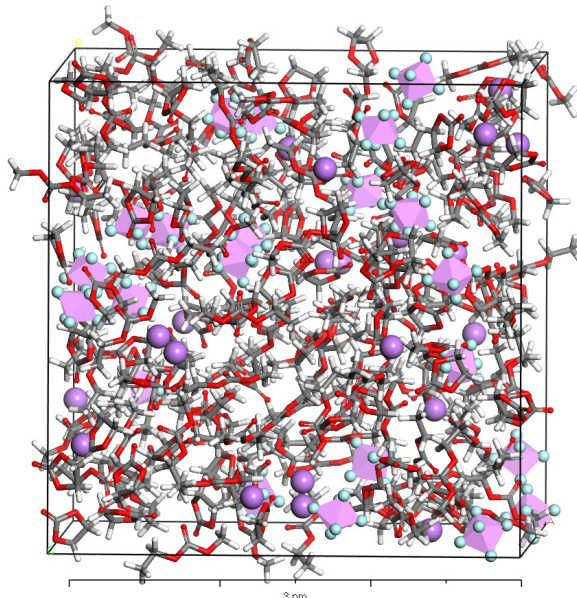
The diffusion coefficient of the positive and negative charge carriers $D_{+/-}$ is derived from the mean square displacement (MSD) via the Einstein relation. The ion conductivity of the charge carriers is derived from the Nernst-Einstein equation.

$$\kappa_{+/-} = \frac{D_{+/-} C q_e^2 N_A}{k_B T} \quad (1)$$

where C is the ion concentration, q_e is the elementary charge unit, N_A is Avogadro's number, k_B is Boltzmann's constant and T is the temperature^[6]. The total conductivity is the sum of the contributions from the positive and negative charge carriers. The results of the MD simulations for all five configurations in terms of temperature, density and ion conductivity are collected into a JSON response in the component *Create Results Post* to create the required data hierarchy. Finally, the component *Post results to FINALES Database* sends the JSON response back to FINALES with a HTTP call including the request ID.



- (a) The top level view of the protocol for the MD simulation tenant. The component *Query FINALES Database* queries the FINALES database for new requests. The subprotocol *Parse MD request* converts the JSON request into the Pipeline Pilot data format. The *Construction (Amorphous Cell)* component generates an atomistic supercell model of the electrolyte formulation requested by the optimizer. The subprotocol *Calculate ion-conductivity (Forcite)* runs a series of MD simulations to calculate the ionic conductivity. The component *Create Results Post* compiles the JSON response that is posted to the FINALES server by the component *Post results to FINALES Database*.



- (b) The atomistic model of the electrolyte in a supercell for the MD simulation. The Li ions are illustrated as large purple spheres. The polyhedra indicate the PF_6^- ions. The ethylene carbonate (EC) and ethyl methyl carbonate (EMC) molecules are shown as stick models.

Figure S2: Depiction of (a) the MD workflow and (b) the supercell used for the MD simulations.

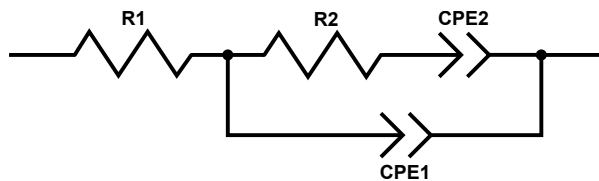


Figure S3: The equivalent circuit used in this study to determine the ionic conductivity of the prepared electrolytes. The resistance $R1$ corresponds to the electrolyte resistance and the other three elements are related to interfacial effects in the measuring cell. The initial values used as inputs for the MADAP package are the first real part of the measured impedance, $150\ \Omega$, $4 \times 10^{-7}\ \text{Fs}^\alpha$, $5 \times 10^{-7}\ \text{Fs}^\alpha$ for $R1$, $R2$, $CPE1$, and $CPE2$, respectively, and $\alpha = 1$ for the CPEs.

2.2 ASAB tenant

This section provides more detailed information regarding the ASAB tenant and the procedures performed prior to the start of the experiments.

The electrochemical cell is electrically connected to a PalmSens4 potentiostat (PalmSens B.V., Houten, Netherlands) providing the protocol and control of the electrochemical impedance spectroscopy (EIS) measurements. The PalmSens4 is triggered by the ASAB software using the PalmSensSDK version 5.9 and results are automatically analyzed using the Modular and Autonomous Data Analysis Platform (MADAP)^[7] version 1.1.0. The electrochemical cell was calibrated using the results of repeated measurements of 1 M lithium hexafluorophosphate (LiPF_6) in EC and EMC (EC:EMC 3:7 by weight). The cell was calibrated to meet the conductivity values obtained from the empirical model reported by Ding *et al.*^[8] and the cell constant was determined to be $(2.40 \pm 0.13)\ \text{cm}^{-1}$. In all EIS experiments, the typical measured impedance response consisted of a high frequency intercept and a medium to low frequency sloping line. The high-frequency intercept was assumed to be the electrolyte resistance, while the low-frequency response was typical of a blocking electrode. The simplest equivalent circuit that could well describe the measured spectra consisted of a resistor representing the electrolyte resistance and an interface term consisting of another resistor in series with a capacitor, the latter two elements being connected in parallel with a double-layer capacitor^[9, 10]. The proposed circuit shown in Figure S3 fitted the spectra very well and reliable values for the electrolyte resistance could be obtained. The conductivity was calculated from the obtained electrolyte resistance using the cell constant determined from the calibration measurements.

Further parameters determined during the calibration of the electrochemical cell and used subsequently in the PalmSensSDK protocol of the EIS experiments and in the inputs for the MADAP package are reported in Table S1.

The transformation of the formulations from mole fractions to volume fractions is performed within the ASAB tenant based on the specification of the stock solutions provided in a configuration file. The results of the transformation are logged locally for future reference in case of trouble shooting.

The configuration file moreover provides the possibility to set parameters such as the total flow rate, definitions of the hardware setup like fluidic connections, paths to output directories, etc. enabling flexible usage and reconfiguration of the ASAB system. Photos of the ASAB system and the electrochemical cell are provided in Figures S4 and S5.

Figure S4 shows the glass vials in the white tray, in which the electrolyte is output for cell assembly and Nuclear Magnetic Resonance (NMR) measurements. The electrochemical cell used in this study is shown in Figure S5a as mounted during operation and Figure S5b shows it in disassembled state.

Table S1: The parameters used in the configuration file of the ASAB tenant regarding the EIS experiments as determined based on the calibration measurements performed prior to the start of the study.

Parameter	Value
EquilibrationTime	0.0 s
Potential	0.0 V
Eac	0.01 V
nFrequencies	11
MaxFrequency	1×10^5 Hz
MinFrequency	1×10^4 Hz
OCPmode	1
OCPMaxOCPTime	300 s
OCPStabilityCriterion	0.5 mV s^{-1}
maxCurrent	10 mA (setting in the SDK: 8)
minCurrent	100 pA (setting in the SDK: 0)
cell constant	2.40 cm^{-1}
initial guess <i>R1</i>	high-frequency real part of the measured impedance
initial guess <i>R2</i>	150Ω
initial guess <i>CPE1</i>	$4 \times 10^{-7} \text{ Fs}^\alpha$
initial guess <i>CPE2</i>	$5 \times 10^{-7} \text{ Fs}^\alpha$
α	1

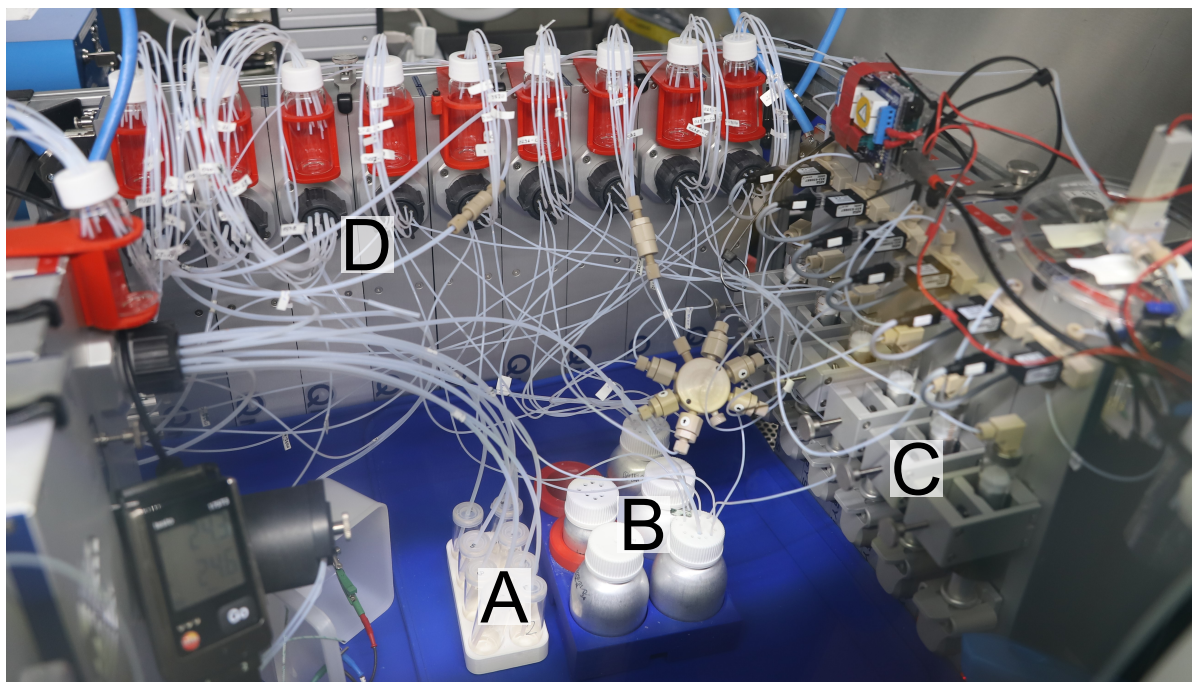


Figure S4: The ASAB hardware setup showing the vials for electrolyte output (A), the reservoirs of the stock solutions (B), the syringe pumps (C) and the rotary valves (D).

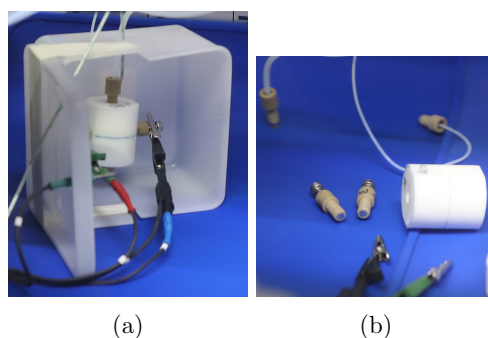


Figure S5: The electrochemical cell used in this study (a) in its assembled state connected to the formulation unit in its operating position and (b) disassembled showing the electrodes and the Polytetrafluoroethylene (PTFE) body.

2.3 AutoBASS tenant

This section provides more detailed information regarding the Autonomous Battery Assembly System (AutoBASS) tenant and its internal mode of operation. The hardware setup is shown in Figure 6.

After picking up a pending request from FINALES, the AutoBASS tenant writes a new task with the specified request ID into a local JSON file and simultaneously blocks the process that continuously gathers new requests. At this point, the tenant enters the *action mode* in which the actual assembly will be carried out by the AutoBASS hardware locally. Before initiating the assembly, manual attention will be needed for the transportation of the electrolyte to the correct position, and the placement of the electrodes, separator, spacers, washer, and casing parts. The generated data, like the images of the components, are stored in the local drive according to the AutoBASS internal procedure. Once the assembly process finished, the data of a single request are collected, prepared, and posted to FINALES. Subsequently, the tenant resumes gathering new requests. Since the images taken during component placement were considered primarily relevant for trouble shooting and were not used as the inputs for the optimizer, it was decided to store this data locally with the tenant and manually share it after the experiments instead of posting it to FINALES. It needs to be noted, that the values reported for the `mass_loading` in the AutoBASS results contained in the dataset accompanying this publication is given as the capacity per unit area of the electrode.

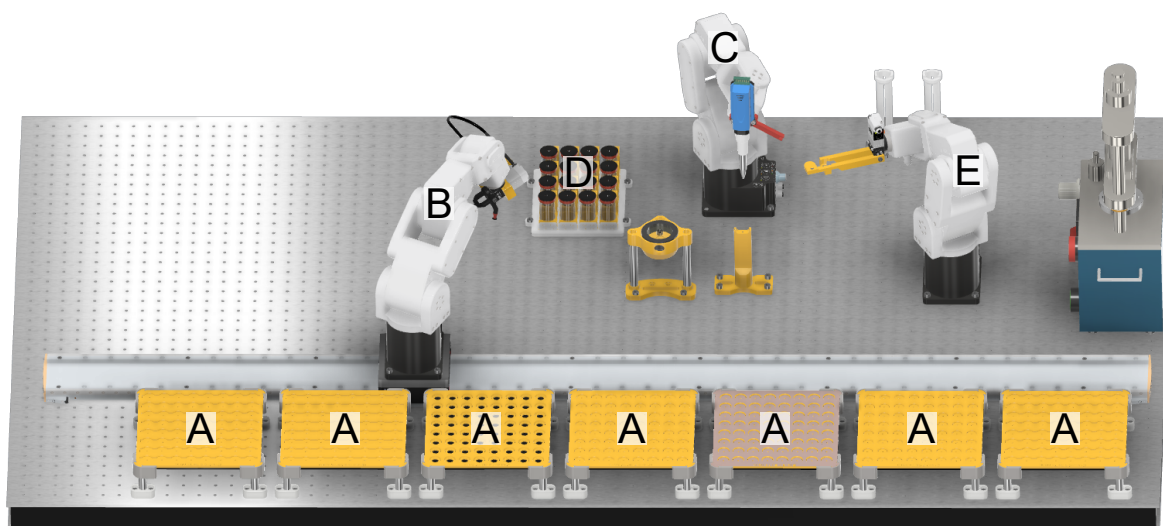


Figure S6: A rendering of the AutoBASS hardware setup showing the components' trays (A), the robot for stacking (B) and the one for pipetting (C), the vials serving as electrolyte reservoirs (D), and the robot arm used for sealing and transporting the cell (E).

2.4 Cyclor tenant

This section provides more detailed information regarding the internal mode of operation of the Cyclor tenant. The hardware of the cyclor is shown in Figure 7.

In reply to a reservation request, the tenant creates a reservation ID and saves this as a parameter in a JSON file for the first channels marked as available. The returned reservation ID is subsequently used to identify the channels when creating and starting the test. For each test, an individually named test protocol and battery description file are created and assigned to the channel. The parameters and the content of these is standardized as reported in Table S2, if not specified differently. Most challenging was the export of the data after exactly 40 cycles for the Degradation model tenant. Since the voltage is used as criterion for charge and discharge, the duration, after which exactly 40 cycles are reached, is not known prior to the experiment. Therefore, the approximation of using a fixed duration after starting the experiment is chosen, which is sufficient to reach at least 40 cycles as estimated globally based on pretest results. Once this preset time elapsed, the result containing the data of the cycles performed up to this point in time is posted. The tenant is therefore continuously checking if a channel passed the export time and starts the export as well as the analysis. The analysis splits up the raw data into the individual charge and discharge cycles and calculates the parameters required as the input for the Degradation model tenant.



Figure S7: The hardware setup of the cyclor used in this study including the control unit on the right and the temperature chamber on the left.

Table S2: Cycling protocol used by the Cycler tenant within this study.

Step	Action	Description
1	rest	Resting for 6 h.
2	formation charge	Apply positive current of 0.154 mA h (C/10) until voltage ≥ 4.2 V is reached.
3	formation CV*	Apply 4.2 V until current value ≤ 0.00008 A (C/20).
4	formation discharge	Apply negative current of 0.154 mA h (C/10) until 2.9 V is reached.
5	loop	Increment counter and jump back to Step 2 until counter < 3 , then continue.
6	rest	Rest for 6 h.
7	charge	Apply positive current of 1.54 mA h (1C) until voltage ≥ 4.2 V is reached.
8	CV*	Apply 4.2 V until current value ≤ 0.00008 A (C/20).
9	discharge	Apply negative current of 1.54 mA h (1C) until 2.9 V is reached.
10	loop	Increment counter and jump back to Step 7 until counter > 200 , then end.

* constant voltage

Data acquisition rate 1 s^{-1} for all steps.

2.5 Overlort

This section provides more detailed information regarding the internal mode of operation of the OVER-Looking ORchestrating Tenant (Overlort).

For the implementation, the FINALES reference tenant was used as a basis.

When requested, it initiates the predefined workflow for this method. Therefore it checks the defined workflow from the final result requested towards earlier steps in the workflow to identify, which quantity is needed next, or it starts the workflow by requesting the Cycler to reserve channels. The Overlort saves all request and result parameters as soon as a task finished processing in a JSON document and consequently is resistant to planned and unexpected stops. By saving all parameters from requests and results, the request for the next quantity can be created based on these parameters. Using the endpoint to request results via the request ID, it keeps track of new results and processes it to create the next request. After a successful reservation, the formulation of the electrolyte specified in the original request is requested, followed by a transportation of the electrolyte to the AutoBASS system. Subsequently, the assembly of cells is requested followed by another transportation of the cells to the respective channels reserved at the beginning. By triggering the request for the cycling of the cells, the Overlort creates one request for each of the eight cells assembled per batch. After processing the result, eight requests for the prediction of the End Of Life (EOL) are posted to FINALES. Finally, the Overlort composes the result for the initially requested quantity and posts it to FINALES, as well as it saves the complete workflow including its request and results locally in a JSON file. This tenant can handle multiple workflows in parallel, as each request and result is internally linked to the request ID of the original workflow request. A graphical representation of the internal workflow followed by the Overlort is shown in Figure S8. The automatic creation of the subsequent request posed a challenge, where further work for a more robust and flexible system would be desirable.

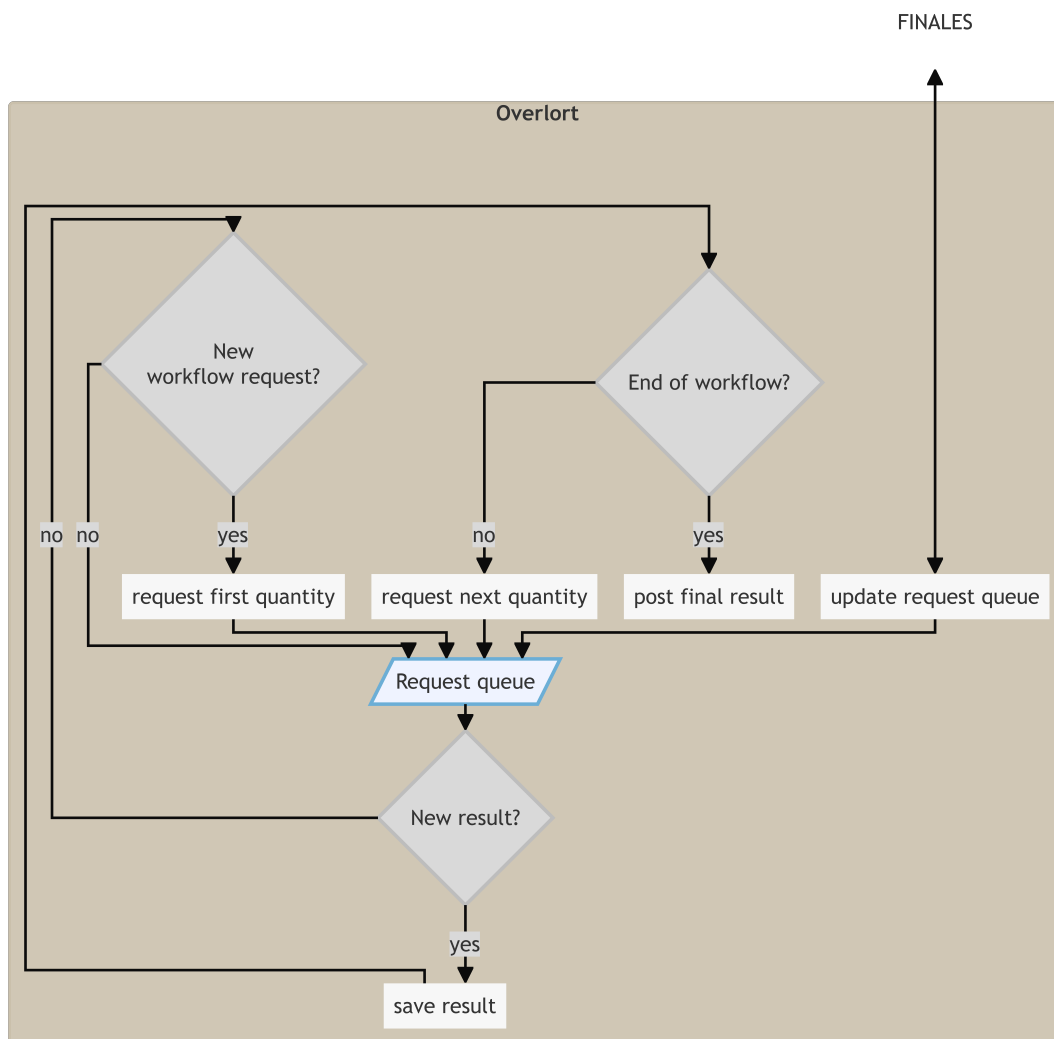


Figure S8: The workflow orchestrated by the Overlort as used in the study.

2.6 Archiving tenant

This section provides more detailed information regarding the Archiving tenant and its internal processes. In this study, the tenant is downloaded as a software package from the Python Package Index (PyPI)^[11] and is subsequently installed on a Linux machine connected to the Internet. It exposes a command that can be run automatically and periodically using a job scheduler, such as “cron”. In the study presented here, the scheduler ran the tenant every second day. The command in question backs up the contents of the SQLite database from the FINALES server to the BIG-MAP Archive, either by generating a new entry or by generating a new version of an existing entry. In either scenario, the newly created record is promptly shared with all users of the private data repository.

Multiple files are attached to a shared record, as illustrated in Figure S9: a copy of the database file and various JSON data files corresponding to the output of different API endpoints of FINALES. JSON is a data interchange format that is easy for machines to parse and generate and is easy for humans to read and write. Note that if a data file remains unaltered between two consecutive backups, it is uploaded only once. Nevertheless, the respective file link appears in both versions of the entry, resulting in saved storage space and reduced upload time.

Files

Preview of capabilities.json >

Files (18.1 MB) ▾

Name	Size	Preview	Download
capabilities.json md5:d7f661cc2d1439a8239229681b764de5b	266.2 kB	Preview	Download
requests.json md5:dff768f79f7f68049dd8930e54c2a46	1.4 MB	Preview	Download
sqlite.db md5:510d24fc92fe65b707eebc7e6d104c	5.9 MB		Download
results_for_requests.json md5:92264b9f2939e11429085a0b9a479f	10.5 MB	Preview	Download
README.md md5:947c5170d97c4e8848e829ec4acc05	5.6 kB	Preview	Download
db_schema.png md5:bda8860cb48f295aa9de82d99c22986	87.8 kB	Preview	Download

License

BIG-MAP Archive License

Keywords

FINALES final run automation ionic conductivity cycle life optimization LIPF6 EC EMC LNO graphite coin cell

References

[10.26434/chemrxiv-2022-grgrd \(DOI\)](https://doi.org/10.26434/chemrxiv-2022-grgrd)
[10.1016/j.matt.2023.07.016 \(DOI\)](https://doi.org/10.1016/j.matt.2023.07.016)
[https://archive.big-map.eu/records/kexm7-xd084 \(URL\)](https://archive.big-map.eu/records/kexm7-xd084)

Figure S9: Files attached to the record on the BIG-MAP Archive by the Archiving tenant on 22nd of December, 2023. *sqlite.db* is a copy of the FINALES internal database file. *results_for_requests.json* contains the results of simulations and experiments for the requests submitted to FINALES.

Ontology Up to recently, there was no widely accepted vocabulary for materials research, batteries and electrochemistry. As part of the BIG-MAP project, we have developed the Battery Interface Ontology (BattINFO), which describes thousands of concepts related to electrochemistry and batteries. More importantly, BattINFO goes beyond traditional vocabularies, as it includes not only human-readable definitions for concepts, but also links concepts to each other with logically consistent relationships, thus rendering meaning machine-readable^[12]. BattINFO is freely available open source at^[13] and at the GitHub repository <https://github.com/BIG-MAP/BattINFO>. The repository includes a graph serialization of the ontology in Turtle format, and an extensive documentation on concepts and example usage available from <https://big-map.github.io/BattINFO/index.html>.

We have selected JSON-LD as the format to implement the mapping between fields in FINALES data to controlled vocabularies. Compared to other formats, JSON-LD is a natural extension of JSON used in FINALES schemas, widely known by software developers, and both human and machine readable^[14]. JSON-LD extends traditional JSON by adding a context object, which maps fields in the file to unique identifiers of concepts from controlled vocabularies. In JSON-LD, each object is an instance of a concept; a special *@id* key holds the unique identifier of the object, and a *@type* key describes the concept the object instantiates.

A result can be encoded as JSON-LD in a myriad of ways. The hierarchy of objects, their attributes and types in the FINALES JSON-LD implementation was agreed from iterative discussions among domain-experts, ontologists and software developers, who have striven to follow three main implementation principles.

First and foremost, software developers ensure the implementation is syntactically sound, i.e. it follows the JSON-LD specification^[14]. For instance, each object must instantiate a class from a controlled vocabulary or ontology, and must contain an identifier when possible. Identifiers should ideally be unique and resolve to a web resource offering more information about the entity.

Second, ontologists and domain experts validate that objects instantiate the right classes from BattINFO and related ontologies, while asserting that links connect compatible instances; for instance:

```
{
  "@type": "Mass",
  "hasNumericalPart": {
    "@type": "Real",
    "hasNumericalValue": 0.08
  },
  "hasMeasurementUnit": "emmo:KiloGram"
}
```

where an object of *@type: Mass* must contain an attribute *hasMeasurementUnit*, whose value must be a valid mass unit, such as *emmo:KiloGram*.

Third, the implementation should facilitate search in a knowledgebase. The ultimate purpose of the implementation is to make FINALES results available in a Graph Database that can be flexibly queried using structured languages, such as SPARQL^[15] or CYPHER^[16]. An excessively nested and inconsistent JSON-LD implementation might require building complex queries to find results, hampering thus access to the data. In this sense, the FINALES implementation has pursued a consistent use of object types and links, while avoiding unnecessary nesting of objects, to facilitate searching for FINALES results within a graph database.

Ontology integration for FINALES Each Archive entry contains a JSON-LD file with results of the EOL and conductivity tasks, all mapped to ontology concepts. This section outlines the mapping and its structure.

First, all information from both single- and multi-task optimization phases were retrieved. Only the final results requested by the optimizers were mapped into linked data files. The intermediate requests from the Overlord tenant were not mapped, to focus efforts in creating a robust mapping for the essential part of the results.

Each optimization phase in FINALES is defined as a *DataCatalog* type with each posted result being a *Dataset* within the catalog. An overview of a single *Dataset* can be seen in Figure S10. The example in the figure is for a conductivity result posted by the ASAB tenant. In case of the computational MD tenant the *hasMeasuredProperty* and *hasSampledSample* are meaningless since simulations do not measure properties nor use samples. Instead, *hasInput* and *hasModelledProperty* are deemed more precise concepts to convey the work of a computational tenant. Furthermore, the MD tenant is mapped to the concepts *PhysicsBasedSimulation*, while the computational Degradation model tenant is mapped to the concept of *PostProcessingModel*. Further concepts differentiating machine learning (ML) models were not available. This led to the use of the broader term *PostProcessingModel*, which does convey the difference to other present computational models of type *PhysicsBasedSimulation*.

The graph edge *hasMeasuredProperty* links the *Dataset* node with all the properties measured during the experiment, which in the case of the ASAB tenant are described in the nodes *IonicConductivity* and *AmbientThermodynamicTemperature*. The nodes and edges implemented for mapping a measurement of ionic conductivity is shown in Figure S11a. Here we define the numeric value of the measurement accompanied by a unit, which showcases how numeric values are generally implemented in the JSON-LD implementation.

The edge *hasSampledSample* maps to the electrolyte formulation used for the experiment. Additional sub-graphs for the electrolyte formulation are shown in Figure S11b. We adhere to these linked data patterns to map electrolyte formulations for FINALES. The MD tenant requires additional information of the number of molecules of the specific components, which are also mapped. All nodes and edges in the linked data descriptions are mapped to well-defined vocabularies, including *smileReference* and *inchiKey*.

The *SoftwareApplication* node in Figure S10 describes the actual tenant posting the results. Since all tenants communicate through the API, this node describes details about the tenant, such as tenant name, authors and creators. Here the creator is defined as the institution of origin for the tenant mapped using the ROR-ID for the research organisation. For the author, the ORCID of the

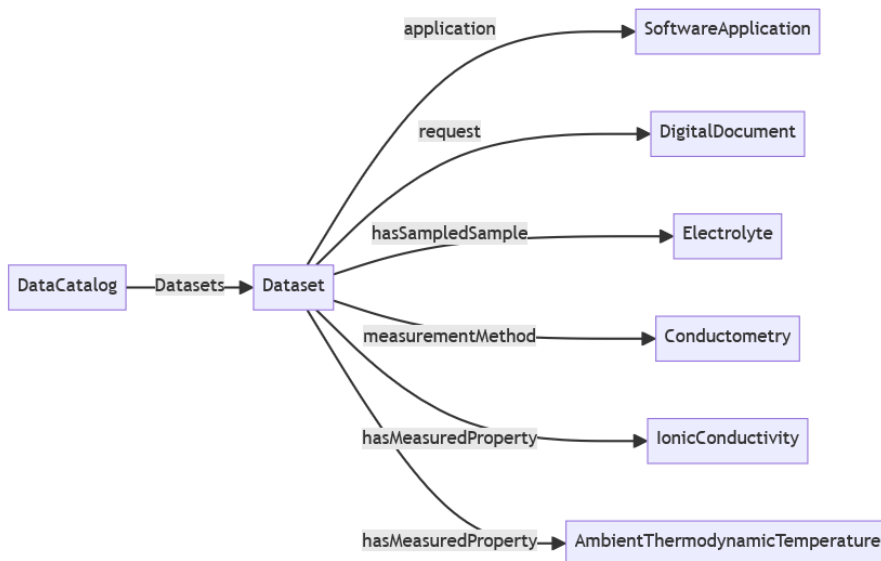
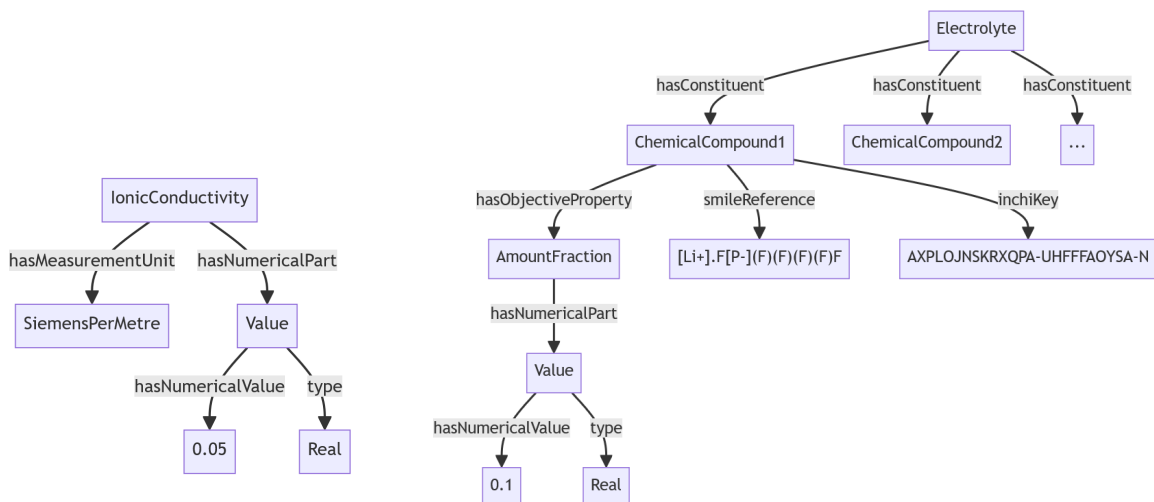


Figure S10: The general structure of the ontological mapped structure of a posted measurement. Each purple box is defined as a node with a type stated in the box, while the gray boxes are defining the edge relationship between nodes. Expanding each node would reveal the metadata the type is populated with. The outermost abstraction is of the `DataCatalog` type, which contains general information shared among results. Each posted result is defined as a single instance of type `Dataset`. The simplified illustration above showcases the structure of a single `Dataset` (provided by the ASAB tenant) within the `DataCatalog`. The `Dataset` contains information on the experimentally specific samples and measurements, and general tenant information for both the request and result.



(a) The ontology mapping for ionic conductivity measurements. Here the value is accompanied by the unit, as is the case for all properties in the implementation. (b) The ontology mapping for an electrolyte formulation. Here a single `ChemicalCompound` is shown with all constituents edges and nodes defining the SMILES, InChIKeys and the fraction used of the compound.

Figure S11: Examples of ontology mappings used in FINALES.

main responsible researcher is used. The `DigitalDocument` node contains information on the request such as the requesting tenant. Here an identical usage of the concept `SoftwareApplication` is used

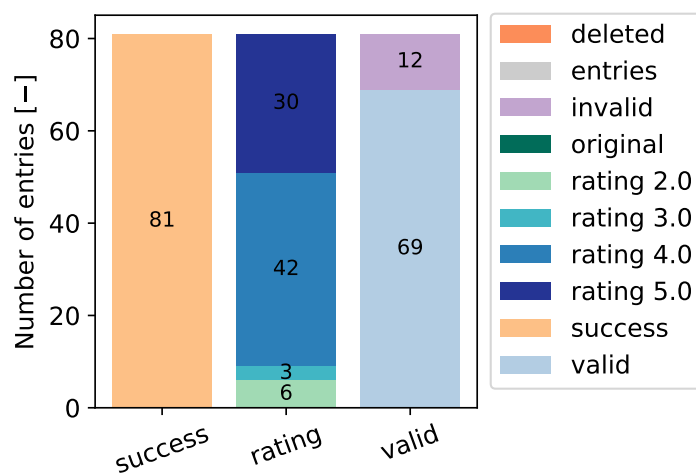
to describe the requesting tenant.

One of the core challenges of the mapping was that not all concepts needed in FINALES are available. Concepts relating to electronic structure simulations are only partially supported in EMMO and the OSMO (<https://gitlab.com/vimmp-semantic/vimmp-ontologies> ontology). A more extensive ontological mapping of the methods deployed in FINALES, would therefore need a vocabulary encompassing quantum chemical calculations as well.

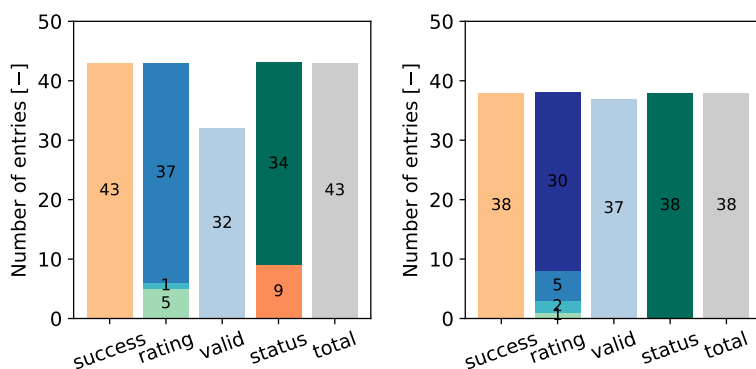
3 Overview of the dataset

3.1 Single-task phase

Figure S12a shows an overview of the data generated during the single-task phase. Figure S12 shows the numbers for the entries by ASAB in Figure S12b and by the MD tenant in Figure S12c. Out of the 43 total entries posted by the ASAB tenant, 9 entries were deleted. 32 valid entries by the ASAB tenant are stored in the database. For the MD tenant, 37 out of a total of 38 entries are valid with only one rating being 2 and therefore below the threshold.



(a) An overview of the data generated during the single-task phase of the campaign.



(b) Bar chart showing various properties of the entries provided by the ASAB tenant. (c) Bar chart showing various properties of the entries provided by the MD tenant.

Figure S12: Overview of entries in the FINALES internal database recorded during the single-task phase of the campaign. The legend shown in (a) is also valid for the figures in (b) - (c).

3.2 Multi-task phase

Figure S13 provides an overview of the data generated during the multi-task phase of the campaign. As can be seen in Figure S13b, the Overlord posted 9 results in total, with only one being deleted. For the ASAB tenant, the data of which is presented in Figure S13c, none of the 44 posted results were deleted this time since the resulting conductivity data did not show severe deviations, even if a leakage occurred. Hence, it was decided to keep the data and accept that the uncertainty of the model may be larger due to a larger spread of ionic conductivity values for formulations affected by the leakage issue. An analysis of the errors occurring during a leakage can be found in section S5.2. The number of valid results amounts to 29 due to 15 results having an insufficient rating. The MD tenant posted 31 results, all of which are valid as can be seen in Figure S13d. The significant difference in the number of generated results between the Overlord compared to the ASAB tenant and the MD tenant is caused by the longer duration of one iteration with the Overlord compared to the other two tenants. A conductivity measurement by ASAB may be performed within one hour. A simulation takes about two hours, however, it has the advantage of running during the night without supervision. In comparison, the preparation of electrolyte, the subsequent assembly of one batch of cells, their cycling and the prediction of the EOL takes approximately one week, which is limiting the throughput significantly. The majority of the time in this workflow is used for the formation and the cycling of the cells. The large number of invalid result entries arises due to failures during the workflow orchestrated by the Overlord. We note that retracting the result of a workflow requires all the results of the related subtasks to be retracted as well, to avoid them losing their context (resulting in database entries without a relation to a result relevant for the optimization). To facilitate the filtering of the results after the end of the campaign, such intermediate results of canceled workflows are retracted by marking them as deleted. The large number of entries with a rating of 1 occurs, because the Degradation model tenant assigned a rating of 1 to all of its results since it relies on the cycling data as an input. The uncertainty of the inputs will affect the output making its predictions at least as uncertain as the input data. Since ratings and success criteria are not trivial to define for each tenant, not all tenants report these fields in their results. Consequently, the total number of datapoints exceeds the number of datapoints reporting a success field and a rating, respectively.

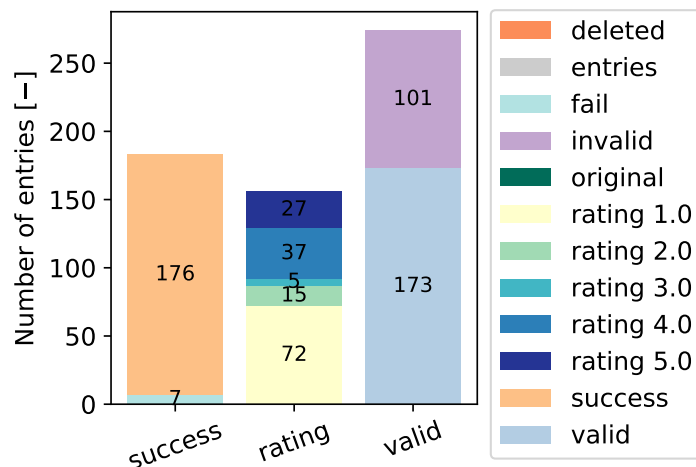
4 Detailed results

4.1 Ionic conductivity

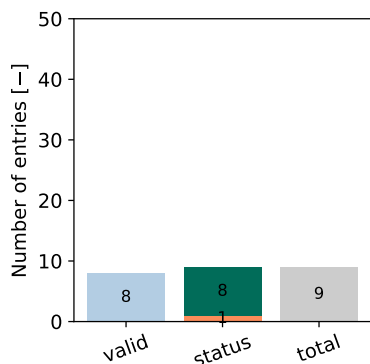
The sequence of the results available in the FINALES database as presented in Figure S14a shows a delay between the first posted result of the `two_electrode` method and the one of the `molecular_dynamics` method in the single-task phase of the campaign. The difference amounts to approximately 8 days. The different timing is caused by the development time of the respective tenants. Furthermore, differences in the data generation rate or downtimes result in periods where mainly simulation data or mainly experimental results are posted.

Within the first 6 reported results, a quick convergence of the experimental data towards a high ionic conductivity is observed and the formulation is not changed significantly for several subsequent results. A possible reason for this behavior could be that, due to the comparatively restricted chemical space accessible in the experiments, the optimizer quickly identified a region of high ionic conductivity. Once simulation data is contributed to the database in result number 12, the optimizer seems to also explore other formulations in the experiment, resulting in lower experimental ionic conductivity prior to going back to the high ionic conductivity formulations. This shows a synergistic effect of combining the different methods as compared to running only one method per quantity. The same observation can be made in Figure S14b, where also the effect of additional experimental data on the requests for the computational ionic conductivity can be observed. A closer look at Figure S14 reveals some formulations not adding up to unity. This may possibly be rounding errors arising for the approximated formulations in the ASAB tenant, which are rounded to two decimals to avoid reporting results appearing overly precise.

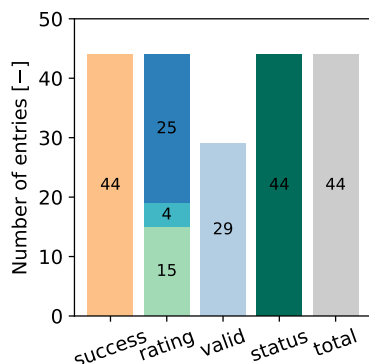
In the top part of Figure 2 in the main article, the best observed formulation and the best predicted



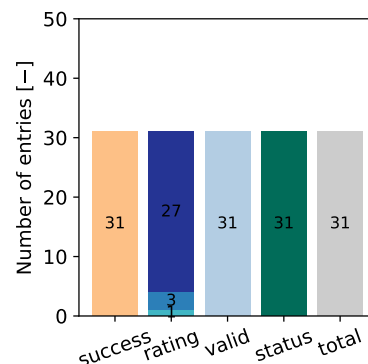
(a) An overview of the data generated during the multi-task phase of the study. Since some methods do not report ratings and success and are therefore regarded as valid as long as their status is not deleted, there are more valid entries than such marked as success.



(b) Bar chart showing various properties of the entries provided by the Overlort tenant.



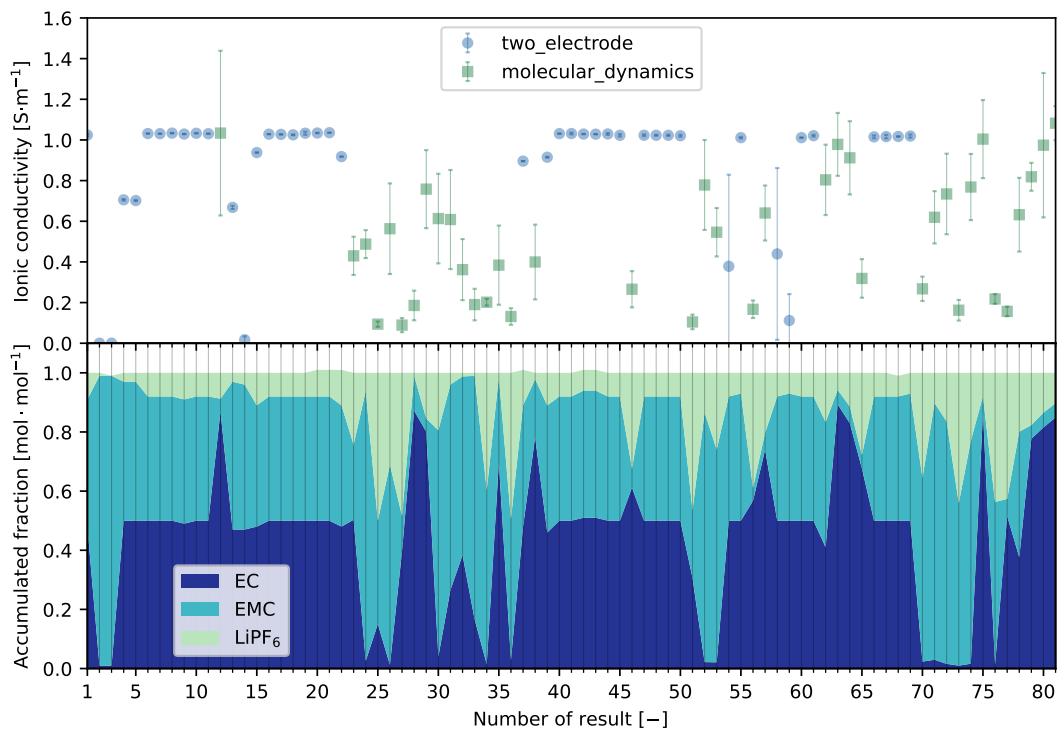
(c) Bar chart showing various properties of the entries provided by the ASAB tenant.



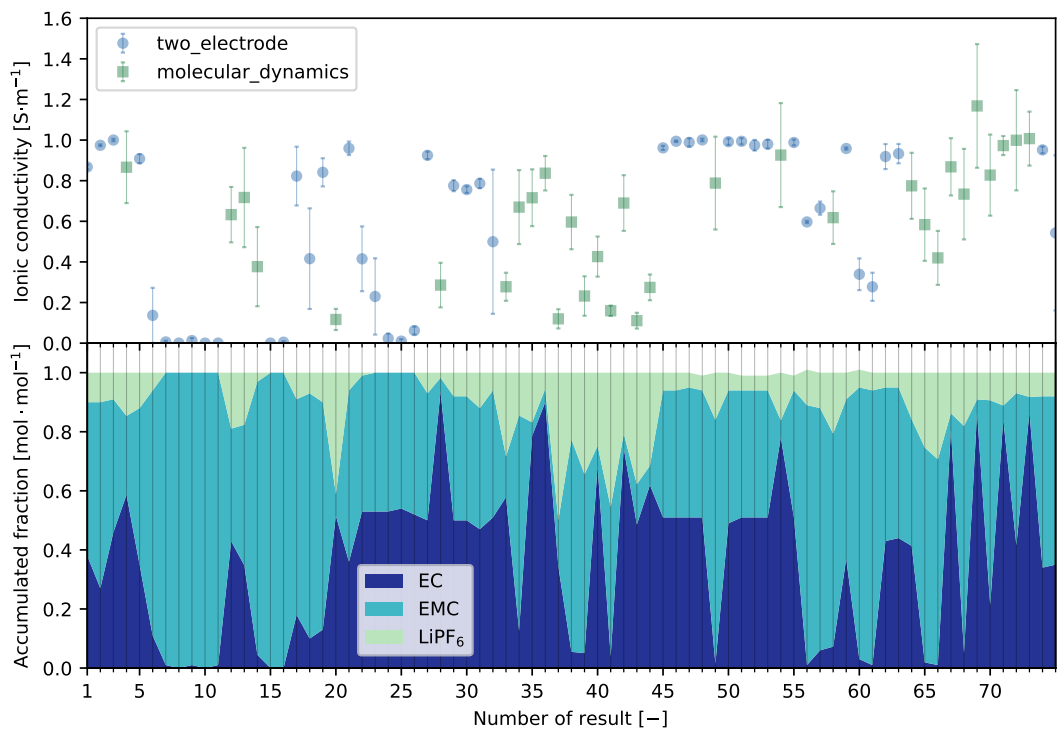
(d) Bar chart showing various properties of the entries provided by the MD tenant.

Figure S13: Overview of entries in the FINALES internal database recorded during the multi-task phase of the campaign. The legend shown in (a) is also valid for the figures in (b) - (d).

one considering the limitations are similar for each of the tenants in the single-task phase. However, there is a significant difference between the two tenants regarding the solvent composition of these predicted optima. One possible cause is that the formulations showing a high ionic conductivity in the experiments are close to the limitations of the experimental tenant, as it is visible in Figure S15a and Figure S15b, which hinders a further exploration towards lower EMC contents. Therefore, the region where the maximum ionic conductivity is predicted for the MD tenant is not accessible to the ASAB tenant, which results in a different observed and predicted optimum when respecting the limitations of the tenants. Furthermore, the dependence of the ionic conductivity on the composition of the solvent is significantly less pronounced than the dependence on the LiPF_6 content as it is visible in the Figures S16 - S17 and also reported in the literature^[8, 17, 18]. Therefore, our system located the region of high ionic conductivity in both phases of this study in a narrow band with respect to the concentration of LiPF_6 , while a precise location with respect to the solvent composition was not achieved. This is likely due to the uncertainty associated with the data^[8] and the optimizer model. In contrast, the predictions of the global maximum for the MD tenant and the ASAB tenant are in good agreement in the single-task phase shown in the top part of Figure 2 in the main article.



(a)



(b)

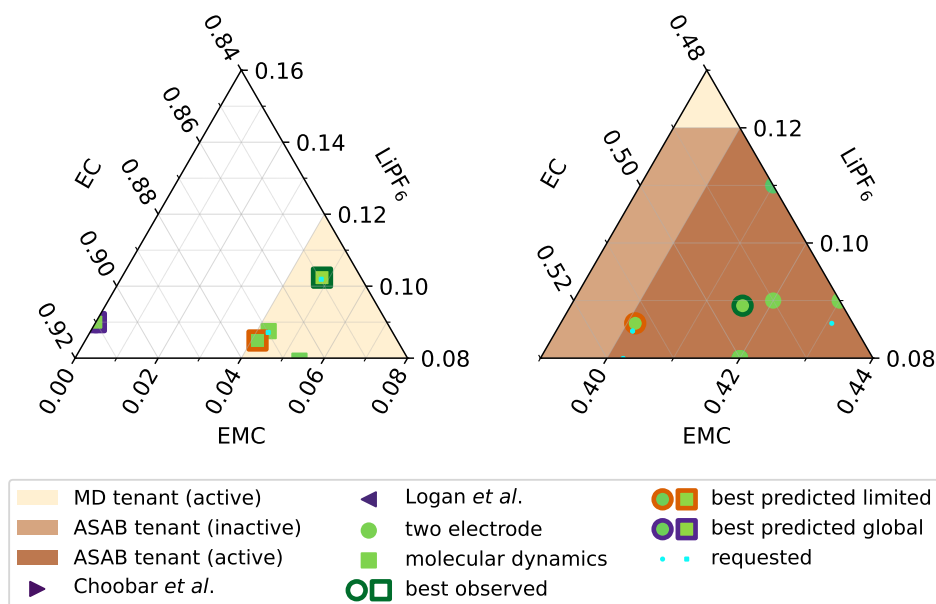
Figure S14: The posted results for ionic conductivity and the corresponding formulations of the electrolyte in the sequence as they were posted to FINALES during the (a) single-task phase and (b) multi-task phase of the study.

The bottom part of Figure 2 in the main article shows a different picture. While all three optima are close to each other for the ASAB tenant, the predicted optimum formulations differ from the formulation with the best observed ionic conductivity for the MD tenant. This could again be due to the optima for the ASAB tenant being located close to its limitations of the accessible chemical space. Also, the global predictions do not match among the tenants in the multi-task phase. A possible reason for this mismatch is the uncertainty of the model associated with extrapolation to regions of the chemical space, where no reported data is available. Furthermore, the model found a high correlation between the computational and experimental results in the single-task phase of this study, which was not observed in the multi-task phase. This is likely due to more noisy experimental data in the multi-task phase of the study, probably leading to a less smooth model. The increased noise likely arises due to the decision to not delete data affected by hardware malfunctioning like leakage, which was done to reduce human intervention to a minimum. An analysis of the influence of leakage on the electrolyte formulations is provided in the section S5.2.

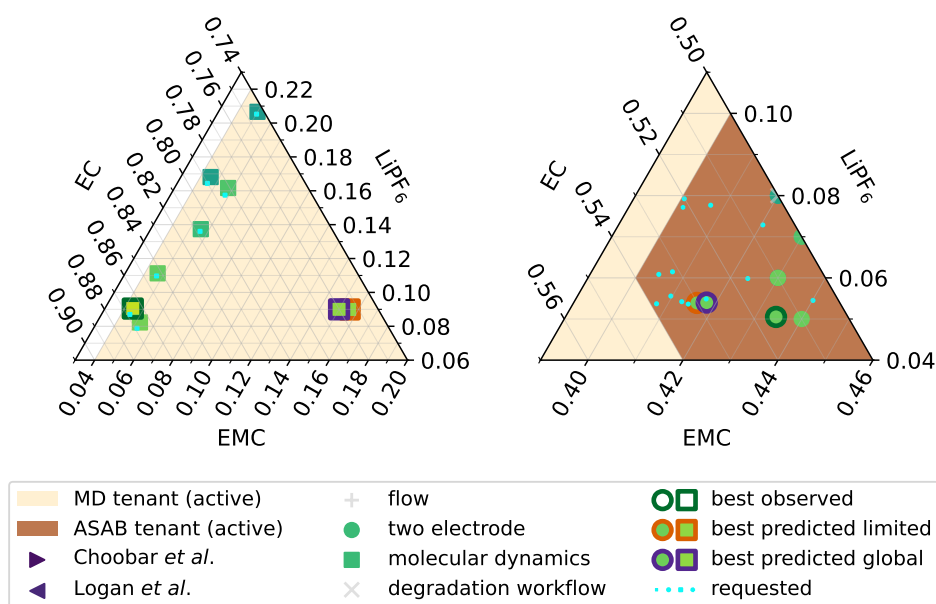
Furthermore, Figures 2 and S15 show that the otherwise small mismatch between the requested formulations and those reported in the results is larger in the region close to the limitations for the ASAB tenant. Although approximations are required in the computational as well as the experimental results, the reported formulations for the computational results are in good agreement with the requested ones.

A possible reason for the mismatch in the results posted by the ASAB tenant could be the proximity to the boundary of the accessible chemical space. The boundaries for the experimental tenant are defined based on the stock solutions supplied to the system. Therefore, the maximum and minimum molar fractions of individual components may only be accessible by using a single one of the stock solutions, since any mixture would result in a dilution of the respective component. This hinders the variation of the remaining components, if one of them is set to an extreme value. In the case of the experimental tenant, the maximum fraction of EC corresponds to the fraction observed in the stock solution containing only EC and EMC. The addition of any other stock solution results in a dilution of EC in the final electrolyte. This issue is visible in Figure 2 in the main article for the single-task and the multi-task phase of the study, respectively. In the single-task phase of the campaign, the mismatch between the requested and reported formulations is even more striking due to a poor choice of the lower limit for EMC prior to the correction. However, the data show that this limit was too low and could not be reached with the stock solutions used in this study. This exemplifies the significance and complexity of defining and reporting the limitations for a tenant.

The temperature ranges covered in the single-task phase of the study are 299.8 K to 301.0 K for the ASAB tenant and 293.4 K to 308.1 K for the MD tenant. In the multi-task phase, the ranges are 299.1 K to 300.5 K for the ASAB tenant and 291.2 K to 307.4 K for the MD tenant. Due to a lack of active temperature control, the ASAB tenant only accepts requests at 300 K and the variation in temperature originates due to temperature fluctuations in the course of the study. In contrast, the MD tenant uses the NHL thermostat^[4] to control the temperature in the simulation supercell, such that the MD simulations can be run at arbitrary temperature. However, we focus on the liquid state of the electrolyte at room temperature, so a default target temperature of 298.0 K for the thermostat was configured in the MD tenant. The MD simulations show large temperature variations between the configurations, since the supercell is a small microscopic system where the local fluctuations cannot be evened out as easily as in a macroscopic system. Based on the temperature ranges covered by the tenants in this study, literature data of ionic conductivity at 293.15 K and 313.15 K as reported in the references^[19, 20] is shown in Figure 3a.



(a)



(b)

Figure S15: Zoomed-in views of the regions with high ionic conductivity identified for the MD tenant (left) and the ASAB tenant (right) during the (a) single-task phase and (b) multi-task phase of the study. The coloring of the data points is based on the mean ionic conductivity using the same colorbar as in Figure 2 of the main article.

4.2 Optimizer Models

The model predictions and uncertainties obtained from training on the dataset at the end of the single-task phase of this study are presented in Figure S16 for the MD tenant and in Figure S17 for the ASAB tenant. It can be seen, that the regions of maximum ionic conductivity are found in a similar area within the chemical space for the MD and ASAB tenant. The uncertainty in the predictions for the MD tenant is higher than the uncertainty in the predictions for the ASAB tenant. The high uncertainty in the high-LiPF₆ and low-EC region can be explained by this region not being accessible

to either of the tenants and therefore, the model is required to extrapolate outside of the training region to obtain predictions in this region. The region of maximum ionic conductivity found in the multi-task phase of the campaign also matches with the one found in the single-task phase for both tenants as can be seen in Figure S18 and Figure S19. However, the model of the ASAB tenant obtained from the data of the multi-task phase is less smooth than the model obtained from the data generated in the single-task phase as gets obvious from comparison of Figure S17 with Figure S19. This could possibly be caused by increased scatter of the datapoints in the multi-task phase and difference in measurement noise.

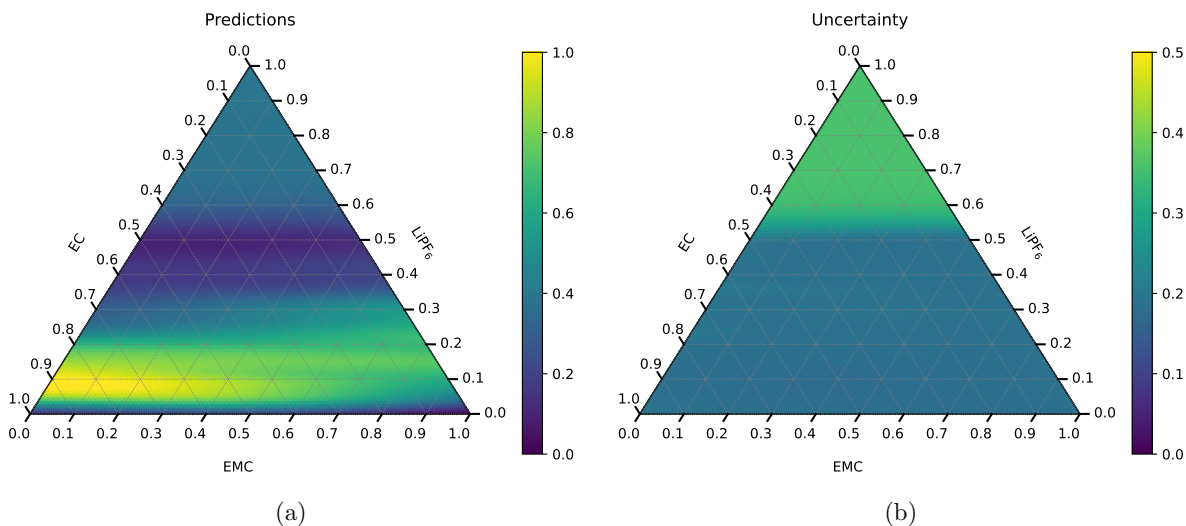


Figure S16: The model predictions (a) and uncertainties (b) for the MD tenant obtained from the optimizer after training it with the data generated in the single-task phase of the study.

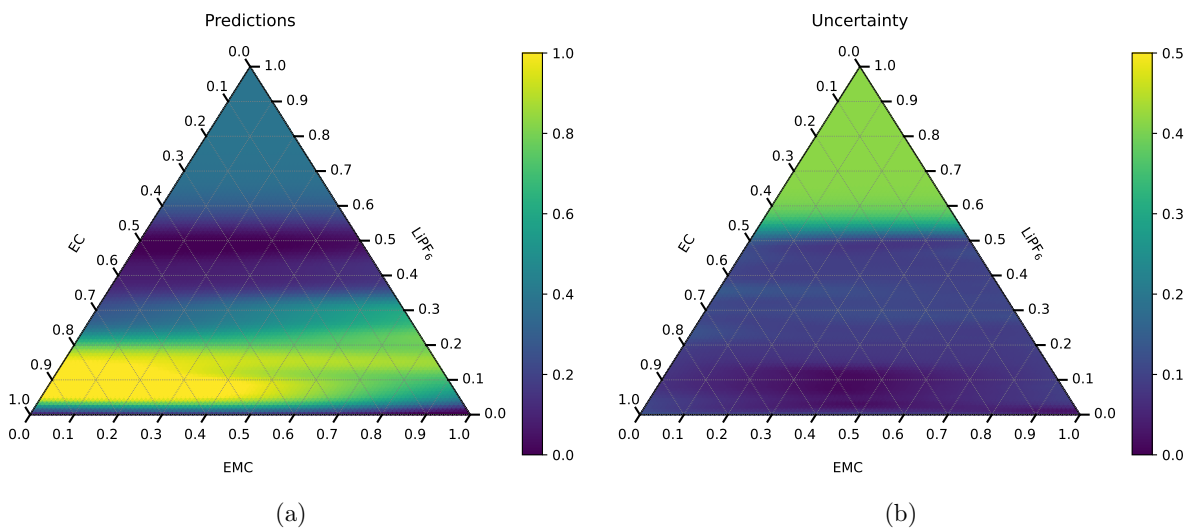


Figure S17: The model predictions (a) and uncertainties (b) for the ASAB tenant obtained from the optimizer after training it with the data generated in the single-task phase of the study.

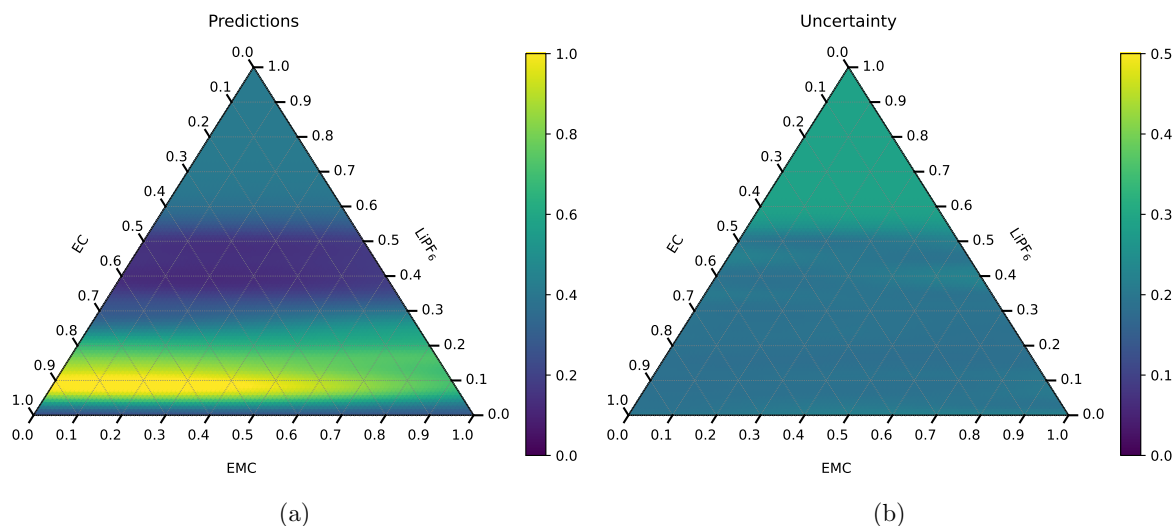


Figure S18: The model predictions (a) and uncertainties (b) for the MD tenant obtained from the optimizer after training it with the data generated in the multi-task phase of the study.

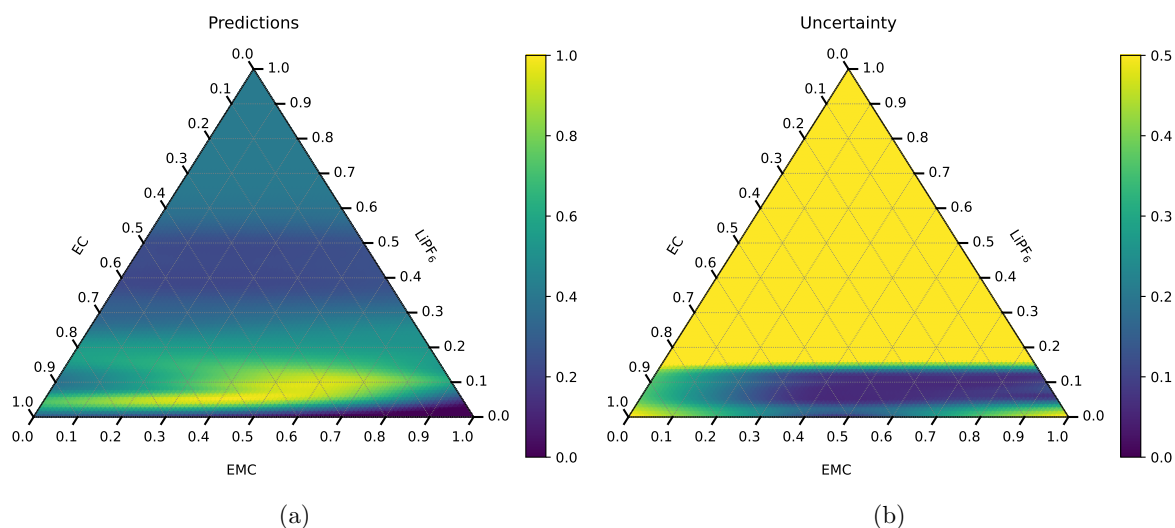


Figure S19: The model predictions (a) and uncertainties (b) for the ASAB tenant obtained from the optimizer after training it with the data generated in the multi-task phase of the study.

4.3 Formulations with maximum ionic conductivity

Table S3 shows the numeric values for the formulations with predicted and observed maximum ionic conductivity as obtained from an optimizer model trained on the dataset after the end of each phase. The data corresponding to formulations predicted while respecting the limitations of the respective tenant, are reported as *limited* in the *Optimum* column. The electrolyte formulations used in the manually posted requests in the multi-task phase of the campaign are reported in Table S4.

Table S3: The optima identified from the model trained on the data after the single-task phase and the multi-task phase, respectively. The optima refer to the formulation with the highest observed ionic conductivity (κ), the highest predicted κ when respecting the limitations, and the globally highest κ , respectively. The formulations are reported as the molar fractions x of the constituents. Ionic conductivity and the respective uncertainty are given in S m^{-1} and the molality is given in mol kg^{-1} .

Phase	Optimum	Parameter	two_electrode	molecular_dynamics
single-task	observed	x_{LiPF_6}	0.09	0.102371
		x_{EC}	0.5	0.849395
		x_{EMC}	0.42	0.048233
		molality	1.03	1.28
		predicted κ	1.0356 ± 0.0004	1.0822 ± 0.1804
	limited	x_{LiPF_6}	0.086045	0.084907
		x_{EC}	0.512727	0.873643
		x_{EMC}	0.401228	0.04145
		molality	0.99	1.05
		predicted κ	1.0452 ± 0.0114	1.028 ± 0.1804
	global	x_{LiPF_6}	0.09	0.09
		x_{EC}	0.91	0.91
		x_{EMC}	0.0	0.0
		molality	1.12	1.12
		predicted κ	1.2811 ± 0.067	1.0369 ± 0.1814
multi-task	observed	x_{LiPF_6}	0.05	0.090458
		x_{EC}	0.51	0.865261
		x_{EMC}	0.43	0.044281
		molality	0.56	1.12
		predicted κ	1.0007 ± 0.0064	1.1681 ± 0.3044
	limited	x_{LiPF_6}	0.053912	0.089922
		x_{EC}	0.53009	0.754623
		x_{EMC}	0.415999	0.155454
		molality	0.60	1.09
		predicted κ	1.0003 ± 0.0577	1.0675 ± 0.1829
	global	x_{LiPF_6}	0.054	0.09
		x_{EC}	0.528	0.76
		x_{EMC}	0.418	0.15
		molality	0.60	1.09
		predicted κ	1.0003 ± 0.0576	1.0675 ± 0.1828

Table S4: The electrolyte formulations used in the manually posted requests for predicted EOL in the multi-task phase. The formulations are reported as the molar fractions x of the constituents.

Formulation type	Fraction	Value
predicted optimum	x_{LiPF_6}	0.077146
	x_{EC}	0.521413
	x_{EMC}	0.401441
same x_{EC} as predicted optimum, but lower x_{LiPF_6}	x_{LiPF_6}	0.01
	x_{EC}	0.521413
	x_{EMC}	0.468587
same x_{EC} as predicted optimum, but higher x_{LiPF_6}	x_{LiPF_6}	0.12
	x_{EC}	0.521413
	x_{EMC}	0.358587

4.4 EOL

The acquired data in the sequence of them being posted to FINALES together with a representation of the respective formulations are shown in Figure S20. A single iteration of the EOL workflow takes several days. The data associated with the manually submitted requests and the EOL experimentally determined from cycling the cells up to 200 cycles are also presented in Figure S20. It must be noted that the predicted optimized formulations used for the manual requests in the multi-task phase as listed in Table S4 differ from the optimized formulations reported in Figure 2 and Table S3, since the model is retrained after each iteration and therefore the predictions based on a model trained later differ from earlier models.

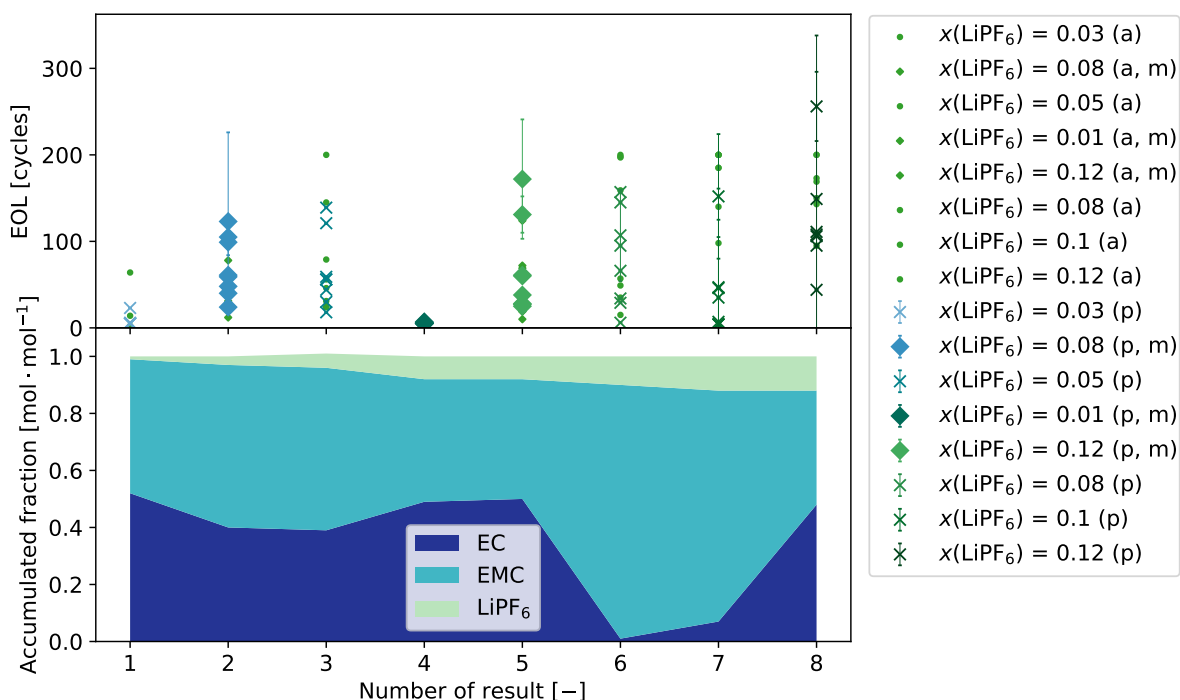


Figure S20: The EOL data collected during the multi-task phase of the campaign, presented in the sequence in which the results were posted. The labels report the molar fraction of LiPF₆ and indicate if the data correspond to a predicted EOL (p) or an EOL determined after the final export (a). The results additionally marked with an m indicate that the request related to this result was manually posted to FINALES.

The cells that did not complete 200 cycles prior to the intermediate export were cycled until the expected time for 200 cycles elapsed in the experiment. Therefore, a comparison between the experimental EOL and the prediction based on the data provided in the intermediate export is possible and presented in Figure S21. It gets clear that the spread of the EOL within a batch is significant in the experiments as well as in the predictions. Furthermore, it can be observed that the spread of the predictions increases for higher EOL in the experiment. This can be understood since the EOL of cells reaching 80 % of their initial capacity within the cycles endured prior to the intermediate export is known and the associated uncertainty of the prediction should be expected to be low. From Figure S21, one can further observe that the model shows a tendency to underestimate the EOL of cells showing an experimental EOL above approximately 100 cycles. This might be due to the model being trained with data originating from shorter cycling experiments. Since the model has not seen how cells with a higher EOL behave later in their lifetime, it cannot accurately extrapolate the behaviour for these cells.

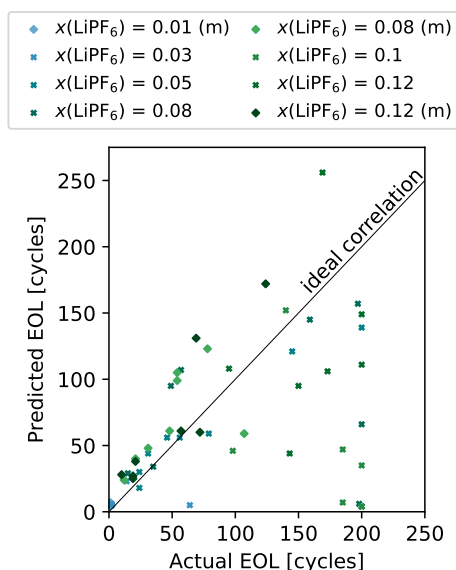
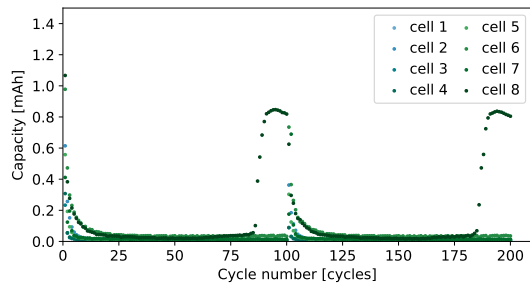


Figure S21: A parity plot between the experimental and the predicted EOL data. The results additionally marked with an *m* indicate that the request related to this result was manually posted to FINALES.

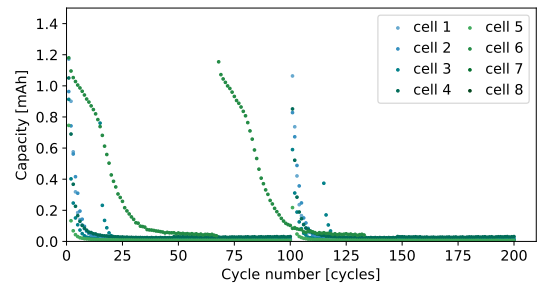
From Figure 3b, the variation of results can clearly be observed for the two batches produced with ~ 0.91 m LiPF₆. Overall, the predicted and the experimentally determined EOL are in reasonable agreement. The only exception is observed for the formulation containing 1.07 m LiPF₆, for which the model significantly underestimated the experimentally observed EOL. It can further be noted that the scatter of the predicted (as well as the actual) EOL is very low for the low-molality formulations. This may again be caused by the cells reaching their EOL prior to the intermediate export of the cycling data. The prediction at 1.07 m LiPF₆ stands out by the median prediction of 21 cycles and only one high predicted EOL of 152 cycles. A possible reason could be, that the duration of approximately 40 cycles has to be estimated prior to the experiments and this estimate is applied globally to all of the cycling experiments in this study. As a consequence, the number of cycles endured by the time of the intermediate export may differ between the cells within and in between batches. This leads to differences in the data used for the prediction, which may affect its quality. In the case of the batch of cells containing the electrolyte with 1.07 m LiPF₆, 5 out of 8 cells reached a lower number of cycles by the time of the export than the remaining 3 cells (see Figure S22e), which might have provided an insufficient database for the prediction. Furthermore, the predicted EOL of the cells with the 1.07 m LiPF₆ electrolyte may additionally be affected by the tendency of the model to underestimate high EOL values.

4.5 Cycling results

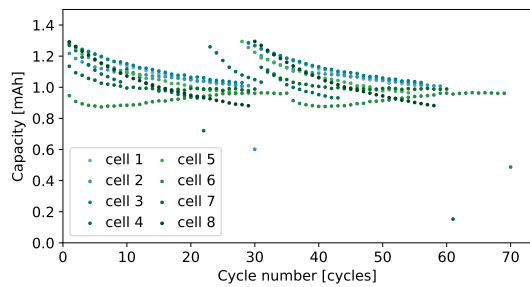
The data regarding the capacity evolution passed to the the Degradation model tenant for the batches of cells used in the multi-task phase are presented in Figure S22.



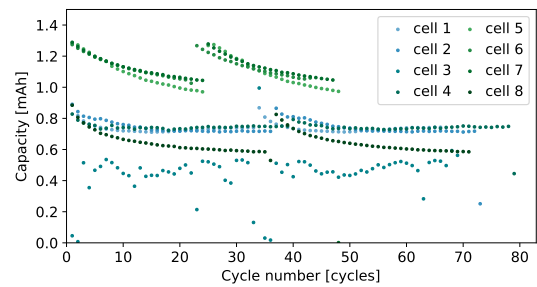
(a) Capacity evolution for the cells containing ~ 0.11 m LiPF₆.



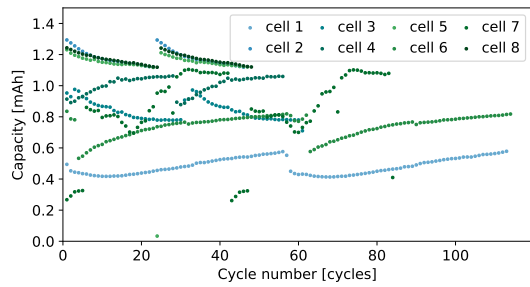
(b) Capacity evolution for the cells containing ~ 0.32 m LiPF₆.



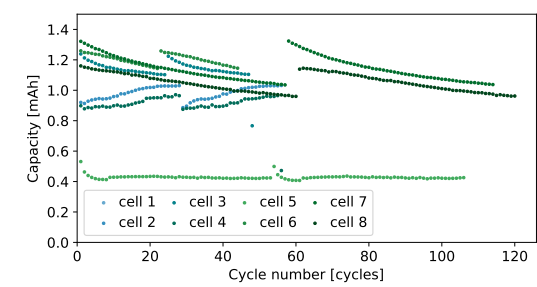
(c) Capacity evolution for the cells containing ~ 0.53 m LiPF₆.



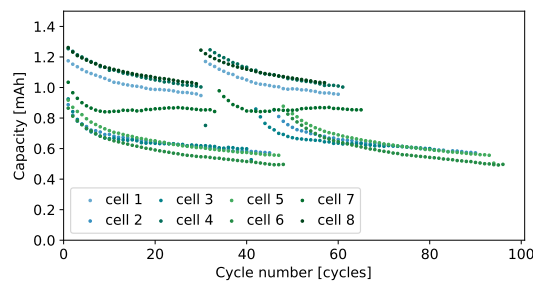
(d) Capacity evolution for the cells containing ~ 0.91 m LiPF₆.



(e) Capacity evolution for the cells containing ~ 1.07 m LiPF₆.



(f) Capacity evolution for the cells containing ~ 1.33 m LiPF₆.



(g) Capacity evolution for the cells containing ~ 1.43 m LiPF₆.

Figure S22: Capacity evolution *versus* the number of cycles endured. The data covers the cycles endured until the time of the intermediate export.

5 Error analysis

5.1 NMR analysis

Since the formulations reported in the results of the ASAB tenant correspond to the set-values, NMR spectra were recorded to investigate the EC:EMC ratio and compare it to the requested and reported ones. To do so, several formulations prepared for cell-assembly were randomly selected to record ^1H -NMR spectra for these formulations. From the ratios of intensities between signals originating from nuclei in the EC and EMC molecules, the molar fraction of these molecules is obtained. The results are reported in Table S5. The NMR analysis of the formulation is limited to the ^1H spectra, because for the other nuclei, no two species can be detected in a single spectrum. The data show deviations between -6.79% and 6.98% of the reported value and two exceptionally high deviations of -38.24% and 32.55% for formulations with a low ratio of EC:EMC. This shows, that the reported formulations are not reliable for low ratios of EC:EMC, while the deviations are lower for intermediate ratios. A possible reason could be the residues of previous electrolyte formulations not being fully removed or limitations of dosing accuracy for too low set flow rates in the experimental setup.

Table S5: The molar ratios of EC:EMC in randomly selected electrolyte formulations prepared by the ASAB tenant for the assembly of coin cells during the execution of the workflow demonstrated in this study. The designations of the multiplets are abbreviated by t for the triplet, s for the singlet, and q for the quartet. The relative deviation between the average ratio and the reported one is given with respect to the reported value.

request ID	Intensities						EC:EMC				relative deviation [%]	
	EMC			EC			s:t	s:s	s:q	average		reported
	t	s	q	s	q	s						
75de3efc-3b15-4849-be5a-8249a6192cd6	3	2.95	2.07	3.02	0.76	0.77	0.73	0.75 ± 0.02	0.70	6.98		
23092bc7-f0c0-4e45-8a84-198857f9caa4	3	2.98	2.10	4.50	1.12	1.13	1.07	1.11 ± 0.03	1.19	-6.79		
b2556b84-754b-49da-90b5-f225ca9a329e*	3	2.98	2.14	4.87	1.22	1.23	1.14	1.19 ± 0.04	1.14	4.75		
cd554e24-2019-43ff-b97e-a05c987566b2*	3	2.90	2.12	4.79	1.20	1.24	1.13	1.19 ± 0.04	1.20	-0.94		
0baa7ad6-1b7d-40d4-b90f-900a21be3d5b**	3	2.69	1.84	0.20	0.05	0.06	0.05	0.05 ± 2.45 · 10 ⁻³	0.09	-38.24		
9f285bed-1eb5-4131-8788-c92fd8937450	3	3.02	2.03	0.06	0.01	0.01	0.01	0.015 ± 9.07 · 10 ⁻⁵	0.011	32.55		

* minor impurity at EMC triplet.

** impurity at EMC triplet.

5.2 Estimation of the effect of leakage issues in the experimental tenant

In the course of the demonstration, the ASAB tenant leaked upon the preparation of several samples. The most likely reason is a high viscosity of some formulations, which results in an increased pressure within the system exceeding the limits of the valves. Leakage issues may have twofold effects on the experiments. If the leakage appears on a valve providing the prepared sample to the electrochemical cell, the cell may not be filled properly resulting in poor contact and poor quality of the measured results. However, the tenant reports the quality of the results in its posts to FINALES which mitigates the effect since results of insufficient quality are disregarded by the optimizer. Another effect of leakage issues arises, if the leakage appears at a valve, through which a stock solution is provided to the union, where the flows are merged. In this case, the volume flow of the affected stock solution is altered resulting in erroneous formulations. In order to provide an impression of the error a leakage imposes on the formulations, a comparatively severe leakage, which was noticed on 6th of November 2023 during the multi-task phase of the demonstration presented in this study, is analyzed in the following. The affected valves were V2, V4, V5, V6, V7, and V8. However, the leakage on V2 and V4 was too little to be analyzed in detail. Therefore, the focus was put on the other four valves. Figure S23 shows the four vials analyzed in the following.

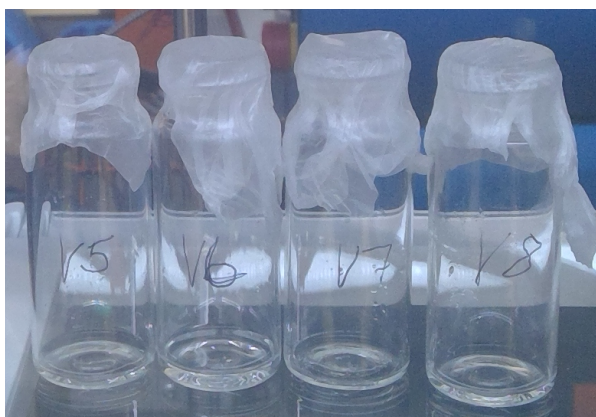


Figure S23: The vials, in which the leaked liquid from valve V5, V6, V7, and V8 was collected, respectively. It can be seen, that the amount of liquid in the vials differs.

Since leaked liquid is caught in glass vials mounted on the system, the mass of the lost liquid could be recorded for some of the vials. The measurements were taken on the 9th of November 2023. The recorded masses together with the stock solution associated with the respective valve are reported in Table S6. The results show, that the most severe leakage occurred for V6, which corresponds to the 1.5 M LiPF_6 in EC:EMC (1:1 by weight) stock solution. According to Ding *et al.*^[8], the viscosity of solutions of LiPF_6 in EC and EMC increases for higher EC content. Hence, it appears reasonable, that the leakage at valve V6 is more severe than at V5 since the stock solution at V5 does not contain EC. The vials V7 and V8 are handling the formulated electrolyte and their leakage is therefore less critical regarding the accuracy of the formulation as mentioned above.

To get a better idea as to which stock solution or mixture was leaked, NMR spectra of the residues were recorded on an *X-Pulse Benchtop NMR* by Oxford Instruments GmbH. Since the amount of some of the residues was too little to sufficiently fill the NMR tube, these samples were filled up using cyclohexane. To reduce additions to a minimum, the external lock of the NMR-device was used and the addition of a reference substance was omitted. The chemical shift scale in the spectra is manually referenced to the singlet of EMC in the ^1H spectra, to the Li signal in the ^7Li spectra and the PF_6^- signal showing the lower chemical shift in the ^{19}F spectra. The results are summarized in Table S7. The NMR-spectra after phasing, baseline correction and 1 Hz exponential apodization are presented in Figures S24 and S25. It must be noted, that the spectra presented in Figures S24 and S25 are presented with different scalings along the y-axis to make the signals visible in all the spectra.

The EC detected in the ^1H -NMR spectrum related to V5 indicates, that the leaked fluid is not

Table S6: The masses of the leaked fluid for the affected valves and the stock solution associated with the respective valve.

valve	stock solution	mass [g]		
		vial + liquid	vial	liquid
V5*	1.5 M LiPF ₆ in EMC	19.0335	18.7906	0.2429
V6	1.5 M LiPF ₆ in EC:EMC (1:1 by weight)	19.8055	18.7202	1.0853
V7**	formulated electrolyte	18.7912	18.7128	0.0784
V8	formulated electrolyte	19.1754	18.7693	0.4061

* The caught liquid shows two phases and does not mix with cyclohexane

** Some of the liquid might have been lost upon removing the vial from the setup.

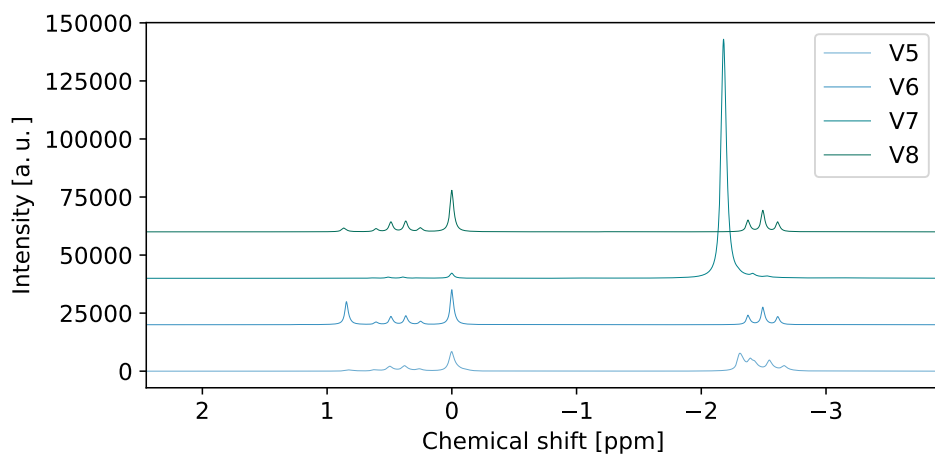
Table S7: The components of the leaked liquids for the respective valves. It must be noted, that the valve V5 does not seem to leak only the stock solution connected to this valve.

valve	stock solution	molecules detected using NMR
V5	1.5 M LiPF ₆ in EMC	LiPF ₆ , EMC, EC, cyclohexane
V6	1.5 M LiPF ₆ in EC:EMC (1:1 by weight)	LiPF ₆ , EMC, EC
V7	formulated electrolyte	LiPF ₆ , EMC, cyclohexane
V8	formulated electrolyte	LiPF ₆ , EMC, EC

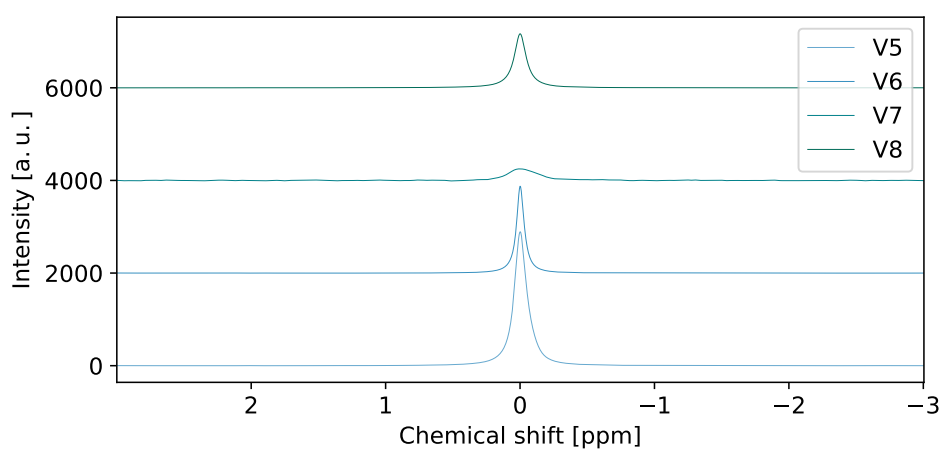
the pure stock solution as this does not contain EC in the case of valve V5. A possible reason could be, that the check valve in the line blocking the flow of the electrolyte formulation from the union back to the valve V5 did not function properly causing the sample to leak at V5 once a too high pressure was generated. The triplet of the EMC is superimposed with another signal, which might arise due to the added cyclohexane to achieve sufficient sample volume for the NMR measurement. The distortion of the signal may be due to the sample being biphasic in the NMR tube. The lack of EC in the sample associated with the leakage at valve V7 may be due to the very little amount of sample available. Cyclohexane had to be added to this sample to achieve sufficient sample volume for the NMR measurement. Therefore, a small amount of EC, which may have been present may be diluted too much to result in a clear signal in the ¹H-NMR spectrum. The recorded ⁷Li and ¹⁹F spectra reveal the presence of LiPF₆ in all of the samples.

Figure S25 shows an enlarged view of the ¹⁹F spectrum obtained for the residue collected from the vial connected to V8. Besides the signals, which can be assigned to the fluorine nuclei in PF₆⁻, this spectrum shows additional signals to the left and right of the reference signal. Using their coupling constant of approximately 930 Hz as an indicator, and assuming they might originate from a degradation product of LiPF₆ with water, they can possibly be assigned to PFO(OH)₂^[21, 22]. However, referenced measurements and ³¹P spectra would be required to confirm this tentative assignment. Consequently, it can be deduced, that the NMR sample was contaminated with water. Based on the data available, it cannot be traced back, whether the contamination appeared after removing the NMR sample from the glovebox or even before. Since the sample tube was closed using a regular NMR tube cap and sealing tape, it is likely, that water had access to the sample, while it was outside of the inert atmosphere of the glovebox. Furthermore, the NMR magnet operates at 40 °C, which may further degradation.

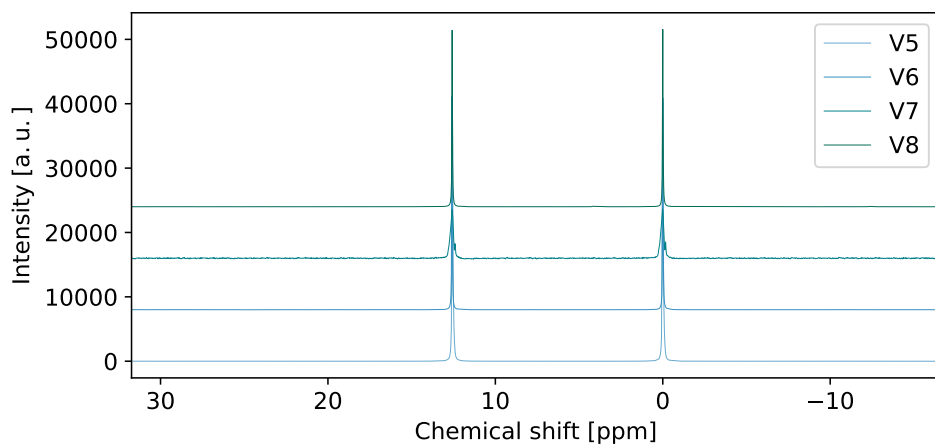
Since the identifier of the first and last request affected by the leakage is known, the maximum period of time, during which the leakage occurred, can be determined based on the timestamps of the request of the first and the result of the last affected sample. The resulting maximum duration of the leakage can thus be determined to be approximately 2 h 10 min. In this time, 3 results were posted and hence potentially affected. This means, that on average 0.6042 g of liquid per electrolyte formulation are lost due to the leakage. For a sample volume of approximately 3 mL for electrochemical measurements and approximately 6 mL for cell assembly. Using the density values at 26.8 °C of 1.0049 g cm⁻³ for EMC as the least dense stock solution and 1.2880 g cm⁻³ for 1.5 M LiPF₆ in EC:EMC



(a) ^1H NMR-spectra.



(b) ^7Li NMR-spectra.



(c) ^{19}F NMR-spectra.

Figure S24: NMR spectra of the leaked solutions caught in the vials.

(1:1 by weight) as the most dense stock solution and neglecting mixing volumes, this results in an approximate volumetric error between 16% and 20% of the target volume for the electrochemical measurements and 8% to 10% of the target volume for the electrolyte formulations prepared for cell assembly. This shows, that severe leakage may affect the quality of the measurement. However, the detection of leakage during autonomous operation is not possible in the current experimental setup.

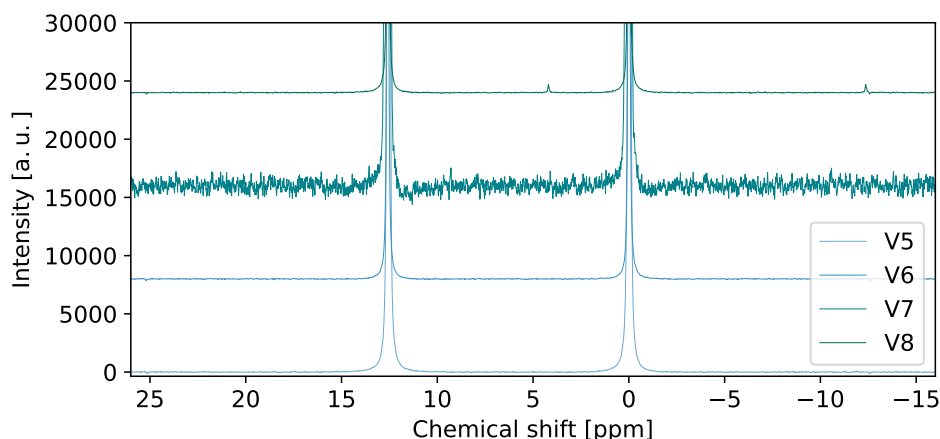


Figure S25: An enlarged view of the ^{19}F spectra showing the additional signals in the spectra related to the residues collected from the vial connected to the valve V8.

To enable the autonomous operation of the ASAB tenant, it was therefore decided that affected data should remain in the database during the multi-task phase. This increases the scatter of the data resulting in larger uncertainty of the model predictions. In the future development of the experimental setup, a monitoring of the pressure or a detection of leakage needs to be considered.

References

- [1] Dassault Systèmes Americas Corporation, Biovia pipeline pilot, **2022**, URL <https://www.3ds.com/products/biovia/pipeline-pilot>.
- [2] Dassault Systèmes Americas Corporation, Biovia materials studio, **2022**, URL <https://www.3ds.com/products/biovia/materials-studio>.
- [3] R. L. C. Akkermans, N. A. Spenley, S. H. Robertson, *Molecular Simulation* **2021**, *47*, 7 540.
- [4] A. A. Samoletov, C. P. Dettmann, M. A. J. Chaplain, *J. Stat. Phys.* **2007**, *128* 1321.
- [5] H. C. Andersen, *J. Chem. Phys.* **1980**, *72* 2384.
- [6] F. Hanke, N. Modrow, R. L. C. Akkermans, I. Korotkin, F. C. Mocanu, N. V. A., M. Veit, *Journal of The Electrochemical Society* **2019**, *167*, 1 013522.
- [7] F. Rahmanian, Modular and Autonomous Data Analysis Platform (MADAP)", **2023**, URL <https://doi.org/10.5281/zenodo.8220661>.
- [8] M. S. Ding, X. K., S. S. Zhang, K. Amine, G. L. Henriksen, T. R. Jow, *Journal of The Electrochemical Society* **2001**, *148*, 10 A1196.
- [9] P. Dolin, B. Ershler, *Acta physicochim. URSS* **1940**, *13* 747.
- [10] J. Huang, C.-K. Li, *Journal of Physics: Condensed Matter* **2021**, *33*, 16 164003.
- [11] F. Liot, big-map-archive-api-client, **2023**, URL <https://pypi.org/project/big-map-archive-api-client>.
- [12] S. Clark, F. L. Bleken, S. Stier, E. Flores, C. W. Andersen, M. Marcinek, A. Szczesna-Chrzan, M. Gaberscek, M. R. Palacin, M. Uhrin, J. Friis, *Advanced Energy Materials* **2022**, *12*, 17 2102702.

- [13] S. Clark, J. Friis, F. L. Bleken, C. W. Andersen, E. Flores, H. Snijder, S. Stier, Big-map/battinfo:v0.6.0, **2023**, URL <https://doi.org/10.5281/zenodo.8260800>.
- [14] M. Sporny, D. Longley, G. Kellogg, M. Lanthaler, N. Lindström, *W3C Recommendation*, Jul **2020**.
- [15] R. Angles, M. Arenas, P. Barceló, A. Hogan, J. Reutter, D. Vrgoč, *ACM Comput. Surv.* **2017**, *50*, 5.
- [16] N. Francis, A. Green, P. Guagliardo, L. Libkin, T. Lindaaker, V. Marsault, S. Plantikow, M. Rydberg, P. Selmer, A. Taylor, In *Proceedings of the 2018 International Conference on Management of Data*, SIGMOD '18. Association for Computing Machinery, New York, NY, USA, ISBN 9781450347037, **2018** 1433–1445, URL <https://doi.org/10.1145/3183713.3190657>.
- [17] F. Rahmanian, M. Vogler, C. Wölke, P. Yan, M. Winter, I. Cekic-Laskovic, H. S. Stein, *Batteries & Supercaps* **2022**, *5*, 10 e202200228.
- [18] A. Narayanan Krishnamoorthy, C. Wölke, D. Diddens, M. Maiti, Y. Mabrouk, P. Yan, M. Grünebaum, M. Winter, A. Heuer, I. Cekic-Laskovic, *Chemistry–Methods* **2022**, *2*, 9 e202200008.
- [19] B. Ghalami Choobar, H. Modarress, R. Halladj, S. Amjad-Iranagh, *The Journal of Physical Chemistry C* **2019**, *123*, 36 21913.
- [20] E. R. Logan, E. M. Tonita, K. L. Gering, L. Ma, M. K. G. Bauer, J. Li, L. Y. Beaulieu, J. R. Dahn, *Journal of The Electrochemical Society* **2018**, *165*, 3 A705.
- [21] C. L. Champion, W. Li, B. L. Lucht, *Journal of The Electrochemical Society* **2005**, *152*, 12 A2327.
- [22] S. Wilken, M. Treskow, J. Scheers, P. Johansson, P. Jacobsson, *RSC Adv.* **2013**, *3* 16359.

7 Discussion and Conclusion

Although today liquid electrolytes are established in state-of-the-art lithium-ion batteries, research for novel electrolyte formulations [44, 46, 55] is still ongoing. The publication presented in chapter 5 [95] is an example that showcases how the combination of physicochemical, spectroscopic and electrochemical results can be used to investigate electrolytes containing novel Hückel-type salts. The investigated salts were previously reported to be stable when exposed to humidity [53, 54], at elevated temperatures and in voltage ranges relevant for lithium-ion batteries [52]. They can further be synthesised in a single step process [52, 54]. Their use would therefore alleviate the high demands on the atmosphere, in which the electrolytes are handled, which harbours the potential to reduce production costs [54]. The study in chapter 5 [95] demonstrates a combination of results obtained from *infrared spectroscopy* (IR) and Raman spectroscopy with data obtained for ionic conductivity, viscosity, and anion self-diffusion coefficients to gain insights about the possible dissociation behaviour of the ions. While the observed viscosity of the electrolyte solutions increases from those containing LiTDI *via* those based on LiPDI to the LiHDI-containing ones, the ionic conductivity does not follow this trend as the highest ionic conductivity in this study is found for electrolytes using LiPDI. [95] Further research is needed to understand this behaviour since the perfluorinated alkyl side chain length of LiPDI is intermediate between those of LiTDI and LiHDI. If the solvation behaviour would follow a trend with the length of the perfluorinated side chain and if this would have direct implications for the ionic conductivity, the trend should also be observed in the ionic conductivity. Niedzicki *et al.* [53] suggest for a similar electrolyte system containing LiHDI a reduced mobility of the ions due to its larger anion as a possible reason for it showing lower ionic conductivity than it would be expected based on its degree of dissociation. The validation of this suggested cause for the deviation of the ionic conductivity of LiPDI from the expected behaviour in the electrolyte system investigated in chapter 5 demands further research. The incorporation of MD results may enable deeper insights into the coordination and dissociation of the salts and may enable a more fundamental understanding of these processes similar to the insights on the motion of ions in electrolyte solutions obtained from MD methods reported by Mistry *et al.* [133]. The determination of self-diffusion coefficients of the cations in the different solutions would further complete the picture and would be of special interest since the motion of the cations is decisive for the operation of lithium-ion batteries [15]. Overall, the results for ionic conductivity and ionicity of the Hückel-type salts in the analysed electrolytes are found to be inferior to those of LiPF₆ [95]. From the data presented in chapter 5 [95], it can be seen, that minor differences in the behaviour of the Hückel-type salts can be found. However, their interrelation with the structure of the respective anions is not conclusively analysed and requires further studies.

In chapter 6.2 [14], the maximum ionic conductivity is found for approximately 1 m LiPF₆ dissolved in the solvent containing EC and EMC, which is in good agreement with literature data [151–153] if the influence of solvent composition is neglected. This agreement indicates, that the MAP was able to capture the trend. The similarity of the values for the experimental ionic conductivity of electrolytes with comparable compositions (see Figure S14 in chapter 6.2) suggests a reasonable repeatability of the results generated by the ASAB setup. Using the bulk properties of the electrolyte as indicators for cell performance, the results reported in chapter 6.2 might suggest a relation between the ionic conductivity of the electrolyte and the EOL of coin cells using the respective electrolyte. However, due to the uncertainty of the EOL in the experiments and the model predictions, the existence of a correlation or even a causality cannot be concluded from the results of this work. [14] Considering the results obtained from the investigation of bulk electrolyte properties shown in chapter 5, the incorporation of further methods may allow to get better indicators, but the effects of interfacial processes also need to be considered in the investigation of cell

performance [30]. Therefore, the scale bridging approach chosen in chapter 6.2 [14] seems promising to be followed further to investigate correlations between the cell chemistry and its performance. The significance of including tests of device performance when optimising materials was also recently mentioned in a publication by Strieth-Kalthoff *et al.* [12], who reported the integration of materials synthesis, property analysis and performance tests in devices for materials to be applied in organic solid-state lasers.

Besides the findings on the level of battery electrolytes, the publications presented in this thesis also provide insights concerning the research methodology used. Studies like the one presented in chapter 5 [95] or those performed by Ding *et al.* [151, 154–158] to establish the composition-property-performance relationships necessary to design electrolytes for specific applications require the use of diverse techniques and expert knowledge. In this thesis, the ASAB system is shown to be capable of performing repetitive tasks in such studies and therefore reducing the amount of human labour required for data generation [13, 14]. One of these tasks that was essential in chapters 6.1 [13] and 6.2 [14] is the formulation of electrolytes. From the data generated during the multi-task phase of the study presented in chapter 6.2 [14] available in [88], the time between reserving a request for an electrolyte formulation and posting the corresponding result ranges between approximately 17 min and 30 min when considering only a single successful attempt of processing the request. If the ASAB setup is started with empty syringes, the formulation of the first sample takes significantly longer than the aforementioned duration due to the initial filling of the syringes. Although the formulation of an individual electrolyte sample may not necessarily be faster than a human researcher could accomplish it in terms of the absolute time required, leaving the experimental work to the ASAB system enables the researcher to spend time on the curation and interpretation of data and the design of new studies. This aspect was recently mentioned by Stier *et al.* [10] as one of the distinctive advantages of MAPs. When deciding whether the experiments for a study should be performed using the ASAB setup or manual execution would be more efficient, the number of samples is an important aspect to consider. The set-up time of the ASAB setup is comparable to the one of a manual experiment as it essentially includes providing stock solutions and connecting all the required instruments in case they were previously disconnected. Similar tasks are required in preparation of experiments performed by a human researcher using the individual devices in their conventional mode of operation. An additional step in preparation of an automated experiment is the implementation of a Python script if the setup is not operated using the ASAB tenant and an instance of FINALES. The high-level functions provided in the software package of the ASAB setup allow this task to be completed reasonably fast for a researcher, who is familiar with basic Python programming. The most significant difference between conventionally performed experiments and those using the ASAB setup is the consumption of time and chemicals for cleaning after the experiments are finished. Since a human researcher often utilises single-use equipment to formulate electrolytes, the clean-up is significantly facilitated. The ASAB setup includes numerous tubes and components that need to be cleaned in between and after experiments and therefore its use is not efficient when measuring only a few samples. However, in studies involving many samples or autonomous research campaigns such as those presented in chapter 6.1 [13] and 6.2 [14], the automation offers a benefit compared to a human researcher performing the tasks, because the negative impact of the more complex cleaning routine after the experiments is less severe in these cases. The cleaning routine for the formulation unit of the ASAB setup requires the researcher to move the tubes from the vials of the stock solutions to a waste container to avoid contamination of the stock solutions during cleaning. Also, the researcher needs to specify the nodes that shall be cleaned. Subsequently, the setup can automatically perform the cleaning and the researcher only needs to manually remove residues from the syringe pumps and empty the waste after completion. This degree of automation significantly reduces the human time required for cleaning of the system and leaves the consumption of chemicals used in this process as an important aspect to optimise when further developing the ASAB setup. An important advantage of the ASAB setup that should also be noted in this context is that it can transport the samples in closed loops to and from the instruments positioned outside of the glovebox without requiring the removal of the samples from the inert atmosphere. This significantly reduces the risk of degradation of the samples due to exposure to air and humidity and saves time that otherwise would be needed for the operation of the airlock. The use of the ASAB setup to provide the samples to the measuring devices is therefore even attractive

for the analysis of manually prepared samples. The above elucidations include several of the operation modes mentioned in chapter 4. Changes between the different modes of operation and the integration of new hardware or analysis software are facilitated by the modular design of the ASAB setup enabling flexible automated experimentation. The categorisation of the ASAB setup in the levels of autonomy as specified by Hung *et al.* [72] and Tom *et al.* [11] depends on the use case. On the scale suggested by Tom *et al.* [11], the ASAB setup provides at least level 2 hardware autonomy. Depending on the mode of operation, the degree of software autonomy can be varied. Upon the integration with FINALES, level 4 MAPs were demonstrated in the publications shown in chapter 6.1 [13] and 6.2 [14]. On the scale defined by Hung *et al.* [72], the experimental processes can be rated as level 4 to 5, while the other categories are not covered in the current implementation of the ASAB setup.

In chapters 6.1 [13] and 6.2 [14], the ASAB setup was connected to FINALES as one of the tenants. Its capability to contribute as an independent tenant was demonstrated as well as its performance as part of a workflow. The latter use of the ASAB tenant enabled the preparation of electrolyte formulations for the use in coin cells that were cycled to obtain EOL data. [13, 14] Such workflows could be implemented as a single tenant, however, this would block tenants such as the ASAB tenant to contribute to the maximum extent. If the ASAB tenant would have been bound in a single tenant dedicated to generating EOL data, it would not have been possible to perform the optimisation of the ionic conductivity in parallel to the EOL optimisation without deploying a second tenant to formulate the electrolyte samples and performing EIS measurements. To efficiently use tenants offering multiple capabilities such as the ASAB tenant, the implementation of workflows in MAPs using the concept of the OVERLORT [159] as demonstrated in chapter 6.2 [14] seems to be a valuable approach.

The connection of the ASAB setup to FINALES further showed, how FAIR [71] data can be generated with such systems. Used in the fully autonomous mode connected to a FINALES server in the publications presented in the chapters 6.1 [13] and 6.2 [14], the ASAB setup contributed to the generation of consistently formatted, inherently digital and machine-readable datasets, which can easily be shared on data platforms, like for example, the BIG-MAP Archive [160], Zenodo [69] or Materials Cloud Archive [70]. This significantly reduces the effort needed to comply with requirements by funding agencies regarding the publication of research data additional to peer-reviewed research articles [161, 162]. The coupling with FINALES is further shown to constitute a simple way to link the ASAB system to data archives like the BIG-MAP Archive [160], which enables a timely sharing of the generated data without the need for manual uploads [14]. The defined structure of the data generated by the ASAB system and its associated tenant additionally facilitates the mapping to ontologies such as BattINFO [68, 81] as it was demonstrated in chapter 6.2 [14].

Furthermore, the FINALES framework as well as the ASAB setup are implemented to promote the recording of metadata related to the performed actions [13, 14]. When collecting relevant metadata, experimentalists often focus on physical parameters that may influence the measurements. However, especially the development of automated experimental setups involves the parallel development of associated software. Frequent changes to the software controlling the experiments are therefore an essential part of the research process in this field. These changes may often be minor adjustments in response to an error that may not immediately result in a new release. Consequently, it is important to carefully document the software versions associated with generated results. This topic is approached in the ASAB tenant presented in chapter 6.2 [14, 86]. On startup, it logs the information about the used software that is available in the configuration file. In this way, data points can be related to a software version and changes in the software affecting the measurement results become traceable. Troubleshooting is therefore less limited to errors occurring in the hardware. This approach is similar to the one followed in AiiDA [78], which stores the code that generated the results as additional nodes in the database.

The publications presented in the chapters 6.1 [13] and 6.2 [14] present the exploitation of synergistic effects between computational methods and experiments by deploying carefully designed data structures

meeting the requirements of both fields. This tight integration of ML, computational methods and the physical experiments combined with the possibility of operating automated setups around the clock can shorten the time for an iteration in active learning loops leading to a faster generation of results [14]. However, pure automation is not achieving the goal of high-quality scientific results. An extensive monitoring of the experimentation process is inevitable to detect errors and include information relevant for the data quality in the output. For example, a procedure for the verification of formulations, which is commonly practised in conventional research, also needs to be implemented in automated research. In the study presented in chapter 6.2 [14], this aim was pursued by the use of NMR analyses that were performed and analysed manually in parallel to the autonomous operation of the remaining MAP and the logging of requested and transformed formulations by the ASAB tenant to enable traceability of the results. Also, the careful calibration of the equipment like the densimeter, viscometer and the electrochemical cell prior to the start of automated or autonomous campaigns worked towards this goal. Ambient conditions like the temperature as well as the oxygen and water content in the atmosphere of the glovebox were monitored manually by a human researcher in this work [14]. With these efforts, this work also enters the field of verification in the realm of automated experimentation, which holds the potential to overcome currently widespread reservations regarding automated experimentation, which often seem to lead to the assumption that automated experimental platforms should preferably be used for low fidelity screenings followed by selected high-fidelity experiments performed by humans. The importance of quality control and verification procedures in automated experimentation are current topics also in the literature as for example Rahmanian *et al.* [163] demonstrated the incorporation of automated quality monitoring in their *Auto-MISCHBARES* system and Strieth-Kalthoff *et al.* [12] also emphasised it in their recent publication.

With the aim of high-quality measurements in mind and based on the experience with the ASAB setup, a field called `quality rating` was included in the schemas of the FINALES tenants for the studies presented in the chapters 6.1 [13, 149] and 6.2 [14, 150]. This field served to convey information about the reliability of the reported data to the optimisers or more generally to the consumers of the data. It can for example be used to select only data of a certain reliability for the training of an ML model. [14] The definition of a reasonable quality rating requires a detailed understanding of the method and the values for the process parameters necessary for its calculation need to be accessible from the output data of the respective method or the recorded metadata. Therefore, the quality rating is highly specific for a method and its definition was not straightforward for all of the tenants in the chapters 6.1 [13] and 6.2 [14]. For some of the tenants the definition of a quality rating was not reasonably possible in the study included in chapter 6.2 [14]. The comparability of the quality ratings for different capabilities is therefore not necessarily a given, but it can at least serve to compare the results for individual capabilities. By restricting the values permitted in the `quality rating` field of the schemas to integers ranging from 1 to 5, an attempt was made to normalise the quality ratings and make them more comparable [14]. However, this does not remedy the fact that the parameters influencing the rating are typically very different. Closely related to the quality rating is the handling of errors occurring during the execution of a measurement in autonomous settings. During the fully autonomous operation of the ASAB setup in the MAP presented in chapter 6.2 [13], the stop of the procedure as described in chapter 4 causes a problem. Since the status of a request is changed to `reserved` once the ASAB tenant starts processing it, this request will remain in this state even if the ASAB setup and tenant were cancelled. Therefore, the status of this request will have to be set back to `pending` manually or the request will not be pulled again after a restart of the ASAB setup and tenant. To avoid skipping requests due to this mechanism, the ASAB tenant [86] is equipped with an error handler that resets the status of the request in case of an error prior to exiting. Since the ASAB setup prepares a sample and subsequently provides it for a measurement, a repetition of a measurement also requires the preparation of another sample. In such a case, resetting the status of the request in case of an error as described previously is a possible way of handling the error. For other tenants such as the AutoBASS tenant [164] and the Cycler tenant [165], a locally saved queue of requests and resuming the failed procedure after a restart proved to be better suited. Apart from such tenant-specific aspects, there are actions such as the login, retrieving requests and posting results that are common to all FINALES tenants. Therefore, a *reference tenant* was implemented in the scope of the study presented in chap-

ter 6.2 [14, 141] to facilitate the implementation of new tenants. The ASAB tenant [86] served as the basis for this reference tenant that was used as a starting point for the implementation of several of the tenants connected to the MAP presented in chapter 6.2 [14].

Additional to the aforementioned achievements, the connection to the FINALES server makes the ASAB setup accessible to a community of users with different background. Since complex low-level procedures and upon the use of the ASAB tenant also certain analysis functionalities are handled internally, users are empowered to obtain results from methods, of which they may not have in-depth expert knowledge or which may not be physically available in their laboratory. [14] This enables them to augment their research with data, which would otherwise not be accessible to them this easily. The automation of the respective procedures does not fully replace a fundamental understanding of the measurement principle, but it will avoid the necessity for the user to be trained in the operation of the specific device utilised by a tenant. The selection of input parameters, basic interpretation of the obtained results or the identification of failed measurements may often be possible based on knowledge obtained from textbooks, whereas conducting a measurement or the analysis of the obtained raw data frequently demands experience with the application of the method and the respective device. Researchers aiming to train themselves in the use of a new method may further benefit from the reduced human time and labour necessary to perform automated experiments since this allows them to perform experiments using various sets of input parameters to explore their effect on the results. The researchers operating a tenant are usually familiar with the method and its challenges. Their expert knowledge can to a certain extent be incorporated in the tenant in the form of reasonable default values and limits for parameters and a selection of relevant metadata that need to be recorded while performing a method. In this way, users of the tenant benefit from the expert knowledge and minimise problems in the analysis or interpretation of the data arising from missing records of relevant metadata. These possibilities are an example of the community aspect of MAPs that was recently emphasised by Stier *et al.* [10].

Apart from the implementation of expert knowledge being limited to typical use cases and standardised procedures, Tom *et al.* [11] and Hung *et al.* [72] note that fully automated processes may not be desired in some applications. NMR measurements such as those reported in chapter 5 [95] are an example, where full automation may not be the best choice, but partial automation of default procedures may still be desirable. The preprocessing of the NMR data to obtain the self-diffusion coefficients presented in chapter 5 [95] is a time consuming task. Especially the phasing of the spectra and the integration of the signals are difficult to reproduce exactly since they involve a certain degree of subjectivity in the choice of the phasing parameters and the limits for the integration. Hence, different researchers performing the analysis may obtain slightly deviating results. Subsequent changes to the preprocessing applied to the data in chapter 5 [95] such as a slight change in the integration limits required the repeated preprocessing of at least one set of spectra. A progressive refinement of the preprocessing routine is therefore inefficient. Challenges to identify the important features necessary to be considered when executing tasks such as phasing a spectrum or integrating signals combined with the comparatively large effort for subsequent minor adjustments in the analysis procedures may represent an entry barrier for beginners, who do not have the possibility to consult an expert. This barrier could possibly be lowered by automated analysis procedures prefilled with reasonable parameters as starting points developed by experts and provided to the community. The approach of automating standard tasks and providing reasonable preset parameters is already used today in commercial software such as *MestReNova* [94] (Mestrelab Research S.L., Spain) or *SpinFlow* [144] (Oxford Instruments plc, United Kingdom). Due to many parameters that can sensitively influence the measurements, such procedures are mainly applicable to standard procedures like the ones used in chapter 5 [95]. More advanced research question or the analysis of complex spectra will still require expert knowledge. Therefore, partially automated data analysis may be reasonably applied in some NMR studies, but the fully automated analysis and interpretation of the resulting spectra is hard to implement for more complex use cases than the one presented in chapter 5 [95] and it may therefore be preferred to have a human researcher perform these tasks. The versatility and modularity of the ASAB setup and the

FINALES framework allow for the degree of automation to be adjusted by the researcher and therefore enable their use even in environments where a more human-centred approach is favoured.

Overall, the results obtained in this thesis show, that a tight integration of automated experimentation, computational methods, workflows and ML models is possible on a geographically distributed scale and the complementary nature of different methods can be exploited in this way. This work further demonstrates that the flexibility required in research applications can be maintained in automated setups. [13, 14] The adjustable degree of automation resulting from the flexibility of the ASAB setup and the FINALES framework enables their application in diverse laboratory environments and applications. It was further shown that the ASAB tenant [86] cannot only contribute directly to a MAP but it can even be integrated into a workflow [14]. This enables contributions to a MAP that would be inconvenient to be implemented in a single tenant. The results of this thesis indicate that further improvements of the ASAB setup and the FINALES framework as well as efforts in the field of automated experimentation in general are well invested to lower the entry barrier for cross-domain collaborations and to make instrumentation and methods more accessible in the research community [14]. Based on the results presented here, the distributed and scale-bridging MAP concept appears suitable to answer questions regarding correlations across scales such as those between bulk properties of the electrolyte and cell performance [14].

8 Outlook

The further development of the ASAB hardware setup could include the addition of sensors to monitor the pressure and, in case, regulate the flow or cancel the execution of a request before the pressure exceeds the limits of the valves. This could counteract the leakage issues mentioned in the chapters 4 and 6.2 [14]. To detect leakages automatically, a capacitive sensor could be used to detect liquid in the capturing vials and stop the current procedure or log an error if the sensor is triggered. Furthermore, tubes with a larger inner diameter could be an alternative solution to lower the pressure in the system. Improvements in the cleaning of the system could be achieved by introducing several connections to the pressurised nitrogen line to allow the gas to enter at various points in the system. A more direct supply of pressurised gas to the instruments can be expected to improve the cleaning results.

For the software, a short-term aim could be the improvement of the initialisation routine to ensure all modules are correctly connected prior to starting an experiment. Further development could focus on recording additional metadata once more sensors are available. Also the automatic retrieval of software versions from the development environment used and logging this information could improve the documentation and enhance traceability of changes in the software. The automation of this functionality would also avoid the error-prone manual input of the respective information in the configuration file as described in chapter 4. Moreover, a functionality to collect the raw data saved by the individual instruments like the NMR device or the densimeter and viscometer from their respective directories into a single directory for each project could facilitate the later use of the data. The overall improvement of the robustness of the software package should be an additional goal for the future. Especially the implementation of a functionality that allows for interruptions of the pumping process without aborting it would improve the handling. The user friendliness could be significantly improved by the addition of a *graphical user interface* (GUI).

Based on the modularity of the ASAB setup, the addition of further functionality could be a midterm aim. The NMR instrument is currently only physically connected to the ASAB setup, but the software operations such as the setup and start of measurements is done manually. Since the NMR device is commercially equipped with an option to trigger measurements using an Arduino[®], a next step could be to implement drivers and actions to connect the Arduino[®] to the ASAB setup. It should be possible to use the existing driver and action for Arduino[®] boards in the ASAB software [140] as a basis for the implementation. Once NMR measurements could automatically be triggered, the automation of the preprocessing of the spectra could be approached where this is reasonable. The integration of the NMR device into the automated capabilities of the ASAB setup would not only add an additional characterisation technique, but would also allow for the inline verification of the generated formulations. An improved design of the electrochemical measuring cell to accommodate a four electrode setup would allow to eliminate influences of the electrodes on the measurements [97]. The integration of the currently unused modules for heating and cooling could open new possibilities like controlling the temperature of the electrolyte or using the UV-VIS module as a further characterisation and verification technique. To expand the accessible chemical space of the system, a solid handling unit, for example based on a screw conveyor, could be considered. This would allow the dosing of conducting salts or other solid electrolyte components without depending on stock solutions.

An important aspect to consider when it comes to the efficient use of the raw materials is to minimise the sample volume. One way to achieve this could be to only fill the minimum amount of sample required for the respective measurement into the tube and move it to the measuring position using gas. Similar to the segmented flow techniques described in [166]. Operating without filling all the dead volume of the tubes

harbours significant potential for the reduction of the used sample volume. Adding capacitive sensors to the pumps and the tubes after measuring positions could support this effort as they could allow an earlier detection of the necessary filling volume. A tighter physical integration with other modules in the laboratory should also be targeted to reduce the manual interventions, which are currently necessary to transfer electrolytes from the ASAB setup to other systems for further processing as described in chapter 6.2 [14].

This thesis is mainly focused on the basic development of the ASAB setup and the demonstration of different use cases in the field of battery research using mostly well-established electrolyte solutions for lithium-ion batteries. In the future, the system could be deployed for novel electrolyte systems to generate comprehensive datasets for explorative studies or tailor electrolytes to meet predefined requirements. Since the software [140] is configurable to also handle other arrangements of the hardware than the one used in this work, it could also be considered to develop a second ASAB setup capable of handling higher viscous fluids. Such a setup could then be used to handle precursors for gel or solid electrolytes or possibly even slurries for electrode materials.

In the bigger picture of the MAPs presented in the chapters 6.1 [13] and 6.2 [14], the further development could aim at the tighter integration of ontologies and the inclusion of more diverse tenants. These advanced MAPs could target more complex optimisation tasks or provide comprehensive datasets for the characterisation of materials or for the deployment in the training of ML models. Furthermore, efforts towards making the framework and the connected services available to a larger community also crossing the borders of individual projects could be a valuable goal in pursuing globally distributed MAPs. [13, 14] To achieve this, improvements regarding the access to the data in the database are inevitable to enable FINALES to distinguish between different projects and studies and also associate users to user groups. This would allow to restrict the access of each user and tenant to the data shared with the appropriate community and would reduce the risk of data leaks. Since industrial partners often require strict data security and confidentiality, even the option of handling a separate database per study should be considered to further minimise the risk of unintentional sharing of data. Like this, FINALES could be used as an interface to laboratories or larger communities, which are involved in several studies at the same time rendering the use of a separate instance of FINALES per study inconvenient. Further possible improvements of the FINALES framework should be considered regarding the installation and the administration of a FINALES instance. Elucidating the details of these topics is out of the scope of this thesis but the current open issues can be found in the respective section in the FINALES GitHub repository accessible under the URL <https://github.com/BIG-MAP/FINALES2/issues>.

Due to the diversity of tasks, it is essential to make the further development of MAPs and automated research an interdisciplinary effort to avoid parallel developments in unrelated fields due to a lack of exchange. Interdisciplinarity should in this case not end at the borders of scientific fields, but it needs to also include experts in the field of law or business to develop strategies for aspects like intellectual property or the pricing of services. This aspect was recently also mentioned by Stier *et al.* [10]. Also, diversity of skills, background and experience needs to be valued and promoted in this process to achieve versatile, impactful and globally distributed MAPs integrating numerous institutions, facilities and methods. Since the number of research groups focusing on the development of MAPs is not yet very large, this should be used as a chance to collaborate and implement standards in this field to avoid concurrent developments of incompatible solutions as this may add barriers and complicate collaborations or exchange of data or resources.

Bibliography

- [1] IPCC, “2023: Summary for Policymakers,” in *Climate Change 2023: Synthesis Report. Contribution of Working Groups I, II and III to the Sixth Assessment Report of the Intergovernmental Panel on Climate Change*, Core Writing Team, H. Lee, and J. Romero, Eds. Geneva, Switzerland: IPCC, 2023, pp. 1–34. doi: 10.59327/IPCC/AR6-9789291691647.001.
- [2] D. Bresser, A. Moretti, A. Varzi, and S. Passerini, “The Role of Batteries for the Successful Transition to Renewable Energy Sources,” in *Batteries: Present and Future Energy Storage Challenges*, S. Passerini, D. Bresser, A. Moretti, and A. Varzi, Eds. John Wiley & Sons, Incorporated, 2020, ch. 1, pp. 3–11, ISBN: 978-3-527-82730-5.
- [3] F. Nobili and R. Marassi, “Fundamental Principles of Battery Electrochemistry,” in *Batteries: Present and Future Energy Storage Challenges*, S. Passerini, D. Bresser, A. Moretti, and A. Varzi, Eds. John Wiley & Sons, Incorporated, 2020, ch. 2, pp. 13–49, ISBN: 978-3-527-82730-5.
- [4] D. Linden and T. B. Reddy, “Basic Concepts,” in *Linden’s Handbook of Batteries*, 4th ed. McGraw-Hill Professional Publishing, 2010, ch. 1, pp. 26–41, ISBN: 9780071624190.
- [5] F. Rahmanian *et al.*, “One-Shot Active Learning for Globally Optimal Battery Electrolyte Conductivity,” *Batteries & Supercaps*, vol. 5, no. 10, 2022. doi: 10.1002/batt.202200228.
- [6] Z. Ogumi, H. Arai, T. Abe, and M. Morita, “Present LIB Chemistries,” in *Batteries: Present and Future Energy Storage Challenges*, S. Passerini, D. Bresser, A. Moretti, and A. Varzi, Eds. John Wiley & Sons, Incorporated, 2020, ch. 6, pp. 149–183, ISBN: 978-3-527-82730-5.
- [7] K. Xu, “Electrolytes and Interphases in Li-Ion Batteries and Beyond,” *Chemical Reviews*, vol. 114, no. 23, pp. 11 503–11 618, 2014. doi: 10.1021/cr500003w.
- [8] C. Ling, “A review of the recent progress in battery informatics,” *npj Computational Materials*, vol. 8, no. 1, 2022. doi: 10.1038/s41524-022-00713-x.
- [9] A. Aspuru-Guzik and K. Persson. “Materials Acceleration Platform: Accelerating Advanced Energy Materials Discovery by Integrating High-Throughput Methods and Artificial Intelligence.” (2018), [Online]. Available: <https://dash.harvard.edu/handle/1/35164974>.
- [10] S. P. Stier *et al.*, “Materials Acceleration Platforms (MAPs) Accelerating Materials Research and Development to Meet Urgent Societal Challenges,” *Advanced Materials*, p. 2 407 791, 2024. doi: 10.1002/adma.202407791.
- [11] G. Tom *et al.*, “Self-Driving Laboratories for Chemistry and Materials Science,” *Chemical Reviews*, vol. 124, no. 16, pp. 9633–9732, 2024. doi: 10.1021/acs.chemrev.4c00055.
- [12] F. Strieth-Kalthoff *et al.*, “Delocalized, asynchronous, closed-loop discovery of organic laser emitters,” *Science*, vol. 384, no. 6697, eadk9227, 2024. doi: 10.1126/science.adk9227.
- [13] M. Vogler *et al.*, “Brokering between tenants for an international materials acceleration platform,” *Matter*, vol. 6, no. 9, pp. 2647–2665, 2023. doi: 10.1016/j.matt.2023.07.016.
- [14] M. Vogler *et al.*, “Autonomous Battery Optimization by Deploying Distributed Experiments and Simulations,” *Advanced Energy Materials*, vol. 14, no. 46, p. 2 403 263, 2024. doi: 10.1002/aenm.202403263.
- [15] K. Nishio and N. Furukawa, “Practical Batteries,” in *Handbook of Battery Materials*, C. Daniel and J. O. Besenhard, Eds. John Wiley & Sons, Ltd, 2011, ch. 2, pp. 27–85, ISBN: 9783527637188. doi: <https://doi.org/10.1002/9783527637188.ch2>.
- [16] A. Kirchev, “Battery Management and Battery Diagnostics,” in *Electrochemical Energy Storage for Renewable Sources and Grid Balancing*, P. T. Moseley and J. Garche, Eds. Elsevier, 2015, ch. 20, pp. 411–435, ISBN: 978-0-444-62616-5. doi: 10.1016/b978-0-444-62616-5.00020-6.

- [17] K. Pinkwart and J. Tübke, "Thermodynamics and Mechanistics," in *Handbook of Battery Materials*, C. Daniel and J. O. Besenhard, Eds. John Wiley & Sons, Ltd, 2011, ch. 1, pp. 1–26, ISBN: 9783527637188. doi: 10.1002/9783527637188.ch1.
- [18] X. Lin *et al.*, "Rechargeable Battery Electrolytes Capable of Operating over Wide Temperature Windows and Delivering High Safety," *Advanced Energy Materials*, vol. 10, no. 43, p. 2001235, 2020. doi: 10.1002/aenm.202001235.
- [19] K. Xu, "Nonaqueous Liquid Electrolytes for Lithium-Based Rechargeable Batteries," *Chemical Reviews*, vol. 104, no. 10, pp. 4303–4418, 2004. doi: 10.1021/cr030203g.
- [20] K. Ozawa, "Brief Survey on the Historical Development of LIBs," in *Batteries: Present and Future Energy Storage Challenges*, S. Passerini, D. Bresser, A. Moretti, and A. Varzi, Eds. John Wiley & Sons, Incorporated, 2020, ch. 5, pp. 131–148, ISBN: 978-3-527-82730-5.
- [21] S.-T. Myung, J. Kim, and Y.-K. Sun, "Anticipated Progress in the Near- to Mid-Term Future of LIBs," in *Batteries: Present and Future Energy Storage Challenges*, S. Passerini, D. Bresser, A. Moretti, and A. Varzi, Eds. John Wiley & Sons, Incorporated, 2020, ch. 7, pp. 185–216, ISBN: 978-3-527-82730-5.
- [22] R. Holze, "Elektrolyte," in F. Böckler *et al.*, Eds., Stuttgart: Thieme Gruppe, 2012. [Online]. Available: <https://roempp.thieme.de/lexicon/RD-05-00683>.
- [23] H. J. Gores and J. M. G. Barthel, "Nonaqueous electrolyte solutions: New materials for devices and processes based on recent applied research," *Pure and applied chemistry*, vol. 67, no. 6, pp. 919–930, 1995. doi: 10.1351/pac199567060919.
- [24] N. Nasajpour-Esfahani *et al.*, "Comprehensive review of lithium-ion battery materials and development challenges," *Renewable and Sustainable Energy Reviews*, vol. 203, p. 114783, 2024. doi: 10.1016/j.rser.2024.114783.
- [25] J. B. Goodenough and Y. Kim, "Challenges for Rechargeable Li Batteries," *Chemistry of Materials*, vol. 22, no. 3, pp. 587–603, 2010. doi: 10.1021/cm901452z.
- [26] Y. Zhang *et al.*, "Electrolyte Design for Lithium-Ion Batteries for Extreme Temperature Applications," *Advanced Materials*, vol. 36, no. 13, 2023. doi: 10.1002/adma.202308484.
- [27] X. Chen, X.-Q. Zhang, H.-R. Li, and Q. Zhang, "Cation-Solvent, Cation-Anion, and Solvent-Solvent Interactions with Electrolyte Solvation in Lithium Batteries," *Batteries & Supercaps*, vol. 2, no. 2, pp. 128–131, 2019. doi: 10.1002/batt.201800118.
- [28] H. J. Gores *et al.*, "Liquid Nonaqueous Electrolytes," in *Handbook of Battery Materials*, C. Daniel and J. O. Besenhard, Eds. John Wiley & Sons, Ltd, Aug. 24, 2011, ch. 17, pp. 525–626, ISBN: 9783527637188. doi: 10.1002/9783527637188.ch17.
- [29] J. Kalhoff, G. G. Eshetu, D. Bresser, and S. Passerini, "Safer Electrolytes for Lithium-Ion Batteries: State of the Art and Perspectives," *ChemSusChem*, vol. 8, no. 13, pp. 2154–2175, 2015. doi: 10.1002/cssc.201500284.
- [30] H. Wan, J. Xu, and C. Wang, "Designing electrolytes and interphases for high-energy lithium batteries," *Nature Reviews Chemistry*, vol. 8, no. 1, pp. 30–44, 2023. doi: 10.1038/s41570-023-00557-z.
- [31] C. L. Berhaut, P. Porion, L. Timperman, G. Schmidt, D. Lemordant, and M. Anouti, "LiTfO as electrolyte salt for Li-ion batteries: transport properties in EC/DMC," *Electrochimica Acta*, vol. 180, pp. 778–787, 2015. doi: 10.1016/j.electacta.2015.08.165.
- [32] J. O. Bockris and A. K. N. Reddy, *Volume 1: Modern Electrochemistry, Ionics*, 2nd ed., A. K. N. Reddy, Ed. Kluwer Academic Publishers, 2002, ch. 4, pp. 361–599, ISBN: 0-306-46909-X. doi: 10.1007/b114546.
- [33] C. C. Miller and J. Walker, "The Stokes-Einstein law for diffusion in solution," *Proceedings of the Royal Society of London. Series A, Containing Papers of a Mathematical and Physical Character*, vol. 106, no. 740, pp. 724–749, 1924. doi: 10.1098/rspa.1924.0100.
- [34] W. Sutherland, "LXXV. A dynamical theory of diffusion for non-electrolytes and the molecular mass of albumin," *The London, Edinburgh, and Dublin Philosophical Magazine and Journal of Science*, vol. 9, no. 54, pp. 781–785, 1905. doi: 10.1080/14786440509463331.

- [35] A. Einstein, "Über die von der molekularkinetischen Theorie der Wärme geforderte Bewegung von in ruhenden Flüssigkeiten suspendierten Teilchen," *Annalen der Physik*, vol. 322, no. 8, pp. 549–560, 1905, Source gallica.bnf.fr / Bibliothèque nationale de France.
- [36] A. Einstein, "Elementare Theorie der Brownschen Bewegung," *Zeitschrift für Elektrochemie und angewandte physikalische Chemie*, vol. 14, no. 17, pp. 235–239, 1908. doi: 10.1002/bbpc.19080141703.
- [37] A. E. Flowers, *Viscosity measurement and a new viscosimeter*. Pennsylvania, 1914. [Online]. Available: <https://hdl.handle.net/2027/mdp.39015057082078> (visited on 10/31/2024), Courtesy of HathiTrust.
- [38] H. Friebolin, *Ein- und zweidimensionale NMR-Spektroskopie: eine Einführung*, 5th ed., in collab. with C. M. Thiele. Wiley-VCH Verlag GmbH & Co. KGaA, 2013, 429 pp., ISBN: 978-3-527-33492-6.
- [39] S. Zugmann, M. Fleischmann, M. Amereller, R. Gschwind, H. Wiemhöfer, and H. Gores, "Measurement of transference numbers for lithium ion electrolytes via four different methods, a comparative study," *Electrochimica Acta*, vol. 56, no. 11, pp. 3926–3933, 2011. doi: 10.1016/j.electacta.2011.02.025.
- [40] A. Noda, K. Hayamizu, and M. Watanabe, "Pulsed-Gradient Spin-Echo ^1H and ^{19}F NMR Ionic Diffusion Coefficient, Viscosity, and Ionic Conductivity of Non-Chloroaluminate Room-Temperature Ionic Liquids," *The Journal of Physical Chemistry B*, vol. 105, no. 20, pp. 4603–4610, 2001. doi: 10.1021/jp004132q.
- [41] B. Zhang, L. Merker, M. Vogler, F. Rahmanian, and H. S. Stein, "Apples to apples: shift from mass ratio to additive molecules per electrode area to optimize Li-ion batteries," *Digital Discovery*, vol. 3, no. 7, pp. 1342–1349, 2024. doi: 10.1039/d4dd00002a.
- [42] J. Liu *et al.*, "Pathways for practical high-energy long-cycling lithium metal batteries," *Nature Energy*, vol. 4, no. 3, pp. 180–186, 2019. doi: 10.1038/s41560-019-0338-x.
- [43] H. Qu, W. Hu, Y. Huang, T. Zhang, H. Fang, and F. Li, "Recent Advances and Practical Challenges in Organic Electrolytes of Sodium-Ion Batteries," *Energy & Fuels*, vol. 38, no. 14, pp. 12472–12486, 2024. doi: 10.1021/acs.energyfuels.4c01974.
- [44] C. Wölke *et al.*, "Single Versus Blended Electrolyte Additives: Impact of a Sulfur-Based Electrolyte Additive on Electrode Cross-Talk and Electrochemical Performance of LiNiO_2 ||Graphite Cells," *Advanced Energy Materials*, vol. 14, no. 36, p. 2402152, doi: <https://doi.org/10.1002/aenm.202402152>.
- [45] P. Yan *et al.*, "Non-aqueous battery electrolytes: high-throughput experimentation and machine learning-aided optimization of ionic conductivity," *Journal of Materials Chemistry A*, vol. 12, no. 30, pp. 19123–19136, 2024. doi: 10.1039/d3ta06249j.
- [46] M. Broszkiewicz, B. Brzozowski, T. Trzeciak, A. Zalewska, J. Ryl, and L. Niedzicki, "Imidazole-Based Lithium Salt LiHDI as a Solid Electrolyte Interphase-Stabilising Additive for Lithium-Conducting Electrolytes," *Molecules*, vol. 29, p. 804, 4 2024. doi: 10.3390/molecules29040804.
- [47] U. Heider, R. Oesten, and M. Jungnitz, "Challenge in manufacturing electrolyte solutions for lithium and lithium ion batteries quality control and minimizing contamination level," *Journal of Power Sources*, vol. 81–82, pp. 119–122, 1999. doi: 10.1016/s0378-7753(99)00142-1.
- [48] C. L. Campion, W. Li, and B. L. Lucht, "Thermal Decomposition of LiPF_6 -Based Electrolytes for Lithium-Ion Batteries," *Journal of The Electrochemical Society*, vol. 152, no. 12, A2327, 2005. doi: 10.1149/1.2083267.
- [49] T. Kawamura, S. Okada, and J.-i. Yamaki, "Decomposition reaction of LiPF_6 -based electrolytes for lithium ion cells," *Journal of Power Sources*, vol. 156, no. 2, pp. 547–554, 2005. doi: 10.1016/j.jpowsour.2005.05.084.
- [50] D. Aurbach *et al.*, "Recent studies on the correlation between surface chemistry, morphology, three-dimensional structures and performance of Li and Li-C intercalation anodes in several important electrolyte systems," *Journal of Power Sources*, vol. 68, no. 1, pp. 91–98, 1997. doi: 10.1016/s0378-7753(97)02575-5.

- [51] J. Vetter *et al.*, “Ageing mechanisms in lithium-ion batteries,” *Journal of Power Sources*, vol. 147, no. 1-2, pp. 269–281, 2005. doi: 10.1016/j.jpowsour.2005.01.006.
- [52] L. Niedzicki *et al.*, “New type of imidazole based salts designed specifically for lithium ion batteries,” *Electrochimica Acta*, vol. 55, no. 4, pp. 1450–1454, 2010. doi: 10.1016/j.electacta.2009.05.008.
- [53] L. Niedzicki *et al.*, “Liquid electrolytes based on new lithium conductive imidazole salts,” *Journal of Power Sources*, vol. 196, no. 3, pp. 1386–1391, Feb. 2011, ISSN: 0378-7753. doi: 10.1016/j.jpowsour.2010.08.097.
- [54] M. Armand *et al.*, “Review-Development of Hückel Type Anions: From Molecular Modeling to Industrial Commercialization. A Success Story,” *Journal of The Electrochemical Society*, vol. 167, no. 7, p. 070562, 2020. doi: 10.1149/1945-7111/ab829c.
- [55] P. Yan *et al.*, “Blended Salt Electrolyte Design for Enhanced NMC811||Graphite Cell Performance,” *Small Structures*, vol. 5, no. 4, 2023. doi: 10.1002/ssstr.202300425.
- [56] PalmSens BV, *PalmSens Python SDK 5.9*, version 5.9, 2023. [Online]. Available: <https://www.palmsens.com/knowledgebase-article/palmsens-sdk-for-python/> (visited on 10/31/2024).
- [57] CETONI GmbH, *CETONI SDK for Python*, version 20200903, 2020. [Online]. Available: https://cetoni.de/downloads/manuals/CETONI_SDK/QmixSDK_Python.html (visited on 10/31/2024).
- [58] F. Rahmanian *et al.*, “Enabling Modular Autonomous Feedback-Loops in Materials Science through Hierarchical Experimental Laboratory Automation and Orchestration,” *Advanced Materials Interfaces*, vol. 9, no. 8, p. 2101987, 2022. doi: <https://doi.org/10.1002/admi.202101987>.
- [59] F. Häse, L. M. Roch, and A. Aspuru-Guzik, “Next-Generation Experimentation with Self-Driving Laboratories,” *Trends in Chemistry*, vol. 1, no. 3, pp. 282–291, 2019. doi: 10.1016/j.trechm.2019.02.007.
- [60] B. Zhang, L. Merker, A. Sanin, and H. S. Stein, “Robotic cell assembly to accelerate battery research,” *Digital Discovery*, vol. 1, no. 6, pp. 755–762, 2022. doi: 10.1039/d2dd00046f.
- [61] F. Strieth-Kalthoff, F. Sandfort, M. Kühnemund, F. R. Schäfer, H. Kuchen, and F. Glorius, “Machine Learning for Chemical Reactivity: The Importance of Failed Experiments,” *Angewandte Chemie International Edition*, vol. 61, no. 29, 2022. doi: 10.1002/anie.202204647.
- [62] P. Raccuglia *et al.*, “Machine-learning-assisted materials discovery using failed experiments,” *Nature*, vol. 533, no. 7601, pp. 73–76, 2016. doi: 10.1038/nature17439.
- [63] F. Rahmanian *et al.*, *Dataset of 5035 Conductivity Experiments for Lithium-Ion Battery Electrolyte Formulations at Various Temperatures*, Zenodo, 2022. doi: 10.5281/ZENODO.7244939.
- [64] L. Nuss, L. Merker, B. Zhang, and H. Stein, *Formation and cycling data for Na-ion batteries from high-throughput synthesis, coating, and assembly*, Zenodo, 2023. doi: 10.5281/ZENODO.7981010.
- [65] B. P. MacLeod, F. G. L. Parlane, and C. P. Berlinguette, “How to build an effective self-driving laboratory,” *MRS Bulletin*, vol. 48, no. 2, pp. 173–178, 2023. doi: 10.1557/s43577-023-00476-w.
- [66] L. M. Roch *et al.*, “ChemOS: An orchestration software to democratize autonomous discovery,” *PLOS ONE*, vol. 15, no. 4, J. Hu, Ed., e0229862, 2020. doi: 10.1371/journal.pone.0229862.
- [67] M. Sim *et al.*, “ChemOS 2.0: An orchestration architecture for chemical self-driving laboratories,” *Matter*, vol. 7, no. 9, pp. 2959–2977, 2024. doi: 10.1016/j.matt.2024.04.022.
- [68] S. Clark *et al.*, “Toward a Unified Description of Battery Data,” *Advanced Energy Materials*, vol. 12, no. 17, 2021. doi: 10.1002/aenm.202102702.
- [69] European Organization For Nuclear Research and OpenAIRE, *Zenodo*, 2013. doi: 10.25495/7GXK-RD71.
- [70] L. Talirz *et al.*, “Materials Cloud, a platform for open computational science,” *Scientific Data*, vol. 7, no. 1, 2020. doi: 10.1038/s41597-020-00637-5.

- [71] M. D. Wilkinson *et al.*, “The FAIR Guiding Principles for scientific data management and stewardship,” *Scientific Data*, vol. 3, no. 1, 2016. doi: 10.1038/sdata.2016.18.
- [72] L. Hung *et al.*, “Autonomous laboratories for accelerated materials discovery: a community survey and practical insights,” *Digital Discovery*, vol. 3, no. 7, pp. 1273–1279, 2024. doi: 10.1039/d4d00059e.
- [73] S.-I. Tobishima and A. Yamaji, “Ethylene carbonate–propylene carbonate mixed electrolytes for lithium batteries,” *Electrochimica Acta*, vol. 29, no. 2, pp. 267–271, 1984. doi: 10.1016/0013-4686(84)87058-9.
- [74] A. Dave *et al.*, “Autonomous Discovery of Battery Electrolytes with Robotic Experimentation and Machine Learning,” *Cell Reports Physical Science*, vol. 1, no. 12, p. 100264, 2020. doi: 10.1016/j.xcrp.2020.100264.
- [75] S. Steiner *et al.*, “Organic synthesis in a modular robotic system driven by a chemical programming language,” *Science*, vol. 363, no. 6423, 2019. doi: 10.1126/science.aav2211.
- [76] R. W. Epps *et al.*, “Artificial Chemist: An Autonomous Quantum Dot Synthesis Bot,” *Advanced Materials*, vol. 32, no. 30, p. 2001626, 2020. doi: <https://doi.org/10.1002/adma.202001626>.
- [77] B. Burger *et al.*, “A mobile robotic chemist,” *Nature*, vol. 583, no. 7815, pp. 237–241, 2020. doi: 10.1038/s41586-020-2442-2.
- [78] G. Pizzi, A. Cepellotti, R. Sabatini, N. Marzari, and B. Kozinsky, “AiiDA: automated interactive infrastructure and database for computational science,” *Computational Materials Science*, vol. 111, pp. 218–230, 2016. doi: 10.1016/j.commatsci.2015.09.013.
- [79] I. Foster, “Globus Online: Accelerating and Democratizing Science through Cloud-Based Services,” *IEEE Internet Computing*, vol. 15, no. 3, pp. 70–73, 2011. doi: 10.1109/mic.2011.64.
- [80] R. Chard *et al.*, “Globus automation services: Research process automation across the space–time continuum,” *Future Generation Computer Systems*, vol. 142, pp. 393–409, 2023. doi: 10.1016/j.future.2023.01.010.
- [81] S. Clark *et al.*, *Big-map/battinfo: V0.6.0*, 2023. doi: 10.5281/zenodo.8260800.
- [82] A. Dave, J. Mitchell, S. Burke, H. Lin, J. Whitacre, and V. Viswanathan, “Autonomous optimization of non-aqueous Li-ion battery electrolytes via robotic experimentation and machine learning coupling,” *Nature Communications*, vol. 13, no. 1, 2022. doi: 10.1038/s41467-022-32938-1.
- [83] A. N. Krishnamoorthy *et al.*, “Data-Driven Analysis of High-Throughput Experiments on Liquid Battery Electrolyte Formulations: Unraveling the Impact of Composition on Conductivity,” *Chemistry–Methods*, vol. 2, no. 9, 2022. doi: 10.1002/cmt.d.202200008.
- [84] E. Flores *et al.*, “Learning the laws of lithium-ion transport in electrolytes using symbolic regression,” *Digital Discovery*, vol. 1, no. 4, pp. 440–447, 2022. doi: 10.1039/d2dd00027j.
- [85] F. Rahmanian, *Modular and Autonomous Data Analysis Platform (MADAP)*, 2023. doi: 10.5281/ZENODO.8220661.
- [86] M. Vogler and L. Merker, *BIG-MAP/FINALES_ASAB_tenant: FINALES ASAB tenant v1.0.1*, version 1.0.1, 2024. doi: 10.5281/ZENODO.11144341.
- [87] J. Keeler, *Understanding NMR Spectroscopy*, 2nd ed. John Wiley & Sons, Ltd, 2010, ISBN: 978-0-470-74608-0.
- [88] S. K. Steensen *et al.*, *FINALES - Electrolyte optimization for maximum conductivity and for maximum cycle life*, Materials Cloud, 2024. doi: 10.24435/MATERIALSCLOUD:QT-1S.
- [89] S. Berger and S. Braun, *200 and more NMR experiments, A practical course*, 2. expand. ed., 1. repr. WILEY-VCH Verlag GmbH & Co. KGaA, 2011, ISBN: 978-3-527-31067-8.
- [90] J. L. Jungnickel and J. W. Forbes, “Quantitative Measurement of Hydrogen Types by Intergrated Nuclear Magnetic Resonance Intensities,” *Analytical Chemistry*, vol. 35, no. 8, pp. 938–942, 1963. doi: 10.1021/ac60201a005.

- [91] D. P. Hollis, "Quantitative Analysis of Aspirin, Phenacetin, and Caffeine Mixtures by Nuclear Magnetic Resonance Spectrometry," *Analytical Chemistry*, vol. 35, no. 11, pp. 1682–1684, 1963. doi: 10.1021/ac60204a043.
- [92] E. O. Stejskal and J. E. Tanner, "Spin Diffusion Measurements: Spin Echoes in the Presence of a Time-Dependent Field Gradient," *The Journal of Chemical Physics*, vol. 42, no. 1, pp. 288–292, 1965. doi: 10.1063/1.1695690.
- [93] A. M. Torres, G. Zheng, and W. S. Price, "Jcompensated PGSE: an improved NMR diffusion experiment with fewer phase distortions," *Magnetic Resonance in Chemistry*, vol. 48, no. 2, pp. 129–133, 2009. doi: 10.1002/mrc.2555.
- [94] Mestrelab Research S.L., *Mestrenova*, version 14.1.2-25024, 2020.
- [95] A. Szcześna-Chrzan *et al.*, "Ionic conductivity, viscosity, and self-diffusion coefficients of novel imidazole salts for lithium-ion battery electrolytes," *Journal of Materials Chemistry A*, vol. 11, no. 25, pp. 13483–13492, 2023. doi: 10.1039/d3ta01217d.
- [96] A. C. Lazanas and M. I. Prodromidis, "Electrochemical Impedance Spectroscopy-A Tutorial," *ACS Measurement Science Au*, vol. 3, no. 3, pp. 162–193, Mar. 2023. doi: 10.1021/acsmesuresci.2c00070.
- [97] S. Wang, J. Zhang, O. Gharbi, V. Vivier, M. Gao, and M. E. Orazem, "Electrochemical impedance spectroscopy," *Nature Reviews Methods Primers*, vol. 1, no. 1, 2021. doi: 10.1038/s43586-021-00039-w.
- [98] M. E. Orazem and B. Tribollet, Eds., *Electrochemical impedance spectroscopy* (The Electrochemical Society series), 2nd edition. John Wiley & Sons, Inc, 2017, ISBN: 1523111380.
- [99] H. W. Bode, *Network Analysis and Feedback Amplifier Design* (The Bell Telephone Laboratories Series). D. Van Nostrand Company, Inc., 1945, 551 pp.
- [100] H. Nyquist, "Regeneration theory," *The Bell System Technical Journal*, vol. 11, no. 1, pp. 126–147, 1932. doi: 10.1002/j.1538-7305.1932.tb02344.x.
- [101] J. E. B. Randles, "Kinetics of rapid electrode reactions," *Discussions of the Faraday Society*, vol. 1, p. 11, 1947. doi: 10.1039/df9470100011.
- [102] T. Shedlovsky, "A conductivity cell for eliminating electrode effects in measurements of electrolytic conductance," *Journal of the American Chemical Society*, vol. 52, no. 5, pp. 1806–1811, 1930. doi: 10.1021/ja01368a008.
- [103] D. González-Salgado, J. Troncoso, and L. Romani, "Experimental Techniques 2: Vibrating Tube Densimetry," in *Volume Properties: Liquids, Solutions and Vapours*, E. Wilhelm and T. M. Letcher, Eds. Royal Society of Chemistry, 2014, pp. 100–114, ISBN: 9781782627043.
- [104] O. Kratky, H. Leopold, and H. Stabinger, "Dichtemessungen an Flüssigkeiten und Gasen auf 10^{-6} g/cm³ bei 0.6 cm³ Präparatvolumen," *Zeitschrift für Angewandte Physik*, vol. 27, pp. 273–277, 1969.
- [105] H. Leopold, "Die digitale Messung der Dichte von Flüssigkeiten," *Elektronik*, 1970.
- [106] H. Leopold, "Digitale Meßwertverarbeitung bei der Dichtemessung," *Elektronik*, vol. 19, 1970.
- [107] H. Stabinger, H. Leopold, and O. Kratky, "Eine neue Methode zur Präzisionsmessung der Dichte von Flüssigkeiten: Kurze Mitteilung," *Monatshefte für Chemie - Chemical Monthly*, vol. 98, no. 2, pp. 436–438, 1967. doi: 10.1007/bf00899963.
- [108] O. Kratky, H. Leopold, and H. Stabinger, "The determination of the partial specific volume of proteins by the mechanical oscillator technique," in *Part D: Enzyme Structure*, ser. Methods in Enzymology, vol. 27, Academic Press, 1973, pp. 98–110. doi: 10.1016/S0076-6879(73)27007-6.
- [109] W. Wagner *et al.*, "5 - Density," in *Measurement of the Thermodynamic Properties of Single Phases*, ser. Experimental Thermodynamics, A. Goodwin, K. Marsh, and W. Wakeham, Eds., vol. 6, Elsevier, 2003, pp. 125–235. doi: 10.1016/S1874-5644(03)80008-5.
- [110] Anton Paar GmbH, A. Rechberger, and R. Amsüss, "Verfahren und Vorrichtung zur Ermittlung der Dichte eines Fluids," AT516420B1, Nov. 15, 2016. [Online]. Available: <https://worldwide.espacenet.com/patent/search?q=pn=AT516420B1>.

- [111] A. Rechberger, R. Amsüss, S. Rossegger, R. Breidler, and G. Steiner, "High Precision Vibration-Type Densitometers Based on Pulsed Excitation Measurements," *Sensors*, vol. 19, no. 7, 2019. doi: 10.3390/s19071627.
- [112] Anton Paar GmbH, W. Belitsch, P. Trummer, and R. Breidler, "Messgerät zur Untersuchung von fluiden Proben," AT517082B1, Nov. 15, 2016. [Online]. Available: <https://worldwide.espacenet.com/patent/search?q=pn=AT517082B1>.
- [113] Anton Paar GmbH, R. Breidler, G. Steiner, and R. Grüllenberger, "Verfahren zur Bestimmung der Dichte von Flüssigkeiten," AT517486B1, Nov. 15, 2022. [Online]. Available: <https://worldwide.espacenet.com/patent/search?q=pn=AT517486B1>.
- [114] OECD, "Test No. 114: Viscosity of Liquids," in *OECD Guidelines for the Testing of Chemicals, Section 1*, OECD Publishing, Paris, 2012. doi: 10.1787/9789264185180-en.
- [115] C. E. Mortimer and U. Müller, *Chemie : das Basiswissen der Chemie*, 10th ed. Thieme, 2010, pp. 174–175, 779 pp., ISBN: 978-3-13-484310-1.
- [116] P. W. Atkins and J. De Paula, *Physikalische Chemie*, 5th ed., trans. by M. Bär. Wiley-VCH Verlag GmbH & Co. KGaA, 2013, p. 331, ISBN: 978-3-527-33247-2.
- [117] S. V. Gupta, *Viscometry for Liquids, Calibration of Viscometers*. Springer International Publishing, 2014, ISBN: 9783319048581. doi: 10.1007/978-3-319-04858-1.
- [118] F. Höppler, "Der exzentrische Fall von Kugeln in Hohlzylindern mit Flüssigkeiten oder Gasen," *Zeitschrift für technische Physik*, vol. 14, pp. 165–169, 1933.
- [119] G. G. Stokes, "On the effect of the internal friction of fluids on the motion of pendulums, Section IV," *Transactions of the Cambridge Philosophical Society*, vol. 9, pp. 48–57, 1851. [Online]. Available: <https://hdl.handle.net/2027/mdp.39015012112531>, Courtesy of HathiTrust.
- [120] R. M. Hubbard and G. G. Brown, "Viscosity of n-Pentane," *Industrial and engineering chemistry*, vol. 35, no. 12, pp. 1276–1280, Dec. 1943.
- [121] R. Hubbard and G. Brown, "Rolling Ball Viscometer," *Industrial & Engineering Chemistry Analytical Edition*, vol. 15, no. 3, pp. 212–218, 1943. doi: 10.1021/i560115a018.
- [122] D. R. MacFarlane, M. Forsyth, E. I. Izgorodina, A. P. Abbott, G. Annat, and K. Fraser, "On the concept of ionicity in ionic liquids," *Physical Chemistry Chemical Physics*, vol. 11, no. 25, p. 4962, 2009. doi: 10.1039/b900201d.
- [123] K. R. Harris, "On the Use of the Angell-Walden Equation To Determine the "Ionicity" of Molten Salts and Ionic Liquids," *The Journal of Physical Chemistry B*, vol. 123, no. 32, pp. 7014–7023, 2019. doi: 10.1021/acs.jpcc.9b04443.
- [124] P. Walden, "Über organische Lösungs-und Ionisierungsmittel: III. Teil: Innere Reibung und deren Zusammenhang mit dem Leitvermögen," *Zeitschrift für physikalische Chemie*, vol. 55, no. 1, pp. 207–249, 1906. doi: 10.1515/zpch-1906-5511.
- [125] W. Xu, E. I. Cooper, and C. A. Angell, "Ionic Liquids: Ion Mobilities, Glass Temperatures, and Fragilities," *The Journal of Physical Chemistry B*, vol. 107, no. 25, pp. 6170–6178, 2003. doi: 10.1021/jp0275894.
- [126] M. Yoshizawa, W. Xu, and C. A. Angell, "Ionic Liquids by Proton Transfer: Vapor Pressure, Conductivity, and the Relevance of ΔpK_a from Aqueous Solutions," *Journal of the American Chemical Society*, vol. 125, no. 50, pp. 15411–15419, 2003. doi: 10.1021/ja035783d.
- [127] J. Frenkel, *Kinetic theory of liquids*, R. H. Flower, P. Kapitza, and N. F. Mott, Eds. Oxford University Press, 1946, ch. 8, p. 441.
- [128] D. Farhat, D. Lemordant, J. Jacquemin, and F. Ghamouss, "Alternative Electrolytes for Li-Ion Batteries Using Glutaronitrile and 2-methylglutaronitrile with Lithium Bis(trifluoromethanesulfonyl) Imide," *Journal of The Electrochemical Society*, vol. 166, no. 14, A3487–A3495, 2019, ISSN: 1945-7111. doi: 10.1149/2.1261914jes.
- [129] M. Videa and C. A. Angell, "Glass Formation, Ionic Conductivity, and Conductivity/Viscosity Decoupling, in $\text{LiAlCl}_4 + \text{LiClO}_4$ and $\text{LiAlCl}_4 + \text{LiAlCl}_3$ -Imide Solutions," *The Journal of Physical Chemistry B*, vol. 103, no. 20, pp. 4185–4190, 1999. doi: 10.1021/jp984276t.

- [130] M. G. McLin and C. A. Angell, "Ion-pairing effects on viscosity/conductance relations in Raman-characterized polymer electrolytes: lithium perchlorate and sodium triflate in PPG(4000)," *The Journal of Physical Chemistry*, vol. 95, no. 23, pp. 9464–9469, 1991. doi: 10.1021/j100176a079.
- [131] S.-Y. Lee, K. Ueno, and C. A. Angell, "Lithium Salt Solutions in Mixed Sulfone and Sulfone-Carbonate Solvents: A Walden Plot Analysis of the Maximally Conductive Compositions," *The Journal of Physical Chemistry C*, vol. 116, no. 45, pp. 23 915–23 920, 2012. doi: 10.1021/jp3067519.
- [132] C. Schreiner, S. Zugmann, R. Hartl, and H. J. Gores, "Fractional Walden Rule for Ionic Liquids: Examples from Recent Measurements and a Critique of the So-Called Ideal KCl Line for the Walden Plot," *Journal of Chemical & Engineering Data*, vol. 55, no. 5, pp. 1784–1788, 2009. doi: 10.1021/je900878j.
- [133] A. Mistry, Z. Yu, L. Cheng, and V. Srinivasan, "On Relative Importance of Vehicular and Structural Motions in Defining Electrolyte Transport," *Journal of The Electrochemical Society*, vol. 170, no. 11, p. 110536, 2023. doi: 10.1149/1945-7111/ad0c66.
- [134] E. R. Logan *et al.*, "A Study of the Physical Properties of Li-Ion Battery Electrolytes Containing Esters," *Journal of The Electrochemical Society*, vol. 165, no. 2, A21–A30, 2018. doi: 10.1149/2.0271802jes.
- [135] T. Kimura, K. Fujii, Y. Sato, M. Morita, and N. Yoshimoto, "Solvation of Magnesium Ion in Triglyme-Based Electrolyte Solutions," *The Journal of Physical Chemistry C*, vol. 119, no. 33, pp. 18911–18917, 2015. doi: 10.1021/acs.jpcc.5b04626.
- [136] M. P. Longinotti and H. R. Corti, "Fractional Walden Rule for Electrolytes in Supercooled Disaccharide Aqueous Solutions," *The Journal of Physical Chemistry B*, vol. 113, no. 16, pp. 5500–5507, 2009. doi: 10.1021/jp810253s.
- [137] M. Petrowsky and R. Frech, "Concentration Dependence of Ionic Transport in Dilute Organic Electrolyte Solutions," *The Journal of Physical Chemistry B*, vol. 112, no. 28, pp. 8285–8290, 2008. doi: 10.1021/jp801146k.
- [138] C. L. Berhaut, D. Lemordant, P. Porion, L. Timperman, G. Schmidt, and M. Anouti, "Ionic association analysis of LiTDI, LiFSI and LiPF₆ in EC/DMC for better Li-ion battery performances," *RSC Advances*, vol. 9, no. 8, pp. 4599–4608, 2019. doi: 10.1039/c8ra08430k.
- [139] M. Vogler, L. Schröder, and B. Zhang, *Helge-Stein-Group/ASAB: ASAB laboratory automation v1.0.1*, 2024. doi: 10.5281/ZENODO.11146671.
- [140] M. Vogler, L. Schröder, and B. Zhang, *Helge-Stein-Group/ASAB: ASAB laboratory automation v2.0.1*, 2024. doi: 10.5281/ZENODO.11146699.
- [141] M. Vogler, S. K. Steensen, F. Ramirez, and G. Pizzi, *BIG-MAP/FINALES2: FINALES v.1.1.0*, 2024. doi: 10.5281/ZENODO.10987727.
- [142] CETONI GmbH, *CETONI Elements*, version 20220926, 2022. [Online]. Available: <https://cetoni.de/cetoni-elements/> (visited on 10/31/2024).
- [143] Anton Paar GmbH, *AP Connect*, Software, version 2.0.2, 2021. [Online]. Available: <https://www.anton-paar.com/de-de/produkte/details/ap-connect/> (visited on 10/31/2024).
- [144] Oxford Instruments plc, *SpinFlow*, version 3.1.0, 2023. [Online]. Available: <https://nmr.oxinst.com/x-pulse-spinflow> (visited on 10/31/2024).
- [145] PalmSens BV, *PSTrace5*, version 5.9.4515, 2023. [Online]. Available: <https://www.palmsens.com/software/ps-trace/> (visited on 10/31/2024).
- [146] F. Rahmanian *et al.*, "Conductivity experiments for electrolyte formulations and their automated analysis," *Scientific Data*, vol. 10, no. 1, 2023. doi: 10.1038/s41597-023-01936-3.
- [147] A. A. Hagberg, D. A. Schult, and P. J. Swart, "Exploring Network Structure, Dynamics, and Function using NetworkX," in *Proceedings of the 7th Python in Science Conference*, G. Varoquaux, T. Vaught, and J. Millman, Eds., Pasadena, CA USA, 2008, pp. 11–15. [Online]. Available: http://conference.scipy.org.s3-website-us-east-1.amazonaws.com/proceedings/scipy2008/paper_2/.

- [148] E. W. Dijkstra, "A note on two problems in connexion with graphs," *Numerische Mathematik*, vol. 1, no. 1, pp. 269–271, 1959. doi: 10.1007/bf01386390.
- [149] H. S. Stein and M. Vogler, *BIG-MAP/finale: Paper Version*, 2023. doi: 10.5281/ZENODO.8009625.
- [150] M. Vogler and F. F. Ramirez, *BIG-MAP/FINALES2_schemas: FINALES schemas v1.0.1*, 2024. doi: 10.5281/ZENODO.11142866.
- [151] M. S. Ding, K. Xu, S. S. Zhang, K. Amine, G. L. Henriksen, and T. R. Jow, "Change of Conductivity with Salt Content, Solvent Composition, and Temperature for Electrolytes of LiPF₆ in Ethylene Carbonate-Ethyl Methyl Carbonate," *Journal of The Electrochemical Society*, vol. 148, no. 10, A1196, 2001. doi: 10.1149/1.1403730.
- [152] E. R. Logan *et al.*, "A Study of the Transport Properties of Ethylene Carbonate-Free Li Electrolytes," *Journal of The Electrochemical Society*, vol. 165, no. 3, A705–A716, 2018. doi: 10.1149/2.0981803jes.
- [153] B. Ghalami Choobar, H. Modarress, R. Halladj, and S. Amjad-Iranagh, "Multiscale Investigation on Electrolyte Systems of [(Solvent + Additive) + LiPF₆] for Application in Lithium-Ion Batteries," *The Journal of Physical Chemistry C*, vol. 123, no. 36, pp. 21 913–21 930, Aug. 2019. doi: 10.1021/acs.jpcc.9b04786.
- [154] M. S. Ding and T. R. Jow, "Conductivity and Viscosity of PC-DEC and PC-EC Solutions of LiPF₆," *Journal of The Electrochemical Society*, vol. 150, no. 5, A620–A628, 2003. doi: 10.1149/1.1566019.
- [155] M. S. Ding, "Liquid Phase Boundaries, Dielectric Constant, and Viscosity of PC-DEC and PC-EC Binary Carbonates," *Journal of The Electrochemical Society*, vol. 150, no. 4, A455–A462, 2003. doi: 10.1149/1.1557968.
- [156] M. S. Ding and T. R. Jow, "How Conductivities and Viscosities of PC-DEC and PC-EC Solutions of LiBF₄, LiPF₆, LiBOB, Et₄NBF₄, and Et₄NPF₆ Differ and Why," *Journal of The Electrochemical Society*, vol. 151, no. 12, A2007–A2015, 2004. doi: 10.1149/1.1809575.
- [157] M. S. Ding and T. R. Jow, "Physicochemical Properties of Non-Aqueous Solvents and Electrolytes for Lithium Battery Applications," *ECS Transactions*, vol. 16, no. 35, pp. 183–214, 2009. doi: 10.1149/1.3123139.
- [158] M. S. Ding, Q. Li, X. Li, W. Xu, and K. Xu, "Effects of Solvent Composition on Liquid Range, Glass Transition, and Conductivity of Electrolytes of a (Li, Cs)PF₆ Salt in EC-PC-EMC Solvents," *The Journal of Physical Chemistry C*, vol. 121, no. 21, pp. 11 178–11 183, May 2017. doi: 10.1021/acs.jpcc.7b03306.
- [159] L. Merker and M. Vogler, *BIG-MAP/FINALES_Overlord_tenant: Overlord Tenant für FINALES*, 2024. doi: 10.5281/ZENODO.11145783.
- [160] F. Liot, V. Granata, G. Pizzi, and N. Marzari, *BIG-MAP Archive*, Feb. 2023. [Online]. Available: <https://archive.big-map.eu/> (visited on 10/31/2024).
- [161] Allianz Der Deutschen Wissenschaftsorganisationen, "Grundsätze zum Umgang mit Forschungsdaten," 2010. doi: 10.2312/ALLIANZOA.019.
- [162] Deutsche Forschungsgemeinschaft, "DFG Guidelines on the Handling of Research Data," 2015. [Online]. Available: <https://www.dfg.de/resource/blob/172098/b08fcad16f1ff5ddca967f1ebde3a8c3/guidelines-research-data-data.pdf> (visited on 10/31/2024).
- [163] F. Rahmanian, S. Fuchs, B. Zhang, M. Fichtner, and H. S. Stein, "Autonomous millimeter scale high throughput battery research system," *Digital Discovery*, vol. 3, no. 5, pp. 883–895, 2024. doi: 10.1039/d3dd00257h.
- [164] B. Zhang, L. Merker, and M. Vogler, *BIG-MAP/FINALES_AutoBASS_tenant: AutoBASS Tenant for FINALES*, 2024. doi: 10.5281/ZENODO.11145983.
- [165] L. Merker and M. Vogler, *BIG-MAP/FINALES_Cycler_tenant: Cycler Tenant for FINALES*, 2024. doi: 10.5281/ZENODO.11145850.

- [166] B. P. Cahill, "Introduction," in *Micro-Segmented Flow, Applications in Chemistry and Biology*, B. P. C. J. Michael Köhler, Ed. Springer Berlin Heidelberg, 2013, pp. 1–3, ISBN: 9783642387807. DOI: 10.1007/978-3-642-38780-7_1.

List of Figures

2.1	A schematic representation of a lithium-ion battery	4
3.1	The relation between a ^1H -NMR spectrum and Pascal's triangle	12
3.2	The pulse sequence of a regular FID	13
3.3	The pulse sequence of a PGSE experiment	14
3.4	The impedance response of the Randles circuit	16
4.1	A schematic overview of the ASAB setup	24
4.2	The formulation unit of the ASAB setup	25
4.3	The flow-through configuration of the NMR instrument	27

Glossary

Bode plot	A plot of $\log(Z)$ and $-\phi$ vs. $\log(\nu)$ with frequency ν and phase ϕ used for the analysis of EIS data. [96]
capability	A unique set of a quantity and a method in a FINALES instance. [14]
cell constant	A calibration constant for measuring cells used in EIS to determine the conductivity of the sample. [102]
chemical shift	A relative measure of the shift in resonance frequency of the observed species in the molecule of interest with respect to a reference substance in NMR measurements. [38]
drive element	The component in a VTD causing the vibration of the U-shaped glass tube. [103]
dynamic viscosity	The viscosity resulting when thinking of the liquid moving in layers with different velocity. [117]
electrochemical stability window	The voltage range between the oxidation and reduction reactions of an electrolyte. This quantity determines the possible operating voltages of the considered cell. [19]
energy density	The amount of energy a battery provides relative to the volume or mass of the battery. [4]
external standard	A reference substance in a separate, small capillary, which is inserted into the sample tube prior to a measurement used to define the chemical shift scale of the spectrum without adding a reference substance into the sample. [38]
Fourier transform	A mathematical procedure transforming data from the time-domain to the frequency-domain. [38]
impedance	The total resistance of a system against the flow of a current. [96]
internal standard	A reference substance added to the sample used to define the chemical shift scale of an NMR spectrum. [38]
ionicity	The deviation of conductivity from the behaviour predicted by the Nernst-Einstein equation. It can be used to investigate the effect of the correlated movement of ions on the conductivity of an electrolyte. [122]
J-coupling	The interaction between nuclei in the vicinity to the observed nucleus in NMR. Also called <i>spin-spin coupling</i> or <i>scalar coupling</i> . [38, 87]

kinematic viscosity	The viscosity resulting when accounting for the fact, that the force applied to the liquid counteracts not only the viscosity but also maintains the velocity within the liquid. [117]
Larmor frequency	The resonance frequency of a nucleus, which can be thought of as the frequency of the precession of the spins around the direction of an applied magnetic field. This relates to the energy of a photon which allows for a transition of the nuclear spin between energy levels. [38]
method	The means by which a result for a quantity is obtained in a FINALES-based MAP. This may be an experimental or computational procedure. [14]
multitenancy	A concept in FINALES-based MAPs allowing for several tenants providing redundant capabilities. [13]
Newtonian fluid	A fluid with a viscosity independent of the shear rate. [114]
non-Newtonian fluid	A fluid, for which the viscosity depends on the shear rate. [114]
Nyquist plot	A plot of $-Z''$ vs. Z' used for the analysis of EIS data. [96]
pick-up element	The component in a VTD recording the vibration period of the U-shaped glass tube. [103]
primary battery	A battery that cannot be recharged. [3]
quantity	A physical quantity or a service available in a FINALES-based MAP. [14]
Randles circuit	An equivalent circuit commonly used in EIS suitable for representing a system with an electrochemical reaction taking place. [96, 98]
secondary battery	A battery that can be recharged. [3]
specific energy	The amount of energy that can be obtained from a battery relative to the mass of the battery (see also <i>energy density</i>). [4]
tenant	The term used to refer to clients and modules in the context of FINALES MAPs. [13]
transfer function	A function representing the relation between the input and the output signal in an EIS measurement. [96]
Walden plot	A plot of the molar ionic conductivity vs. fluidity, which provides information about the ionicity of the conducting salt in an electrolyte. [122, 125]
Walden rule	The product of the limiting conductivity and the viscosity of the solvent of an electrolyte is constant. [124]

Acknowledgments

First, I would like to express my sincere gratitude to my supervisor **Prof. Helge S. Stein** for giving me the opportunity to work on this thesis. I am grateful for the support you provided and for the trust you placed in my abilities. Thank you also for challenging me to continuously expand my knowledge, gain new skills and embrace steep learning curves. I am especially thankful that you made me a part of the early FINALES core development team and for actively pushing this project ahead. During this project, I gained numerous new skills and would like to thank all the partners and contributors for this exciting experience, all the motivation, input, ideas, suggestions, and encouragements. Without the determination and support of **Assoc. Prof. Arghya Bhowmik**, **Dr. Felix Hanke**, **Dr. Giovanni Pizzi**, and **Prof. Tejs Vegge**, the FINALES framework would not have been as successful as it was. Special thanks in this context go to **Dr. Francisco F. Ramírez** and **Simon K. Steensen** for teaching me how to collaborate in software development projects and the overall very productive teamwork.

Of course this thesis would not have been possible without being integrated in a motivated and ambitious research group. Therefore, I would like to thank all the group members for actively supporting me in acquiring new skills in programming, electrochemistry and various adjacent fields. My thank goes to **Bojing Zhang** for showing me how to program an Arduino[®] board and using it with the solenoid valve, to **Dr.-Ing. Fuzhan Rahmanian** for her support in coding questions, **Aleksei Sanin** and **Stefan Fuchs** for valuable discussions about the detailed design and verification of the conductivity cell, and **Jackson K. Flowers** for fruitful scientific discussions. Thank you all for being such a dynamic and motivated team. A special heartfelt thank you goes to **Leon Merker** for the good collaboration and the trustful communication during our time as a team of two remote doctoral students. I thank you and **Dr. Sibylle Riedel** for fruitful discussions and your honest feedback. When it comes to trustful conversations, I would like to also express my deep gratitude to **Dr. Katarina Cicvarić** for being my mentor with an open ear for my concerns and practical suggestions.

I also owe thanks to **Dr. Raiker Witter** and **Dr. Benno Meier** for their support with learning how to use the NMR device and analysing the obtained results. Short chats with you resolved issues that reading textbooks could not. I am also grateful for the thorough work done by **Lisa Schröder** during her bachelor thesis. It was a pleasure to work with you. Further, I am thankful for the support I received from **Dr. Pascal Acker** during the start of my time as a doctoral student.

I would also like to express my gratitude to **Prof. Maximilian Fichtner** for employing me in his group and being open to discuss various solutions to scientific as well as administrative challenges. Besides the technical and scientific support, I would like to also thank **Annika Groß** and **Sarah Hameister** for sharing their positive nature and lightening the mood in challenging situations. Also, I would like to say thank you to **Heike Kull** and the team around the **WattsNext** game for the fun time we had focusing on topics quite different from our scientific work.

Last but certainly not least, my thank goes to my **family** and **friends** for accompanying me during my doctoral phase. As always, you all patiently listened to the topics that were on my mind and found encouraging words or a funny comment to make. **Patricia Kneer** deserves a special mention for making me aware of the announcement for this opportunity. Thank you for your friendship and attentiveness. Finally, my deepest and heartfelt gratitude goes to **Dominik Sterk**. Apart from sparking my interest in programming and telling me about your projects using graphs and pointers, your tireless support even during the most challenging times of my doctoral phase enabled me to follow my high hopes and outgrow myself. Without having you by my side, I would not have entered this field.

Scientific Contributions

Peer reviewed research articles

Autonomous Battery Optimization by Deploying Distributed Experiments and Simulations

M. Vogler, S. K. Steensen, F. F. Ramírez, L. Merker, J. Busk, J. M. Carlsson, L. H. Rieger, B. Zhang, F. Liot, G. Pizzi, F. Hanke, E. Flores, H. Hajiyani, S. Fuchs, A. Sanin, M. Gaberšček, I. E. Castelli, S. Clark, T. Vegge, A. Bhowmik and H. S. Stein

Advanced Energy Materials, vol. 14, no. 46, p. 2403263, 2024. doi: 10.1002/aenm.202403263

Apples to apples: shift from mass ratio to additive molecules per electrode area to optimize Li-ion batteries

B. Zhang, L. Merker, **M. Vogler**, F. Rahmanian and H. S. Stein

Digital Discovery, vol. 3, no. 7, pp. 1342–1349, 2024. doi: 10.1039/D4DD00002A

Brokering between tenants for an international materials acceleration platform

M. Vogler, J. Busk, H. Hajiyani, P. B. Jørgensen, N. Safaei, I. E. Castelli, F. F. Ramirez, J. Carlsson, G. Pizzi, S. Clark, F. Hanke, A. Bhowmik and H. S. Stein

Matter, vol. 6, no. 9, pp. 2647–2665, 2023. doi: 10.1016/j.matt.2023.07.016

Ionic conductivity, viscosity, and self-diffusion coefficients of novel imidazole salts for lithium-ion battery electrolytes

A. Szczęśna-Chrzan, **M. Vogler**, P. Yan, G. Z. Żukowska, C. Wölke, A. Ostrowska, S. Szymańska, M. Marcinek, M. Winter, I. Cekic-Laskovic, W. Wieczorek and H. S. Stein

Journal of Materials Chemistry A, vol. 11, no. 25, pp. 13 483–13 492, 2023. doi: 10.1039/d3ta01217d

Conductivity experiments for electrolyte formulations and their automated analysis

F. Rahmanian, **M. Vogler**, C. Wölke, P. Yan, S. Fuchs, M. Winter, I. Cekic-Laskovic and H. S. Stein

Scientific Data, vol. 10, no. 1, 2023. doi: 10.1038/s41597-023-01936-3

One-Shot Active Learning for Globally Optimal Battery Electrolyte Conductivity

F. Rahmanian, **M. Vogler**, C. Wölke, P. Yan, M. Winter, I. Cekic-Laskovic and H. S. Stein

Batteries & Supercaps, vol. 5, no. 10, 2022. doi: 10.1002/batt.202200228

From materials discovery to system optimization by integrating combinatorial electrochemistry and data science

H. S. Stein, A. Sanin, F. Rahmanian, B. Zhang, **M. Vogler**, J. K. Flowers, L. Fischer, S. Fuchs, N. Choudhary and L. Schröder

Current Opinion in Electrochemistry, vol. 35, p. 101053, 2022. doi: 10.1016/j.coelec.2022.101053

Oral Presentations

Autonomous battery research in geographically distributed MAPs

M. Vogler

LMS Seminars, Villigen, Switzerland (October 3, 2024)

Combinatorial formulation, physicochemical and electrochemical investigation of battery electrolytes

M. Vogler, Helge S. Stein

BIG-MAP EUnified Battery Data Space Workshop, Grindelwald, Switzerland (online) (January 29 - 31, 2024)

Lessons learned from an international Materials Acceleration Platform

M. Vogler, J. Busk, H. Hajjani, P. B. Jørgensen, N. Safaei, I. E. Castelli, F. F. Ramirez, J. M. Carlsson, G. Pizzi, S. Clark, F. Hanke, A. Bhowmik, H. S. Stein

European Materials Research Society 2023 Spring Meeting, Strasbourg, France (May 29 - June 2, 2023)

Design, demonstration, and lessons learned from a European materials acceleration platform

M. Vogler, J. Busk, H. Hajjani, P. B. Jørgensen, N. Safaei, I. E. Castelli, F. F. Ramirez, J. M. Carlsson, G. Pizzi, S. Clark, F. Hanke, A. Bhowmik, H. S. Stein

11th International Workshop on Combinatorial Materials Science and Technology, Golden Colorado, USA (September 26 - 30, 2022)

Posters

Automated Investigation of Battery Electrolytes

M. Vogler, H. S. Stein

POLiS Annual Conference 2024, June 18 - 19, 2024 (Karlsruhe, Germany)

A distributed MAP for autonomous battery research

M. Vogler, S. K. Steensen, F. F. Ramirez, L. Merker, J. Busk, J. M. Carlsson, L. H. Rieger, B. Zhang, F. Liot, G. Pizzi, F. Hanke, E. Flores, H. Hajjani, S. Fuchs, A. Sanin, M. Gaberšček, I. E. Castelli, S. Clark, T. Vegge, A. Bhowmik, and H. S. Stein

Battery 2030+ Annual Conference 2024, Grenoble, France (May 28 - 29, 2024)

Physicochemical characterization of alternative conducting salts for lithium ion battery electrolytes

M. Vogler, A. Szczęsna-Chrzan, P. Yan, G. Z. Żukowska, C. Wölke, A. Ostrowska, S. Szymańska, M. Marcinek, M. Winter, I. Cekic-Laskovic, Władysław Wieczorek and H. S. Stein

BIG-MAP 6th project meeting, Brussels, Belgium (October 24 - 25, 2023)

Physicochemical characterization of alternative conducting salts for lithium ion battery electrolytes

M. Vogler, A. Szczęsna-Chrzan, P. Yan, G. Z. Żukowska, C. Wölke, A. Ostrowska, S. Szymańska, M. Marcinek, M. Winter, I. Cekic-Laskovic, W. Wieczorek and H. S. Stein

16th International conference on materials chemistry (MC16), Dublin, Ireland (online) (July 3 - 6, 2023)

Datasets

Ionic conductivity, viscosity, and self-diffusion coefficients of novel imidazole salts for lithium-ion battery electrolytes

A. Szczęsna-Chrzan, **M. Vogler**, P. Yan, G. Z. Żukowska, C. Wölke, A. Ostrowska, S. Szymańska, M. Marcinek, M. Winter, I. Cekic-Laskovic, W. Wieczorek and H. S. Stein

Zenodo, doi: 10.5281/zenodo.14044558

FINALES (06/2022) – Electrolyte Optimization for Minimum Density and Maximum Viscosity

M. Vogler, J. Busk, H. Hajiyani, P. B. Jørgensen, N. Safaei, I. E. Castelli, F. F. Ramirez, J. M. Carlsson, G. Pizzi, S. Clark, F. Hanke, A. Bhowmik and H. S. Stein

Materials Cloud, doi: 10.24435/materialscloud:ph-jb

FINALES - Electrolyte optimization for maximum conductivity and for maximum cycle life

S. K. Steensen, **M. Vogler**, F. F. Ramirez, L. Merker, J. Busk, J. M. Carlsson, L. H. Rieger, B. Zhang, F. Liot, G. Pizzi, F. Hanke, E. Flores, H. Hajiyani, S. Fuchs, A. Sanin, M. Gaberšček, I. E. Castelli, S. Clark, T. Vegge, A. Bhowmik and H. S. Stein

Materials Cloud, doi: 10.24435/materialscloud:qt-1s

Dataset of 5035 Conductivity Experiments for Lithium-Ion Battery Electrolyte Formulations at Various Temperatures

F. Rahmanian, **M. Vogler**, C. Wölke, P. Yan, S. Fuchs, M. Winter, I. Cekic-Laskovic and H. S. Stein

Zenodo, doi: 10.5281/zenodo.7244939

A Rights and Permissions from publishers

A.1 Ionic conductivity, viscosity, and self-diffusion coefficients of novel imidazole salts for lithium-ion battery electrolytes

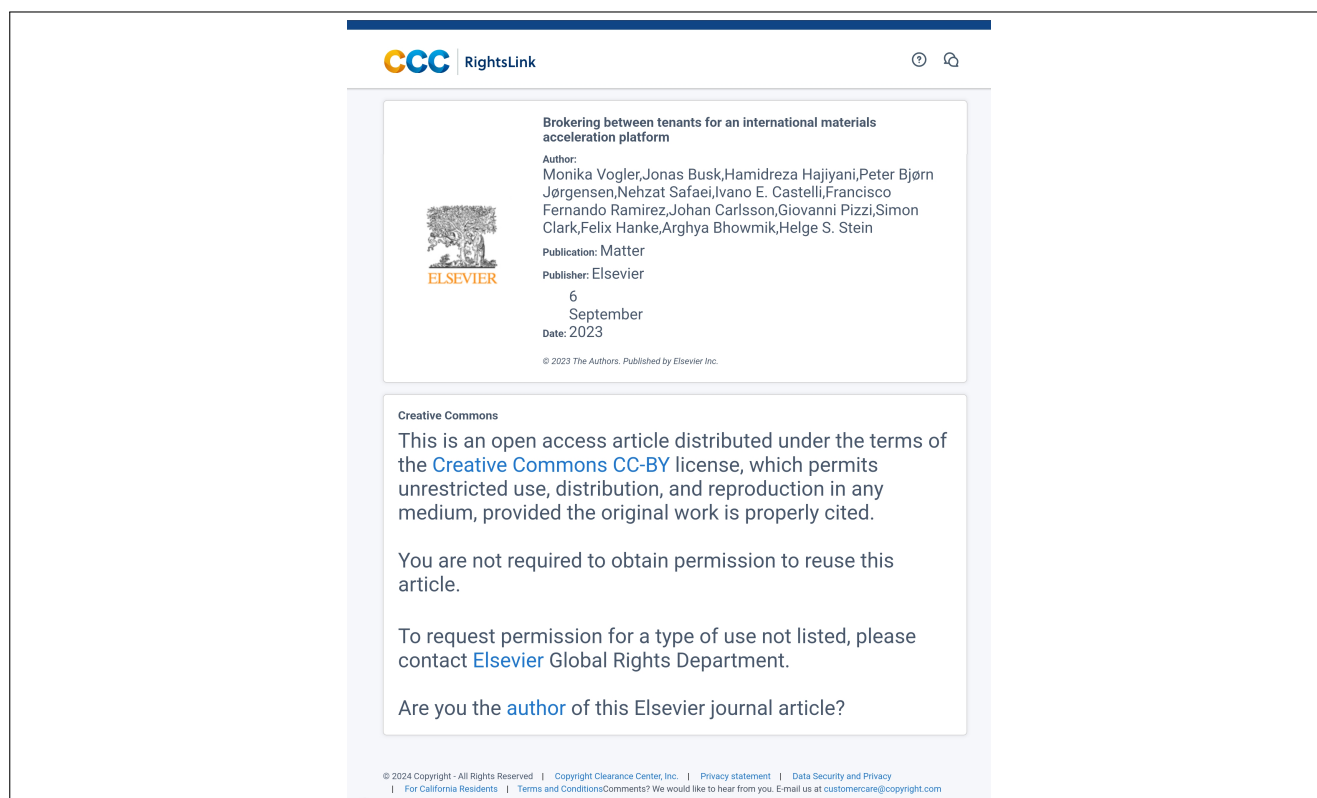
Ionic conductivity, viscosity, and self-diffusion coefficients of novel imidazole salts for lithium-ion battery electrolytes

A. Szczęsna-Chrzan, M. Vogler, P. Yan, G. Z. Żukowska, C. Wölke, A. Ostrowska, S. Szymańska, M. Marcinek, M. Winter, I. Cekic-Laskovic, W. Wieczorek and H. S. Stein, *J. Mater. Chem. A*, 2023, **11**, 13483 DOI: 10.1039/D3TA01217D

This article is licensed under a [Creative Commons Attribution 3.0 Unported Licence](#). You can use material from this article in other publications without requesting further permissions from the RSC, provided that the correct acknowledgement is given.


Read more about [how to correctly acknowledge RSC content](#).


A.2 Brokering between tenants for an international materials acceleration platform



The screenshot shows the RightsLink interface for the article "Brokering between tenants for an international materials acceleration platform". The page header includes the CCC RightsLink logo and navigation icons. The article title is displayed prominently. Below the title, the author list is provided: Monika Vogler, Jonas Busk, Hamidreza Hajiyani, Peter Bjørn Jørgensen, Nehzat Safaei, Ivano E. Castelli, Francisco Fernando Ramirez, Johan Carlsson, Giovanni Pizzi, Simon Clark, Felix Hanke, Arghya Bhowmik, Helge S. Stein. The publication information is listed as Matter, Elsevier, 6 September 2023. A Creative Commons license notice states that the article is open access under the CC-BY license, allowing unrestricted use, distribution, and reproduction in any medium, provided the original work is properly cited. It also notes that permission is not required to reuse the article, but for other types of use, contact with Elsevier Global Rights Department is advised. A question asks if the user is the author of the article. The footer contains copyright information for 2024, including links to the Privacy statement, Data Security and Privacy, and Terms and Conditions.

A.3 Autonomous battery optimisation by deploying distributed experiments and simulations

 RightsLink 🔍



Autonomous Battery Optimization by Deploying Distributed Experiments and Simulations
Author: Monika Vogler, Simon Krarup Steensen, Francisco Fernando Ramirez, et al
Publication: Advanced Energy Materials
Publisher: John Wiley and Sons
Date: Oct 18, 2024

© 2024 The Author(s). Advanced Energy Materials published by Wiley-VCH GmbH

Open Access Article

This is an open access article distributed under the terms of the [Creative Commons CC BY](#) license, which permits unrestricted use, distribution, and reproduction in any medium, provided the original work is properly cited.

You are not required to obtain permission to reuse this article.

For an understanding of what is meant by the terms of the Creative Commons License, please refer to [Wiley's Open Access Terms and Conditions](#).

Permission is not required for this type of reuse.

Wiley offers a professional reprint service for high quality reproduction of articles from over 1400 scientific and medical journals. Wiley's reprint service offers:

- Peer reviewed research or reviews
- Tailored collections of articles
- A professional high quality finish
- Glossy journal style color covers
- Company or brand customisation
- Language translations
- Prompt turnaround times and delivery directly to your office, warehouse or congress.

Please contact our Reprints department for a quotation.
Email corporatesaleseurope@wiley.com or corporatesalesusa@wiley.com or corporatesalesDE@wiley.com.

© 2024 Copyright - All Rights Reserved | Copyright Clearance Center, Inc. | Privacy statement | Data Security and Privacy
| For California Residents | Terms and ConditionsComments? We would like to hear from you. E-mail us at customer@copyright.com

B Additional resources and tools

During the compilation of this thesis, several tools were used that are not given in the bibliography due to their more general character. They are instead reported in the following table. Commonly used services such as online search engines and standard libraries as well as the tools used in the process of creating the included publications are not listed here.

Name	Application	Reference/URL
dict.cc	dictionary	dict.cc GmbH, Vienna, Austria https://www.dict.cc/ , last accessed 31.10.2024 © Paul Hemetsberger
DeepL	dictionary	DeepL SE, Cologne, Germany https://www.deepl.com/de/translator , last accessed 31.10.2024
Duden	dictionary	Cornelsen Verlag GmbH, Berlin, Germany https://www.duden.de , last accessed 28.10.2024 © Cornelsen Verlag GmbH
ETO Map of Science	literature research	Emerging Technology Observatory https://sciencemap.eto.tech/?mode=map , last accessed 18.07.2024 CC BY-NC 4.0 (https://creativecommons.org/licenses/by-nc/4.0/)
Connected Papers	literature research	https://www.connectedpapers.com/ , last accessed 18.07.2024 (uses <i>Semantic Scholar Open Research Corpus</i> ¹) licensed under ODC-BY (https://opendatacommons.org/licenses/by/1-0/) ¹ Waleed Ammar <i>et al.</i> "Construction of the Literature Graph in Semantic Scholar," in: <i>Proceedings of the 2018 Conference of the North American Chapter of the Association for Computational Linguistics: Human Language Technologies, Volume 3 (Industry Papers)</i> , Association for Computational Linguistics, 2018. DOI: 10.18653/v1/n18-3011.
PubChem	research chemicals	https://pubchem.ncbi.nlm.nih.gov , last accessed 30.10.2024 National Library of Medicine, 8600 Rockville Pike, Bethesda, MD 20894
Inkscape™: Open Source Scalable Vector Graphics Editor	graphics	https://inkscape.org/ , last accessed 20.07.2024 GNU General Public License version 3 (https://www.gnu.org/licenses/gpl-3.0) © Inkscape-Developers Team

Name	Application	Reference/URL
Gimp	graphics	https://www.gimp.org/ , last accessed 20.07.2024 GNU General Public License version 3 (https://www.gnu.org/licenses/gpl-3.0) © Spencer Kimball, Peter Mattis and the GIMP-Developers Team
TeX Live 2023	typesetting	https://www.tug.org/texlive/ , last accessed 20.07.2024
TeXstudio (version 4.8.4)	typesetting	https://www.texstudio.org/ , last accessed 20.07.2024 GNU General Public License version 2 (https://www.gnu.org/licenses/old-licenses/gpl-2.0.en.html) © TeXstudio: Benito van der Zander, Jan Sundermeyer, Daniel Braun, Tim Hoffmann; Texmaker: Pascal Brachet; QCodeEdit: Luc Bruant; HTML-Export: Joël Amblard
JabRef (version 5.15)	reference management	https://www.jabref.org/ , last accessed 31.10.2024 MIT License © 2003-2024 JabRef Authors
Einführung in \LaTeX	typesetting	H. Voß, <i>Einführung in LaTeX</i> , 3., korrigierte Auflage, Lehmanns Media, 2017.
TUM Templates	typesetting	The LaTeX Project Public License (LPPL Version 1.3c) © The LaTeX4E! Team
Python (version 3.12.2)	data processing (Figures 3.1a, 3.4a, 3.4b)	Python Software Foundation https://www.python.org/ Copyright © 2001-2023 Python Software Foundation; All Rights Reserved
Matplotlib (version 3.9.2)	creating parts of Figures 3.1a, 3.4a, 3.4b	https://matplotlib.org/ , last accessed 20.07.2024 License agreement for matplotlib versions 1.3.0 and later https://matplotlib.org/stable/project/license.html © 2012-2024 Matplotlib Development Team; All Rights Reserved
numpy (version 2.1.2)	data processing (Figures 3.1a, 3.4a, 3.4b) and analysis of the time needed for a formulation reported in chapter 7	C. R. Harris <i>et al.</i> , "Array programming with NumPy," <i>Nature</i> , vol. 585, no. 7825, pp. 357–362, 2020. doi: 10.1038/s41586-020-2649-2.
pandas (version 2.2.3)	data processing (Figures 3.1a, 3.4a, 3.4b)	The pandas development team, "pandas-dev/pandas: Pandas," doi: 10.5281/zenodo.3509134. W. McKinney, "Data Structures for Statistical Computing in Python," 2010, doi: 10.25080/Majora-92bf1922-00a.
nmrglue (version 0.10)	data processing (Figure 3.1a)	J. J. Helmus and C. P. Jaroniec, "Nmrglue: an open source Python package for the analysis of multidimensional NMR data," in: <i>Journal of Biomolecular NMR</i> , vol. 55, no. 4, 2013, pp. 355–367. doi: 10.1007/s10858-013-9718-x.

Name	Application	Reference/URL
Visual Studio Code	programming	https://code.visualstudio.com/ , last accessed 20.07.2024 Microsoft Software License Terms (https://code.visualstudio.com/License) © Microsoft Corporation. All rights reserved.
SQLite	database interaction	alexvzz Apache License Version 2.0 (extension for Visual Studio Code)
Edit csv	visualisation of CSV files	janisdd MIT License (extension for Visual Studio Code)
Git	version control	https://git-scm.com , last accessed 28.10.2024
TUM-Zitierleitfaden	citations	Technische Universität München, Universitätsbibliothek https://mediatum.ub.tum.de/1225458 , last accessed 28.10.2024 CC BY-SA 4.0 (https://creativecommons.org/licenses/by-sa/4.0/)